Charged-current neutrino interactions with nucleons and nuclei at intermediate energies

TESIS DOCTORAL

Guillermo Daniel Megías Vázquez

Departamento de Física Atómica, Molecular y Nuclear

Facultad de Física

UNIVERSIDAD DE SEVILLA

Mayo 2017

Charged-current neutrino interactions with nucleons and nuclei at intermediate energies

Memoria de Tesis Doctoral realizada por

Guillermo Daniel Megías Vázquez

para optar al grado de Doctor en Física Nuclear

Dirigida por los Doctores

Maria B. Barbaro

Juan A. Caballero Carretero

Departamento de Física Atómica, Molecular y Nuclear

Facultad de Física

UNIVERSIDAD DE SEVILLA

Mayo 2017

Agradecimientos

Más de cuatro años de trabajo decaen a su estado fundamental en estas páginas, las cuales constituyen una ventana abierta hacia un mundo, el de la investigación, donde muchas veces lo último que uno sabe es por donde empezar. Sobre todo, cuando uno se enfrenta a la difícil tarea de sintetizar en unas breves líneas la gratitud hacia todas las personas que, de una u otra forma, han hecho posible este ilusionante proyecto.

En primer lugar, quiero tener unas palabras de agradecimiento con mi director de tesis, Juan Antonio Caballero, por la confianza depositada en mí para el desarrollo de este trabajo y su dedicación e interés constante en llevar este proyecto adelante. Un excelente investigador, tanto a nivel profesional como personal, que además ha sido protagonista en mi formación académica desde que tuviera el placer de disfrutar de sus clases hará ya unos años. Recuerdo cuando en la asignatura de Física de Partículas, propuso como trabajo de investigación "adoptar una partícula". En esos momentos mi duda osciló entre acoger al neutrino o al muón. Lo que yo no imaginaba por aquel entonces era que pasados varios años estaría viendo en su madurez a esas partículas *ligeras* a las que un día vi nacer.

Del mismo modo, agradezco especialmente a mi codirectora de tesis, Maria Barbaro, su apoyo y dedicación sincera durante estos años así como su hospitalidad durante mis estancias en Turín. A todo ello, hay que añadir el innegable esfuerzo de haber corregido toda esta tesis desde la distancia y su ayuda y rapidez siempre que he necesitado algún informe para los distintos enredos burocráticos. Mención especial también merecen Quique Amaro y Nacho Ruiz Simó de la Universidad de Granada con quienes he colaborado en los últimos meses, así como la generosidad y hospitalidad de Carlotta Giusti durante mi breve estancia en la Universidad de Pavia. De todos ellos guardo grandes recuerdos.

Si bien no aparece implícitamente como director de esta tesis, gran parte del conocimiento adquirido durante esta etapa y plasmado en estas páginas se lo debo a Bill Donnelly, de quien admiro profundamente su gran sabiduría en el campo de la Física y a quien agradezco sus ideas y su sincero interés durante mi estancia en el MIT. La hospitalidad de Bill así como la de su mujer, Barbara, hicieron de mi experiencia en Boston un recuerdo imborrable.

En el plano económico, caben mencionar las ayudas recibidas por los distintos proyectos de investigación de la Universidad de Sevilla y del Ministerio de Economía y Competitividad (anteriormente de Ciencia), así como a los contratos predoctorales de la Fundación Cámara y de los Proyectos de Excelencia de la Junta de Andalucía, pero cabe más aún agradecer honestamente el esfuerzo de los distintos funcionarios y, en general, el de los trabajadores, que con sus impuestos contribuyen a mantener la cada vez más complicada labor científica en este país.

Tampoco puedo obviar en estas líneas el indudable valor humano y profesional de todos los investigadores que he conocido en distintos congresos a lo largo del mundo, donde he adquirido una visión más amplia de la investigación en sus distintos ámbitos. Asimismo, en el plano más local, tengo que agradecer al *Cluster* por aguantar con vida y a todos los compañeros del departamento el buen ambiente en el trabajo y fuera de él, por los almuerzos y los cafés juntos y por los cada vez más olvidados viernes de nachos y futbolín que me hicieron ver de una forma más "realista" los procesos de dispersión.

Pero no sólo el mundo de la Física ha contribuido a la realización de este proyecto. Esta memoria no hubiera sido posible sin esas personas que dan un valor medible al observable que es la vida. A los que están incluso cuando no he tenido tiempo para quedar, y a los que en cierto modo me tendré que volver a presentar. Por ello, no puedo terminar estas páginas sin agradecer a quienes están siempre ahí para leer estás líneas (aunque sólo interaccionen débilmente con ellas) y a los que ya no están para verlas desde tan cerca. En especial a mi madre y a mi padre por ayudarme y enseñarme a llegar hasta el día de hoy; y a Bibi por su cariño, sus ánimos y por aguantar todos mis *muones*.

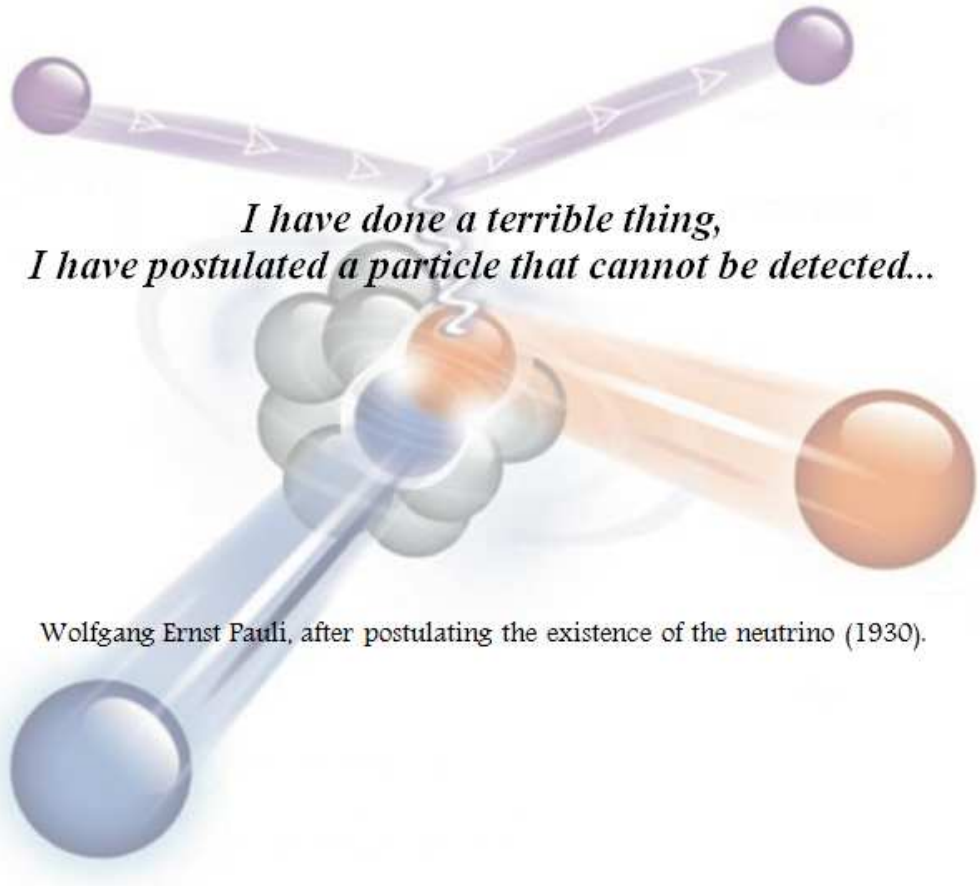

I have done a terrible thing,
I have postulated a particle that cannot be detected...

Wolfgang Ernst Pauli, after postulating the existence of the neutrino (1930).

Abstract

Nowadays, the interest in neutrinos extends to a large variety of fields in Astrophysics, Nuclear Physics and Particle Physics. One of the open questions in theoretical physics is the description of neutrino oscillations for which an accurate interpretation of neutrino-nucleus reactions is crucial. In this context, recent years have witnessed an intense experimental and theoretical activity to determine the properties of neutrinos and their interaction with matter.

This PhD Thesis is thus focused on the analysis of charged-current neutrino-nucleus reactions at kinematics of interest for neutrino oscillation experiments, where the neutrino energy is typically in the GeV region. Additionally, weak interactions in the nuclear medium at intermediate energies are an extraordinary opportunity to study the dynamics of the nuclear many-body system, beyond the information accesible from electron and hadron probes, and to gain a deeper knowledge of the axial structure and the strangeness content of the nucleons.

In any accelerator-based neutrino oscillation experiment, neutrinos are produced as the decay products of successive reactions, thus implying a wide-ranged energy beam. Hence, when interacting with the nuclear matter, a large variety of nuclear effects come into play, going from quasielastic scattering to deep inelastic processes, multi-nucleon excitations or meson production via nucleon resonances. Accordingly, robust models that properly describe neutrino-nucleus interactions over the whole experimental range (of the order of 10s of MeV up to 10s of GeV) are required for the experimental analyses. Notice also that the kinematics involved demand a relativistic description of the microscopic nuclear structure.

In this thesis, the analysis of these processes are addressed by using realistic models that provide, within a fully relativistic framework, an accurate description of the different reaction mechanisms of relevance for neutrino oscillation measurements. We begin analyzing neutrino scattering off free nucleons and describing the weak hadronic responses together with the inner structure of the nucleons. With the aim of achieveing a consistent analysis of charged-current quasielastic (CCQE) neutrino interactions with nuclei, we present the so-called SuSAv2 model, which is based on the superscaling behavior exhibited by electron scattering data and makes use of the relativistic mean field (RMF) theory to describe the nuclear effects arising in neutrino-nucleus interactions. This prescription accounts for the final-state interactions (FSI) between the outgoing nucleon and the residual nucleus and allows for a description in terms of the different isovector/isoscalar and axial/vector reaction channels that play a role in weak interactions. At very high kinematics, where FSI are negligible, we approach our model to the relativistic plane wave impulse approximation (RPWIA) where no FSI affect the outgoing nucleon.

Furthemore, a basic feature in this thesis also concerns the evaluation of multi-nucleon excitations, in particular two-body meson exchange currents (2p-2h MEC) contributions, which are proved to be an essential ingredient to interpret neutrino cross section measurements at interme-

diate energies. In this regard, we develop a highly accurate parametrization of the 2p-2h MEC nuclear responses based on a fully relativistic microscopic calculation.

In order to test the reliability of this SuSAv2-MEC model, we firstly compare our predictions with the large amount of existing inclusive $^{12}\mathrm{C}(e,e')$ data over the whole energy spectrum. In this connection, we also extend our description to the complete inelastic regime performing a detailed analysis of the inelastic structure functions for protons and neutrons. All this provides a solid benchmark to assess the validity of our model for the analysis of charged-current neutrino-nucleus cross sections. Regarding this point, we compare our calculations with recent CCQE and inclusive ν_μ and $\overline{\nu}_\mu$ measurements on $^{12}\mathrm{C}$ from different collaborations: MiniBooNE, T2K, MINERνA, NOMAD and SciBooNE, covering an energy range from a few MeV to tens of GeV. This comparison also allows us for a deeper understanding of the nuclear reaction mechanisms at different kinematics as well as their influence in terms of the energy and momentum transfers to the nucleus. In this regard, the SuSAv2- MEC approach is applied to the analysis of diverse nuclei of relevance for future neutrino oscillation experiments with the aim of shedding light on the experimental uncertainties arising from nuclear effects in both initial and final states. Furthermore, the SuSAv2-MEC can easily make predictions at high kinematics in which other microscopic-based models would require demanding, time-consuming calculations.

Moreover, we also focus on the difference between electron and muon neutrino reactions, where a detailed knowledge of ν_μ and ν_e cross sections is decisive in connection to the $\nu_\mu \rightarrow \nu_e$ oscillation experiments aiming at the determination of the neutrino mass hierarchy and the search for CP violation in the leptonic sector.

In summary, this PhD thesis constitutes an extensive analysis of the different neutrino-nucleus interaction mechanisms of interest for neutrino oscillation experiments and conforms an open window for further works and collaborations in hadronic and nuclear physics.

Contents

Chapter 1

Introduction

1.1 A brief history of neutrino

When Wolfgang Pauli postulated the existence of the neutrino in 1930 to preserve energy and momentum conservation in the β-decay process, he was afraid that this extremely light and elusive particle would never be detected: "*I have done a terrible thing, I have postulated a particle that cannot be detected*". This statement summarized the features of the neutrino, an electrically neutral and weakly interacting particle, whose mass was supposed to be negligible. Eighty years later, and with a well-proved existence, neutrino interactions provide an extraordinary opportunity to investigate relevant issues in several areas of Physics.

Nowadays, several neutrino experiments around the world have provided conclusive evidence of neutrino oscillations which implies neutrinos are not massless particles. The accurate determination of neutrino masses is one of the open questions in Particle Physics. Nevertheless, interest in neutrinos transcends the study of their intrinsic properties and extends to a large variety of fields as Astrophysics, Nuclear Physics and Particle Physics.

In 2012, the discovery of the Higgs boson at LHC [1] completed the Standard Model (SM) of Particle Physics, one of the essential theories in Modern Physics. Neutrino oscillations, that imply that neutrinos are not massless, have brought some limits on the validity of the Standard Model. The SM does not take proper account of the baryonic matter-antimatter asymmetry of the Universe, in which neutrino can play an important role. In this sense, violation of CP-symmetry (charge conjugation parity symmetry) has been found on the quarks domain, though further studies could be valuable in the lepton-hadron sector. On this subject, neutrino oscillations have proved their relevance in explaining violation of CP-symmetry (charge conjugation parity symmetry) in the quarks domain [2, 3].

In this context, neutrinos are essential to study astrophysical processes such as solar energy production, where nuclear reactions in the core generate an important flux of neutrinos, as well as in supernovae explosions. Neutrinos are a powerful tool to study hadronic and nuclear properties. Indeed, a great challenge of Nuclear Physics is to explore the structure of the nucleon and its excited states by means of electromagnetic and weak probes. The conclusions drawn in these processes are of relevance to test the validity of current hadronic models. The information obtained by weak interactions also complements the one received from electromagnetic processes.

Specifically, the vector-axial (V-A) weak interaction, related to the vector and axial hadronic currents, allows the study of QCD properties such as the axial structure of the nucleon, hardly

decipherable by using electron or photon scattering. In this sense, the charged-current neutrino-nucleon scattering (CC ν-N) is the more efficient way to analyze the nucleon axial form factor. This subject is addressed in detail in this thesis. Moreover, the study of neutral-current neutrino-nucleon processes (NC ν-N) shed light on the strange sea quark-gluon effects on the nucleon.

Despite its relevance in several fields of Physics, neutrinos are still elusive particles. They only interact through weak forces and are hardly detectable, so they can only be clearly observed through the detection of the secondary particles produced in the process. For this reason, heavy targets are often employed in neutrino experiments in order to increase neutrino-nucleus cross sections. At the same time, a proper theoretical understanding of the weak nuclear response is a prerequisite for the analysis of current and future neutrino oscillation experiments.

Therefore, a precise study of neutrino oscillations requires an adequate description of their interactions with nuclei and nucleons. The neutrino-nucleus reaction mechanisms are diverse, going from the quasielastic scattering to deep inelastic scattering, multi-nucleon processes or the excitation of nucleon resonances (see Chapters 3-5 for details). Most of these regimes require both better theoretical and experimental understanding. Accordingly, it would be advantageous to employ the knowledge extracted from electron-nucleus scattering as a solid benchmark to assess the validity of the theoretical neutrino interaction approaches in the different nuclear regimes (see Chapter 6) as well as to improve the understanding of current neutrino oscillation experiments.

Theoretical models on (e, e') reactions can still be improved by taking care of the recent developments in the inelastic structure functions along with the progress on parton density functions (PDFs) through QCD calculations. Furthermore, the employment of theoretical models including multinucleon excitations and realistic mean field theories, in addition to the large amount of (e, e') data for different nuclei, will likely help us to deepen our understanding of the reaction mechanisms in electromagnetic reactions and its extension to the weak sector, *i.e.*, to the analysis of neutrino interactions. This, makes research on neutrino interactions an attractive ingredient for the future of Particle and Nuclear Physics.

1.2 Neutrino Properties and Historical Context

As previously mentioned, the “birth” of neutrino dates back to 1930, when Pauli postulated its existence from the analysis of the continuum energy spectrum observed in the beta decay process. This was inconsistent with the image of only electrons being emitted in the nuclear process. The "possible" existence of an extra particle (the neutrino) with negligible mass and electrically neutral, that is, a "silent" partner, was needed in order to preserve energy and momentum conservation. Thus the beta decay process would imply the emission of not only electrons but also of new, unknown, particles that would gather the energy loss in the process. Hence, the description of the β-decay process was defined as: $n \rightarrow p + e^{-} + \overline{\nu}$.

In the 30’s and 40’s new particles were discovered, specifically, the muon, very similar to the electron but with a much larger mass, and the pion, the particle proposed by Yukawa to explain the strong interaction between nucleons inside the nuclei. A careful study of the pion proved that it decayed into a muon which emerged with an almost perpendicular track in relation to the pion, ensuring the existence of an extraordinary light particle in the process. It was suggested to be a neutrino. A few months later, the experimental proof of the muon decay into an electron led to the conclusion that the latter must be accompanied by two neutrinos.

In the early 1950's and despite the different hypotheses about the existence of the neutrino, there had no experimental evidence yet. It was in 1956, when Cowan and Reines [4] developed a method to observe the inverse β decay ($\overline{\nu} + p \rightarrow n + e^+$), in which this elusive particle was clearly, unambiguously detected. In these experiments, the actual particle taken into consideration was the antineutrino ($\overline{\nu}$). But how could one distinguish between neutrino and antineutrino? This distinction was explained by Davis and Harmer [5] in the late 1950s, showing that whereas the process $\nu + n \rightarrow p + e^-$ was commonly detected, on the contrary, the $\overline{\nu} + n \rightarrow p + e^-$ one never took place. This was the beginning of the lepton number assignment to neutrinos and the rest of leptons as well as its conservation law. Therefore, neutrinos in muon decay should be particle and antiparticle, whose difference comes from its own helicity. This subject will be addressed in detail later.

The hypothesis of neutrinos with different flavors came up after realizing that, unlike the process $\mu \rightarrow e + \nu + \overline{\nu}$, the reaction $\mu \rightarrow e + \gamma$ was not observed. Consequently, it was proposed the existence of two different kinds of neutrinos, one related to the electron and another one to the muon. Therefore, some of the processes mentioned above are really given as:

$$\begin{aligned} n &\rightarrow p + e^- + \overline{\nu}_e \\ \pi^+ &\rightarrow \mu^+ + \nu_\mu \\ \pi^- &\rightarrow \mu^- + \overline{\nu}_\mu \\ \mu^+ &\rightarrow e^+ + \nu_e + \overline{\nu}_\mu \\ \mu^- &\rightarrow e^- + \nu_\mu + \overline{\nu}_e \end{aligned}$$

Neutrino flavors

The Standard Model of Particle Physics contains three different neutrino flavors (ν_e, ν_μ and ν_τ), which respectively form a doublet with the corresponding charged leptons (e, μ and τ) as shown in Table. 1.1. In the 1990s, the LSND experiment [6] suggested the possibility of further neutrinos to explain neutrino masses and introduced a new type of neutrinos, called "sterile" neutrinos, whose existence is still under investigation. This particle would not interact with any other (except through gravity). The search for sterile neutrinos is an active area of particle physics and it is expected that future neutrino oscillation facilities could shed more light on this issue.

Helicity

Within the framework of the SM, neutrinos are massless leptons and exhibit purely negative helicity (left-handed), *i.e.*, their spin is antiparallel to their momentum; whereas the reverse occurs for antineutrinos,*i.e.*, their spin projection points out parallel (positive helicity) to the momentum. This reflects the parity violation in electroweak processes. In the SM, only left-handed neutrinos and right-handed antineutrinos exist. Nevertheless, the discovery that neutrinos have mass could modify this description. Moreover, it is not clear yet if neutrinos are Majorana particles, that is, neutrino and antineutrino are the same particles. Neutrinoless double beta decay, which can be viewed as two beta decay events with the produced antineutrinos immediately annihilating with one another, is a possible way to detect if neutrinos are their own antiparticles. Experiments are underway to search for this type of decay.

	Charged leptons				Neutrinos			
	Name	Symbol	Charge	Mass (MeV)	Name	Symbol	Charge	Mass (MeV)
1st gen.	Electron	e^-	-1	0.511	Electron neutrino	ν_e	0	$< 3 \cdot 10^{-6}$
	Positron	e^+	+1		Electron antineutrino	$\overline{\nu}_e$	0	
2nd gen.	Muon	μ^-	-1	105.658	Muon neutrino	ν_μ	0	< 0.19
	Antimuon	μ^+	+1		Muon antineutrino	$\overline{\nu}_\mu$	0	
3rd gen.	Tauon	τ^-	-1	1766.99	Tauon neutrino	ν_τ	0	< 18.2
	Antitauon	τ^+	+1		Tauon antineutrino	$\overline{\nu}_\tau$	0	

Table 1.1: The Protoypical Family of Leptons.

Neutrino mass

The experimental evidence of solar and atmospheric neutrino oscillations [7–9] led to the conclusion that neutrinos are not massless, even though, at present, we do not know the absolute values of their masses but only the upper limits (see Table 1.1).

In addition to the three different flavors, there are also three mass states ν_1, ν_2 and ν_3 with masses m_1, m_2 and m_3 respectively, which are associated to the flavor states through the Pontecorvo-Maki-Nakagawa-Sakata (PMNS) matrix [10, 11],

$$\begin{pmatrix} \nu_e \\ \nu_\mu \\ \nu_\tau \end{pmatrix} = \begin{pmatrix} U_{e1} & U_{e2} & U_{e3} \\ U_{\mu 1} & U_{\mu 2} & U_{\mu 3} \\ U_{\tau 1} & U_{\tau 2} & U_{\tau 3} \end{pmatrix} \begin{pmatrix} \nu_1 \\ \nu_2 \\ \nu_3 \end{pmatrix}. \tag{1.1}$$

The PMNS matrix can be expressed as the product of four sub-matrices [2], which contain three mixing angles (θ_{12}, θ_{13} and θ_{23}). These parameters determine the degree to which the mass and flavour states are mixed, as well as diverse CP-violation terms.

1.3 Neutrino Oscillations

In 1998 the Super-Kamiokande facility [7] revealed the flavor change in atmospheric neutrinos. A few years later, the Sudbury Neutrino Observatory experiment (SNO) [8] concluded that the loss observed in the incoming electron solar neutrino flux was due to neutrino oscillations. These observations were confirmed in subsequent years in different neutrino experiments based on the use of reactors and accelerators [9].

The neutrino oscillation phenomenon, predicted by Bruno Pontecorvo [10], indicates the possibility that a specific neutrino (electronic, muonic or tauonic) transforms into a one with different flavor. This effect is of high experimental and theoretical relevance as it implies neutrinos are not massless. In this context, a proper understanding of cross sections in neutrino-nucleus reactions is essential.

In the simple hypothesis that only two families of neutrino exist, the probability that a neutrino of energy E_ν changes its flavor from ν_i to ν_f after traveling a distance L is given by

$$P(\nu_i \to \nu_f) = \sin^2 2\theta \sin^2 \left(\frac{\Delta m^2 L}{4E_\nu} \right), \tag{1.2}$$

where θ is the mixing angle related to the combination of the different flavor states into the mass states. The mass square difference parameter $\Delta m^2 = m_1^2 - m_2^2$ is the difference between the two

mass states and is the only mass parameter that can be measured in neutrino oscillation experiments, which cannot give information on the absolute masses. The ratio between L/E_ν and Δm^2 is optimized in neutrino facilities to maximize the sensitivity to neutrino oscillations. In the three-flavor case the formula for the oscillation probabilities is more complicated and depends upon three mass squares differences ($\Delta m^2_{12} = m^2_1 - m^2_2$, $\Delta m^2_{13} = m^2_1 - m^2_3$, $\Delta m^2_{23} = m^2_2 - m^2_3$), three oscillation angles (θ_{12}, θ_{13}, θ_{23}) and a phase δ_{CP} corresponding to the possible violation of CP symmetry in the leptonic sector. The measurements of the latter is one of the most important challenges for future neutrino oscillation experiments. Thus the oscillation probability is given by

$$P_{\nu_\alpha \to \nu_\beta}(L,E) = \delta_{\alpha\beta} - 4\sum_{i>j} Re(U^*_{\alpha i}U_{\beta i}U_{\alpha j}U^*_{\beta j}) \sin^2\left(\frac{\Delta m^2_{ij}}{4E}L\right)$$
$$+ \quad 2\sum_{i>j} Im(U^*_{\alpha i}U_{\beta i}U_{\alpha j}U^*_{\beta j}) \sin\left(\frac{\Delta m^2_{ij}}{2E}L\right), \ \Delta m^2_{ij} \equiv m^2_i - m^2_j \, . \tag{1.3}$$

The Particle Data Group [2] provides a review of the up-to-date values of the oscillation parameters, shown in Table 1.2.

Parameter	Value
θ_{12}	$33.9^\circ \pm 1.0^\circ$
θ_{13}	$9.1^\circ \pm 0.6^\circ$
θ_{23}	$39^\circ < \theta_{23} < 51^\circ$
Δm^2_{12}	$(7.50 \pm 0.20)10^{-5}$ eV^2
Δm^2_{23}	$(2.32^{+0.12}_{-0.08})10^{-3}$ eV^2

Table 1.2: Current world knowledge of neutrino oscillation parameters. Δm^2_{13} is determined through $\Delta m^2_{13} = \Delta m^2_{12} + \Delta m^2_{23}$.

There are two methods to determine neutrino oscillations:

- Appearance mode: These experiments are focused on the search for a new neutrino flavor, absent in the original beam, or an enhancement of neutrinos of a given flavor in the initial beam. These effects are detected through the corresponding charged lepton produced via charged-current weak interaction:

  $$\nu_l + N \to l^- + X \tag{1.4}$$

  with $l = e, \mu, \tau$ and X the final hadron state. These processes will be addressed in following chapters.

- Disappearance mode: It is based on the reduction of the expected number of a particular neutrino flavor at the detector, as the case of the SNO experiment [8]. This method requires an accurate understanding of the neutrino beam at the source.

Neutrino sources employed in oscillation experiments are diverse, going from nuclear reactors ($\overline{\nu}_e$), atmospheric ($\nu_e, \overline{\nu}_e, \nu_\mu, \overline{\nu}_\mu$), solar ($\nu_e$) and accelerators ($\nu_e, \overline{\nu}_e, \nu_\mu, \overline{\nu}_\mu$). In the case of solar and atmospheric neutrinos, there are some constraints on L and E_ν which prevent from an optimum combination of these parameters for the oscillation measurements. Therefore, the current

efforts focus on accelerator-based neutrino experiments where a better sensitivity to oscillations can be achieved. A detailed analysis of current neutrino experimental facilities will be presented in Sect. 1.6.

1.4 Interaction with Matter

The neutrino interaction with matter is purely weak, acting at very short distances with a low intensity, and being able to modify the flavor of the particles involved. Such interaction is described by the electroweak theory, developed by Weinberg [12], Salam [13] and Glashow [14] in the 1970s, by the exchange of the weak bosons $W^{\pm}$ and Z. The $W^{\pm}$ boson is connected with charged-current (CC) scattering processes where there is a charge exchange in the interaction vertex, whereas the Z boson is associated to neutral-current scattering where no charge exchange occurs. Moreover, the fact that the electroweak interaction is 5 to 6 orders of magnitude lower than the electromagnetic one, leads to extremely low cross sections which makes experimental procedure highly demanding. In addition to this, the low intensity of weak interactions allows for a perturbative analysis, so that the Born approximation, that is, the 1-boson exchange between the leptonic and hadronic vertices, represents an accurate approach.

Unlike electromagnetic scattering, the weak processes do not conserve parity, which provides specific information about the axial structure of the nucleon. In particular, the charged-current neutrino-nucleon (ν-N) scattering contains the most precise information about the nucleon axial form factors (addressed in Chapter 2). On the other side, neutral current processes give essential details about the strange sea quarks in the nucleon structure.

In Fig. 1.1, the Feynman diagrams related to the elastic lepton-hadron reactions are shown. In weak interactions, a distinction between charged current processes, where a charged lepton is emitted, and neutral current ones, where the neutrino does not change in the final state, is considered.

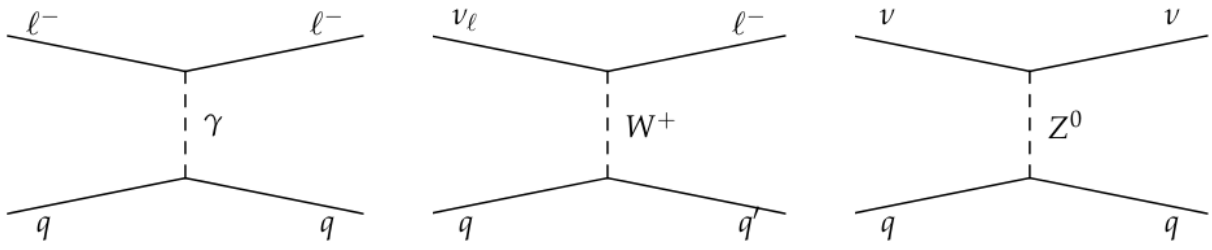

(a) Electromagnetic scattering (b) Charged-current scattering (c) Neutral-current scattering

Figure 1.1: Lepton-hadron elastic scattering processes: a) Electromagnetic interaction. b) Charged-current weak interaction. c) Neutral-current weak interaction.

Compared to CC neutrino reactions, the experimental study of NC processes is a fairly demanding task due to the considerable difficulties to obtain information in a process with a reduced cross section and without charged leptons in the final state. Thus, the event recognition lies on the hadron detection.

1.4.1 Neutrino-nucleus scattering

At the lowest neutrino energies, the most probable interaction is the elastic scattering where the energy transfer to the nucleus is not enough to release an unbound nucleon so the nucleus recoils intact. The quasielastic (QE) scattering appears once the energy transfer is large enough to scatter off a nucleon from the nucleus. When this process occurs via neutral-current scattering, all neutrinos and anti-neutrinos can scatter off both neutrons and protons in what is referred to as neutral-current quasielastic (NCQE) scattering: $\nu_l(\overline{\nu}_l) + N \rightarrow \nu_l(\overline{\nu}_l) + N$. Once neutrinos acquire sufficient energy to create the charged lepton's mass they can also undergo the analogous charged-current quasielastic (CCQE) interaction: $\nu_l + n \rightarrow p + l^-$ and $\overline{\nu}_l + p \rightarrow n + l^+$. For $E_{\nu_\mu} \approx 1$ GeV, CCQE is the dominant interaction.

The interaction of neutrinos with nuclei at intermediate energies, of the order of 100s of MeV up to 10s of GeV, plays an important role in the precise determination of neutrino oscillation parameters. At these energies, nuclear effects are very significant, providing also relevant information on the axial hadronic currents. From the experimental point of view, the data analysis needs to consider a large number of nuclear effects that distort the signals and produce new sources of background that are absent in the elementary neutrino-nucleon processes. In this sense, a complete theoretical model should include, at least, three kinds of contributions: (i) quasielastic (QE) for low-intermediate energy transfers, (ii) nucleon correlations and two-body contributions and (iii) the complete inelastic spectrum, containing pion production arising from the $\Delta(1232)$ resonance peak, non-resonant contributions, other meson production as well as higher-energy nucleonic resonances and deep inelastic scattering processes.

In this work, we focus on intermediate and high energies covering from QE reactions to deep inelastic scattering processes. The different reaction mechanisms are briefly described in the following lines:

- **Quasielastic scattering**: The most relevant contribution at intermediate energies ($E_\nu \sim 1$ GeV) in which a neutrino scatters off a single bound nucleon being the latter ejected from the nuclear target. We can distinguish between NCQE neutrino interactions, where a neutrino is emitted, and CCQE neutrino interactions with a charged lepton in the final state. Regarding the notation employed in the experimental literature, CCQE-like scattering (or CC0π) is defined as the process where one lepton and no pions are detected in the final state. In this sense, QE-like processes are contaminated with other contributions such as short-range correlations (SRC), multinucleon emissions (np-nh) induced by meson-exchange currents (MEC) and by rescattering processes, pion absorption in the nuclear medium and pionless resonance decay.

- **2p-2h MEC contributions**: This corresponds to a weak boson being exchanged by a pair of nucleons (2-body current) leading to the emission of two nucleons from the primary vertex. This contribution is essential to interpret properly the "dip" region between the QE and Δ peaks for (e, e') reactions as well as to reproduce the neutrino QE-like experimental data.

- **Resonance production**: At higher energies, which implies large Q^2 values, neutrinos gain access to inelastic scattering processes. Here the target nucleon is "knocked" into a baryonic resonance, a Δ or a heavier resonance $N*$ depending on the energy transfer. These resonances decay into a variety of final states with combinations of nucleons and mesons. Neutrino-induced pion production is the dominant process in the region 0.5 GeV $< E_\nu <$ 10 GeV.

- **Deep inelastic scattering (DIS)**: At higher energies the neutrino is able to transfer sufficient momentum so the inner structure of the nucleon can be resolved. The neutrino can scatter directly off any of the quarks inside the nucleon, including those which form the "sea" of quarks and anti-quarks that are constantly popping in and out of existence. At lower transfer momentum the nucleons contain mostly up, down and strange quarks, but higher transfer momentum values get access to higher-mass and shorter-lived quarks too. DIS is the dominant process for $E_\nu > 10$ GeV and its most visible consequence is the break up of the nucleon containing the struck quark.

The different reaction mechanisms contributing to (anti)neutrino-nucleus interactions are shown in Fig. 1.2 as function of the incoming (anti)neutrino energy. In order to give a more complete description of the scattering mechanisms, the nuclear response in terms of the energy transferred to the nucleus is schematically represented in Fig. 1.3 for a fixed momentum transfer q. In the latter, we can observe how small energy transfers of the order of tens of MeV result in elastic scattering off the nucleus followed by a collective excitation of the nucleus. Intermediate energies are related to the process where the lepton scatters off a bound nucleon giving a broad QE peak centered around $\sim Q^2/2M$ (being M the nucleon mass). At higher energies, multinucleon excitations and nucleonic resonances start to be relevant as well as DIS processes when the incident energy is enough for the nucleon break-up. Notice also the overlap of the different reaction mechanisms in the intermediate kinematical region (1-10 GeV). This effect should be considered carefully when analyzing neutrino-nucleus experimental data.

1.4.2 Elastic neutrino-nucleon interactions and nucleon form factors

Doing calculations for the interaction of neutrinos with nuclei presents additional complexity over electrons with nuclei since, in addition to the purely vector electromagnetic responses, new axial and interference vector-axial contributions arising from weak leptonic and hadronic currents come into play.

Although essentially composed of only three quarks, nucleons are constantly interacting via exchange of gluons which in turn can produce other temporary quark/anti-quark pairs. The four-momentum of the weak boson (Q^2) determines how much of the nucleon's internal structure is resolved by a weak interaction. The description of the inner structure of the nucleon can be provided by the use of nucleon form factors, that are given as phenomenological functions expressed in terms of Q^2. The type of interaction determines which form factors enter in the process. A more detailed description of hadronic form factors will be addressed in Chapter 2.3.

With respect to the nucleon structure, elastic neutrino-nucleon scattering processes are particularly important to neutrino physics for two reasons. First, they provide essential information on the weak nucleon form factors which are difficult or inaccessible for other scattering probes. Second, the previous processes enable the kinematics to be completely reconstructed, and hence the initial neutrino energy can be determined. This is critical for measurements of the oscillation parameters. In spite of this, most of the experiments employ heavy targets in order to get larger cross sections. This makes the analysis of the process much more complex, *i.e.*, a great caution should be drawn on how to reconstruct the kinematics, and how to get information on the weak nucleon form factors.

Regarding the weak nucleon form factors in CCQE neutrino scattering we can distinguish vector, $F_1(Q^2)$ and $F_2(Q^2)$, axial, $F_A(Q^2)$, and pseudoscalar, $F_P(Q^2)$, ones, related to the corre-

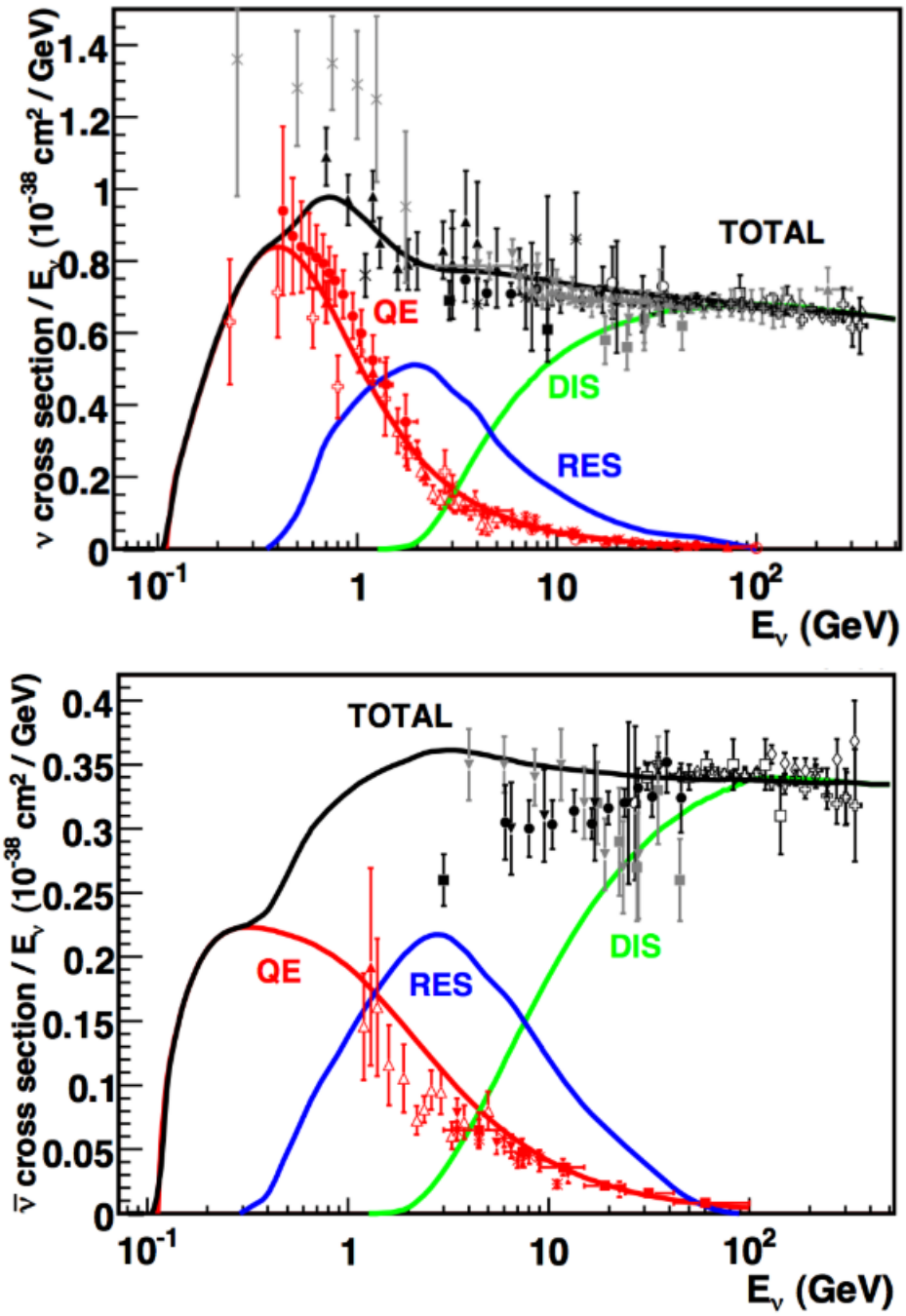

Figure 1.2: Total neutrino (left) and antineutrino (right) cross sections per nucleon in terms of the incident neutrino energy (E_ν). Different reaction channels are shown separately. The figures are taken from [15].

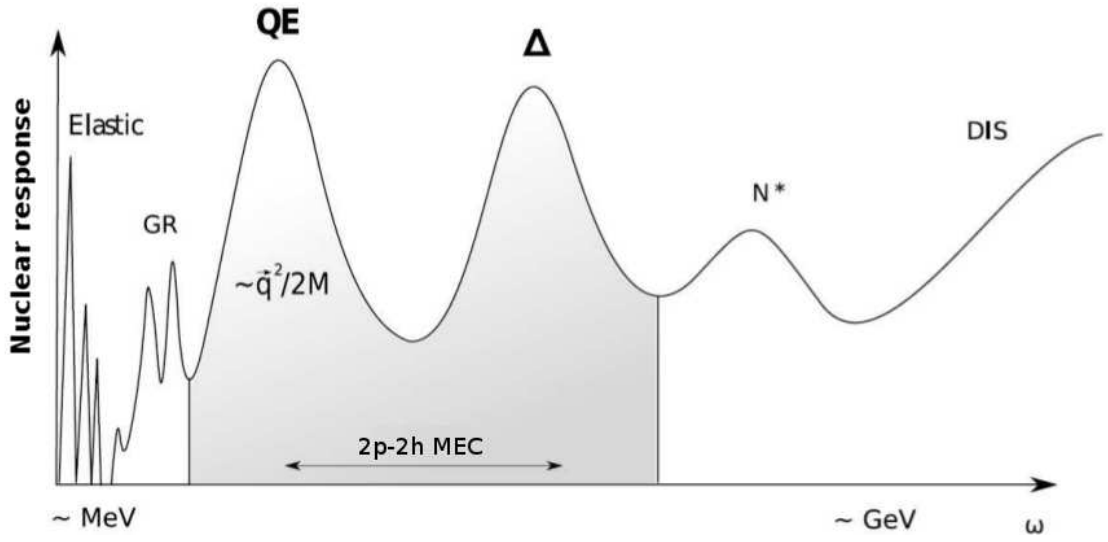

Figure 1.3: Regimes of the nuclear response in terms of the energy transfered (ω) to the nucleus.

sponding components of the hadronic current. The vector form factors, as a consequence of the *conserved vector current hypothesis (CVC)* [16], can be defined in terms of the electromagnetic ones related to electron-nucleon scattering. Concerning the axial form-factor, $F_A(Q^2)$, it is common to assume a "dipole" form, where two control parameters must be determined experimentally: the "axial charge" $g_A = 1.26$ from beta-decay, and the "axial mass" $M_A = 1.014 \pm 0.014$ GeV from CCQE neutrino scattering on deuterium and pion production by electrons [17]. It should be noted though that the dipole form is an assumption motivated by the analysis of electromagnetic form factors [18]. A study of the differences between dipole and monopole axial form factor is shown in Appendix D as well as in [19]. Although, to date, neutrino experiments do not have the precision required to test explicitly the Q^2-dependence of the weak form factors, a dipole form works nicely in most situations [18]. Finally, the pseudoscalar form factor, F_P, is related to the axial one via the "Goldberger-Treiman" relation. The basic features of these functions are analyzed in Chapter 2.3.

1.5 Theoretical approaches to neutrino-nucleus scattering

With the aim of achieving a complete theoretical description of neutrino-nucleus interactions, several theoretical groups have developed different models to account for the different ingredients needed for a deep understanding of experimental data. The first MiniBooNE CCQE measurements for neutrino interactions on ^{12}C motivated a large theoretical effort to explain the apparent discrepancy between the experimental cross sections and the theoretical predictions, which seem to underestimate the data [20, 21]. A first approach to disentangle this apparent discrepancy was to increase the value of the nucleon axial mass (M_A) from the world's averaged value (1.032 GeV) emerging from deuterium bubble chamber experiments [22, 23] to $\sim$ 1.35 GeV. However, while improving the theoretical agreement with the MiniBooNE data, such a high value of M_A does not match with other experimental data, as NOMAD [24], nor with former elastic neutrino cross sections on light nuclei [25–29]. The key to this issue lays on the definition of the CCQE event in the experiment. Whilst theorist define CCQE as the event where one nucleon is knocked out in the final state along with a charged lepton, MiniBoone defined CCQE as an event with one lepton and no pion observed in the final state, which has been "renormalized" to *CCQE-like*. Therefore, the definition of CCQE-like event also includes effects beyond the Impulse Approximation, *i.e.*,

the neutrino only interacts with a single-bound nucleon. Thus, nucleon-nucleon correlations and multinucleon emission processes, such as 2p-2h MEC contributions, should be accounted for in the analysis of experimental data.

From this baseline, a large number of theoretical groups began to investigate on this topic. In particular, Martini et al. employed a local Fermi gas model [30], taking into account RPA correlations, coherent and incoherent pion production as well as quasielastic excitations. Besides this, the inclusion of contributions arising from np-nh excitations [30] led them to a reasonable agreement with MiniBooNE data without resorting any effective parameter or increasing the M_A value. A similar approach was taken by Nieves et al. [31], achieving a good agreement with data after a subtraction of $\sim 10\%$. Moreover, the Pavia group made use of a relativistic Green's function approach [32] including the imaginary part of the relativistic optical potential to describe final-state interactions (FSI). Their predictions are in accordance with data for some particular choices of the optical potentials. The contributions of one-body and two-body currents have also been analyzed in [33] using the spectral function formalism. A semiphenomelogical model that considers the quantum-kinetic transport theory (GiBUU) has been also applied for the analysis of electromagnetic and weak interactions [34], using a parametrization of the transverse electromagnetic contributions as a basis for 2p-2h neutrino interactions.

In this thesis, the analysis of the electron and neutrino-nucleus interactions in the QE and inelastic regimes will be carried out within the framework of the SuperScaling Approach (SuSA), which assumes the existence of universal scaling functions for both electromagnetic and weak interactions. The analysis of inclusive (e,e') experimental data [35–38] has proved that scaling is fulfilled with very good accuracy. This implies that the reduced cross section exhibits independence of the momentum transfer (first-kind scaling) and of the nuclear target (second-kind scaling) when expressed as a function of the appropriate scaling variable, itself a function of the energy and momentum transfer. In a recently improved version, called SuSAv2 model, we have employed the Relativistic Mean Field Theory (RMF) and the Relativistic Plane Wave Impulse Approximation (RPWIA) to obtain a complete set of *scaling functions* that embody all the nuclear dependence of the interaction, being valid for all nuclei. The description of the the many-body physics of the interacting nucleons within the SuSAv2 model, takes into account the different contributions of both longitudinal and transverse nuclear responses, as well as the isovector and isoscalar channels. This is of great interest for charged-current (CC) neutrino reactions, which are purely isovector. Regarding the 2p-2h MEC contributions and contrary to other works on this topic, we employ a microscopic calculation in a fully relativistic framework without further approximations. The SuSAv2-MEC predictions, based on the use of the RMF/RPWIA model plus the 2p-2h MEC fully microscopic calculations, have been succesfully applied to the analysis of (e,e') and CCQE neutrino-nucleus reactions covering from low to very high energies [38, 39].

1.6 Experimental status

Once neutrino oscillations were confirmed in solar and atmospheric neutrinos [7, 8], an ample experimental program was developed with the aim of studying these oscillations and determining precisely their masses through the oscillation parameters. This deep research has renewed the interest on neutrino cross sections as an essential ingredient on the analysis of neutrino oscillation experiments as well as on the study of the weak nucleon structure. Nevertheless, due to the extremely reduced cross sections in weak reactions, neutrino experiments are highly complicated. In the words of Haim Harari [40], "Neutrino physics is largely an art of learning a great deal by

observing nothing".

In this section, we focus on accelerator-based neutrino experiments which provide better controlable conditions for the study of oscillations. The purpose of these facilities is either the direct measurement of oscillation parameters or the production of data that can help to reduce the systematic and theoretical uncertainties related to neutrino-nucleus scattering. Most of current and future experiments have a baseline of hundreds of km and operate in the 1-10 GeV region. At these kinematics, the most relevant contribution to the cross section comes from the charged-current quasielastic (CCQE) scattering processes. In Table 1.3, we briefly compare the main features of some recent and forthcoming experiments. We can observe a predominant use of carbon as nuclear target in most facilities whereas other experiments employ heavier nuclei, obtaining higher cross sections but also providing, in some situations, outstanding spatial and energy resolution as the case of the liquid-argon time-projection chamber (LArTPC) technology. The neutrino energies cover a range from hundreds of MeV to a few GeV in MiniBooNE [20, 21], SciBooNE [41], MINOS [42] and NOνA [43] whereas it steps up to tens of GeV for T2K [44,45], MINERνA [46,47], NOMAD [24] or ArgoNeuT [48, 49]. Neutrino beams in most experiments are generated through the decay of pions into muons and neutrinos, the latter being directed towards the final target.

Experiment	Nuclear Target	Beam	Process Detected	E_ν range (GeV)
MiniBooNE	CH_2	$\nu_\mu, \overline{\nu}_\mu$	CCQE-like, Pion production	0.2-3.0
MINERνA	CH, C, Fe, Pb	$\nu_\mu, \overline{\nu}_\mu, \nu_e, \overline{\nu}_e$	CCQE-like, Pion production, DIS, Inclusive	1-20
T2K	C_8H_8	$\nu_\mu, \overline{\nu}_\mu, \nu_e, \overline{\nu}_e$	CCQE-like, Inclusive	0.2-30
ArgoNeuT	Ar	$\nu_\mu, \overline{\nu}_\mu$	Pion production, Inclusive	0.5-10.0
SciBooNE	C_8H_8	ν_μ	CCQE-like, Inclusive, Kaon production, Pion production	0.2-3.0
NOMAD	64%C, 22%O, 6%N, 5%H, 1.7%Al	$\nu_\mu, \overline{\nu}_\mu$	CCQE	2.5-300
MINOS	Fe	ν_μ	CCQE-like, Pion production	0.2-6.0
NOνA	CH_2	ν_μ	CCQE-like	0.2-3.0
MicroBooNE	Ar	$\nu_\mu, \overline{\nu}_\mu$	CCQE-like	0.2-5.0
Hyper-Kamiokande	H_2O	$\nu_\mu, \overline{\nu}_\mu$	CCQE-like	0.3-5.0
DUNE	Ar	$\nu_\mu, \overline{\nu}_\mu$	CCQE-like, Inclusive	0.2-15.0

Table 1.3: Overview of current and forthcoming accelerator-based neutrino-oscillation experiments.

A complete knowledge on the neutrino beam is essential to the success of neutrino oscillation experiments. Unlike most electron experiments, the neutrino beams are not monochromatic. In general, to produce intense beams of high energy neutrinos, protons from a synchrotron are accelerated to be extracted afterwards and sent against a target (commonly made of beryllium) where they produce π and K mesons. The mesons are collimated and pass in a long vacuum tube of hundred meters where they decay into leptons and neutrinos (see Fig. 1.4 for details). After the vacuum tube, there is a region with absorbing material in which photons and electrons are stopped first, followed by hadrons and finally muons. Only neutrinos reach the experimental area where different detectors are installed. Due to these different processes, the neutrino beams are not monochromatic. Their degree of breadth depends on the focusing of the charged hadrons produced in the primary collision as well as on the energy of the primary beam. Therefore, in any experiment the neutrino beam involves a broad energy distribution around a maximum, and the true energy for a detected event is thus not known. At the same time, the inaccuracy on the meson flux determination affects the prediction of the final neutrino flux. In order to reduce flux uncertainties, two identical detectors are employed. These are located near the neutrino production region (*near detector*) and in the place where a maximum or minimum oscillation is expected (*far detector*). Moreover, the reliability of neutrino cross section measurements strongly depend on a precise determination of the net neutrino flux. Given that the uncertainties in the meson flux have an impact on the neutrino flux, several investigations have been carried out to analyze the hadron productions in pA (proton-nucleus) collisions, such as the HARP experiment [50] whose results have improved the neutrino flux prediction in facilities such as MiniBooNE.

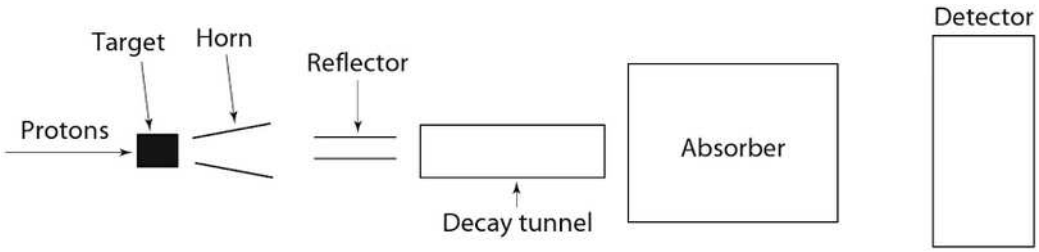

Figure 1.4: Layout of neutrino beam production on neutrino oscillation experiments.

Event selection is another important issue in neutrino experiments as different experiments use diverse criteria to identify CCQE events which depend on their hadron identification ability. In this way, MiniBooNE and MINERνA do not have complete information about protons or neutrons in the final state, so processes such as multi-nucleon emission (np-nh MEC) can be measured as CCQE events. These type of measurements are called CCQE-like events (see discussion in previous sections). On the contrary, experiments as NOMAD and SciBooNE make use of the recoil proton information to distinguish purely CCQE events. Thereupon some recent neutrino experiments and their main features are briefly described.

MiniBooNE

MiniBooNE is an experiment at Fermilab designed to observe neutrino oscillations, being BooNE an acronym for the Booster Neutrino Experiment. A neutrino beam consisting primarily of muon neutrinos is directed to a detector filled with 800 tons of mineral oil (CH_2) and lined with 1,280 photomultiplier tubes. An excess of electron neutrino events in the detector would support the

short-baseline neutrino oscillation indicated by the LSND Collaboration (Liquid Scintillator Neutrino Detector) result [6]. It collected data and measurements from 2002 up to 2012.

In particular, the experiment is focused on detecting the $\nu_e(\overline{\nu}_e)$ appearance from the $\nu_\mu(\overline{\nu}_\mu)$ beam in the $\Delta m^2 \sim 1$ eV^2 region through CCQE-like interactions. This mass difference is much larger than the one observed in solar and atmospheric oscillations. Furthermore, MiniBooNE presents a high statistics (POT=7×10^{20}), remarkably greater than the one in solar and atmospheric neutrinos.

A detailed comparison of the (anti)neutrino beam for different facilities is shown in Fig. 1.5. In particular, the MiniBooNE flux is peaked at $E_\nu \sim 0.7$ GeV, where the dominant process is the QE scattering. This makes the MiniBooNE results in neutrino-nucleus cross sections a very useful tool in our theoretical study.

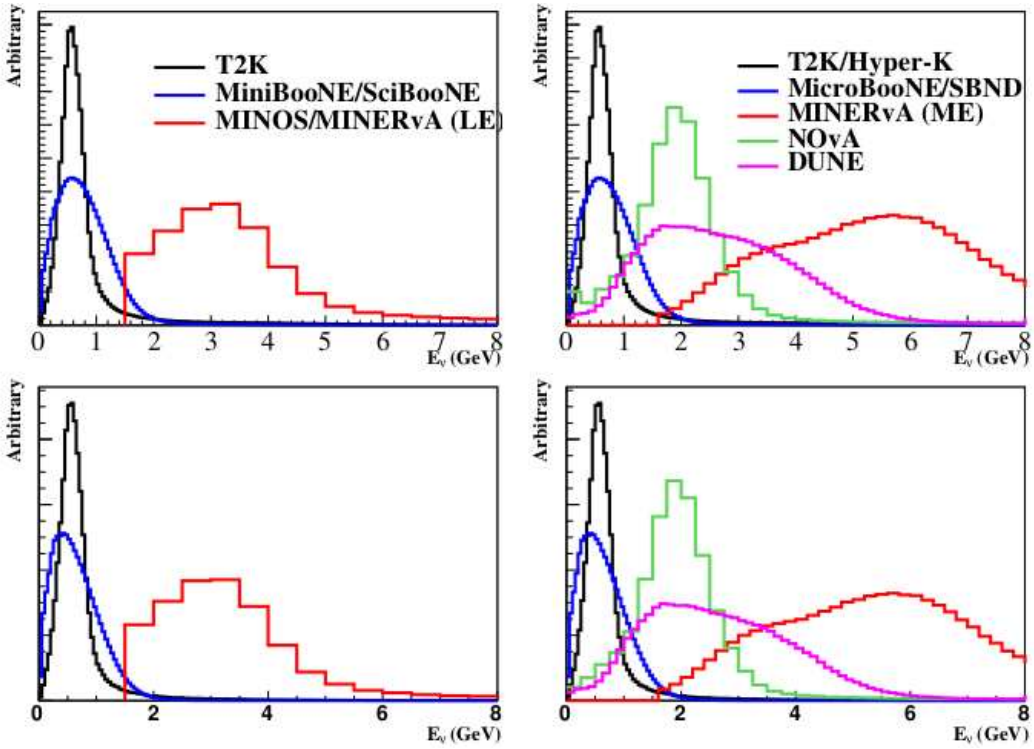

Figure 1.5: Muon neutrino and muon antineutrino flux predictions from current and future accelerator based neutrino experiments. The plots on the top represent neutrino flux predictions, whereas the plots on the bottom are anti-neutrino flux predictions. Predictions are all arbitrary normalized. Left plots are current experiments (T2K, MiniBooNE, MINERνA with low energy (LE) NuMI), and right plots are forthcoming experiments (Hyper-Kamiokande, MicroBooNE, NOνA, DUNE, MINERvA with medium energy (ME) NuMI). Figure taken from [51].

MiniBooNE is the first step of the BooNE experiment. At this stage, neutrino oscillation measurements are obtained with a single detector which records Cherenkov and scintillation photons from the charged particles produced in neutrino reactions. After verifying these oscillations, MiniBooNE will move forward to a second stage with two detectors in order to determine more precisely the oscillation parameters.

The BooNE experimental line consists of three main components, as shown in Fig. 1.6, a primary beam of protons, a secondary beam of mesons and a third one of neutrinos. Protons are accelerated up to 8 GeV in the Booster synchrotron where they are directed to a beryllium target. The secondary mesons produced after the collision are driven towards a toroidal magnetic field where the neutrinos originated after the meson decay are directed towards the detector. Finally, the neutrino flux is calculated by using a Geant-4 simulation.

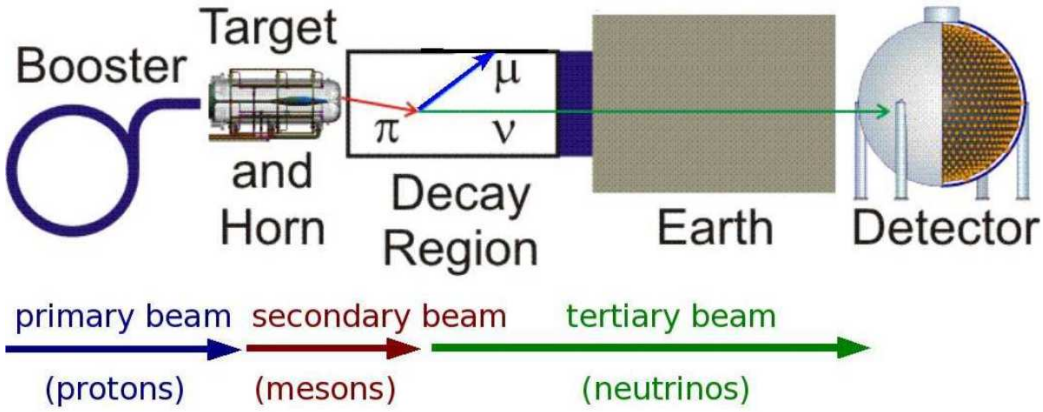

Figure 1.6: Scheme of the MiniBooNE beamline and detector.

The main purpose of these measurements is to determine the CCQE double differential cross section for the process $\nu_\mu + n \rightarrow \mu^- + p$, using ^{12}C as target. The identification of the CCQE event on the MiniBooNE detector only depends on the Cherenkov light arising from the primary muon and the subsequent electron after its decay (see Fig. 1.7). The scintillation light is produced by the charged lepton and the recoil proton. However, the reconstruction method employed at FermiLab prevents this light to be separated from the dominant Cherenkov one. Thus, the proton is typically under the Cherenkov threshold, enabling a proton-lepton coincidence detection.

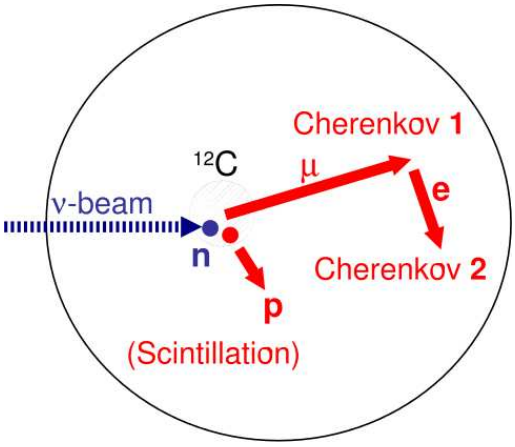

Figure 1.7: Schematic overview of CCQE scattering in the MiniBooNE detector.

This lack of sensitivity makes the results less dependent of the uncertainties related to the final-state model employed to described the final proton. On the contrary, this prevents from disentangling between purely quasielastic processes and other possible reaction mechanisms, *i.e.*,

multi-nucleon excitations, nucleon correlations or processes where pion production is abosorbed in the target nucleus. These contributions are not, strictly speaking, CCQE but are considered in that way in the experimental definition, as they have the same final state (CCQE-like events).

The previously-described CCQE process, including muon decay, can be summarized as follows:

$$\begin{aligned} 1: &\quad \nu_\mu + n \rightarrow \mu^- + p \\ 2: &\quad \hookrightarrow e^- + \overline{\nu}_e + \nu_\mu \end{aligned}$$

On the other hand, the primary background stems from the CC pion production which is described as,

$$\begin{aligned} 1: &\quad \nu_\mu + p(n) \rightarrow \mu^- + p(n) + \pi^+ \\ 2: &\quad \hookrightarrow \mu^+ + \nu_\mu \\ 3: &\quad \hookrightarrow e^- + \overline{\nu}_e + \nu_\mu \\ 4: &\quad \hookrightarrow e^+ + \nu_e + \overline{\nu}_\mu \end{aligned}$$

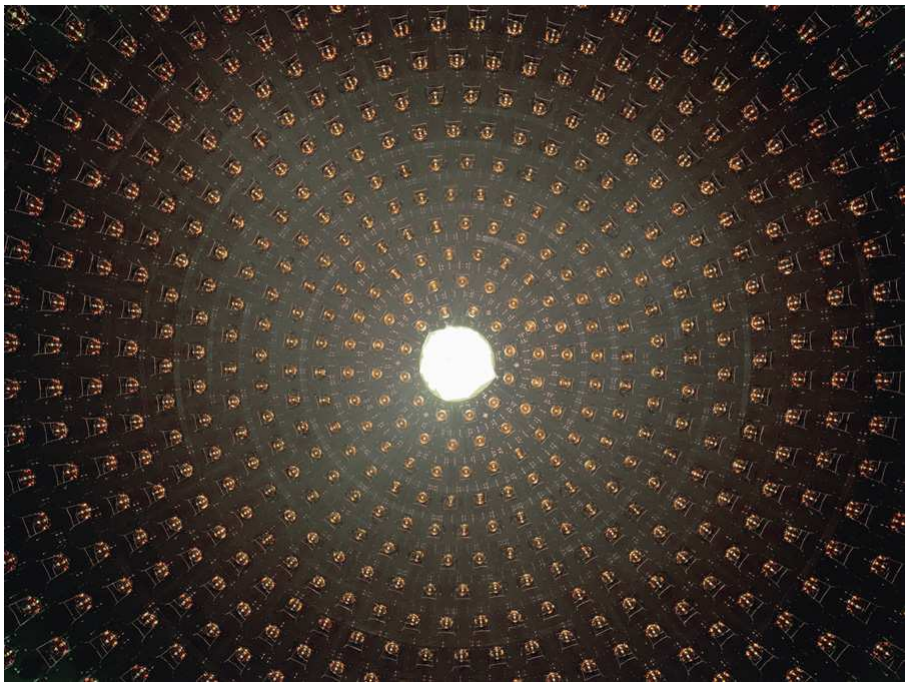

Figure 1.8: The inside of the MiniBooNE tank is filled with 818 tons of scitillator mineral oil (CH_2) and covered with 1280 inward-facing photomultiplier tubes. Picture taken from the BooNE website.

MiniBooNE has produced a large amount of data concerning CCQE, CC pion production as well as NC cross sections. The preliminary analysis of these data led to propose a larger value of the nucleon axial-mass with respect to the world average value obtained in previous deuterium filled bubble chamber experiments. However, this result could be explained as a consequence of the measurements of CCQE-like events which also include multinucleon processes or nucleon correlations.

Finally, it is also worth mentioning the MicroBooNE Collaboration [52], a further step into the BooNE experiment. The MicroBooNE collaboration is currently operating a large Liquid Argon Time Projection Chamber (LArTPC) that is located on the Booster neutrino beam line at Fermilab. The experiment first started collecting neutrino data in October 2015. MicroBooNE will measure low energy neutrino cross sections and investigate the low energy excess events observed by the MiniBooNE experiment. The detector also serves as a next step in a phased program towards the construction of massive kiloton scale LArTPC detectors for future long-baseline neutrino physics (DUNE) and is the first detector in the short-baseline neutrino program at Fermilab.

SciBooNE

As mentioned before, two facilities have made use of the 8-GeV Booster beam at FermiLab, MiniBooNE and SciBooNE. The SciBooNE experiment was built at Fermilab to get precise measurements of neutrino and antineutrino cross sections on carbon and iron targets. The SciBooNE Collaboration has measured the intrinsic properties of the neutrino beam produced in the "Booster" unit which sends this flux to MiniBooNE (next experimental stage) improving its precision. The SciBooNE detector consists of scintillator-bar detector (carbon target), a muon range detector and an electron capture detector (ECD).

SciBooNE satisfactorily completed its measurements in 2008 and their results have already been published [41].

MINERνA

The aim of the MINERνA Collaboration is to study neutrino-nucleus interactions in detail. Its main objective is to support neutrino oscillation experiments through the analysis of neutrino interactions at intermediate energies. It measures neutrino reactions covering an energy range from 1 to 20 GeV. The detector is placed on the NUMI line at FermiLab and it is equipped with different targets (C, CH, Fe, Pb) in order to achieve precise measurements of the nuclear effects. Its design allows to reconstruct and analyze the track of the involved particles. The facility started working in 2010 and several data have been already taken [46, 47, 53].

The source of MINERνA's neutrino beam is the Neutrinos at the Main Injector beamline, or NuMI. The NuMI neutrino beam is created by firing protons from Fermilab's Main Injector into a carbon target resembling a yardstick, located inside a magnetic focusing horn. The interaction of protons with the target produces a stream of positively and negatively charged particles. The horn produces a magnetic field used to focus either the positive or negative particles into a 675 meter long decay pipe. There the particles decay in flight to produce muons and muon neutrinos (from positive particles) or anti-muons and muon anti-neutrinos (from negative particles). The approximately 240 meters of rock and muon absorbers between the end of the decay region and the near detector hall absorb all particles except the neutrinos, creating a clean neutrino beam for use in the particle detectors.

Neutrinos passing through a particle detector will collide with nuclei in the various materials making up the detector. These interactions produce ionizing radiation and secondary charged particles that leave measurable energy deposits in the detector. These energy deposits are used to identify and study the neutrino interactions. Highly energetic muons created in neutrino interactions are capable of escaping the MINERνA detector and entering MINOS. MINERvA uses data

collected by MINOS to identify and measure these energetic particles.

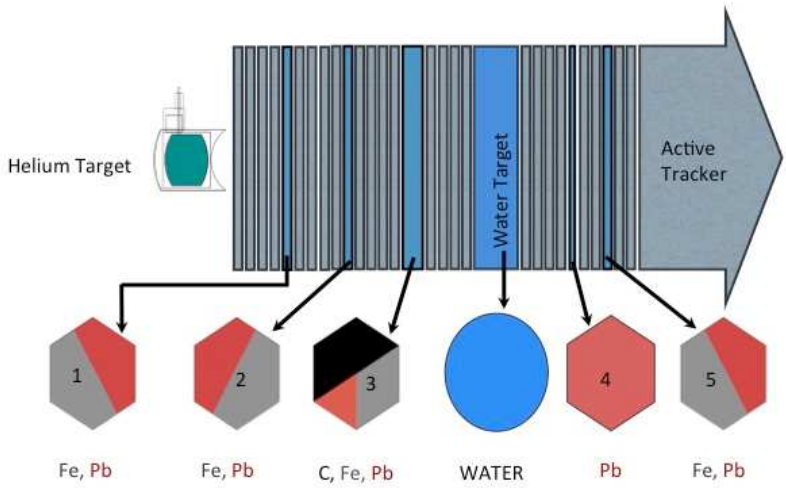

Figure 1.9: Side-view of the MINERνA experiment. The neutrino beam travels left to right through the various detector components [46].

MINERνA has produced CCQE-like cross sections on CH [46, 47] which are in agreement with theoretical estimations including also multinucleon excitations, without further ingredients or larger axial mass values. Its recent measurements on DIS cross sections for different nuclei [54] could be valuable to assess the relevant ingredients for the neutrino reaction models at very high energies.

K2K

The K2K experiment [9] was designed in Japan to confirm atmospheric neutrino oscillations using Super-Kamiokande as detector. A schematic diagram of this detector is shown in Fig. 1.10. This consists of a water Cherenkov detector, a water-based liquid scintillator (*SciFi, oxygen target*) and a muon range detector (MRD). Thus, the impact of 12-GeV protons on an aluminium target produces neutrinos with an energy spread from 1 to 1.5 GeV. Finally, in the SciFi detector the neutrino cross section is measured.

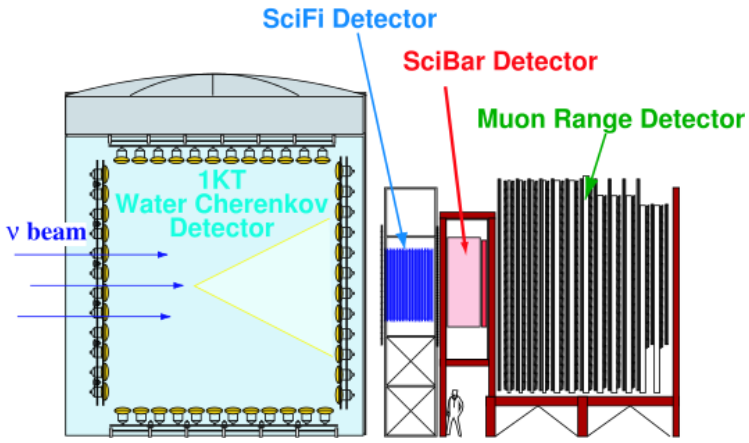

Figure 1.10: Schematic view of K2K detector [9].

T2K

The T2K experiment (Tokai to Kamioka) is a long-baseline neutrino experiment in Japan which is focused on neutrino oscillations and can be considered the successor of K2K. It employs a high-resolution detector with the aim of determining the neutrino energy spectrum as well as its flavor and the resulting cross sections.

T2K has made a search for oscillations from muon neutrinos to electron neutrinos, already published [55] as well as its work on the measurement of oscillations from muon neutrinos to tau ones. A large set of experimental data from forward to backward angles has also been published for the analysis of CC0π production processes as well for the inclusive ones [44, 45, 56].

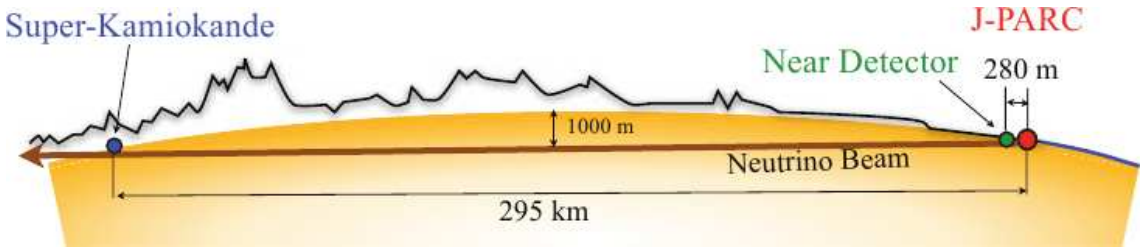

Figure 1.11: Schematic view of T2K detector [44].

The T2K experiment sends an intense beam of muon neutrinos from Tokai, which is on the east coast of Japan, to Kamioka at a distance of 295 km in western Japan. The neutrino beam is produced from collisions between a proton beam and a graphite target; these collisions produce pions, which quickly decay to muons and muon neutrinos. The muons and any remaining protons and pions are stopped by a second layer of graphite, but the neutrinos pass through it.

T2K studies neutrino oscillations with two separate detectors, both of which are 2.5 degrees away from the centre of the neutrino beam. The ND280 near detector is located at 280 metres distance from the target, and measures the number of muon neutrinos in the beam before any oscillation occurs. T2K neutrinos have much higher energies than solar neutrinos, and high-energy neutrinos are more likely to interact. A small number of muon neutrinos interact with scintillator or water in the ND280, and many of these interactions produce a muon. The muon can be detected since it ionises gas which is placed immediately after the interaction points. These ND280 measurements are used to predict the number of muon neutrinos that would be seen in the "far detector" SuperKamiokande if there were no oscillations.

The walls of SuperKamiokande are lined with more than 10,000 sensitive photo-multipliers, which detect the cone of Cerenkov light as a ring (see Figure 1.12). This detector system can distinguish muons originated from muon neutrinos (which produce a sharp ring) from electrons arising from electron neutrinos (which produce a more diffuse ring).

A next step into the Kamiokande investigations is the Hyper-Kamiokande experiment [57], which will operate in the same beam line as T2K. This detector consists of a megaton scale water tank and ultra high sensitivity photosensors. The Hyper-Kamiokande detector is both a "microscope", used to observe elementary particles, and also a "telescope" for observing the Sun and su-

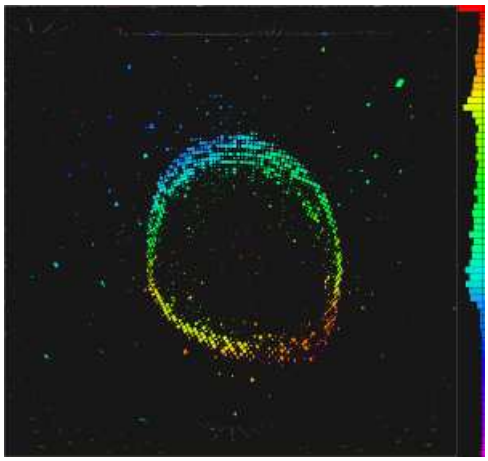

Figure 1.12: Experimental view of muon rings in the T2K detector [44].

pernovas, using neutrinos. The Hyper-Kamiokande project has an extremely rich physics portfolio that spans from the study of the CP violation in the leptonic sector and neutrino mixing parameters using accelerator neutrino and anti-neutrino beams to proton decay, atmospheric neutrinos and neutrinos from astronomical origin.

NOMAD

The NOMAD experiment (Neutrino Oscillation MAgnetic Detector) was designed to search for ν_τ appearance from neutrino oscillations in the CERN wide-band neutrino beam produced by the 450 GeV proton synchrotron. The single-particle reconstruction and lepton identification capability of the NOMAD detector allowed the search for ν_τ appearance in most of the leptonic and hadronic τ decay channels and also to look for $\nu_\mu \rightarrow \nu_e$ oscillations. A second phase of the NOMAD analysis started after the completion of the oscillation searches, with the aim of exploiting the high quality of the available neutrino data samples for precise measurements of cross sections and particle production. This activity could be also of interest for oscillation studies.

The NOMAD detector consisted of a high resolution magnetic detector. In 2000, NOMAD completed its search for $\nu_\mu \rightarrow \nu_\tau$ through their charged-current interactions followed by the τ decay into one or two neutrinos and by the corresponding τ decay daughters. No oscillation signal was found but the limit set was in accordance with the expectations of the proposal, thus demonstrating the validity of the kinematic method used by NOMAD to search for ν_τ charged-current interactions.

This collaboration produced interesting results about the total CCQE muon neutrino cross section on ^{12}C [24] which, unlike MiniBooNE, do not claim for a larger axial mass value of the nucleon.

ArgoNeuT

The ArgoNeuT (Argon Neutrino Test) Experiment ran on the NuMI beam line at the FermiLab, from September 2009 to February 2010. It is the first stage of a project that makes use of Liquid Argon Time Projection Chambers (LArTPCs) as neutrino detectors. ArgoNeuT has collected thou-

sands of beam neutrino events in the 0.1 -10 GeV energy range during its run and some results have been recently published, including the first measurements of the inclusive muon neutrino charged current differential cross sections on argon [48, 49].

In a LArTPC experiment, the free electrons are drifted towards the anode in a uniform electric field where they are registered on wires in multiple (at least two) planes, due to electromagnetic induction and collection of the electrons on the last plane of wires. Because the wires in different planes are at an angle with respect to each other, it is possible to get the full 3D reconstruction of an event. The LArTPC, given its ability for simultaneous precise 3D and calorimetric reconstruction of particle interactions, is an extremely interesting detector technology. It connects physics goals, like sterile neutrino search, with technology development milestones that will lead to a multi-kiloton long-baseline neutrino experiment. This has provided the first ever data for low energy neutrino interactions within a LArTPC, paving the way for construction of larger detectors. Its goals included measurements of the CC inclusive cross sections in the 1-5 GeV range, examining the effects of Final State Interactions (FSI) and testing the Particle ID capabilities of the LArTPC, especially the e/γ separation crucial for future neutrino experiments.

νSTORM

νSTORM (Neutrinos from STORed Muons) is a proposed storage ring facility [58, 59] to deliver beams of muon antineutrinos and electron neutrinos from positive muon decays (muon neutrinos and electron antineutrinos from negative muon decays), with a central muon momentum of 3.8 GeV/c and a momentum acceptance of 10%. The facility will allow searches for eV-scale sterile neutrinos at better than 10 sigma sensitivity. It will be able to provide measurements of neutrino and antineutrino-nucleus scattering cross sections with percent-level precision and will serve as a first step towards developing muon accelerators for particle physics. The flux of the neutrino beam can be determined with percent-level accuracy to perform cross-section measurements for future neutrino oscillation experiments and to resolve the hints for eV-scale sterile neutrinos. νSTORM may be considered as a first step towards a Neutrino Factory and a Muon Collider. In this sense, our studies about the difference between electron neutrino reactions and muon neutrino ones could be valuable for the analysis of its experimental results.

DUNE

The Deep Underground Neutrino Experiment (DUNE), conducted with the detectors installed in the Long-Baseline Neutrino Facility (LBNF) at FermiLab, is expected to achieve important discoveries in forthcoming years, making definitive determinations of neutrino properties, the dynamics of the supernovae that produced the heavy elements necessary for life, and the possibility of proton decay.

With the LBNF facilities and the detectors provided by DUNE [60], the DUNE Collaboration proposes to disentangle the puzzle of neutrinos with broad sensitivity to neutrino oscillation parameters in a single experiment. The focus of the scientific program is the determination of the neutrino mass hierarchy and the analysis of leptonic CP violation by precisely measuring differences between the oscillations of muon-type neutrinos and antineutrinos into electron-type neutrinos and antineutrinos, respectively. Furthermore, the DUNE experiment also focuses on determining the ordering of the neutrino masses as well as on searching for neutrinos beyond the currently known three.

1.7 Structure and motivation of this thesis

As already mentioned in previous sections, most events analyzed by the different collaborations correspond to CCQE processes where a muonic neutrino is scattered by a bound nucleon ($\nu_\mu + n \rightarrow \mu^- + p$). The employment of realistic nuclear models is crucial for the analysis of these and forthcoming experiments, such as NOνA, MINERνA, MiniBooNE or T2K, focused on the search for neutrino oscillations $\nu_\mu \rightarrow \nu_e$.

A proper interpretation of neutrino oscillations implies an accurate description of the CCQE process in a wide range of neutrino energies. It should be noted that the beam neutrino energy is not precisely determined and only an energy distribution of the incoming flux is predicted. Therefore, a control over the uncertainties associated to the nuclear model is indispensable. Likewise, background processes are also important and hard to disentangle from the CCQE signal as the case of the pion production and its subsequent absorption by the nuclear target. Other effects, such as nucleon correlations, meson-exchange currents related to multi-nucleon knock-out or final-state interactions (FSI), can also contribute significantly to the final result and have to be appropriately accounted for in the nuclear models.

Moreover, the oscillation probability directly depends on the neutrino energy, which must be reconstructed from the final-state particles. This reinforces the need to dispose of realistic models that provide an accurate description of the mechanisms involved in neutrino-nucleus interactions. These models are in turn used in the simulations with which experiments define their analyses and interpret their data so it is essential to improve the understanding of neutrino interactions in order to improve neutrino oscillation measurements.

Therefore, the focus of the following chapters is to study electroweak scattering processes, deepening in neutrino-nucleus reactions along the different nuclear regimes of interest for neutrino oscillations. This will be addressed by using realistic models that treat the process in a fully relativistic way, describing both hadronic and nuclear structure. This is directly connected with the growing interest in neutrino-oscillation experiments where an accurate theoretical description of weak interactions is essential to interpret properly the experimental results.

The structure of this thesis will be the following: in Chapter 2 we analyze the case of charged-current neutrino-nucleon elastic interactions where the weak response functions and the nucleon form factors are described; in Chapter 3 we present the formalism of quasielastic neutrino-nucleus interactions within the SuSAv2 model, which is based on the superscaling behavior and the relativistic mean field theory. The Chapter 4 focuses on the 2p-2h MEC contributions as an essential ingredient for the analysis of experimental data, where we make use of an accurate parametrization of fully relativistic microscopic calculations. The extension of the SuSAv2 model to the inelastic regime is detailed in Chapter 5. Afterward, in Chapter 6 we compare the previous theoretical description with electron-nucleus scattering data for all kinematics. This constitutes a solid benchmark to assess the validity of our model for the analysis of the existing charged-current neutrino experimental data, as detailed in Chapter 7. Finally, in Chapter 8 we present a summary and the main conclusions of this PhD thesis.

Chapter 2

Charged-current elastic neutrino-nucleon scattering

In this chapter we introduce the formalism employed to describe elastic charged-current neutrino-nucleon (CC ν-N) scattering processes, which will be of relevance to understand properly the CCQE neutrino-nucleus reactions. Accordingly, we also analyze the relevance of the diverse electromagnetic and weak nucleon form factors and the different single-nucleon responses. This analysis is carried out within the Born Approximation, where a single W boson is exchanged, thus resulting an accurate approach due to the reduced value of the weak coupling constant and the large W-boson mass.

2.1 General formalism

The kinematics of the CC ν-N scattering process ($\nu_l + n \rightarrow l^- + p$), where l represents e, μ or τ, and the frame of reference employed are schematically shown in Fig. 2.1. In this figure, the elastic neutrino-neutron interaction via the exchange of a W^- is displayed, leading to a final state composed of an outgoing lepton and a proton. The antineutrino-nucleon process ($\overline{\nu}_l + p \rightarrow l^+ + n$) is analogous to the previous one.

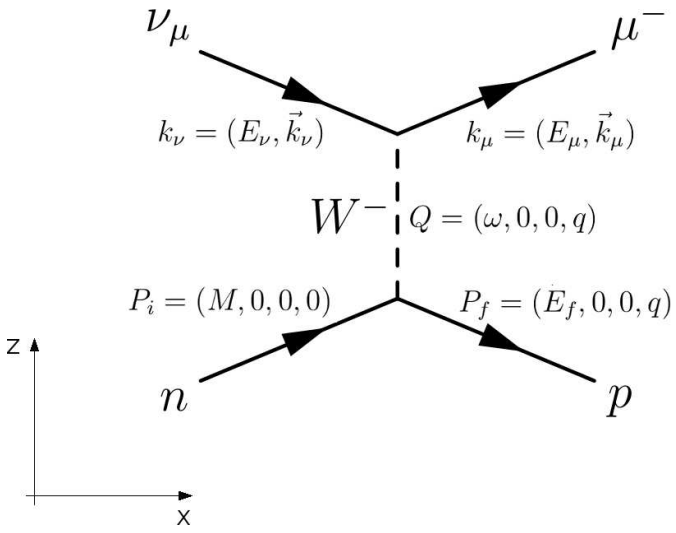

Figure 2.1: Frame of reference and kinematics involved in the CC neutrino-nucleon process where the outgoing lepton is a muon.

Accordingly, the charged-current neutrino (antineutrino) interaction, which is purely isovector, is associated to isospin $T = 1$ as there is a charge exchange where the initial neutron (proton) turns into a proton (neutron) in the final state. This implies an isospin change in the Z-component as $|\Delta T_Z| = 1$. In neutral current interactions ($\nu + N \rightarrow \nu + N$), this Z-component is zero in such a way that isoscalar contributions would also be permitted.

The frame of reference selected for these processes is the laboratory frame in which the initial nucleon is at rest. It is taken for simplicity the momentum transfer to the nucleon along the Z axis and, therefore, the final momentum of the nucleon. Thus, the initial and final momenta of the leptons are contained in the XZ plane. For completeness, the following analysis has also been addressed briefly for the electromagnetic electron-nucleon interaction ($e^- + N \rightarrow e^- + N$) in Appendix A.

The notation employed for the kinematics in CC weak processes is summarized as follows:

- Incident neutrino ν_l:
  - 4-momentum: $k_\nu = (E_\nu, \vec{k}_\nu)$
  - Mass: $m_\nu = 0 \rightarrow E_\nu = |\vec{k}_\nu|$
- Final lepton l^-:
  - 4-momentum: $k_l = (E_l, \vec{k}_l)$
  - Mass: m_l
  - Scattering angle: θ_l
- Initial nucleon n:
  - 4-momentum: $P_i = (M_n, 0)$
  - Mass: M_n
- Final nucleon p:
  - 4-momentum: $P_f = (E_f, \vec{q})$
  - Mass: M_p
- Exchanged boson W^-:
  - 4-momentum: $Q_\nu = (\omega, \vec{q_\nu} \equiv \mathbf{q}_\nu)$

The energy-momentum conservation law in the leptonic and hadronic vertexes implies the following relations:

Leptonic vertex

- Energy conservation: $E_\nu - E_l = \omega$
- Momentum conservation: $\vec{k}_\nu - \vec{k}_l = \vec{q} \Rightarrow q^2 = E_\nu^2 + |\vec{k}_l|^2 - 2E_\nu|\vec{k}_l|\cos\theta_l$

Hadronic vertex

- Energy conservation[1]: $E_f = \omega + M_N \Rightarrow \omega^2 + 2M_N\omega = q^2 \Rightarrow -Q^2 \equiv |Q^2| = 2M_N\omega$
- Momentum conservation: $\vec{q} = \vec{P}_i + \vec{P}_f \Rightarrow \vec{q} = \vec{P}_f$

As shown in the previous equations, the kinematical variables E_ν, E_l and θ_l are not independent so the kinematics of the process is completely defined by determining two of them.

[1]Notice that a generic nucleon mass M_N is employed. This can be either the neutron or proton mass depending on the neutrino or antineutrino case, respectively.

Interaction hamiltonian

The transition amplitude S_{fi} of the neutrino-nucleon scattering process is obtained from the associated interaction hamiltonian (H_W),

$$S_{fi} = -i \int d^4X H_W(X) \, . \tag{2.1}$$

with the hamiltonian expressed as

$$H_W(X) = \left[\frac{g}{2\sqrt{2}}\right]^2 J_\mu^{(l)\dagger}(X) A^\mu_{(N)}(X) = \left[\frac{g}{2\sqrt{2}}\right]^2 J_\mu^{(l)\dagger}(X) D_W^{\mu\nu}(Q) J_\nu^{(N)}(X) \, , \tag{2.2}$$

where g is the dimensionless weak coupling constant, related with the Fermi constant, G_F, as

$$\frac{G_F}{\sqrt{2}} = \frac{g^2}{8M_W^2} \quad ; \quad M_W = 80.401(38) \text{ GeV} \, . \tag{2.3}$$

The 4-potential $A^\mu_{(N)}(X)$, *i.e.*, the field generated by the nucleon in the interaction with the corresponding lepton, can be described in terms of the hadronic current, $J_\nu^{(N)}$, and the weak propagator, $D_W^{\mu\nu}$,

$$\begin{aligned} A^\mu_{(N)}(X) &= \int d^4Y \overbrace{\int \frac{d^4Q}{(2\pi)^4} \left(\frac{-g^{\mu\nu} + Q^\mu Q^\nu / M_W^2}{Q^2 - M_W^2 + i\varepsilon} \right) e^{iQ\cdot(X-Y)}}^{D_W} J_\nu^{(N)}(Y) \\ &\approx \int d^4Y \int \frac{d^4Q}{(2\pi)^4} e^{iQ\cdot(X-Y)} \left(\frac{1}{M_W^2} \right) J^\mu_{(N)}(Y) \, , \end{aligned} \tag{2.4}$$

where the approximation $|Q^2| \ll M_W^2$ ($M_W = 80.401$ GeV/c^2), valid for energies corresponding to the elastic and QE regimes, has been considered.

Next we introduce the leptonic and hadronic currents, used to obtain the double differential cross section.

Leptonic and hadronic currents

The leptonic $j_\mu^{(l)}$ current is defined as a sum of vector (γ^μ) and axial ($\gamma^\mu\gamma^5$) terms associated to the vector and axial structure of the nucleon. The axial term makes possible the parity violation in weak interactions. The previous definition is general for all weak processes and, in particular, for the charged current ones. On the contrary, the analysis of the leptonic current ($j_\mu^{(e)}$) in electromagnetic (e, e') processes only involves the vector component. Thus, the weak leptonic current is defined as

$$j_\mu^{(l)} = \overline{\psi}_l(k_l, s_l)\gamma^\mu(1 \mp \gamma^5)\psi_{\nu_l}(k_{\nu_l}, s_{\nu_l}) \, , \tag{2.5}$$

where the -(+) sign refer to neutrino (antineutrino) processes.

Likewise, the hadronic currents for charged-current weak processes, $J^\mu_{(N)}$, are also composed of vector and axial terms associated to the vector and axial structure of the nucleon. On the contrary, only the vector part remains for electromagnetic interactions (see Appendix A for details),

$$J^\mu_{(N)} = \overline{\psi}_{P_f}(P_f, S_f)\widetilde{\Gamma}^\mu \psi_{P_i}(P_i, S_i) \, , \tag{2.6}$$

where

$$\widetilde{\Gamma}^{\mu} = \underbrace{F_1^V \gamma^{\mu} + \frac{iF_2^V}{2M_N}\sigma^{\mu\nu}Q_{\nu}}_{\widetilde{\Gamma}_V^{\mu}} + \underbrace{G_A\gamma^{\mu}\gamma^5 + F_P Q^{\mu}\gamma^5}_{\widetilde{\Gamma}_A^{\mu}} \quad . \tag{2.7}$$

At first order in perturbation theory and considering plane waves, the wave functions related to the hadronic and leptonic particles can be defined as

$$\psi_{\alpha}(X) = \sqrt{\frac{m_{\alpha}}{E_{\alpha}V}}u_{\alpha}(p_{\alpha}, s_{\alpha})e^{-ip_{\alpha}\cdot X} \, , \tag{2.8}$$

where $u(p_{\alpha}, s_{\alpha})$ are the Dirac spinors and α the corresponding single particle state.

In the previous expresion for the hadronic current (2.6), the inner structure of the nucleon is described by means of the purely-isovector nucleon form factors (F_1^V, F_2^V, G_A and F_P), arising from the CC weak interaction and dependent on Q^2. The isospin symmetry allows for a description of the isovector form factors F_1^V and F_2^V in terms of the electromagnetic Dirac, $F_1^{p,n}$ and Pauli, $F_2^{p,n}$, form factors for protons and neutrons.

Conserved vector current (CVC)

When comparing both electron-nucleon and charged-current neutrino-nucleon scattering, it can be observed that the electromagnetic current (see Appendix A) and the vector component of the weak one are related through the conserved flavor current. This is knwon as the CVC (conserved vector current) hypothesis and implies that the weak vector component is conserved. In the words of J.D. Walecka [16], the CVC implies that the vector part of the single nucleon matrix element of the charge changing weak current, whatever the detailed dynamic structure of the nucleon, can be obtained from electron scattering through the electromagnetic interaction.

The CVC hypothesis assumes that the vector part of the hadronic current and the electromagnetic current are components of the same conseved-current isospin multiplet and thus their form factors are interrelated,

$$F_1^V(Q^2) = \frac{F_1^p(Q^2) - F_1^n(Q^2)}{2} \, , \quad F_2^V(Q^2) = \frac{\mu_p F_2^p(Q^2) - \mu_n F_2^n(Q^2)}{2} \, , \tag{2.9}$$

where $\mu_p = 2.793$ and $\mu_n = -1.913$ are the corresponding proton and neutron magnetic moments. For completeness, the isoscalar form factors are defined as

$$F_1^S(Q^2) = \frac{F_1^p(Q^2) + F_1^n(Q^2)}{2} \, , \quad F_2^S(Q^2) = \frac{\mu_p F_2^p(Q^2) + \mu_n F_2^n(Q^2)}{2} . \tag{2.10}$$

Finally, the axial form factor, G_A, describes the axial-pseudovector structure of the nucleon whereas the F_P one englobes the pseudoscalar structure. All these form factors have been studied in detail in the literature and will be carefully analyzed in Section 2.3. Additional information on the electroweak form factors can also be found in [61–63].

Neutrino-nucleon elastic cross section

The double differential cross section for the elastic neutrino-nucleon interaction can be expressed, in terms of the outgoing lepton energy (E_l) and the solid scattering angle (Ω_l), as:

$$\frac{d^2\sigma}{dE_l d\Omega_l} = \frac{|\vec{k}_l|}{|\vec{k}_{\nu_l}|}\frac{G_F^2}{4\pi^2}\delta\left(\omega - \frac{|Q^2|}{2M_N}\right)\widetilde{\eta}_{\mu\nu}\widetilde{W}^{\mu\nu}\,, \tag{2.11}$$

where $\widetilde{\eta}_{\mu\nu}$ and $\widetilde{W}^{\mu\nu}$ are the leptonic and hadronic tensors, respectively, which arise from the contraction of the leptonic and hadronic currents. The leptonic tensor reads,

$$\widetilde{\eta}_{\mu\nu} = j_\mu^{(l)^\dagger} j_\nu^{(l)} = k_{f,\mu}k_{i,\nu} - k_f\cdot k_i g_{\mu\nu} + k_{f,\nu}k_{i,\mu} \pm i\varepsilon_{\mu\nu\alpha\lambda}k_f^\alpha k_i^\lambda\,, \tag{2.12}$$

being the axial contribution negative for neutrinos and positive for antineutrinos as a consequence of their different helicity. Moreover, the hadronic tensor $\widetilde{W}^{\mu\nu}$ is given by:

$$\begin{aligned}\widetilde{W}^{\mu\nu} &= J_{(N)}^{\mu^\dagger}J_{(N)}^{\nu} = \widetilde{W}_V^{\mu\nu} + \widetilde{W}_A^{\mu\nu} + \widetilde{W}_{VA}^{\mu\nu}\\ &= -W_1(Q^2)g^{\mu\nu} + W_2(Q^2)\frac{P_i^\mu P_i^\nu}{M_N^2} + i\frac{W_3(Q^2)}{2M_N^2}\varepsilon^{\mu\nu\rho\sigma}P_{i,\rho}Q_\sigma\\ &\quad + \frac{W_4(Q^2)}{M_N^2}Q^\mu Q^\nu + W_5(Q^2)\frac{P_i^\mu Q^\nu + Q^\mu P_i^\nu}{2M_N^2}\,,\end{aligned} \tag{2.13}$$

where $W_i(Q^2)$ are the hadronic structure functions defined in terms of the nucleon form factors [63],

$$W_1 = \frac{|Q^2|}{4M_N^2}\left[\left(F_1^V + F_2^V\right)^2 + (G_A)^2\right] + G_A^2 \tag{2.14}$$

$$W_2 = (F_1^V)^2 + \frac{|Q^2|}{4M_N^2}(F_2^V)^2 + (G_A)^2 \tag{2.15}$$

$$W_3 = 2G_A(F_1^V + F_2^V) \tag{2.16}$$

$$W_4 = \frac{|Q^2| - 4M_N^2}{(4M_N^2)^2}(F_2^V)^2 - \frac{F_P G_A}{M_N} + \frac{|Q^2|}{4M_N^2}(F_P)^2 \tag{2.17}$$

$$W_5 = W_2\,. \tag{2.18}$$

In the previous expression (2.13), the antisymmetric term corresponds to the axial contributions and, in particular, to the interference vector-axial term associated to W_3. The contraction of the leptonic and hadronic tensors $\widetilde{\eta}_{\mu\nu}\widetilde{W}^{\mu\nu}$ results in the following expression,

$$\begin{aligned}\frac{d^2\sigma}{dE_l d\Omega} &= \frac{|\vec{k}_l|}{E_{\nu_l}}\frac{G_F^2}{4\pi^2}\delta\left(\omega - \frac{|Q^2|}{2M_N}\right)\widetilde{\eta}_{\mu\nu}\widetilde{W}^{\mu\nu}\\ &= |\vec{k}_l|E_l\frac{G_F^2}{4\pi^2}\delta\left(\omega - \frac{|Q^2|}{2M_N}\right)\left\{2W_1\sin^2\frac{\theta}{2} + W_2E_l\cos^2\frac{\theta}{2} \pm W_3\frac{E_{\nu_l}+E_l}{M_N}E_l\sin^2\frac{\theta}{2}\right.\\ &+ \frac{m_l^2}{E_l(E_l+|\vec{k}_l|)}\left[W_1\cos\theta - \frac{W_2}{2}\cos\theta \pm \frac{W_3}{2}\left(\frac{E_{\nu_l}+E_l}{M_N}\cos\theta - \frac{E_l+|\vec{k}_l|}{M_N}\right)\right.\\ &+ \left.\left.\frac{W_4}{2}\left(\frac{m_l^2}{M_N^2}\cos\theta + \frac{2E_l(E_l+|\vec{k}_l|)}{M_N^2}\sin^2\frac{\theta}{2}\right) - W_5\frac{E_l+|\vec{k}_l|}{2M_N}\right]\right\}\,.\end{aligned} \tag{2.19}$$

where the +(-) sign in W_3 is related to the helicity of neutrinos (antineutrinos), respectively. A similar expresion is found for the electromagnetic case but neglecting the presence of the axial form factors in the hadronic structure functions W_i (see [63]). In situations where the lepton mass is negligible, as in the ultrarelativistic limit, the expression (2.19) can be reduced to

$$\begin{aligned}\frac{d^2\sigma}{dE_l d\Omega_l} &= \frac{|\vec{k}_l|}{E_{\nu_l}}\frac{G_F^2}{4\pi^2}\delta\left(\omega - \frac{|Q^2|}{2M_N}\right)\widetilde{\eta}_{\mu\nu}\widetilde{W}^{\mu\nu} \\ &= |\vec{k}_l|E_l\frac{G_F^2}{4\pi^2}\delta\left(\omega - \frac{|Q^2|}{2M_N}\right)\left\{2W_1\sin^2\frac{\theta}{2} + W_2 E_l\cos^2\frac{\theta}{2} + W_3\frac{E_{\nu_l}+E_l}{M_N}E_l\sin^2\frac{\theta}{2}\right\}. \quad (2.20)\end{aligned}$$

We can also evaluate the single differential cross section by integrating (2.19),

$$\frac{d\sigma}{d\Omega_l} = \frac{G_F^2}{4\pi^2}\frac{|\vec{k}_l|}{E_{\nu_l}}f_{rec}^{-1}\widetilde{\eta}_{\mu\nu}\widetilde{W}^{\mu\nu}\Big|_{\cos\theta=\cos\theta_0}, \quad (2.21)$$

where the nucleon recoil factor (f_{rec}) emerges as

$$f_{rec} \equiv 1 + \frac{E_{\nu_l}(|\vec{k}_l| - E_l\cos\theta)}{M_N|\vec{k}_l|}. \quad (2.22)$$

2.2 Weak response functions

The previous expression for the elastic cross section (2.21) can be also decomposed in terms of the single-nucleon response functions (R_K) [64], which are given as the different $\mu\nu$ components of the hadronic tensor ($W^{\mu\nu}$),

$$\left[\frac{d\sigma}{d\Omega}\right]_\chi = \sigma_0\mathcal{F}_\chi^2, \quad (2.23)$$

where the $\chi = +(-)$ term is referred to neutrino (antineutrino) processes[2]. The σ_0 term is given as

$$\sigma_0 = \frac{G_F^2\cos\theta_c^2}{2\pi^2}k_l E_l\cos^2\frac{\widetilde{\theta}}{2}f_{rec}^{-1}, \quad (2.24)$$

where θ_c is the Cabibbo angle [65], $\cos\theta_c = 0.975$, and a generalized angle, $\widetilde{\theta}$, is also defined as

$$\tan^2\widetilde{\theta}/2 \equiv \frac{|Q^2|}{v_0} \quad ; \quad v_o = (E_\nu + E_l)^2 - q^2 = 4E_\nu E_l - |Q^2|. \quad (2.25)$$

The nucleon structure information is contained in the $\mathcal{F}_\chi^2$ term,

$$\mathcal{F}_\chi^2 = [V_{CC}R_{CC} + 2V_{CL}R_{CL} + V_{LL}R_{LL} + V_T R_T] + \chi[2V_{T'}R_{T'}], \quad (2.26)$$

which is expressed in terms of the leptonic kinematic factors (V_K) and the hadronic response functions (R_K). This expression can be seen as a generalized Rosenbluth decomposition [66]. The diverse terms included in the above expression, (2.26), are related to the different $\mu\nu$ combinations of the $\widetilde{\eta}_{\mu\nu}\widetilde{W}^{\mu\nu}$ contraction:

[2]It can be proven that $\left[\frac{d\sigma}{d\Omega}\right]_\chi = \sigma_0\mathcal{F}_\chi^2 = \frac{G_F^2}{4\pi^2}\frac{|\vec{k}_f|}{|\vec{k}_i|}f_{rec}^{-1}\widetilde{\eta}_{\mu\nu}W^{\mu\nu}$ where $\frac{v_0}{2}\mathcal{F}_\chi^2 = \widetilde{\eta}_{\mu\nu}W^{\mu\nu}$

- CC (charge-charge): $\mu\nu = 00$.
- LL (longitudinal-longitudinal): $\mu\nu = 33$.
- CL (charge-longitudinal): $\mu\nu = 03, 30$
- T (transverse): $\mu\nu = 11, 22$
- T' (transverse vector-axial interference): $\mu\nu = 12, 21$

where the charge terms are related to the time component and the longitudinal ones are those along the direction of the momentum transfer to the nucleon. The 1 and 2 contributions correspond to the transverse components.

For the contraction $\widetilde{\eta}_{\mu\nu}\widetilde{W}^{\mu\nu}$, it should be noticed that the vector current satisfies the current conservation property, $Q_\mu J_V^\mu = 0$. Thus the time and longitudinal components of the leptonic and hadronic currents are related through the energy and momentum transfer, $\omega J_V^0 = q J_V^z \equiv q J_V^3$, and hence,

$$\eta_{VV}^{03} = \eta_{VV}^{30} = \frac{\omega}{q}\eta_{VV}^{00} \quad ; \quad \eta_{VV}^{33} = \left(\frac{\omega}{q}\right)^2 \eta_{VV}^{00} \tag{2.27}$$

$$W_{VV}^{03} = W_{VV}^{30} = \frac{\omega}{q}W_{VV}^{00} \quad ; \quad W_{VV}^{33} = \left(\frac{\omega}{q}\right)^2 W_{VV}^{00}\,. \tag{2.28}$$

2.2.1 Leptonic factors

Following the previous expressions, (2.21) and (2.23), it can be proven that the different leptonic factors, V_K, can be expressed as the individual components of the leptonic tensor, $\widetilde{\eta}_{\mu\nu}$:

$$V_{CC} = \frac{2}{v_0}\eta_{00} = 1 - \delta^2 \tan^2\frac{\widetilde{\theta}}{2} \tag{2.29}$$

$$V_{CL} = \frac{2}{v_0}\frac{1}{2}\left[\eta_{03} + \eta_{30}\right] = \frac{2}{v_0}\eta_{03} = \frac{\lambda}{\kappa} + \frac{\delta^2}{\rho'}\tan^2\frac{\widetilde{\theta}}{2} \tag{2.30}$$

$$V_{LL} = \frac{2}{v_0}\eta_{33} = \left(\frac{\lambda}{\kappa}\right)^2 + \left(1 + \frac{2\lambda}{\kappa\rho'} + \rho\delta^2\right)\delta^2\tan^2\frac{\widetilde{\theta}}{2} \tag{2.31}$$

$$V_T = \frac{2}{v_0}[\eta_{11} + \eta_{22}] = \frac{1}{2}\rho + \tan^2\frac{\widetilde{\theta}}{2} - \frac{\delta^2}{\rho'}\tan^2\frac{\widetilde{\theta}}{2}\left(\frac{\lambda}{\kappa} + \frac{1}{2}\rho\rho'\delta^2\right) \tag{2.32}$$

$$V_{T'} = \frac{2}{v_0}\frac{i}{2}[\eta_{12} + \eta_{21}] = \frac{1}{\rho'}\tan^2\frac{\widetilde{\theta}}{2}\left(1 - \frac{\lambda\rho'}{\kappa}\delta^2\right)\,, \tag{2.33}$$

where it has been assumed $m_\nu = 0$, and an adimensional variable, δ, related to the muon mass (m_μ) has been introduced

$$\delta \equiv \frac{m_\mu}{\sqrt{|Q^2|}}\,. \tag{2.34}$$

The rest of variables are defined as

$$\rho \equiv \frac{|Q^2|}{q^2} = \frac{\tau}{\kappa^2}\,, \tag{2.35}$$

$$\rho' \equiv \frac{q}{E_\nu + E_\mu} = \frac{\tan\widetilde{\theta}/2}{\sqrt{\rho + \tan^2\widetilde{\theta}/2}} \in (0,1)\,. \tag{2.36}$$

2.2.2 Hadronic response functions

Once defined the kinematic factors, V_K, we detail the hadronic response functions, R_K, which are related to the components of the hadronic tensor $\widetilde{W}^{\mu\nu}$ as follows,

$$R_{CC} = W^{00} \tag{2.37}$$

$$R_{CL} = -\frac{1}{2}\left(W^{03} + W^{30}\right) \tag{2.38}$$

$$R_{LL} = W^{33} \tag{2.39}$$

$$R_T = W^{11} + W^{22} \tag{2.40}$$

$$R_{T'} = -\frac{i}{2}\left(W^{12} - W^{21}\right)\,. \tag{2.41}$$

These response functions can be also decomposed in terms of the vector and axial components arising from the hadronic current.

$$R_{CC} = R_{CC}^{VV} + R_{CC}^{AA} \tag{2.42}$$

$$R_{CL} = R_{CL}^{VV} + R_{CL}^{AA} \tag{2.43}$$

$$R_{LL} = R_{LL}^{VV} + R_{LL}^{AA} \tag{2.44}$$

$$R_T = R_T^{VV} + R_T^{AA} \tag{2.45}$$

$$R_{T'} = R_{T'}^{VA}\,. \tag{2.46}$$

Furthermore, the tensorial contraction can be expressed as a sum of symmetric (S) and asymmetric parts (A),

$$\widetilde{\eta}_{\mu\nu}\widetilde{W}^{\mu\nu} = \widetilde{\eta}^S_{\mu\nu}\widetilde{W}^{\mu\nu}_S + \widetilde{\eta}^A_{\mu\nu}\widetilde{W}^{\mu\nu}_A \tag{2.47}$$

$$\widetilde{W}^{\mu\nu}_S = \widetilde{W}^{\mu\nu}_{VV} + \widetilde{W}^{\mu\nu}_{AA} \quad ; \quad \widetilde{W}^{\mu\nu}_A = \widetilde{W}^{\mu\nu}_{VA}\,. \tag{2.48}$$

As a consequence of the conserved vector current (see Eqs. 2.27 and 2.28), the CC and LL responses can be simply written in terms of the CC one,

$$R_{CL}^{VV} = -\frac{\omega}{q}R_{CC}^{VV} \tag{2.49}$$

$$R_{LL}^{VV} = \left(\frac{\omega}{q}\right)^2 R_{CC}^{VV}\,. \tag{2.50}$$

This implies that all polar-vector contributions can be reduced to a single longitudinal response, defined as the the sum of the contributions (0,0), (0,3), (3,0) and (3,3) components,

$$V_{CC}R_{CC}^{VV} + 2V_{CL}R_{CL}^{VV} + V_{LL}R_{LL}^{VV} = V_L R_L^{VV} \equiv X_L^{VV} \,, \tag{2.51}$$

where the response R_L^{VV} is simply reduced to the pure time component of the hadronic tensor, and it is given by

$$R_L^{VV}(q,\omega) = \left(\frac{q^2}{|Q^2|}\right)^2 \left[W_{VV}^{00} - \frac{\omega}{q}(W_{VV}^{03} + W_{VV}^{30}) + \left(\frac{\omega}{q}\right)^2 W_{VV}^{33}\right] = W_{VV}^{00} = R_{CC}^{VV} \,, \tag{2.52}$$

and the corresponding V_L term is defined, according to the current conservation, as

$$V_L = V_{CC} - 2\left(\frac{\omega}{q}\right) V_{CL} + \left(\frac{\omega}{q}\right)^2 V_{LL} \,. \tag{2.53}$$

The previous reduction for the vector term is not allowed for the axial current, as it is not conserved, namely, $Q_\mu J_A^\mu \neq 0$. In this case, we obtain

$$V_{CC}R_{CC}^{AA} + 2V_{CL}R_{CL}^{AA} + V_{LL}R_{LL}^{AA} \equiv X_{C/L}^{AA} \,. \tag{2.54}$$

To complete the analysis we need to study the transverse contributions (μ,ν)=(1,1) and (2,2), as well as the interference V-A channel arising from crossed terms (μ,ν)=(1,2) and (2,1),

$$V_T[R_T^{VV} + R_T^{AA}] \equiv X_T \,. \tag{2.55}$$

$$2V_{T'}R_{T'}^{VA} \equiv X_{T'} \,. \tag{2.56}$$

Following this procedure, the complete single-nucleon response results

$$\mathcal{F}_\chi^2 = X_L^{VV} + X_{C/L}^{AA} + X_T + \chi X_{T'} \,. \tag{2.57}$$

In the case of electromagnetic (e,e') interactions, which are purely vector, the hadronic response functions considered are only the purely vector R_L and R_T, which are defined analogously to the weak ones but considering the electromagnetic form factors for protons and neutrons. This, together with the expression of the differential cross section for electron-nucleon reactions, is detailed in Appendix A.

Hadronic response functions and nucleon form factors

Next, we detail the dependence of the previous hadronic responses with the nucleon form factors. Accordingly, considering the hadronic tensor given in (2.13), making use of the notation:

$$\lambda \equiv \frac{\omega}{2M_N} \quad ; \quad \kappa \equiv \frac{q}{2M_N} \quad ; \quad \tau \equiv \frac{|Q^2|}{4M_N^2} \tag{2.58}$$

and the energy-conservation property in elastic scattering,

$$\omega = \frac{|Q^2|}{2M_N} \Rightarrow \lambda = \tau \,, \tag{2.59}$$

the response functions for neutrino induced reactions can be described in terms of the isovector nucleon form factors as follows,

$$R_L^{VV} = W_{VV}^{00} = R_{CC}^{VV} = \frac{\kappa^2}{\tau}\left[G_E^{(1)}\right]^2 , \tag{2.60}$$

where we have applied the conserved current property (see Eq. 2.52), and $G_E^{(1)}$ is the weak Sachs form factor related to the isovector Dirac and Pauli form factors,

$$G_E^{(1)} = F_1^V - \tau F_2^V , \tag{2.61}$$

with the superscript (1) denoting the isovector nature of the charged-current weak interaction. On the contrary, as the axial current is not conserved, it is necessary to calculate each single term:

$$R_{CC}^{AA} = W_{AA}^{00} = \frac{\kappa^2}{\tau}\left(\frac{\lambda}{\kappa}\right)^2\left[G_A'^{(1)}\right]^2 \tag{2.62}$$

$$R_{LL}^{AA} = W_{AA}^{33} = \frac{\kappa^2}{\tau}\left[G_A'^{(1)}\right]^2 \tag{2.63}$$

$$R_{CL}^{AA} = -\frac{1}{2}\left(W_{AA}^{03} + W_{AA}^{30}\right) = -\frac{\kappa^2}{\tau}\left(\frac{\lambda}{\kappa}\right)\left[G_A'^{(1)}\right]^2 , \tag{2.64}$$

with G_A' expressed as a combination of the axial (G_A) and pseudoscalar ($G_P = \frac{F_P}{2M_N}$) form factors,

$$G_A'^{(1)} = G_A - \tau G_P . \tag{2.65}$$

The transverse responses are given as

$$R_T^{VV} = W_{VV}^{11} + W_{VV}^{22} = 2\tau\left[G_M^{(1)}\right]^2 \tag{2.66}$$

$$R_T^{AA} = W_{AA}^{11} + W_{AA}^{22} = 2(1+\tau)\left[G_A\right]^2 \tag{2.67}$$

$$R_{T'}^{VA} = -\frac{i}{2}\left(W_{VA}^{12} - W_{VA}^{21}\right) = -2\sqrt{\tau(1+\tau)}G_M^{(1)}G_A , \tag{2.68}$$

where $G_M^{(1)}$ is the weak Sachs form factor:

$$G_M^{(1)} = F_1^V + F_2^V . \tag{2.69}$$

2.3 Hadronic structure

The study of neutrino-nucleon and neutrino-nucleus interactions requires to achieve a deep knowledge of the hadronic current that involves the nucleon form factors, where the latter are intimately related to the inner structure of the nucleon. In this section, we analyze various parametrizations of the nucleon form factors and comment on their differences.

2.3.1 Vector structure

As introduced in Section 2.1, the vector part of the weak hadronic current (2.6) is given in terms of two independent isovector functions, $F_1^V(Q^2)$ y $F_2^V(Q^2)$, associated to the electromagnetic Dirac

($F_1^{n,p}(Q^2)$) and Pauli ($F_2^{n,p}(Q^2)$) form factors (2.9) by means of the CVC hypothesis. These electromagnetic form factors have been experimentally determined by measuring differential cross sections. In this context, it is common to use the electric ($G_E^{n,p}(Q^2)$) and magnetic ($G_M^{n,p}(Q^2)$) Sachs form factors,

$$G_E^{n,p} \equiv F_1^{n,p} - \tau F_2^{n,p} \tag{2.70}$$

$$G_M^{n,p} \equiv F_1^{n,p} + F_2^{n,p} , \tag{2.71}$$

where $\tau \equiv |Q^2|/4M^2$. The terms $G_E^{n,p}$ y $G_M^{n,p}$ are known, respectively, as electric and magnetic Sachs form factors, and depend on the 4-momentum transferred (Q^2) to the nucleon.

For electron-nucleon scattering and considering the static limit $Q^2 \to 0$, the nucleon structure is not revealed; the incident lepton interacts with a "point-like" particle with charge "$+e$" for the proton and electrically neutral for the neutron. At these kinematics, the nucleon form factors must fulfill some requirements,

$$F_1^p(0) = 1 , \qquad F_2^p(0) = 1 ; \tag{2.72}$$

$$F_1^n(0) = 0 , \qquad F_2^n(0) = 1 ; \tag{2.73}$$

$$G_E^p(0) = 1 , \qquad G_M^p(0) = \mu_p = 2.793 ; \tag{2.74}$$

$$G_E^n(0) = 0 , \qquad G_M^n(0) = \mu_n = -1.913 , \tag{2.75}$$

whereas in the asymptotic limit, $|Q^2| \to \infty$, the behavior of the nucleon form factors can be obtained by making use of perturbative QCD (pQCD).

Accordingly, the weak isovector Sachs form factors, $G_E^{(1)}(Q^2)$ and $G_M^{(1)}(Q^2)$, are defined in terms of the electromagnetic ones as,

$$G_E^{(1)} = G_E^p - G_E^n \equiv F_1^V - \tau F_2^V \tag{2.76}$$

$$G_M^{(1)} = G_M^p - G_M^n \equiv F_1^V + F_2^V , \tag{2.77}$$

with $G_E^{(1)}(0) = 1/2$ and $G_M^{(1)}(0) \equiv \mu_V = (\mu_p - \mu_n)/2 = 2.353$, being μ_V the isovector magnetic moment.

2.3.2 Dynamical description of the electromagnetic form factors

Once determined the relationship between the electromagnetic and the weak form factors and their behavior in extreme situations: static limit ($Q^2 \to 0$) and asymptotic limit ($|Q^2| \to \infty$), we focus on the explicit dependence of $G_{E,M}^{n,p}$ with Q^2 for low and intermediate kinematics. For this purpose, we consider the most common parametrizations and models for the nucleon form factors.

Galster dipolar parametrization

This parametrization, firstly introduced in 1971 [18], is widely used by the theoretical and experimental community and gives a reasonable description of the proton experimental data for $|Q^2| \leq 1$ GeV^2 ($\sim 5\%$). In the neutron case, the description is not very accurate due to the data uncertainty. It presents a high simplicity based on a dipolar functional form,

$$G_E^p(Q^2) = G_D^V(Q^2) \tag{2.78}$$

$$G_E^n(Q^2) = -\mu_n \tau G_D^V \xi_n \tag{2.79}$$

$$G_M^p(Q^2) = \mu_p G_D^V(Q^2) \tag{2.80}$$

$$G_M^n(Q^2) = \mu_n G_D^V(Q^2)\,, \tag{2.81}$$

where $\xi_n = (1 + \lambda_n \tau)^{-1}$ with $\lambda_n = 5.6$ and $\tau = |Q^2|/4M_N^2$, and $\mu_p = 2.793$ and $\mu_n = -1.913$ are the proton and neutron magnetic moments. The dipolar form factor, G_D^V, is described as:

$$G_D^V(Q^2) = \frac{1}{\left(1 + \frac{|Q^2|}{M_V^2}\right)^2} \equiv \frac{1}{\left(1 + \lambda_D^V \tau\right)^2} \quad ; \qquad G_D^V(0) = 1 \quad ; \quad G_D^V(|Q^2| \to \infty) = 0\,, \tag{2.82}$$

where the parameter values are $\lambda_D^V = 4M_N^2/M_V^2 = 4.97$ and $M_V = 0.843$ GeV. For $Q^2 \to 0$, the form factors are fixed by the electric charge and the nucleon magnetic moments. Typically this parametrization is constrained to be consistent with experimental data for the neutron charge radius. However, recent and more precise experimental results [67] have shown the limitation of this parametrization to fit all these data. This has motivated the analysis of other approaches.

Kelly parametrization

Recently, a new parametrization of the electromagnetic form factors has been developed by J.J. Kelly [68]. This is basically an extension of the Galster one, providing a reasonable description of all experimental data. In this approach, the electric and magnetic form factors are defined as,

$$G(Q^2) \propto \frac{\sum_{k=0}^{n} a_k \tau^k}{1 + \sum_{k=1}^{n+2} b_k \tau^k}\,, \tag{2.83}$$

where both numerator and denominator are polynomials in τ. With $n = 1$ and $a_0 = 1$, this parametrization provides excellent fits to G_E^p, G_M^p/μ_p and G_M^n/μ_n using only four parameters. However, this approach is less successful for G_E^n. More specific details can be found in [68].

VMD models: GKeX parametrization

A more accurate description of the nucleon form factors can be obtained from the VMD (vector meson dominance) models. Within this phenomenological description, the form factors are expressed in terms of mesonic propagators and meson-nucleon form factors. The most representative VMD models are the Gari-Krumpelmann parametrization [69], which incorporates the description

for high $|Q^2|$ introduced by the pQCD; and the recently-developed GKeX parametrization, also known as Lomon prescription [70]. The validity of the GKeX parametrization extends over all range of Q^2 where electron data exist (0.1-10 GeV). This description represents an extension of the Gari-Krumpelmann one, including also the effects arising from the vector mesons: ρ, ρ', ω, ω' and ϕ.

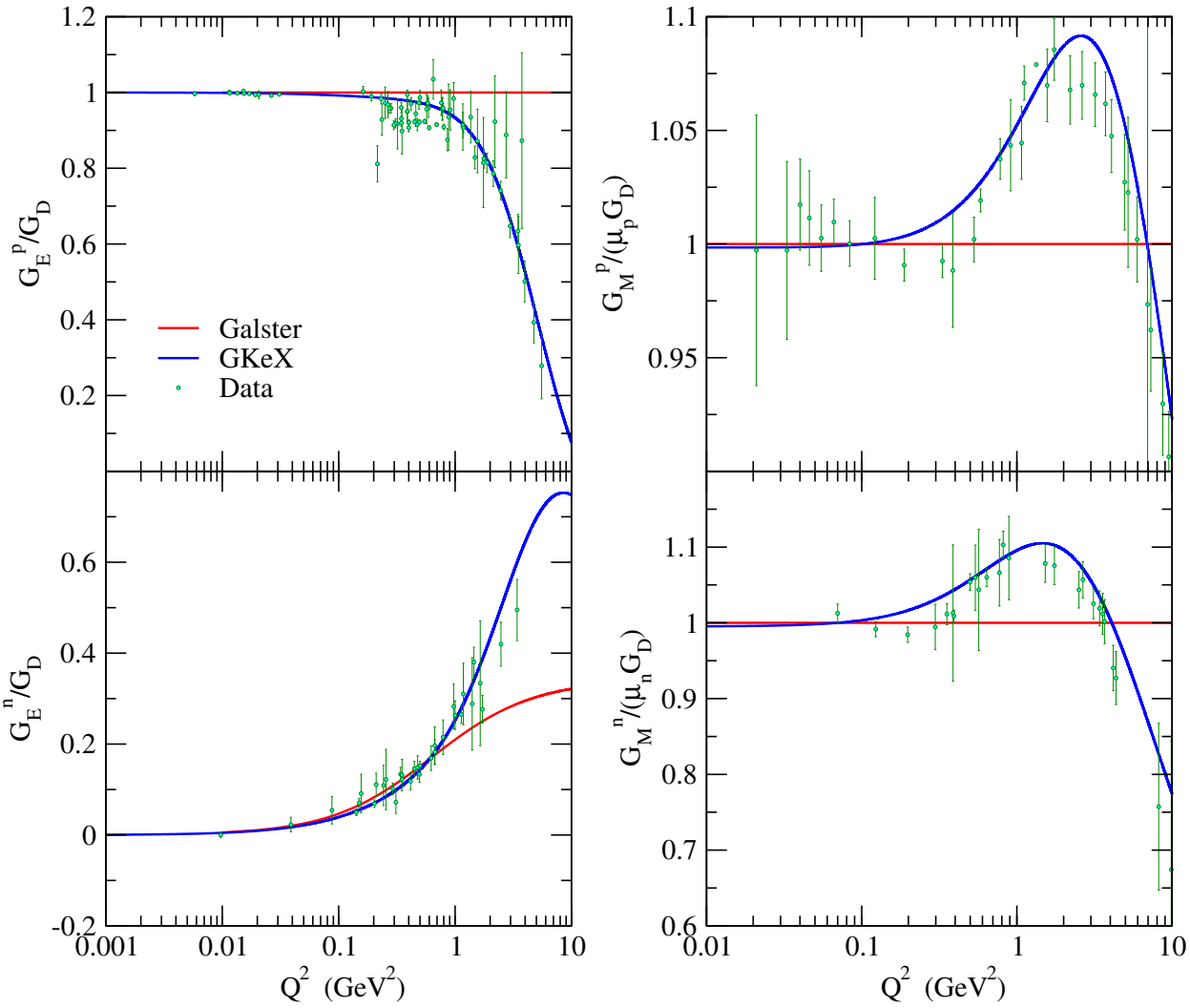

Figure 2.2: Electromagnetic Sachs form factors as a function of $|Q^2|$ for the Galster and GKeX parametrizations and divided by the appropriate dipole factor. Experimental data taken from [71].

In Fig. 2.2 we compare the electromagnetic form factors, $G_E^{n,p}$ y $G_M^{n,p}$, divided by the appropriate dipole term for the Galster and GKeX parametrizations. Both are very similar for low $|Q^2|$ values, whereas their differences increase substantially with $|Q^2|$. Furthermore, the GKeX model reproduces the experimental results accurately, due to its more sophisticated description of the nucleon structure. For completeness, we also show in Fig. 2.3 the isovector form factors, $G_E^{(1)}$ y $G_M^{(1)}$, associated to the weak current for both parametrizations. This analysis reinforces the idea of using the GKex parametrization in the nucleon form factors employed in the study of QE processes. Additionally, a detailed analysis of various nucleon form factors' parametrizations and their relevance on the charged-current quasielastic neutrino-nucleus cross section will be analyzed in Chapter 7.

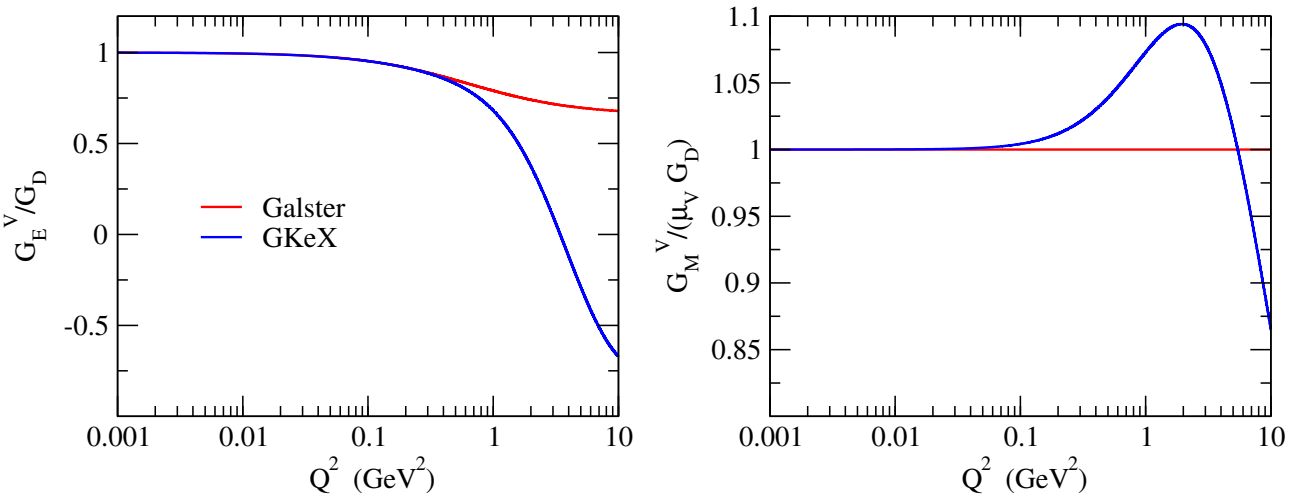

Figure 2.3: Isovector form factors as a function of $|Q^2|$ for the Galster and GKeX paramterizations where μ_V makes reference to the isovector magnetic moment.

2.3.3 Axial structure

The weak hadronic current shown in Eq. (2.6) also depends on the axial $G_A(Q^2)$ and pseudoscalar $G_P(Q^2)$ form factors. The axial one, G_A, has been widely studied in last years [71, 72] in order to determine its functional structure. On the contrary, the pseudoscalar $G_P \equiv F_P/2M_N$, is harder to analyze, being its contribution very small in most of the kinematical situations addressed and negligible for the momentum transferred involved in β-decay processes. Moreover, current data are not precise enough to determine the functional form of G_A, which is usually parametrized using a dipole form, analogously to the vector form factors,

$$G_A(Q^2) = \frac{g_A}{\left(1 + \frac{Q^2}{M_A^2}\right)^2}\,, \tag{2.84}$$

where $g_A = -1.267$ is the axial-vector coupling constant and $M_A = 1.032(36)$ GeV is the nucleon axial mass. The g_A parameter is determined through β-decay processes with neutrons in the elastic limit $Q^2 \to 0$ [73], and the axial mass M_A value has been extracted from deuterium-filled bubble chamber experiments [17]. More information regarding the functional form of G_A and the possible quenching of g_A can be found, respectively, in Appendices D and E.

The axial and pseudoscalar form factors can be connected making use of the PCAC (partially conserved axial current) hypothesis (see [74] for details), through the Goldberger-Treiman relation,

$$G_P(Q^2) = \frac{4M_N^2}{Q^2 + m_\pi^2} G_A(Q^2) \quad ; \quad m_\pi : \text{pion mass}\,. \tag{2.85}$$

In current neutrino-nucleus investigations, one of the main sources of uncertainty comes from the axial form factor, and specifically, its dependence with Q^2 and M_A. In this sense, recent CCQE neutrino experiments on ^{12}C, such as MiniBooNE or MINERνA, have estimated higher M_A values ($M_A \approx 1.35$ GeV) in disagreement with the standard estimations. It must be taken into account that the standard value, $M_A = 1.03$ GeV, is consistent with deuterium experimental data where nuclear effects are negligible as well as with weak pion production data at low $|Q^2|$. Hence the increase of

the axial mass value in these experiments must be interpreted as the lack of some ingredients in the model employed for the data analysis. In particular, the role played by multinucleon effects, such as 2p-2h MEC in CCQE neutrino-nucleus experiments will be explored in Chapter 7 as a possible explanation of the "apparent" increase of M_A.

In Fig. 2.4, we analyze the axial form factors, G_A and G_P, using the world average axial mass value as well as an increase value of 1.35 GeV. Whilst small differences emerge at very low $|Q^2|$, we can observe how G_A increases with M_A for large values of $|Q^2|$. On the contrary, this effect is not visible for G_P due to the factor $\frac{1}{1+|Q^2|/m_\pi^2}$ where $m_\pi \ll M_A$. Moreover, the pseudoscalar form factor falls to zero faster than the axial one which turns into a less relevant contribution of pseudoscalar effects in the region of elastic, QE scattering and beyond.

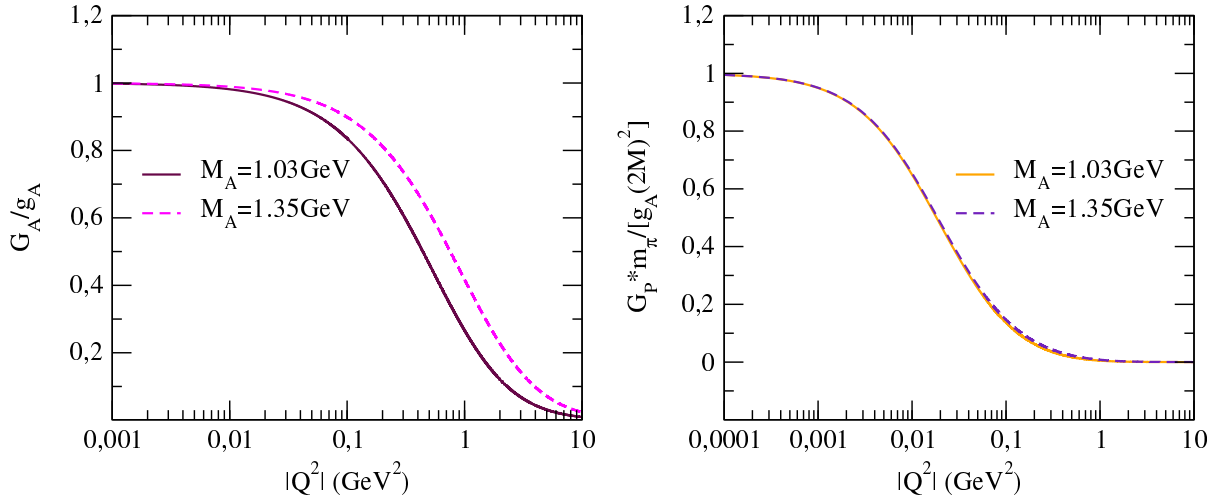

Figure 2.4: Axial (G_A) and pseudoscalar (G_P) form factors for two M_A values as a function of $|Q^2|$.

Finally, it is worth mentioning that the differences between neutrino and antineutrino cross sections, which arise basically from the V-A interference term (2.21), start to disappear as $|Q^2|$ increases. Notice that the $R_{T'}^{VA}$ response (see Eq. 2.68) depends on G_A that approaches zero for large $|Q^2|$.

Chapter 3

Charged-current quasielastic neutrino-nucleus scattering

After presenting the formalism of neutrino-nucleon elastic scattering, in this chapter we extend our theoretical description to charged-current neutrino-nucleus interaction in the quasielastic regime and the study of nuclear effects. This is of interest for most recent neutrino experiments that employ different nuclear targets to measure the oscillation parameters at energies where the quasielastic regime dominates.

Unlike the elastic scattering where we only consider the inner structure of the nucleon, quasielastic reactions require a description of the nuclear structure. In this PhD thesis, the description of the lepton-nucleus interaction and, in particular, the nuclear dynamics, is addressed within the context of the SuperScaling Approach (SuSA), which assumes the existence of universal scaling functions for both electromagnetic and weak interactions. For a proper understanding of this approach, we give a brief description of the relativistic Fermi gas model that will help to introduce the basis of the SuSA model as a semiphenomelogical approach based on the analysis of inclusive (e,e') data. Next, we extend our description to the relativistic mean field (RMF) theory and the relativistic plane wave impulse approximation (RPWIA) models as a more sophisticated procedure to include final-state interaction (FSI) effects as well as the mean field generated by the nuclear constituents in the neutrino-nucleus interaction. The RMF has the merit of treating final-state interactions in a relativistic framework, which is of relevance for the analysis of neutrino experiments. In neutrino-nucleus interactions, after the final-state particles have been created, they propagate out through the nucleus, undergoing strong interactions with the other nucleons inside the nucleus. These "final-state interactions" can significantly alter the momentum and direction of the final-state particles as well as the type and number of particles. Accordingly, pions and nucleons can be absorbed within the nuclear medium or their collisions with other nucleons can generate additional particles. Thus a consistent and relativistic treatment of these interactions is essential to determine the contribution of the different reaction mechanisms to neutrino-nucleus cross section.

The description of the the many-body physics of the interacting nucleons within the RMF and RPWIA models is therefore included in our framework, in the so-called SuSAv2 (SuperScaling Approach version 2) model. This approach has been recently applied to the analysis of QE electron scattering data [38] for several nuclear targets as well as to charged-current quasielastic (CCQE) neutrino-nucleus experiments [39], yielding an accurate description of the experimental data in both cases.

3.1 General formalism of the CCQE process

In this section we show schematically the kinematics involved in studies of lepton scattering from nuclei, focusing on charge-changing neutrino reactions. Most kinematic variables have been previously defined in Chapter 2 for elastic neutrino-nucleon scattering. Here we employ that notation for (ν_l, l^-) and $(\overline{\nu}_l, l^+)$ neutrino-nucleus reactions.

We specifically analyze the CCQE neutrino scattering process in which an incident beam of neutrinos with 4-momentum $k^\mu = (E_\nu, \mathbf{k}_\nu)$ interacts with a nucleus. In the final state, a charged lepton with 4-momentum $k'^\mu = (E'_l, \mathbf{k}'_l)$ emerges as well as an outgoing nucleon. This process is mediated by a weak boson (W) and can be described as,

$$\nu_\mu(\overline{\nu}_\mu) + A \rightarrow \mu^-(\mu^+) + p(n) + (A-1) \tag{3.1}$$

with A the nuclear target and $(A-1)$ the residual nucleus after the interaction. Compared to the elastic case, the complexity of the nuclear dynamics introduces some uncertainties in the description, related to the inner structure of the nucleus or final-state interactions described above. Many theoretical approaches evaluate these processes in the Impulse Approximation (IA), which assumes the incident lepton to only interact with a single bound nucleon as shown in Fig. 3.1. The influence of the remaining nucleons over the entire process is taken into account in different ways depending on the nuclear model employed. Hence, the IA describes the nuclear many-body matrix element as a sum of single-nucleon current matrix elements.

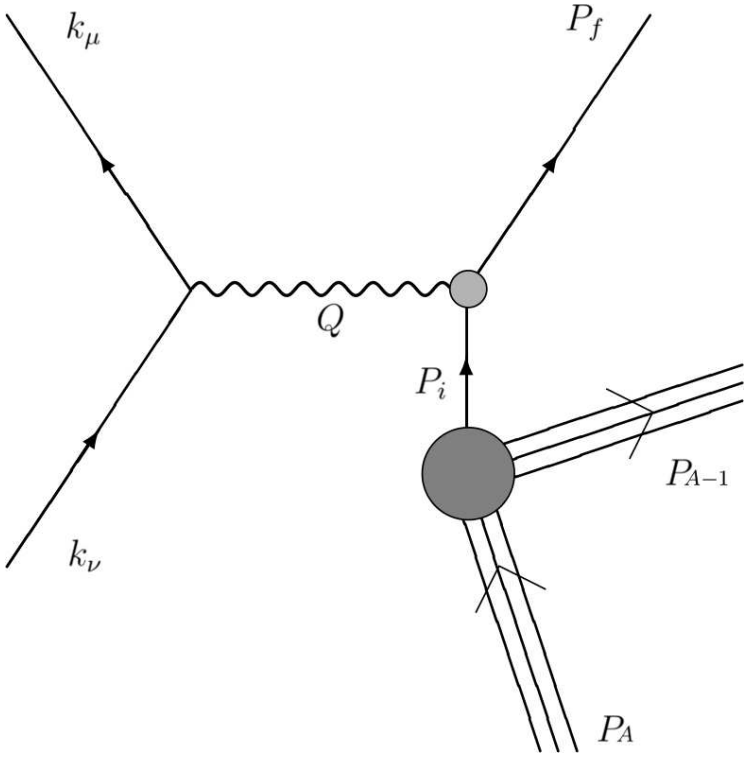

Figure 3.1: Schematic view of the charged-current neutrino-nucleus scattering process in the Impulse Approximation (IA).

3.1.1 Lepton scattering kinematics

Going into detail to the description of lepton kinematics, the neutrino and final-lepton energies are given as

$$E_{\nu_l} = \sqrt{m_\nu^2 + k_\nu^2} \tag{3.2}$$

$$E_l = \sqrt{m_l^2 + k_l'^2}, \tag{3.3}$$

where m_ν and m_l are the masses of the incident neutrino and outgoing lepton, respectively. The 4-momentum transfer to the nucleus $Q^\mu = (\omega, \mathbf{q})$ is given by

$$\omega = E_\nu - E_l \tag{3.4}$$

$$\mathbf{q} = \mathbf{k}_\nu - \mathbf{k}_l', \tag{3.5}$$

being ω and $\mathbf{q}$ the energy transfer and 3-momentum transfer, respectively. Given an excitation from target rest mass M_i to some final rest mass $M_f \geq M_i$ (that is, the final hadronic rest frame total energy is $W = M_f$), we define a sort of excitation energy

$$\omega_0 \equiv \frac{1}{2M_i}\left(M_f^2 - M_i^2\right) \geq 0\,, \tag{3.6}$$

related to the mass excess of the residual nucleus. This value sets a minimum neutrino energy for the QE neutrino interaction to take place. In the case of NCQE scattering, this would be the minimum energy required for the process whereas in the CCQE one we must also consider the energy needed to create the outgoing-lepton mass. Then from energy-momentum conservation one has

$$\omega = \omega_0 + \frac{|Q^2|}{2M_i}. \tag{3.7}$$

Solving Eqs. (3.4) and (3.7), one gets expressions for the scattered lepton's energy and 3-momentum. Defining

$$\epsilon_1 \equiv \sqrt{M_i^2 + 2M_i E_\nu + m_\nu^2 + k_\nu^2 \sin^2\theta_l} \tag{3.8}$$

$$\epsilon_2 \equiv \sqrt{M_i(E_\nu - \omega_0) + \widetilde{M}^2}, \tag{3.9}$$

where θ_l is the lepton scattering angle (the angle between $\mathbf{k}_\nu$ and $\mathbf{k}_l'$) and $\widetilde{M} = \sqrt{(m_l^2 + m_\nu^2)/2}$, it can be shown that

$$k_l' = \frac{1}{\epsilon_1^2}\left[\epsilon_2^2(k_\nu\cos\theta_l) + (M_i + E_\nu)\sqrt{\epsilon_2^4 - m_l^2\epsilon_1^2}\right] \tag{3.10}$$

$$E_l = \frac{1}{\epsilon_1^2}\left[\epsilon_2^2(M_i + E_\nu) + (k_\nu\cos\theta_l)\sqrt{\epsilon_2^4 - m_l^2\epsilon_1^2}\right], \tag{3.11}$$

where for the results to be real for all scattering angles, the beam energy must be greater than $E_{\nu,min}$,

$$E_{\nu,min} = m_l + \omega_0 + \frac{m_l\omega_0 + (m_l^2 - m^2)/2}{M_i - m_l}. \tag{3.12}$$

This result represents the minimum energy required for the CCQE process in terms of the lepton mass and the mass excess of the residual nucleus. In addition, the contribution of the ω_0 parameter

is generally smaller than the lepton mass. In the particular case of (ν, μ^-) reaction on ^{12}C, we have $m_\mu \gg \omega_0$ as the mass excess of the residual nitrogen, $\sim$ 15 MeV, is much smaller than the muon mass, $m_\mu \approx 105$ MeV. Taking into account the mass difference between leptons and nucleus, the third term in Eq. (3.12) gives a negligible contribution in most of the cases.

Hence, for given values of the excitation energy ω_0, beam energy E_ν and the scattering angle θ_l, the quantities $\epsilon_{1,2}$ can be computed and from them the final lepton's energy and 3-momentum are fixed. The 4-momentum transfer is then given as well.

3.2 Relativistic Fermi Gas Model and SuperScaling Approach

Next, in order to describe the structure of the nuclear responses in our theoretical prescription, we introduce the concept of scaling and the main features of the relativistic Fermi gas model [75, 76] that has been used as a basis for the study of scaling and superscaling behaviors.

3.2.1 The concept of scaling and superscaling

Scaling is a phenomenon observed in several areas of Physics and is a fundamental part of the scientific methodology. This is not new; we can think of Galileo's observations of the oscillations of a pendulum, Kepler's discovery of the equal area law for planetary motion and Newton's inverse square law of gravitation. The establishment of a scaling relationship between physical quantities reveals an underlying driving mechanism, and it is the task of Physics to understand and to provide a formalism for that mechanism.

The concept of y scaling in lepton-nucleus reactions was firstly introduced by West [77] as an analog of x scaling in high-energy physics. There it was shown that a collection of non-relativistic point-like charged "nucleons" with negligible final-state interactions leads to an inclusive quasielastic electron scattering cross section that can be written in terms of a factor containing a single-nucleon cross section times a specific function. In the limit of large momentum transfers, this function scales; that is, it becomes a function of only one variable, usually represented by y, and largely independent on the momentum transfer.

Further studies focused on the analysis of this scaling behavior on inclusive electron-nucleus scattering data in a relativistic framework [77] show that this behaviour can also be observed for different nuclei [36, 78]. Concerning the difficulties for this analysis, it should be noticed that the explicit energy dependence of the cross sections complicates the attempt to factorize the electron-nucleus cross section by extraction of a unique single-nucleon cross section. In addition to this, there also exists the question of the off-mass-shell extrapolation of the single-nucleon current as well as the fact that FSI and multi-nucleon interactions can also affect the scaling analysis.

In the particular case of QE electron-nucleus scattering processes, in most of the models based on IA, the inclusive (e,e') cross section can be approximated by a single-nucleon cross section times a specific function of (q,ω). In this case, the lepton interacts with a many-body system in such a way that the energy ω and momentum q are transferred only to individual constituents of the complex system. Scaling occurs at some specific kinematics, where the specific function scales, that is, it becomes dependent on only a single quantity, namely, the scaling variable ψ. This quantity, whose definition is discussed later, is in turn a function of q and ω: $\psi = \psi(q,\omega)$. The function that results once the single-nucleon cross section has been divided out is called the *scaling function*

$f = f(q,\psi)$. In other words, to the extent that at some kinematics this function depends on ψ, but not on q, one says that ψ-scaling occurs.

The study of the scaling function can shed light on the dynamics of the nuclear system. Indeed, within some specific approaches, the scaling function is related to the momentum distribution of the nucleons in the nucleus (or, more generally, with the spectral function) [79, 80].

When studying (e,e') processes it is useful to introduce the following concepts:

- ***Scaling* of first kind**. This is related to the concept of y-scaling: it is satisfied when the scaling function does not explicitly depend on the transferred momentum, but only on ψ including its implicit dependence on q and ω.
- ***Scaling* of second kind**. It is observed when the scaling function is independent of the nuclear species.
- ***Scaling* of zeroth kind**. It occurs when the scaling functions linked to the different channels that make up the cross section, longitudinal (L) and transverse (T), are equal. Hence in inclusive electron scattering, zeroth-kind scaling means that the electromagnetic (EM) scaling functions satisfy $f = f_L = f_T$, where f represents the scaling function associated to the total cross section whereas $f_{L,T}$ refer to the scaling functions obtained from the separate longitudinal and transverse responses.
- ***Superscaling***. Finally, when scaling of both the first and second kinds occurs simultaneously one has superscaling [35, 36].

With these ingredients it is clear that the natural starting point for such an examination is the relativistic Fermi gas (RFG) model in which the nucleus is described as a noninteracting gas of nucleons. Indeed, this model fulfills exactly all of the kinds of scaling previously defined.

The RFG has the appeal of simplicity while maintaining important aspects in the problem such as Lorentz covariance and gauge invariance in a fully relativistic way. Naturally it ignores potentially important effects such as those stemming from strong final-state interactions or two-body MEC and employs an oversimplified initial-state spectral function; nevertheless, such ingredients can be added to the basic model and appear not to invalidate it as a basic starting point for analyses of scaling.

The general procedure used to define scaling functions consists of constructing the inclusive cross section, or nuclear response functions, within a particular theoretical model (or experimental data) and divide them by the appropriate single-nucleon quantity computed within the RFG model.

Here the word "appropriate" entails two aspects to be considered. First, the usual analysis in the region of the quasielastic (QE) peak assumes that the dominant process is elastic scattering from nucleons in the nuclear ground state followed by quasifree ejection of the nucleons from the nucleus, and hence the appropriate single-nucleon form factors are the elastic ones. Second, the nucleons in the nuclear ground state are moving (Fermi motion) and accordingly the single-nucleon cross section used must take this into account.

3.2.2 Nuclear effects and dynamical parameters in the RFG model

The RFG model can be taken as a guide for incorporating relativistic ingredients to more sophisticated models and, particularly, as a first approximation to the nuclear dynamics involved in the QE

region. Within this context, an effective parameter, the Fermi momentum (k_F), sets the transition between occupied states and free nucleons. This parameter is not fixed for all nuclei due to the different nuclear densities which are proportional to k_F^3. On the other hand, the width of the QE response goes as k_F. Typically, the Fermi momentum ranges from $\sim$ 55 MeV/c for deuterium, 200 MeV/c for ^{4}He, to as large as about 250 MeV/c for very heavy nuclei. Moreover, the RFG model accounts for some nuclear effects which are relevant for a scaling analysis such as the Pauli blocking (PB) effects and an average nucleon separation energy, named energy shift (E_{shift}). Pauli blocking affects the low momentum and energy region and will be carefully analyzed in Sect. 3.5.1.

A summary of E_{shift} and k_F values within the RFG model for different nuclei is shown in Table 3.1. These efective parameters have been determined by means of a detailed analysis of inclusive electron scattering data [37].

Nucleus	k_F (MeV/c)	E_{shift} (MeV)
Lithium	165	15
Helium	200	15
Carbon	228	20
Magnesium	230	25
Aluminium	236	18
Calcium	241	28
Iron	241	23
Nickel	245	30
Tin	245	28
Gold	245	25
Lead	248	31

Table 3.1: Estimation of the k_F and E_{shift} parameters within the context of the RFG model for different nuclear species.

The energy shift, E_{shift}, is introduced in the theoretical description to account phenomenologically for the shift observed in the QE peak when the cross section is plotted as a function of ω. This energy shift depends on the different nucleus and can be q-dependent as in the RMF model.

3.2.3 Nuclear responses and QE cross section in the RFG model

With the aim of analyzing the scaling properties, we need to determine the RFG cross section for QE reactions as well as the nuclear responses associated. Here we present the basic formalism for neutrino-induced reactions within the context of the RFG.

In the laboratory system and considering the Born approximation, the charged-current QE (anti)neutrino-nucleus cross section can be written in the form

$$\frac{d^2\sigma}{d\Omega_l d\omega} = \sigma_0 \mathcal{F}_\chi^2 \,, \tag{3.13}$$

where σ_0 is the same as defined for elastic scattering (see Eq. 2.24) in Chapter 2. The whole information on the nuclear structure is contained in $\mathcal{F}_\chi^2$, given as

$$\mathcal{F}_\chi^2 = V_L R_L^{VV} + V_{CC} R_{CC}^{AA} + 2V_{CL} R_{CL}^{AA} + V_{LL} R_{LL}^{AA} + V_T R_T + \chi V_{T'} R_{T'} \,, \tag{3.14}$$

where the kinematical factors V_K coming from the leptonic tensor are the same as defined for elastic scattering in Eqs. (2.29-2.35) and $\chi = +1(-1)$ for neutrino (antineutrino) induced reactions.

As defined in Chapter 2, the weak response functions are given by

$$R_{CC} = W^{00} \tag{3.15}$$
$$R_{CL} = -\frac{1}{2}\left(W^{03} + W^{30}\right) \tag{3.16}$$
$$R_{LL} = W^{33} \tag{3.17}$$
$$R_{L} = W^{00} \quad \text{only for vector terms} \tag{3.18}$$
$$R_{T} = W^{11} + W^{22} \tag{3.19}$$
$$R_{T'} = -\frac{i}{2}\left(W^{12} - W^{21}\right) \tag{3.20}$$

in terms of the inclusive nuclear tensor and composed of vector and axial contributions. Contrary to the case of elastic scattering, here the responses depend not only on the hadronic structure but also on the nuclear many-body system.

Within the RFG model, the nuclear tensor $W^{\mu\nu}$ associated to the (anti)neutrino-nucleus scattering process involves a struck nucleon of momentum $P_i = [E(\mathbf{p}), \mathbf{p}]$ with corresponding on-shell energy $E(\mathbf{p}) = (\mathbf{p}^2 + M^2)^{1/2}$ lying below the Fermi momentum k_F . The neutrinos supply energy (ω) and momentum (q) to the nucleus resulting in a four-momentum $(P_i + Q)^\mu$ lying above the Fermi surface. Conserving energy and momentum and integrating over the momenta in the Fermi sea, the nuclear tensor reads:

$$W^{\mu\nu} = \frac{3\mathcal{N}M^2}{4\pi k_F^3} \int \frac{d^3p}{E(\mathbf{p})E(\mathbf{p}+\mathbf{q})} \times \theta(k_F - |\mathbf{p}|)\theta(|\mathbf{p}+\mathbf{q}| - k_F) \times\delta(\omega - [E(\mathbf{p}+\mathbf{q}) - E(\mathbf{p})]) \times \widetilde{W}^{\mu\nu}_{s.n.}(P_i + Q, P_i) \tag{3.21}$$

where $\widetilde{W}^{\mu\nu}_{s.n.}(P_i + Q, P_i)$ is the single-nucleon hadronic tensor previously shown for the elastic case in (2.13), but obtained by Lorentz transforming the measured responses at the nucleon rest frame to the system where the struck nucleon has 4-momentum P_i^μ.

After integration over the hadronic variables, the nuclear response functions can be written as

$$R_K = \mathcal{N}\Lambda_0 U_K f_{RFG}(\psi), \quad K = CC, CL, LL, T, T', \tag{3.22}$$

where $\mathcal{N}$ is the appropriate nucleon number, and with

$$\Lambda_0 = \frac{\xi_F}{\mathcal{D} M_N \eta_F^3 \kappa} \cong \frac{1}{2\kappa k_F \mathcal{D}} \,. \tag{3.23}$$

The term $\mathcal{D}$ is a relativistic correction given by

$$\mathcal{D} = 1 + \frac{1}{2}\xi_F(1 + \psi^2) \,. \tag{3.24}$$

In Eq. (3.22), $f_{RFG}(\psi)$ is the RFG scaling function defined in the region $\psi' \in (-1, 1)$, and simply given by

$$f_{RFG}(\psi') = \frac{3}{4}(1 - \psi'^2)\theta(1 - \psi'^2) \,, \tag{3.25}$$

where ψ is the scaling variable defined as

$$\psi \equiv \frac{1}{\sqrt{\xi_F}} \frac{\lambda - \tau}{\sqrt{(1+\lambda)\tau + \kappa\sqrt{\tau(\tau+1)}}} \tag{3.26}$$

and we have introduced the following dimensionless variables

$$\begin{aligned}
\xi_F &= \sqrt{1+\eta_F^2} - 1, && (3.27)\\
\eta_F &= \frac{k_F}{M_N} \ll 1, && (3.28)\\
\kappa &= q/(2M_N), && (3.29)\\
\lambda &= \omega/(2M_N) \qquad M_N\text{: nucleon mass}, && (3.30)\\
\tau &= \frac{|Q^2|}{(2M_N)^2} = \kappa^2 - \lambda^2\,. && (3.31)
\end{aligned}$$

At the naïve quasielastic peak where $\lambda = \tau$ (which corresponds to $\omega = |Q^2|/2M_N$) one has $\psi = 0$ and finds that the RFG response region is mapped into the range $-1 \leq \psi \leq +1$ [36]. However, the scaling function does not consider the separation energy between nucleons in the Fermi state, in such a way that the maximum of the QE peak does not correspond exactly with $\omega = |Q^2|/2M_N$. Then, we introduce the E_{shift} parameter into the scaling variable through $\omega' = \omega - E_{shift}$ to fulfill the previous condition. The shifted scaling variable is given as

$$\psi' \equiv \frac{1}{\sqrt{\xi_F}} \frac{\lambda' - \tau'}{\sqrt{(1+\lambda')\tau' + \kappa\sqrt{\tau'(\tau'+1)}}} \tag{3.32}$$

with

$$\begin{aligned}
\lambda' &= \omega'/(2M_N), && (3.33)\\
\tau' &= \kappa^2 - \lambda'^2\,. && (3.34)
\end{aligned}$$

Finally, the single-nucleon responses $U_K \equiv U_K^{s.n}$ are basically the same R_K functions shown in the elastic case (see equations (2.60-2.68)) but also including some extra terms related to corrections of higher order in k_F, which arise from the integration of the nuclear tensor (3.21).

For $K = CC$ we have

$$\begin{aligned}
U_{CC} &= U_{CC}^{VV} + \left(U_{CC}^{AA}\right)_{\text{c.}} + \left(U_{CC}^{AA}\right)_{\text{n.c.}} && (3.35)\\
U_L^{VV} &\equiv U_{CC}^{VV} = \frac{\kappa^2}{\tau}\left[(G_E^{(1)})^2 + \widetilde{W}_2\Delta\right], && (3.36)
\end{aligned}$$

where

$$\widetilde{W}_2 = \frac{(G_E^{(1)})^2 + \tau(G_M^{(1)})^2}{1+\tau} \tag{3.37}$$

$$\Delta = \xi_F(1-\psi^2)\left[\frac{\sqrt{\tau(1+\tau)}}{\kappa} + \frac{\xi_F}{3}\frac{\tau}{\kappa^2}(1-\psi^2)\right] \tag{3.38}$$

and we have written the axial-vector response as the sum of conserved (c.) plus non conserved (n.c.) parts,

$$\left(U_{CC}^{AA}\right)_{\text{c.}} = \frac{\kappa^2}{\tau} G_A^2 \Delta \tag{3.39}$$

$$\left(U_{CC}^{AA}\right)_{\text{n.c.}} = \frac{\kappa^2}{\tau}\frac{\lambda^2}{\kappa^2} {G'_A}^2. \tag{3.40}$$

For $K = CL, LL$ we have

$$U_{CL} = U_{CL}^{VV} + \left(U_{CL}^{AA}\right)_{\text{c.}} + \left(U_{CL}^{AA}\right)_{\text{n.c.}} \tag{3.41}$$

$$U_{LL} = U_{LL}^{VV} + \left(U_{LL}^{AA}\right)_{\text{c.}} + \left(U_{LL}^{AA}\right)_{\text{n.c.}} , \tag{3.42}$$

where the vector and conserved axial-vector parts are determined by current conservation as

$$U_{CL}^{VV} = -\frac{\lambda}{\kappa} U_{CC}^{VV} \tag{3.43}$$

$$\left(U_{CL}^{AA}\right)_{\text{c.}} = -\frac{\lambda}{\kappa}\left(U_{CC}^{AA}\right)_{\text{c.}} \tag{3.44}$$

$$U_{LL}^{VV} = \frac{\lambda^2}{\kappa^2} U_{CC}^{VV} \tag{3.45}$$

$$\left(U_{LL}^{AA}\right)_{\text{c.}} = \frac{\lambda^2}{\kappa^2}\left(U_{CC}^{AA}\right)_{\text{c.}} , \tag{3.46}$$

while the n.c. parts are

$$\left(U_{CL}^{AA}\right)_{\text{n.c.}} = -\frac{\kappa^2}{\tau}\frac{\lambda}{\kappa} {G'_A}^2 \tag{3.47}$$

$$\left(U_{LL}^{AA}\right)_{\text{n.c.}} = \frac{\kappa^2}{\tau} {G'_A}^2 . \tag{3.48}$$

Finally the transverse responses are given by

$$U_T = U_T^{AA} + U_T^{AA} \tag{3.49}$$

$$U_T^{VV} = 2\tau (G_M^{(1)})^2 + \widetilde{W}_2 \Delta \tag{3.50}$$

$$U_T^{AA} = 2(1+\tau) G_A^2 + G_A^2 \Delta \tag{3.51}$$

$$U_{T'}^{VA} = 2 G_A (G_M^{(1)}) \sqrt{\tau(1+\tau)}[1 + \Delta'] \tag{3.52}$$

with

$$\Delta' = \sqrt{\frac{\tau}{1+\tau}} \frac{\xi_F (1-\psi^2)}{2\kappa} . \tag{3.53}$$

To summarize, the quasielastic nuclear response functions have the general structure

$$R_K^{QE} = \frac{1}{k_F} f_{RFG}(\psi') \frac{\mathcal{N}}{2\kappa \mathcal{D}} U_K^{s.n.} \equiv \frac{1}{k_F} f_{RFG}(\psi') G_K \tag{3.54}$$

with

$$G_K = \frac{\mathcal{N}}{2\kappa \mathcal{D}} U_K^{s.n.} . \tag{3.55}$$

For completeness, the electromagnetic electron-nucleus ($e+A \to e'+N+(A-1)$) cross section can be determined in a similar way but only considering the purely-vector terms of the hadronic tensor (2.13) introduced in (3.21). This results in:

$$\frac{d^2\sigma}{d\Omega_e d\omega} = \sigma_{Mott}(v_L R_L^{ee'} + v_T R_T^{ee'}) \tag{3.56}$$

where σ_{Mott} is the Mott cross section and the v_L and v_T terms are the leptonic factors associated to the electromagnetic interactions. In this connection, some similarities can be found with regard to the elastic electron-nucleon interaction equations (see Appendix A for further details).

The electromagnetic nuclear responses, $R_L^{ee'}$ and $R_T^{ee'}$, exhibit the same functional form as the vector longitudinal (3.35) and vector transverse nuclear (3.49) ones obtained for the charged-current neutrino interaction, but considering the isovector form factors, $G_{E,M}^{(1)}$, as well as the isoscalar ones, $G_{E,M}^{(0)}$. Furthermore, the isoscalar and isovector combination can also be related to proton and neutron contributions as shown in Section 2.3.1. Accordingly we can define the electromagnetic nuclear responses as follows,

$$R_{L,T}^{ee'} = \frac{1}{k_F} f_{RFG}(\psi') \frac{1}{2\kappa\mathcal{D}} U_{L,T}^{e,e'} \quad ; \quad G_{L,T}^{ee'} = \frac{1}{2\kappa\mathcal{D}} U_{L,T}^{e,e'}\,, \tag{3.57}$$

where

$$U_L^{ee'} = \frac{\kappa^2}{\tau}\left[\widetilde{G}_E^2 + \widetilde{W}_2^{ee'}\Delta\right] \tag{3.58}$$

$$U_T^{ee'} = 2\tau\widetilde{G}_M^2 + \widetilde{W}_2^{ee'}\Delta\,, \tag{3.59}$$

with

$$\widetilde{G}_E^2 = Z(G_E^p)^2 + N(G_E^n)^2 = \frac{A}{4}\left[(G_E^{(0)})^2 + (G_E^{(1)})^2\right] + M_T G_E^{(0)} G_E^{(1)} \tag{3.60}$$

$$\widetilde{G}_M^2 = Z(G_M^p)^2 + N(G_M^n)^2 = \frac{A}{4}\left[(G_M^{(0)})^2 + (G_M^{(1)})^2\right] + M_T G_M^{(0)} G_M^{(1)} \tag{3.61}$$

$$\widetilde{W}_2^{ee'} = \frac{\widetilde{G}_E^2 + \tau\widetilde{G}_M^2}{1+\tau}\,, \tag{3.62}$$

being $A = Z + N$ and $M_T = (Z - N)/2$. Notice that the terms M_T only contribute for asymmetric nuclei ($N \neq Z$).

3.2.4 Scaling functions

In the previous expressions for the nuclear responses, (3.22) and (3.57), and the subsequent differential cross sections, we have observed that the RFG scaling functions were the same for all longitudinal and transverse channels. While this is true for the RFG model where a universal scaling function emerges from the calculation, the scaling functions that can be extracted from experimental data or different nuclear models can differ between the different channels. In this sense, the general procedure used to define scaling functions consists of constructing the inclusive cross section and the response functions within a particular model (or just taking experimental data) and divide them by the corresponding single-nucleon quantities computed within the RFG model. Thus, we define a global scaling function as well as a specific one for the different channels:

- Scaling functions obtained from the cross section:

$$f^{QE(e,e')} = \frac{\frac{d^2\sigma}{d\Omega_e d\omega}}{\sigma_{Mott}(v_L G_L^{ee'} + v_T G_T^{ee'})} \qquad \text{for } (e,e') \tag{3.63}$$

$$f^{QE(\nu)} = \frac{\frac{d^2\sigma}{d\Omega_l d\omega}}{\sigma_0(V_L G_L^{VV} + V_{CC} G_{CC}^{AA} + 2V_{CL} G_{CL}^{AA} + V_{LL} G_{LL}^{AA} + v_T G_T + \chi v_{T'} G_{T'})} \qquad \text{for CC } (\nu, l^-); (\overline{\nu}, l^+) \tag{3.64}$$

- Specific scaling functions for the individual channels:

$$f_K = k_F \frac{R_K}{G_K}\,. \tag{3.65}$$

Likewise, the proton and neutron scaling functions can be also isolated as well as the isovector and isoscalar ones:

$$f_K^{p,n} = k_F \frac{R_K^{p,n}}{G_K^{p,n}}, \tag{3.66}$$

$$f_K^{(0),(1)} = k_F \frac{R_K^{(0),(1)}}{G_K^{(0),(1)}}\,. \tag{3.67}$$

3.3 SuperScaling Approach: a semiphenomelogical model

Making use of the previous description of the scaling formalism, our aim in this PhD thesis is to achieve a complete theoretical description of neutrino-nucleus reactions that can be applied up to very high energies. This description has to fulfill two basic requirements; it has to be relativistic and it must describe QE electron scattering data from low-intermediate up to high energies. In this sense, the analysis of the large amount of existing (e,e') data is taken as a solid benchmark to test the validity of the model for neutrino reactions at different kinematics and for several nuclei.

Accordingly, the SuperScaling Approach (SuSA) was developed in previous works [64, 81]. This model is based on the superscaling function extracted from QE electron scattering data so as nuclear effects can be analyzed through a semiphenomelogical scaling function $f(\psi') \equiv f_{SuSA}(\psi')$ extracted from the ratio between the experimental QE cross section and the appropriate single-nucleon one [35, 36, 78] (see Section 3.2 for definitions):

$$f(\psi') = \frac{\left(\frac{d^2\sigma}{d\Omega_e d\omega}\right)_{exp}}{\sigma_{Mott}(v_L G_L^{ee'} + v_T G_T^{ee'})} \tag{3.68}$$

The scaling function extracted from the analysis of inclusive electron data at different kinematics and for several nuclei (see Fig. 3.2) shows a spread whose width is rather narrow in the region of $\psi' < 0$ that corresponds to low-intermediate kinematics (below the QE peak). On the contrary, the scaling does not work properly in the region above the QE peak where other contributions can play also an important role. Notice the wide spread of data as ψ' increases.

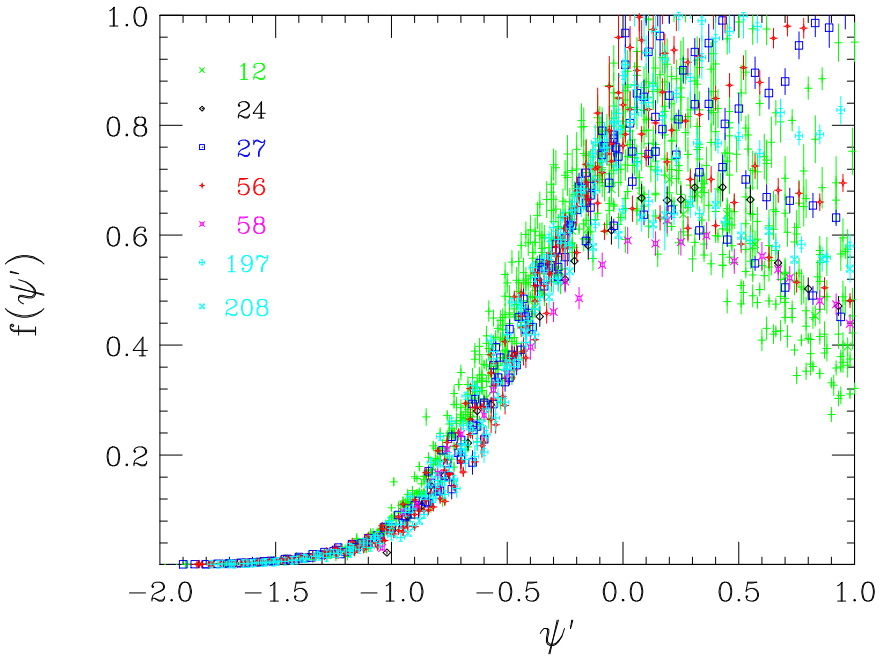

Figure 3.2: Scaling function $f(\psi')$ as a function of ψ' for different nuclei ($A \geq 12$) and several kinematics covering from forward to very backward angles as well as from low to very high incident energies. The values of A corresponding to different symbols are shown in the figure. Data taken from [36].

Nevertheless, the scaling behavior becomes particularly clear if one studies the experimental cross section separated into its longitudinal $f_L(\psi')$ and transverse $f_T(\psi')$ contributions, as shown in Fig. 3.3. The separate longitudinal and transverse contributions lead to the conclusion that the longitudinal experimental data superscale throughout the whole region of the QE peak, whereas the transverse data do not scale, being scaling violations more prominent in the region above the QE peak ($\omega > \omega_{QEP}$, *i.e.*, $\psi' > 0$). Scaling violations at high ω occur because of other non-QE processes, such as meson production and resonance excitations, which are predominantly transverse, come into play. At very high transfer energies (i.,e. high ψ'-values) deep inelastic scattering starts to be relevant. Likewise, 2p-2h states induced by meson-exchange currents are known to have a relevant contribution in the "dip" region between the QE and the Δ peaks. As we detail in Chapter 4, 2p-2h MEC contributions are predominantly transverse for electromagnetic interactions. All these contributions beyond the IA are responsible for scaling violations, mainly observable in the transverse channel.

Other mechanisms, not included in the present work, can introduce some effects in the general discussion. This is the case of RPA nucleon-nucleon correlation effects [30] that can modify the longitudinal and transverse responses because of the very different isospin character of the two channels. However, RPA is only relevant for very low energy/momentum transfers and, in overall, they are expected to be very small.

The prescription adopted in the first version of the SuperScaling Approach has been to employ the experimental longitudinal responses to define a general scaling function for both electromagnetic longitudinal and transverse channels. This implies that both L and T scaling functions are roughly the same after subtracting the non-scaling contributions related to processes beyond the QE regime, that is, zeroth kind scaling is fulfilled. As we shall illustrate, the most modern version

of the model (SuSAv2) contains corrections to this assumption based on Relativistic Mean Field theory.

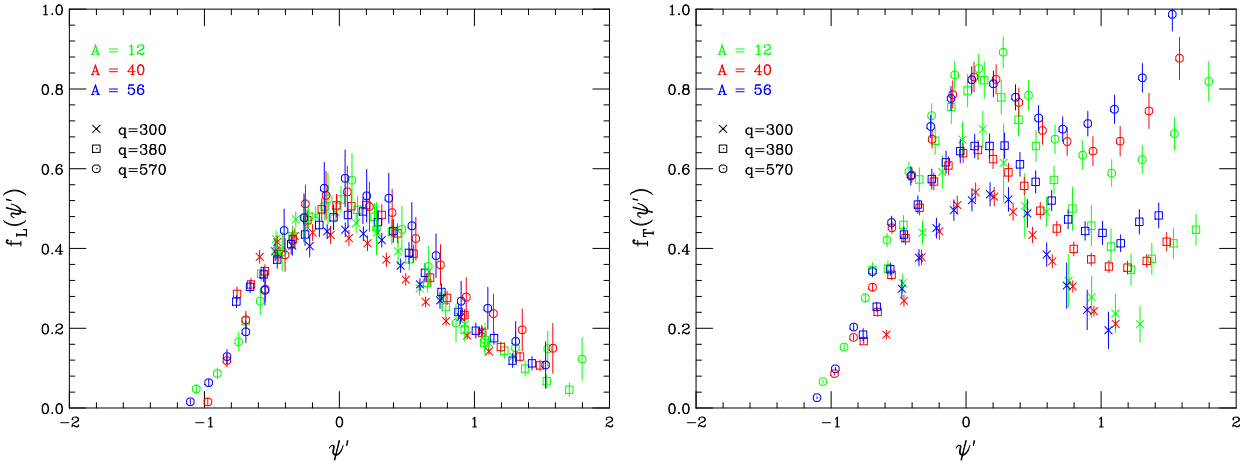

Figure 3.3: Scaling function, $f_L(\psi')$ and $f_T(\psi')$, from the longitudinal and transverse response, respectively, as a function of ψ' for different nuclei ($A \geq 12$) and for different values of q (in MeV/c). Data taken from [82].

From the analysis of the separate longitudinal data shown in Fig. 3.3 (left panel), a "universal" phenomenological L superscaling function f_L has been extracted. In Fig. 3.4, we show the data analysis. The solid curve refers to a fit of the longitudinal data given by the following parametrization, which corresponds to the SuSA scaling function,

$$f_{SuSA}(\psi') \equiv f_L(\psi') = \frac{p_1}{[1 + p_2^2(\psi' - p_3)^2](1 + e^{p_4\psi'})} \tag{3.69}$$

where $p_1 = 2.9883$, $p_2 = 1.9438$, $p_3 = 0.67310$ and $p_4 = -3.8538$. The RFG scaling function is also shown for reference (dashed line).

Note that $f_{SuSA}(\psi')$ presents an asymmetric shape and a tail that extends towards positive values of ψ', *i.e.*, $\omega > \omega_{QEP}$. Its maximum reaches about ~ 0.6. In contrast, the RFG scaling function is symmetric in the scaling variable ψ', is limited strictly to the region $-1 \leq \psi' \leq +1$ and has a maximum value of 3/4. This behavior clearly differs from data and, hence, the RFG does not reproduce the scaling behavior shown by the incusive electron scattering data.

The previous superscaling behavior shown in Fig. 3.4 has been evaluated with other models based on the harmonic oscillation shell model (HO+FSI) and the relativistic Fermi gas (RFG+FSI) that incorporate different descriptions of FSI (see [83] for details). Some asymmetry in the corresponding scaling functions emerges from these calculations, mainly due to the FSI, but the theoretical predictions still differ significantly from the data. In subsequent sections we provide a detailed study of the longitudinal and transverse scaling function within the framework of the RMF theory, analyzind the specific role played by FSI and the relativistic nuclear dynamics.

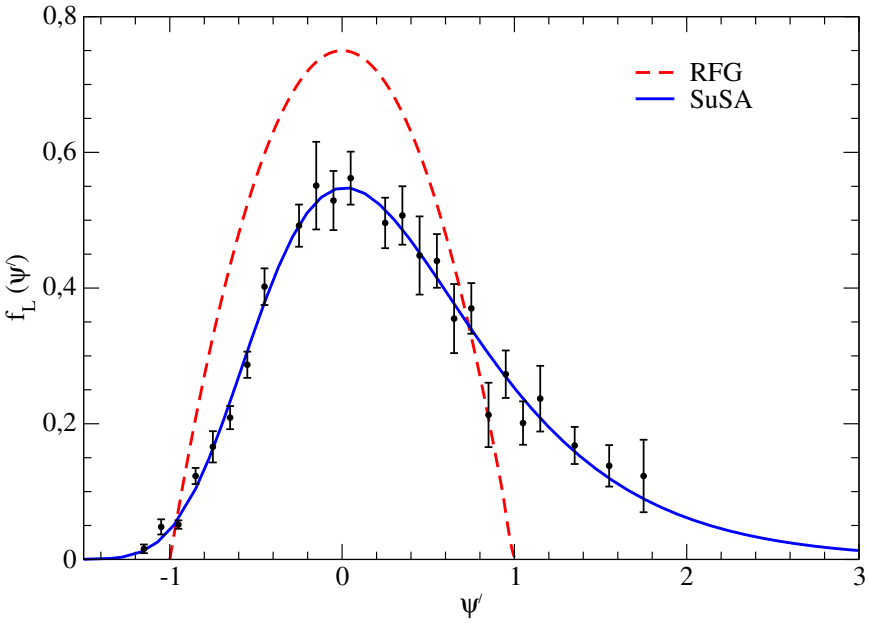

Figure 3.4: Averaged experimental $f_{SuSA}(\psi)$ versus ψ' in the quasielastic region together with a phenomenological parameterization of the selected (e,e') longitudinal scaling data obtained from the R_L data on [82]. The integral of the curve has been normalized to unity. The RFG scaling function is also shown as reference.

.

Moreover, in spite of the difficulty in analyzing the transverse scaling function, previous studies [84] based on the modeling of the QE longitudinal response and contributions from non-QE channels have provided some evidence that the scaling of zeroth kind is not fully satisfied by data. In particular, these studies have found $f^{ee'}_{T,\text{exp}} > f^{ee'}_{L,\text{exp}}$, a result that has motivated a deep study of the scaling behavior as addressed in the next section.

3.4 Extension of the Superscaling Approach from Relativistic Mean Field Theory: the SuSAv2 Model

As defined before, the SuperScaling Approach (SuSA) is based on the scaling properties of the longitudinal response extracted from (e,e') data to predict charged-current quasielastic (CCQE) neutrino- and antineutrino-nucleus cross sections [85]. Thus, SuSA is based on the hypothesis that the neutrino cross section scales as does the electron scattering cross section. This feature is observed in most of the models based on IA (see, for instance, [85–87]). Accordingly, the SuSA model uses the experimental scaling function $f^{ee'}_{L,\text{exp}}$ as a universal scaling function and then builds the different nuclear responses by multiplying it by the corresponding single-nucleon responses. In most IA approaches, one finds that once the single-nucleon cross section is removed in defining the scaling functions, the longitudinal and transverse responses are basically the same.

However, within the framework of the RMF theory, one finds that 0th-kind scaling is mildly broken for momentum transfers in the 1 GeV region being $f_T(\psi') > f_L(\psi')$. Moreover, notice that the extraction of $f^{ee'}_{L,\text{exp}}$ entails the analysis of the purely-vector longitudinal (e,e') nuclear response, which combines isoscalar+isovector contributions. In contrast, CC neutrino-nucleus re-

actions involve only isovector couplings and are mainly dominated by purely transverse responses ($T_{VV} + T_{AA}$ and T'_{VA}). Thus, one could question the validity of the SuperScaling Approach. This subject was studied in [88] by analyzing the scaling functions evaluated with the RMF model. There, it was found that, contrary to what one might expect, the (e,e') longitudinal scaling function agrees with the total (ν_l, l^-) one (which is mainly transverse) better than does the transverse scaling function from (e,e'). This result is explained by the different roles played by the isovector and isoscalar nucleon form factors in each process (see [88] for details).

These previous studies have motivated a superscaling analysis based on the RMF theory in order to improve the analysis of neutrino reactions. Within the RMF model [89] the bound and scattered nucleon wave functions are solutions of the Dirac-Hartree equation in the presence of energy-independent real scalar (attractive) and vector (repulsive) potentials. Since the same relativistic potential is used to describe the initial and final nucleon states, the model is shown to preserve the continuity equation [90] (this is strictly true for the CC2 current operator [86]); hence the results are almost independent of the particular gauge selected [86, 87]. In the RMF model the nucleons are dynamically and strongly *off-shell* and, as a consequence, the cross section is not factorized into a spectral function and an elementary lepton-nucleus cross section.

The RMF has achieved significant success in describing QE electron scattering data. On the one hand, its validity has been widely proved through comparisons with QE (e,e') data (see [86] and Sect. 3.5.2). In this connection, an important result is that the model reproduces surprisingly well the magnitude and shape of $f^{ee'}_{L,\mathrm{exp}}$, *i.e.,* it yields an asymmetric longitudinal scaling function, with more strength in the high-ω tail, and with a maximum value (∼0.6) very close to the experimental one. On the other hand, the model predicts $f^{ee'}_T > f^{ee'}_L$. For instance, at $q = 500$ MeV/c (1000 MeV/c) the transverse RMF scaling function at the maximum is 13% (20%) larger than the longitudinal one. This violation of zeroth-kind scaling was analyzed in [88], where it was shown that the origin of such an effect lies in the distortion of the lower components of the outgoing nucleon Dirac wave function by the FSI.

However, the RMF model also presents some drawbacks. First, it predicts a moderate dependence of the scaling function on the transferred momentum q. For increasing values of q the RMF model presents: i) a strong shift of the scaling functions to higher ω values, ii) too much enhancement of the area under the tail of the functions, and iii) correspondingly too severe a decrease in the maximum of the scaling functions. Despite these shortcomings, the scaling functions obtained within the RMF model reproduce reasonably well the experimental longitudinal scaling function in a wide kinematical region (see Section 3.5). Second, getting results with the RMF model is computationally very expensive, especially when the model is employed to predict neutrino cross sections where one has to fold in the flux distribution of the incident neutrino or to compute totally integrated cross sections. Hence in what follows, after correcting for the too strong q-dependence of the RMF model, we shall implement the main features of the model in a new version of the SuSA approach, called "SuSAv2", that makes it possible to obtain numerical predictions to compare with data using fast codes, yet retaining the basic physics of the RMF.

In summary, in this work we extend the original SuSA model by incorporating in its formalism information from the RMF model. Thus we build the new model in such a way that it reproduces the experimental longitudinal scaling function, produces $f^{ee'}_T > f^{ee'}_L$, takes into account the differences in the isoscalar/isovector scaling functions and avoids the problems of the RMF model in the region of high momentum transfer.

3.4.1 RMF and RPWIA scaling behavior

In this section we present a systematic analysis of the scaling functions computed with the Relativistic Mean Field (RMF) and the Relativistic Plane Wave Impulse Approximation (RPWIA). Both models are based on the relativistic impulse approximation (RIA) and provide a fully relativistic description of the scattering process. The bound state Dirac-spinors are the same in both models and correspond to the solutions of the Dirac equation with scalar and vector potentials. The two prescriptions differ in the treatment of the final state: the RPWIA describes the outgoing nucleon as a relativistic plane wave while the RMF model accounts for the FSI between the outgoing nucleon and the residual nucleus using the same mean field as used for the bound nucleon. In what follows, we analyze the scaling functions involved in (e,e'), (ν,μ^-) and $(\overline{\nu},\mu^+)$ reactions as functions of the momentum transfer q. Due to the large number of existing electron and neutrino experimental data for ^{12}C, most of the calculations presented in this thesis correspond to this nucleus. The extension to other nuclear systems will be addressed in following chapters.

We first split all different response functions by isolating the isoscalar ($T = 0$) and isovector ($T = 1$) contributions in electron scattering, and the vector and axial contributions for neutrino and antineutrino induced reactions: VV (vector-vector), AA (axial-axial), VA (vector-axial). This strategy will allow us to extract clear information on how the FSI affect the different sectors of the nuclear current. Furthermore, it will make it easier to explore the relationships between the different responses linked to (e,e'), (ν,μ^-) and $(\overline{\nu},\mu^+)$ reactions.

Assuming charge symmetry, the two channels, L and T, accesible in electron scattering (3.57) can be decomposed as a sum of isoscalar ($T = 0$) and isovector ($T = 1$) contributions. In terms of the scaling functions, the nuclear responses are defined as,

$$\begin{aligned} R^{ee'}_{L,T}(q,\omega) &= \frac{1}{k_F}\Big[f^{T=1,ee'}_{L,T}(\psi')G^{T=1}_{L,T}(q,\omega) \\ &+ f^{T=0,ee'}_{L,T}(\psi')G^{T=0}_{L,T}(q,\omega)\Big]\,. \end{aligned} \tag{3.70}$$

Similarly, the charge-changing muon-neutrino (antineutrino) responses (3.54) can be given as,

$$R^{VV,\nu(\overline{\nu})}_{L}(q,\omega) = \frac{1}{k_F}f^{VV,\nu(\overline{\nu})}_{L}(\psi')G^{VV}_{L}(q,\omega) \tag{3.71}$$

$$R^{AA,\nu(\overline{\nu})}_{CC}(q,\omega) = \frac{1}{k_F}f^{AA,\nu(\overline{\nu})}_{CC}(\psi')G^{AA}_{CC}(q,\omega) \tag{3.72}$$

$$R^{AA,\nu(\overline{\nu})}_{CL}(q,\omega) = \frac{1}{k_F}f^{AA,\nu(\overline{\nu})}_{CL}(\psi')G^{AA}_{CL}(q,\omega) \tag{3.73}$$

$$R^{AA,\nu(\overline{\nu})}_{LL}(q,\omega) = \frac{1}{k_F}f^{AA,\nu(\overline{\nu})}_{LL}(\psi')G^{AA}_{LL}(q,\omega) \tag{3.74}$$

$$\begin{aligned} R^{\nu(\overline{\nu})}_{T}(q,\omega) &= \frac{1}{k_F}\Big[f^{VV,\nu(\overline{\nu})}_{T}(\psi')G^{VV}_{T}(q,\omega) \\ &+ f^{AA,\nu(\overline{\nu})}_{T}(\psi')G^{AA}_{T}(q,\omega)\Big] \end{aligned} \tag{3.75}$$

$$R^{\nu(\overline{\nu})}_{T'}(q,\omega) = \frac{1}{k_F}f^{VA,\nu(\overline{\nu})}_{T'}(\psi')G^{VA}_{T'}(q,\omega). \tag{3.76}$$

The G_K's terms in (3.70) and (3.71–3.76) are the single-nucleon responses defined in (3.55). Notice that the previous scaling functions f_K for neutrino induced reactions are purely isovector.

In the following we examine three basic features of the scaling functions in the RPWIA and RMF models: shape, position and height of the peak, and the integrals of the scaling functions over ψ'.

3.4.2 Shape of the scaling functions

The goal here is to study the shape of all scaling functions. In Fig. 3.5 (Fig. 3.6), for different values of q, we present the transverse (longitudinal) RMF scaling functions normalized to the maximum value corresponding to a reference function, in this case $f_T^{VV,\nu}$, and relocated so that the maximum is at $\psi' = 0$. As already mentioned, the scaling variable ψ' depends on q, ω and E_{shift}. Thus, for each scaling function, E_{shift} is taken so that the maximum is located at $\psi' = 0$. The results within the RPWIA model are presented in Fig. 3.7.

We do not present results of f_{CC}^{AA}, f_{CL}^{AA}, f_{LL}^{AA} for neutrino and antineutrino scattering, and $f_T^{T=0}$ for electron scattering because they are very sensitive to small effects due to cancellations and/or to the smallness of the denominator (G function) which appears in the definition of the scaling function (3.55). The first three are seen to be insignificant for neutrino reactions as it will be shown in Chapter 7, whereas the fourth does not enter in that case and is known to be a minor correction in the QE regime for electron scattering.

The results from the RPWIA model show that all scaling functions have the same shape (see Fig. 3.7). This comment also applies to models based on nonrelativistic and semirelativistic descriptions (see [85, 91]).

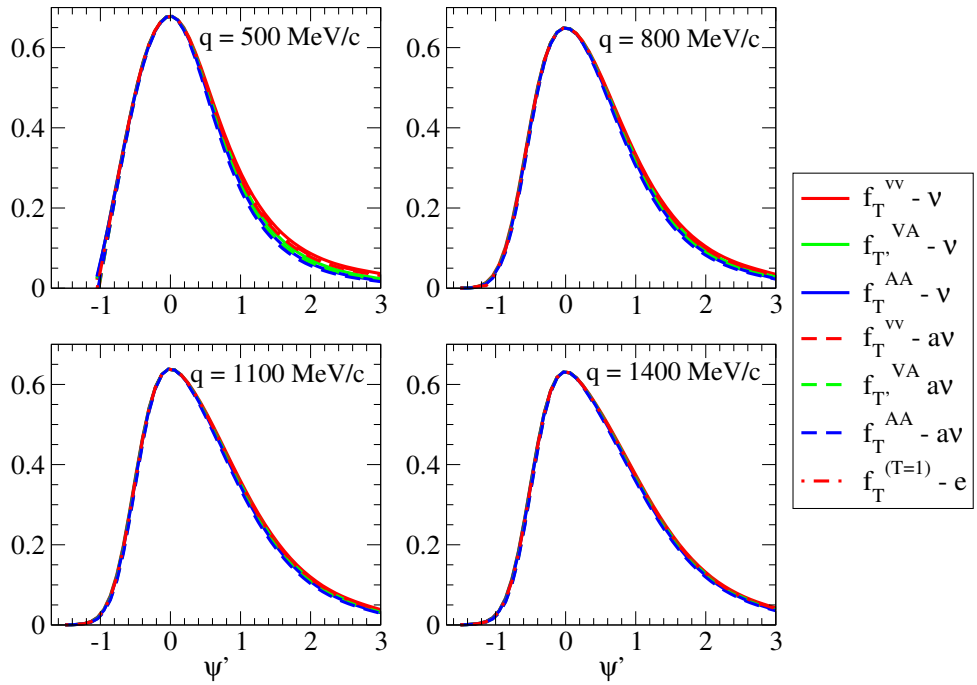

Figure 3.5: Transverse RMF scaling functions normalized to the maximum value corresponding to an arbitrary reference function and relocated at $\psi' = 0$ (see text for details). The convention used to label the different curves is as follows: "e" for electron-induced reactions and "ν" ("aν") for neutrino- (antineutrino-) induced reactions.

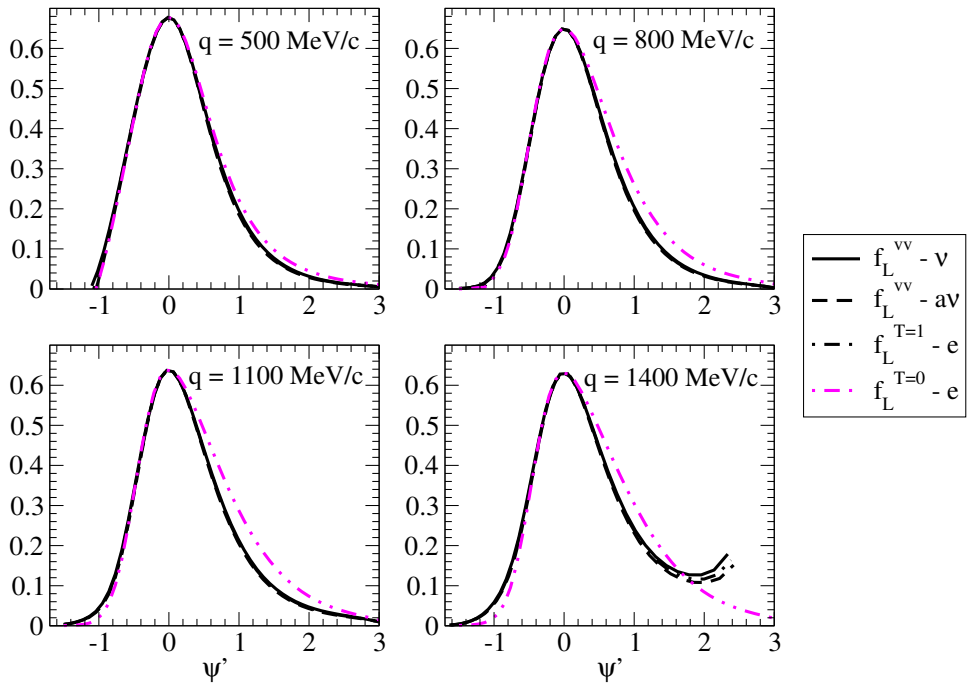

Figure 3.6: As in Fig. 3.5, but now for the longitudinal RMF scaling functions.

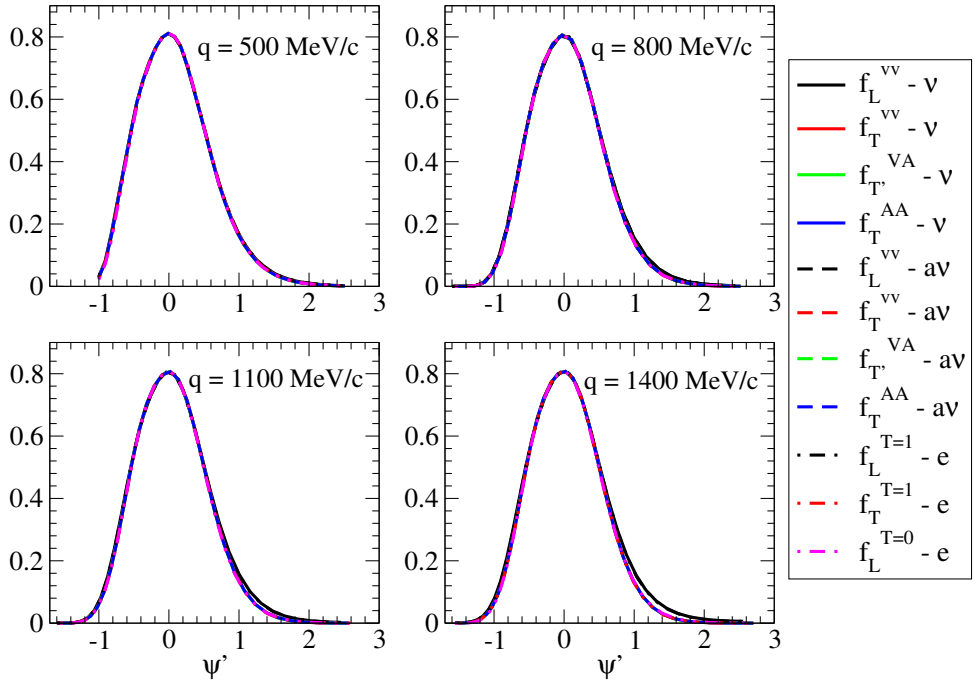

Figure 3.7: As in Fig. 3.5, but in this case the results correspond to RPWIA. Transverse and longitudinal sets are presented together.

Within the RMF model, all transverse scaling functions approximately collapse in a single one. On the contrary, the longitudinal responses are grouped in two sets: one corresponding to the pure electron isovector and neutrino (antineutrino) VV-responses, *i.e.*, $f_L^{T=1,ee'}$ and $f_L^{VV,\nu(\overline{\nu})}$, and the other to the isoscalar contribution for electrons, namely, $f_L^{T=0,ee'}$. This result emerges for all q-values and tends to be rather general. It is also noticeable that the tail is higher and more extended for the transverse responses, whereas for the longitudinal ones it tends to go down faster.

It is worth observing that in all cases the RMF scaling functions display a much more pronounced asymmetric shape than the RPWIA ones, an effect related to the specific treatment of final state interactions.

3.4.3 Height and position of the peak of the scaling function

In the top (bottom) panel in Fig. 3.8 the peak-height of the transverse (longitudinal) set of scaling functions is presented as function of q. The results correspond to RMF and RPWIA predictions. We observe that the peak-heights of the scaling functions within RPWIA are almost q-independent (and very close to RFG value of 3/4), while the RMF ones present a mild q-dependence in the transverse set and a somewhat stronger one for the longitudinal set. It is well known that FSI tend to decrease the peak-height of the responses putting the strength in the tails, especially at high energy loss. This is particularly true for the RMF approach [86, 92] and models based on the Relativistic Green Function (RGF) [93, 94]. Similar effects have also been observed within semirelativistic approaches [85, 91].

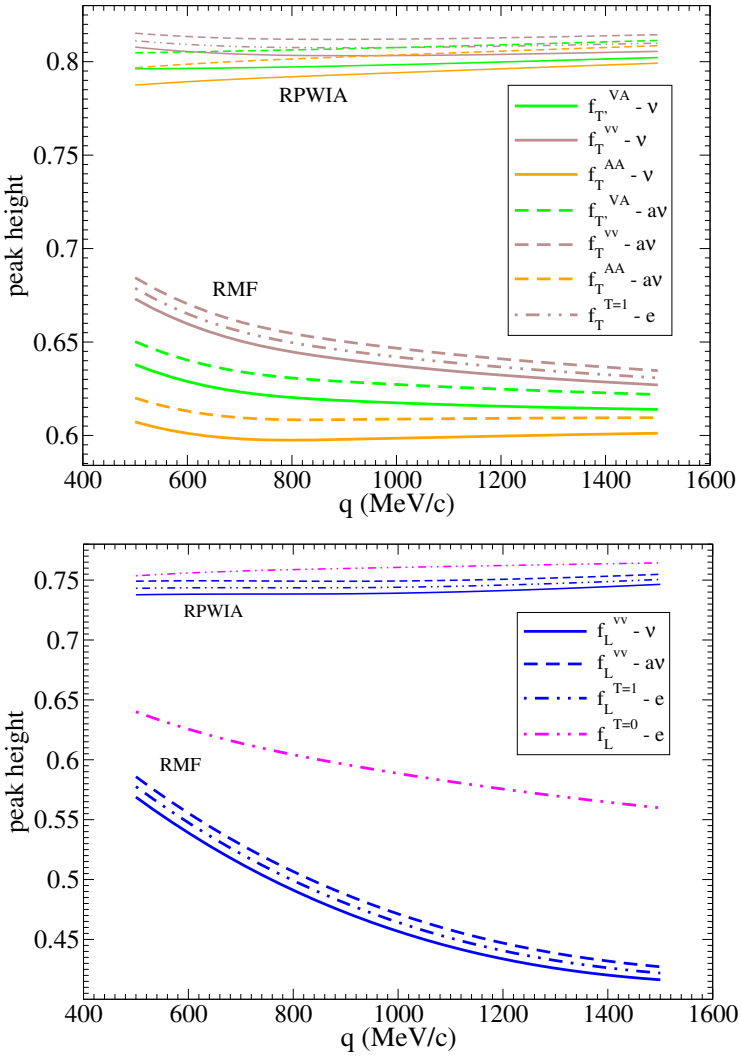

Figure 3.8: Top panel: Peak height of the transverse set of scaling functions as a function of the transferred momentum q. The upper set of lines corresponds to the prediction within RPWIA (thin lines), while the lower set of lines has been obtained with the RMF model. Bottom panel: As for the top panel, but now for the longitudinal set of scaling functions.

More specifically, in Fig. 3.8, we see that the discrepancies between the RMF and RPWIA peak-height results average to ∼25% in the transverse set. On the other hand, those discrepancies are more strongly q-dependent in the longitudinal sector, reaching ∼30% (∼70%) in the lower (higher) q-region for the longitudinal isovector responses (blue lines). Finally, the difference between the isoscalar longitudinal (e,e') scaling function produced by RMF and RPWIA (magenta dashed-dotted lines) is somewhat smaller: ∼20% (∼30%) for lower (higher) q.

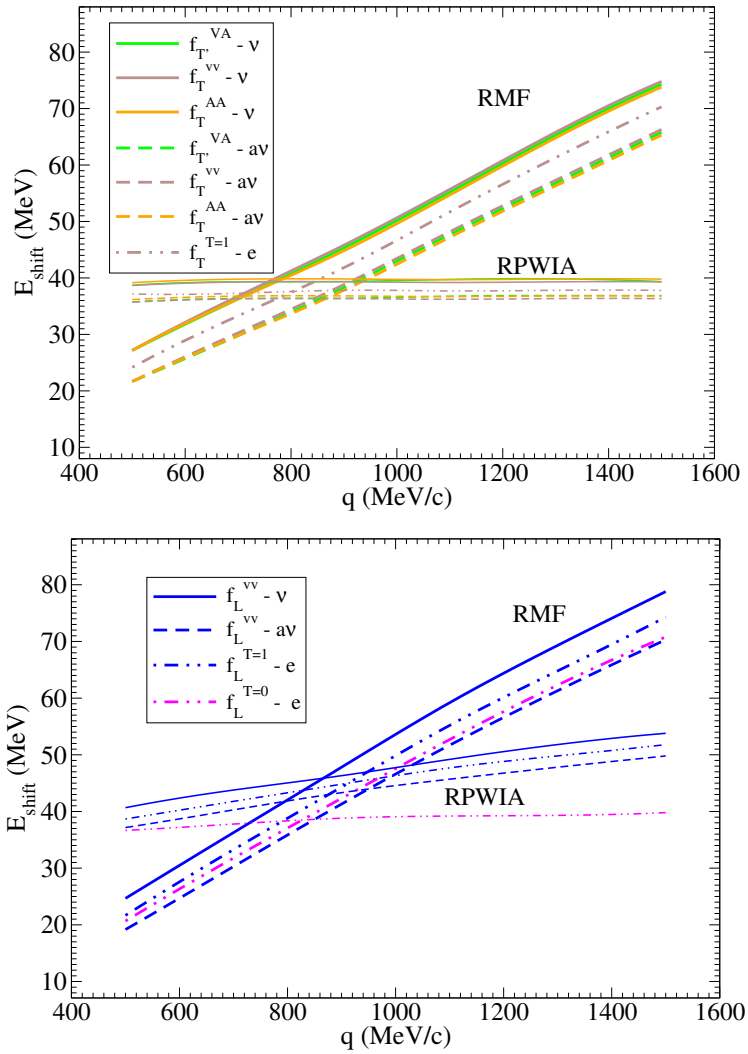

Figure 3.9: Top panel: Shift energy, E_{shift}, needed in order to have the corresponding scaling function peak located at $\psi' = 0$, as function of q. Results for the transverse set of scaling functions. Bottom panel: As for the top panel, but now for the longitudinal set of scaling functions.

In Fig. 3.9 we study the position of the peak of the transverse and longitudinal sets. To this scope we display the energy shift, E_{shift}, needed to place the peak of the scaling function at $\psi' = 0$ as a function of q. In the top panel of Fig. 3.9 we see that for the RPWIA transverse scaling function, E_{shift} is almost q-independent, while the corresponding RMF shift increases almost linearly with the momentum transfer. This q-linear dependence of E_{shift} was already observed and discussed within the framework of a semirelativistic model based on the use of the Dirac-equation-based potential [91]. Approximately the same behavior is observed for the longitudinal set (bottom panel in Fig. 3.9), although in this case the RPWIA results are softly linearly dependent on q. It is also worth mentioning that the three transverse scaling functions linked to the same neutrino or antineutrino process, f_T^{VV}, f_T^{AA} and $f_{T'}^{VA}$, collapse in a single line for RMF as for RPWIA.

From the analysis of Figs. 3.8 and 3.9 one may conclude that $f_L^{T=1,ee'}$ presents the same behavior (height and position) as $f_L^{VV,\nu(\overline{\nu})}$ (blue lines). The differences between these three curves are approximately constant and arise from the differences in the bound states involved in the reaction: proton+neutron in (e,e'), neutron in (ν,μ^-) and proton in $(\overline{\nu},\mu^+)$. The Coulomb-FSI, namely, the electromagnetic interaction between the struck nucleon and the residual nucleus, which plays a role when the outgoing nucleon is a proton, could also introduce a difference; however, we find that its effects are negligible and that the differences between, for instance, $f_L^{VV,\nu}$ and $f_L^{VV,\overline{\nu}}$ in RPWIA (where no Coulomb-FSI are involved) are almost the same as in RMF (see Figs. 3.8 and 3.9).

The strong q-dependence of the RMF peak position, which keeps growing with the momentum transfer, is a shortcoming of the model, whose validity is questionable at very high q. Indeed for high q the outgoing nucleon carries a large kinetic energy so the effects of FSI should be suppressed for such kinematics. In fact, it would be desirable that the RMF results tend to approach the RPWIA ones for increasing momentum transfer, *i.e.,* the scaling functions should become more symmetric, and a saturation of the peak-height reduction and of the energy shift should be observed. That trend is consistent with the scaling arguments [36, 37, 86], *i.e.*, the experimental evidence of a universal scaling function for increasing q. This is one of the motivations to use an alternative model if one aims to reproduce the experimental (e,e') data at medium-to-high momentum transfers.

A possible alternative for the behavior of the peak height, peak position and shape of the scaling functions is to implement the RMF model at low to intermediate-q and the RPWIA one for higher q-values, as it is proposed in following sections.

3.4.4 Sum rules

In Fig. 3.10, the values of the integrals over ψ' of the different scaling functions within RMF model are presented versus q. These are given by

$$S_i(q) = \int_{-\infty}^{\infty} f_i(\psi, q)\, d\psi \,. \tag{3.77}$$

The integration limits, denoted by $(-\infty, +\infty)$, extend in reality to the range allowed by the kinematics. The above integral in the case of the longitudinal (e,e') scaling function was shown to coincide, apart from some minor discrepancies ascribed to the particular single-nucleon expressions considered and the influence of the nuclear scale introduced, with the results obtained using the standard expression for the Coulomb Sum Rule (see [95] for details)[1]. Hence in what follows we denote the functions $S_i(q)$ simply as sum rules.

We see that all integrals of the transverse set are above unity and increase almost linearly with q. On the contrary, the integrals of $f_L^{VV,\nu(\overline{\nu})}$ and $f_L^{T=1,ee'}$ (blue lines) are below unity and decrease with q up to $q = 1100$ MeV/c. From $q = 900$ MeV/c they begin to be stable around the value 0.7. Then, from $q = 1200$ MeV/c to higher q-values the integrals start growing again. However, notice that in that q-region the result of the integrals is very sensitive to the behavior of the tail of these particular scaling functions (see Fig. 3.6). Finally, the values of the integral of the longitudinal isoscalar function, $f_L^{T=0,ee'}$, is approximately constant and close to unity. The behavior of the integrals of the two longitudinal scaling functions for (e,e') is consistent with the analysis of the Coulomb sum rule for these two models (see [95]).

[1] Coulomb sum rule (CSR) in inclusive electron scattering states that by integrating the longitudinal strength over the full range of ω at large q, one should get the total charge (number of protons) of the nucleus.

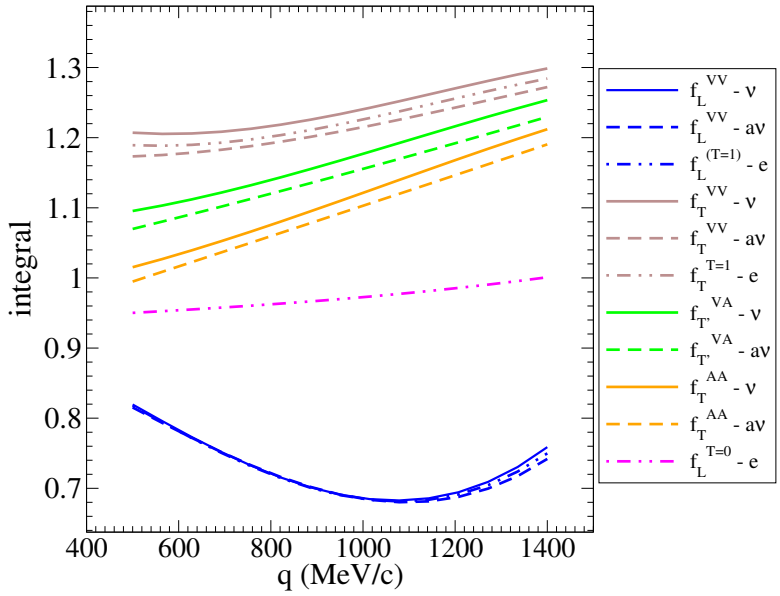

Figure 3.10: Integrals of RMF scaling functions as functions of q.

Although not shown here, we have also studied the integrals within RPWIA. In general, one observes that they are almost q-independent in all cases: ∼1 for the longitudinal set and ∼1.05 for the transverse set.

3.5 Analysis of the SuSAv2 model

In this section we build the SuSAv2 model as a combination of the original SuSA model and some of the physical ingredients contained in the RMF and RPWIA models.

As we have shown in the previous sections, the RMF model has a q-dependence that is too strong whereas, on the contrary, the SuSA approach does not account for the difference between the longitudinal and transverse (e,e') scaling functions. Similarly, SuSA neglects the possible differences in the scaling function linked to isospin effects (isovector, isoscalar, isovector+isoscalar) or to the character of the current (VV, AA and VA).

Thus, we aim to improve the SuSA model by introducing into it specific information from the RMF approach. Thus, the SuSAv2 model is based on the following four assumptions:

1. $f_L^{ee'}$ superscales, *i.e*, it is independent of the momentum transfer (scaling of first kind) and of the nuclear species (scaling of second kind). It has been proved that $f_L^{ee'}$ superscales for a range of q relatively low ($300 < q < 570$ MeV/c), see [36]. As in the original SuSA model, here we assume that superscaling is fulfilled by Nature.

2. $f_T^{ee'}$ superscales. It has been shown that $f_T^{ee'}$ approximately superscales in the region $\psi < 0$ for a wide range of q ($400 < q < 4000$ MeV/c), see [37]. However we assume that once the contributions from non-QE processes are removed (MEC, Δ-resonance, DIS, *etc.*) the superscaling behaviour could be extended to the whole range of ψ.

3. The RMF model reproduces quite well the relationships between all scaling functions in the *whole* range of q. This assumption is supported by the fact that RMF model is able to

reproduce the experimental scaling function, $f^{ee'}_{L,\text{exp}}$, and the fact that it naturally yields the inequality $f^{ee'}_T > f^{ee'}_L$.

4. At very high q the effects of FSI disappear and all scaling functions must approach the RPWIA results.

Contrary to what is assumed in the SuSA model, where only $f^{ee'}_{L,\text{exp}}$ is used as *reference* scaling function to build all nuclear responses, within SuSAv2 we use three RMF-based *reference* scaling functions (which will be indicated with the symbol $\widetilde{f}$): one for the transverse set, one for the longitudinal isovector set and another one to describe the longitudinal isoscalar scaling function in electron scattering. This is consistent with the study of the shape of the scaling functions discussed in the previous section, where three different sets of scaling functions emerged.

We employ the experimental scaling function $f^{ee'}_{L,\text{exp}}$ as guide in our choices for the *reference* ones. In Fig. 3.11 we display the RMF longitudinal scaling function, f_L, for several representative values of q. Notice that the functions have been relocated by introducing an energy shift (see later) so that the maximum is at $\psi' = 0$. It appears that scaling of first kind is not perfect and some q-dependence is observed. Although all the curves are roughly compatible with the experimental error bars, the scaling function that produces the best fit to the data corresponds to $q \approx 650$ MeV/c. This is the result of a χ^2-fit to the 25 experimental data of $f^{ee'}_{L,exp}$, as illustrated in the inner plot in Fig. 3.11.

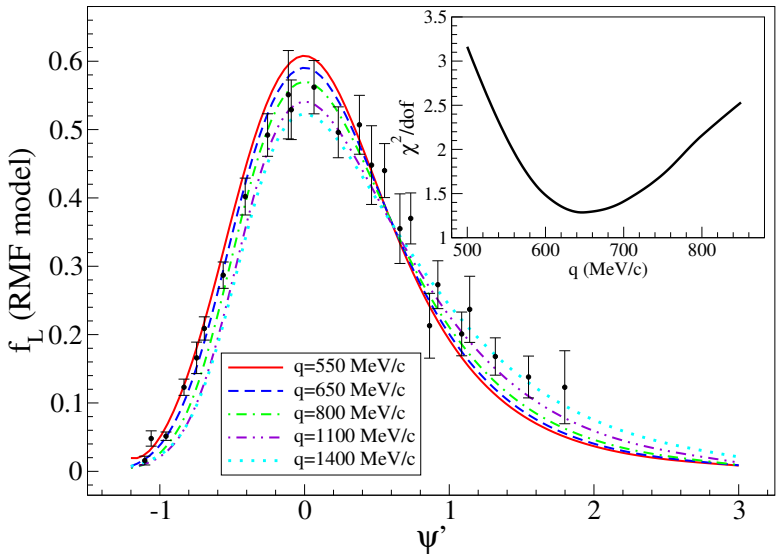

Figure 3.11: Longitudinal scaling function for (e, e') computed within RMF. The scaling functions have been shifted to place the maximum at $\psi' = 0$. In the inner smaller plot the reduced-χ^2, defined as $\chi^2/25 = \frac{1}{25}\sum_{i=1}^{25}[(f^{ee'}_{L,exp,i} - f^{RMF}_{L,i})/\sigma^{exp}_{L,i}]^2$ where $\sigma^{exp}_{L,i}$ are the errors of the experimental data, is presented versus q. The minimum χ^2 is around $q = 650$ MeV/c. Data from Ref. [82].

According to this result, we identify the reference scaling functions with $f^{T=1,ee'}_L$, $f^{T=0,ee'}_L$ and $f^{T=1,ee'}_T$ evaluated within the RMF model at $q = 650$ MeV/c and relocated so that the maximum is at $\psi' = 0$ (we will account for the energy shift later):

$$\widetilde{f}_T \equiv f^{T=1,ee'}_T|^{RMF}_{q=650} \tag{3.78}$$

$$\widetilde{f}_{L,T=1} \equiv f^{T=1,ee'}_L|^{RMF}_{q=650} \tag{3.79}$$

$$\widetilde{f}_{L,T=0} \equiv f^{T=0,ee'}_L|^{RMF}_{q=650}\,. \tag{3.80}$$

Thus, by construction, the (e,e') longitudinal scaling function built within SuSAv2 is $f_L|^{SuSAv2} = f_L|^{RMF}_{q=650} \approx f^{ee'}_{L,exp}$. In order to work with these reference scaling functions we need analytical expressions for them. To that end, we have used a skewed-Gumbel function which depends on four parameters. The expressions that parametrize the reference scaling functions are presented in Appendix B.

Next step before building the responses (see Eqs. (3.70-3.76)) is to define the rest of scaling functions starting from the reference ones. According to the third assumption for the construction of SuSAv2, we define:

$$f_L^{VV,\nu(\overline{\nu})}(q) \equiv \mu_L^{VV,\nu(\overline{\nu})}(q)\widetilde{f}_L^{T=1} \tag{3.81}$$
$$f_T^{VV,\nu(\overline{\nu})}(q) \equiv \mu_T^{VV,\nu(\overline{\nu})}(q)\widetilde{f}_T \tag{3.82}$$
$$f_T^{AA,\nu(\overline{\nu})}(q) \equiv \mu_T^{AA,\nu(\overline{\nu})}(q)\widetilde{f}_T \tag{3.83}$$
$$f_{T'}^{VA,\nu(\overline{\nu})}(q) \equiv \mu_T^{VA,\nu(\overline{\nu})}(q)\widetilde{f}_T\,, \tag{3.84}$$

where we have introduced the ratios μ defined for the transverse and longitudinal sets as:

$$\mu_T^{VV,\nu(\overline{\nu})}(q) \equiv f_T^{VV,\nu(\overline{\nu})}(q)/f_T^{T=1,ee'}(q) \tag{3.85}$$
$$\mu_T^{AA,\nu(\overline{\nu})}(q) \equiv f_T^{AA,\nu(\overline{\nu})}(q)/f_T^{T=1,ee'}(q) \tag{3.86}$$
$$\mu_{T'}^{VA,\nu(\overline{\nu})}(q) \equiv f_{T'}^{\nu(\overline{\nu})}(q)/f_T^{T=1,ee'}(q) \tag{3.87}$$
$$\mu_L^{VV,\nu(\overline{\nu})}(q) \equiv f_L^{VV,\nu(\overline{\nu})}(q)/f_L^{T=1,ee'}(q)\,. \tag{3.88}$$

From the results of these ratios, presented in Fig. 3.12, it emerges that one can assume $\mu_T^{VV,\nu(\overline{\nu})}(q) \approx 1$, with an error of the order of ∼1%. The same assumption could be made for $\mu_{T'}^{\nu(\overline{\nu})}(q)$ and $\mu_T^{AA,\nu(\overline{\nu})}(q)$ but in this case the error averages to ∼3% and ∼7%, respectively. Regarding the longitudinal isovector set, although not shown, one gets $\mu_L^{VV,\nu(\overline{\nu})} \approx 1$ with an error of the order ∼1%.

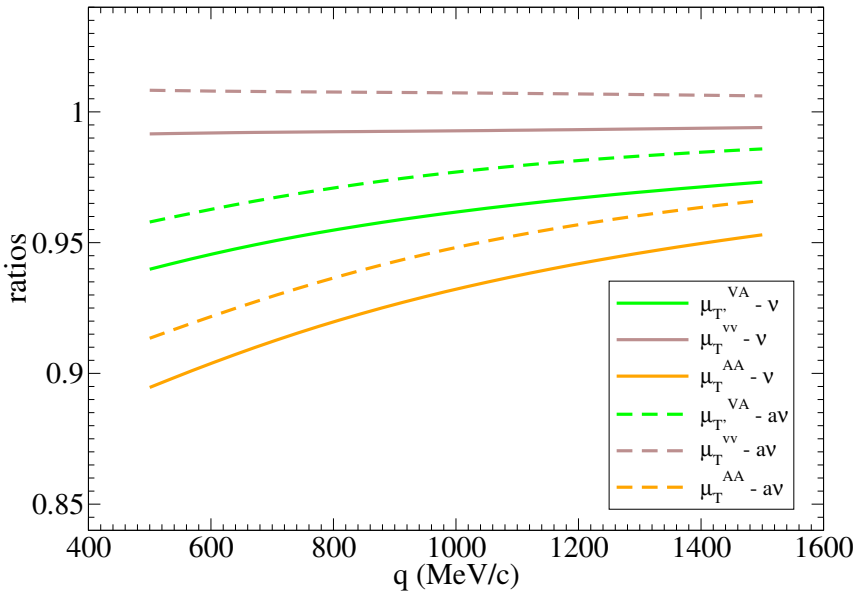

Figure 3.12: Ratios of the transverse scaling functions.

Therefore it is a good approximation to set all of the μ-ratios equal to unity in Eqs. (3.81-3.84), *i.e.*, to assume: $f_T^{VV,\nu(\overline{\nu})} = f_T^{AA,\nu(\overline{\nu})} = f_{T'}^{VA,\nu(\overline{\nu})} = \widetilde{f}_T$ and $f_L^{VV,\nu(\overline{\nu})} = \widetilde{f}_L$. Notice that since

$f_T^{T=0,ee'}$ and $f_{CC,CL,LL}^{AA,\nu(\overline{\nu})}$ are not defined (see Sect. 3.4.2) we will also assume $f_T^{T=0,ee'} = \widetilde{f}_{L,T=1}$ and $f_{CC,CL,LL}^{AA,\nu(\overline{\nu})} = \widetilde{f}_{L,T=1}$.

Finally, in order to implement the approaching of the RMF results to the RPWIA ones at high kinematics, that is, the disappearance of FSI at high q, we build the SuSAv2 L and T scaling functions as linear combinations of the RMF-based and RPWIA reference scaling functions:

$$\mathcal{F}_L^{T=0,1} \equiv \cos^2\chi(q)\widetilde{f}_L^{T=0,1} + \sin^2\chi(q)\widetilde{f}_L^{RPWIA} \tag{3.89}$$

$$\mathcal{F}_T \equiv \cos^2\chi(q)\widetilde{f}_T + \sin^2\chi(q)\widetilde{f}_T^{RPWIA}, \tag{3.90}$$

where $\chi(q)$ is a q-dependent angle given by

$$\chi(q) \equiv \frac{\pi}{2}\left(1 - \left[1 + e^{\left(\frac{q-q_0}{\omega_0}\right)}\right]^{-1}\right) \tag{3.91}$$

with q_0 and w_0 the transition parameters between RMF and RPWIA prescriptions which will be defined in Sect. 6.1. The reference RPWIA scaling functions, $\widetilde{f}_K^{RPWIA}$, are evaluated at q=1100 MeV/c, while the reference RMF scaling functions, $\widetilde{f}_K$, are evaluated at q=650 MeV/c and are shown in Fig. 3.13. The q-values chosen for the reference scaling functions were previously discussed whereas the explicit expressions of the RMF ($\widetilde{f}_K$) and RPWIA ($\widetilde{f}_K^{RPWIA}$) scaling functions are given in Appendix B. With this procedure we get a description of the responses based on RMF behavior at low-intermediate q values while for higher momentum transfers it mimics the RPWIA trend. The transition between RMF and RPWIA behaviors occurs at intermediate q-values, namely, $\sim q_0$, in a region of width $\sim w_0$, as detailed in Sect. 6.1.

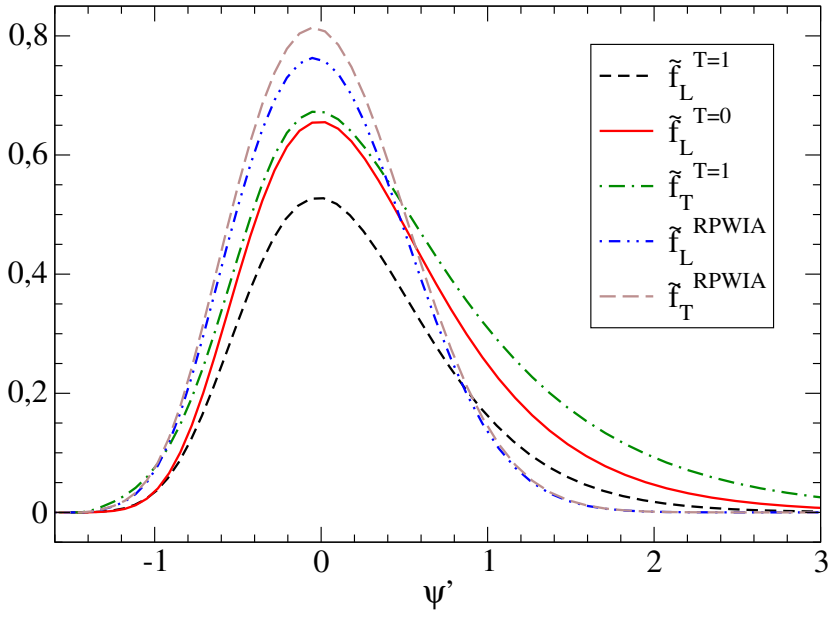

Figure 3.13: Reference scaling functions for (e,e') and CC neutrino induced reactions in the SuSAv2 model.

The response functions (see Eqs. (3.70) and (3.71–3.76)) are simply built as:

$$R_L^{ee'}(q,\omega) = \frac{1}{k_F}\left[\mathcal{F}_{L,T=1}(\psi')G_L^{T=1}(q,\omega) + \mathcal{F}_{L,T=0}(\psi')G_L^{T=0}(q,\omega)\right] \tag{3.92}$$

$$R_T^{ee'}(q,\omega) = \frac{1}{k_F}\mathcal{F}_T(\psi')\left[G_T^{T=1}(q,\omega) + G_T^{T=0}(q,\omega)\right] \tag{3.93}$$

$$R_L^{VV,\nu(\overline{\nu})}(q,\omega) = \frac{1}{k_F}\mathcal{F}_{L,T=1}(\psi')G_L^{VV}(q,\omega) \tag{3.94}$$

$$R_{CC}^{AA,\nu(\overline{\nu})}(q,\omega) = \frac{1}{k_F}\mathcal{F}_{L,T=1}(\psi')G_{CC}^{AA}(q,\omega) \tag{3.95}$$

$$R_{CL}^{AA,\nu(\overline{\nu})}(q,\omega) = \frac{1}{k_F}\mathcal{F}_{L,T=1}(\psi')G_{CL}^{AA}(q,\omega) \tag{3.96}$$

$$R_{LL}^{AA,\nu(\overline{\nu})}(q,\omega) = \frac{1}{k_F}\mathcal{F}_{L,T=1}(\psi')G_{LL}^{AA}(q,\omega) \tag{3.97}$$

$$R_T^{\nu(\overline{\nu})}(q,\omega) = \frac{1}{k_F}\mathcal{F}_T(\psi')\left[G_T^{VV}(q,\omega) + G_T^{AA}(q,\omega)\right] \tag{3.98}$$

$$R_{T'}^{\nu(\overline{\nu})}(q,\omega) = \frac{1}{k_F}\mathcal{F}_T(\psi')G_{T'}^{VA}(q,\omega). \tag{3.99}$$

Furthermore, in order to reproduce the peak position of RMF and RPWIA scaling functions, discussed in Sect. 3.4.3, within SuSAv2 we consider a q-dependent energy shift, namely, $E_{shift}(q)$. This quantity modifies the scaling variable $\psi(q,\omega) \longrightarrow \psi'(q,\omega,E_{shift})$ as described in Section 3.2.3. In particular, we build this function $E_{shift}(q)$ from the results of the RMF and RPWIA models presented in Fig. 3.9. Thus, $E_{shift}(q)$ for the reference RMF scaling function $\widetilde{f_T}[\psi'(E_{shift})]$ is the parametrization of the brown dot-dot-dashed line in the top panel of Fig. 3.9. The same procedure is used to parametrize $E_{shift}(q)$ corresponding to the $\widetilde{f_{L,T=1}}$ and $\widetilde{f_{L,T=0}}$, but in this case using, as an average, the blue dot-dot-dashed line from the bottom panel of Fig. 3.9. Moreover, for the RPWIA case we use for the longitudinal and transverse responses the corresponding RPWIA $E_{shift}(q)$ curves shown in Fig. 3.9.

Notice that for $q \lesssim 300-350$ MeV/c it is difficult to extract the peak position of the RMF scaling function from the data so we have set a minimum shift energy, $E_{shift} = 10$ MeV. This choice of $E_{shift}(q)$ depending on the particular q-domain region considered is solely based on the behavior of the experimental cross sections and their comparison with our theoretical predictions (see results in next sections). In the past we have considered a fixed value of E_{shift} [37] (different for each nucleus) to be included within the SuSA model in order to fit the position of the QE peak for some specific q-intermediate values. Here we extend the analysis to very different kinematics covering from low to much higher q-values. On the other hand, the RMF model leads the cross section to be shifted to higher values of the transferred energy. This shift becomes increasingly larger for higher q-values as a consequence of the strong, energy-independent, highly repulsive potentials involved in the RMF model. Comparison with data (see the results in the next sections) shows that the shift produced by RMF is too large. Moreover, at very high q-values, one expects FSI effects to be less important and lead to results that are more similar to those obtained within the RPWIA approach. This is the case when FSI are described through energy-dependent optical potentials. Therefore, as already mentioned, our choice for the functional dependence of $E_{shift}(q)$ is motivated as a compromise between the predictions of our models and the comparisons with data.

3.5.1 Pauli blocking effects on SuSA and SuSAv2 models

In this Section, we show the relevance of Pauli Blocking (PB) effects on the SuSA and SuSAv2 models. The phenomenon of Pauli blocking arises from the exclusion principle, which dictates that two fermions cannot share the identical set of quantum eigenstates. As a fermion, a nucleon is not permitted to be in a state which is already occupied by another nucleon, reducing the available phase space and hence the lepton-nucleus cross section.

Within the RFG model, the bound nucleons are simulated as a "gas" of particles, with a uniform momentum distribution from the lowest state up to an empirically-determined maximum k_F. In this case, the Pauli principle requires the final-state nucleon's momentum to exceed the Fermi-momentum.

As detailed in Sect. 3.2, the RFG model combines the free-nucleon cross sections with a potential well in the form of binding energy as well as Pauli blocking to restrict the available kinematics of struck nucleons. These effects are implemented when integrating the nuclear tensor (3.21) by means of a factor proportional to:

$$\theta(k_F - |\mathbf{p}|)\theta(|\mathbf{p}+\mathbf{q}| - k_F) \times \delta(\omega - [E(\mathbf{p}+\mathbf{q}) - E(\mathbf{p})]) \,. \tag{3.100}$$

The first term requires the nucleon participating in the interaction to have momentum below k_F, the second enforces Pauli blocking requiring the struck nucleon to be above the Fermi momentum, whereas the third assures energy conservation. Therefore, the Pauli-blocked regime occurs at low momentum transfers when $|\mathbf{p}| < k_F$ which, regarding the expression above, implies $q \leq 2k_F$.

Moreover, the SuperScaling model works well for high enough momentum and energy transfers, whereas in the low q and ω region (typically, $q \leq 400$ MeV/c and $\omega \leq 50$ MeV) it is inadequate and some prescription that accounts for Pauli blocking and collective nuclear excitations should be used. In the phenomenological SuSA approach, Pauli blocking effects are not trivial to implement and have been neglected in the first applications of the model [19, 64, 81]. In this thesis we introduce PB using the procedure proposed in [96, 97], which generalizes the simple RFG prescription [75] – only valid for a step-like momentum distribution – to accommodate more realistic momentum distributions. In summary, the prescription consists in subtracting from the scaling function $f(\psi'(\omega, q))$ its mirror function $f(\psi'(-\omega, q))$,

$$f_{blocked}(\psi'(\omega,q)) = f(\psi'(\omega,q)) - f(\psi'(-\omega,q)) \quad ; \quad \text{for} \quad \omega < 0 \,. \tag{3.101}$$

This incorporates a correct blocking of unphysical excitations, which are then excluded in a more satisfactory way than through the *ad hoc* factor $[1 - n(\mathbf{p}+\mathbf{q})/n(0)]$ commonly used in the literature [98, 99]. If applied to a non-Pauli-blocked version of the RFG, this procedure yields exactly the correct Pauli blocking for that model. Moreover, this method does not require the knowledge of the nucleon momentum distribution $n(p)$.

In Fig. 3.15, Pauli blocking effects in the scaling function for ^{12}C ($k_F = 228$ MeV/c) and different fixed values of the transferred momentum are shown. The Pauli-blocked regime appears at $q \lesssim 2k_F = 456$ MeV/c and, in particular, PB effects are noticeable for $q < 250$ MeV. At these kinematics, the subtractions to the non-Pauli-blocked scaling function come mainly from $\omega < 50$ MeV/c. We also note how $f(\psi')$ does not scale when plotted versus ω (3.15) where the curves are shifted to lower ω values as q decreases.

When displayed versus the scaling variable ψ' (Fig. 3.14), we notice that the non-blocked scaling function is exactly the same for all kinematics and is only limited for the range of ω-values compatible with the fixed q value. As also observed, the PB effects only have an impact in the region of low ψ' which is related to the lower values of ω.

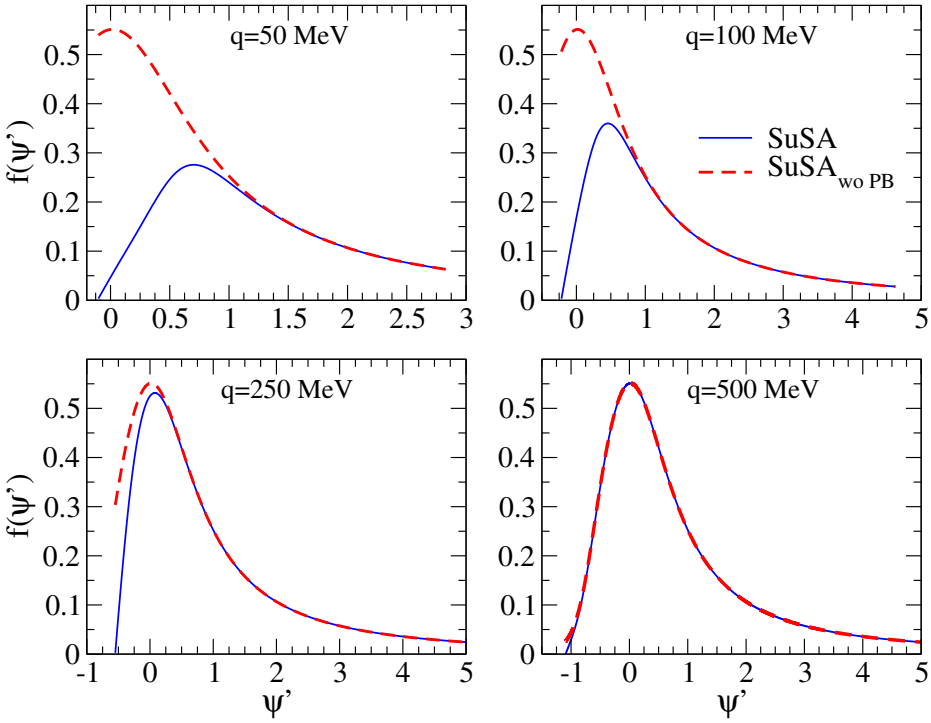

Figure 3.14: Superscaling function versus ψ' at different q-fixed values and evaluated for the SuSA model with (SuSA) and without (SuSA$_{woPB}$) Pauli blocking. .

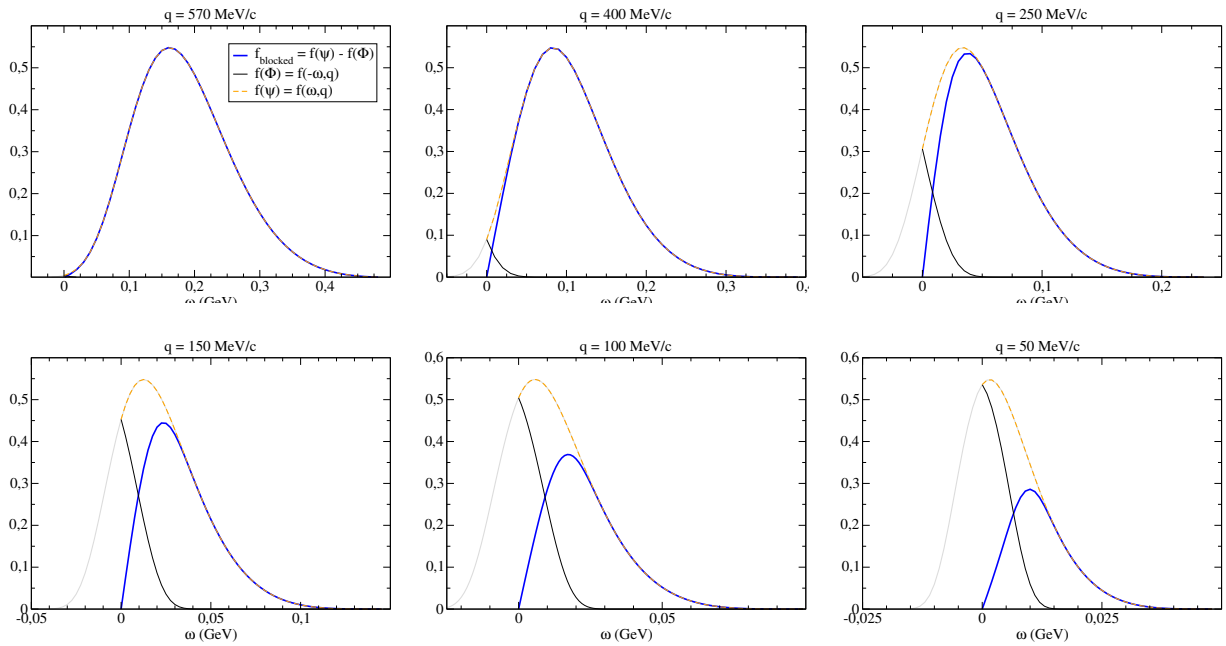

Figure 3.15: Superscaling function versus ω at different q-fixed values and evaluated for the SuSA model with (f$_{blocked}$) and without (f(ψ)) Pauli blocking. The mirror function (f(Φ)) is also shown as reference.

Next we show the effects of PB in the SuSA and SuSAv2 models when comparing with (e,e') data on ^{12}C. For this purpose, we display in Fig. 3.16 the SuSA results with and without PB and compare them with a few sets of data at the kinematics in which PB effects are significant, *i.e.,* very low q. In the region of low-ω, the PB effects can be observed on the width and peak height of the cross sections. In general we conclude that the agreement between SuSA and data improves when PB is introduced. SuSA without PB (green-dashed) produces cross sections too wide, while SuSA with PB (brown) provides narrower cross sections in better agreement with data. This is particularly true in panels (1) and (2) in Fig. 3.16. The same comments apply to Fig. 3.17 where SuSAv2 with and without PB is compared with the same set of low-q data. The lowest energy transfer data, corresponding to the excitation of resonant and collective states, cannot be described by any of the present models.

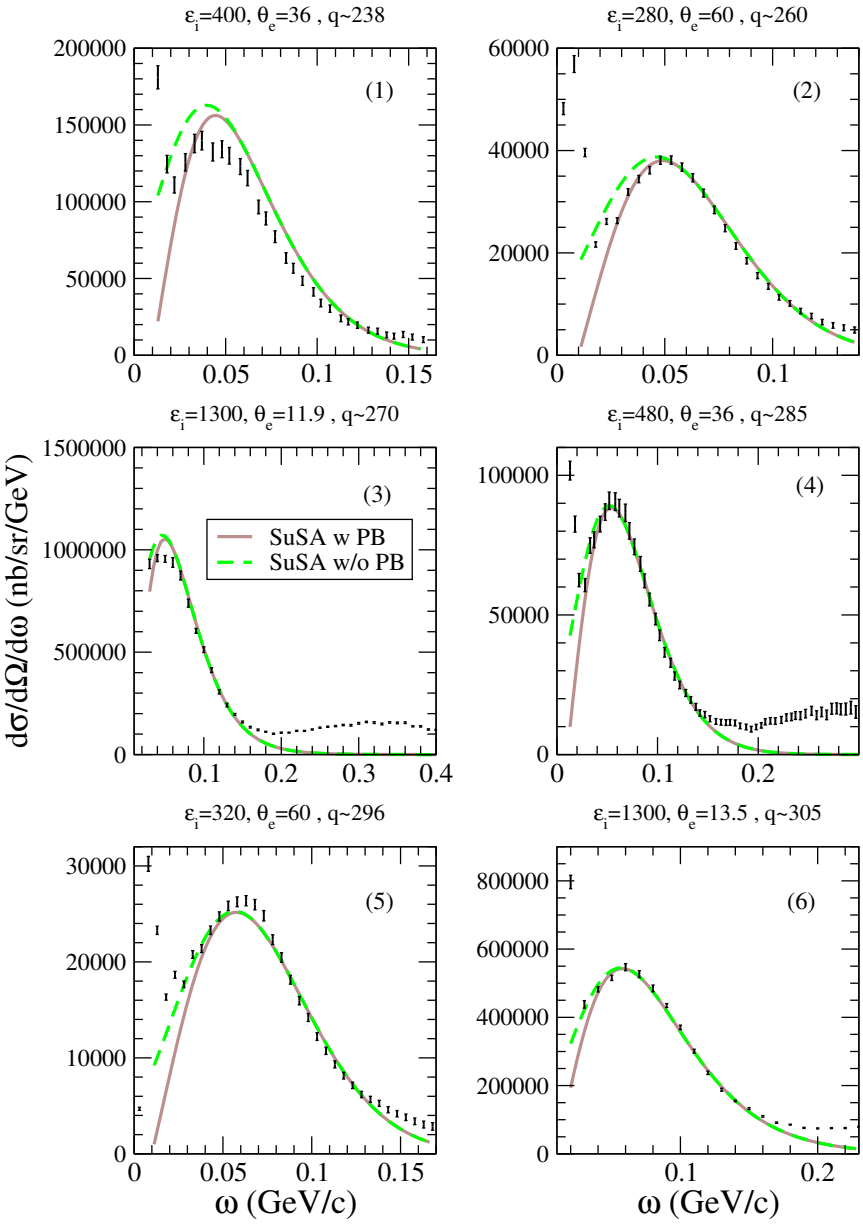

Figure 3.16: SuSA with and without Pauli Blocking is compared with (e,e') data. E_{shift} = 10 MeV has been employed. Data taken from [100, 101].

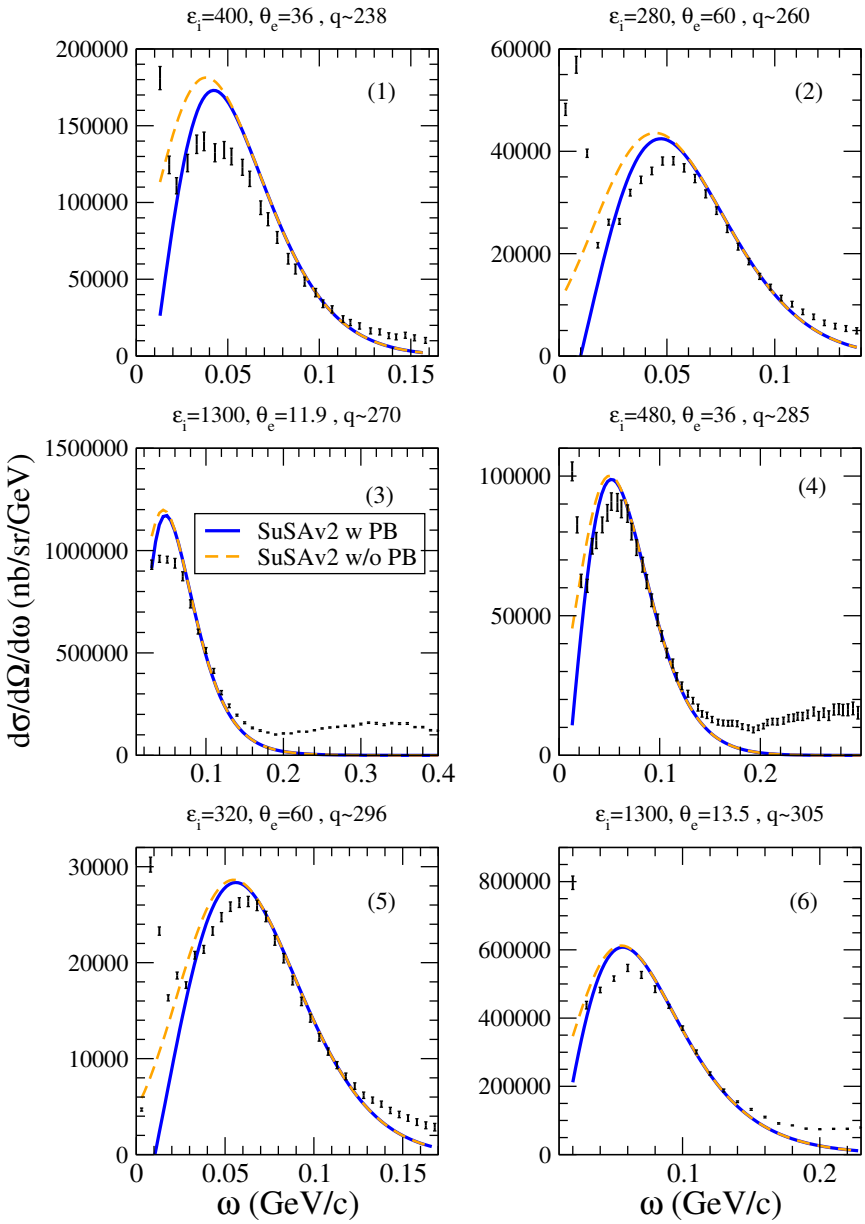

Figure 3.17: SuSAv2 with and without Pauli Blocking is compared with (e,e') data. Data taken from [100, 101].

A clear difference between SuSA and SuSAv2 (Figs. 3.16 and 3.17) is that the latter clearly overestimates the data in the region below and close to the peak whereas the SuSA model underestimates all data for medium and high q-values (Figs. 3.19-3.20). However, in all cases the maximum is placed at $\omega \lesssim 50-60$ MeV where, as discussed in Sect. 3.5.2, the validity of the models based on IA is questionable and no definitive conclusions can be drawn based on comparison of model and data in this ω-region. Nevertheless, the agreement of the SuSAv2 model with data in the low-energy range can be improved by determining more accurately the q_0 transition parameter between RMF and RPWIA contributions, as shown in Sect. 6.1, in such a way that the effects of FSI via the RMF model be more significant for lower kinematics, thus reducing the resulting cross section.

The effect of Pauli Blocking is also of relevance for the analysis of CCQE neutrino cross sections, particularly at low kinematics, as will be shown in Chapter 7.

3.5.2 Analysis of the SuSAv2 model for (e,e') reactions within the QE regime

In this section we present a systematic comparison of inclusive $^{12}C(e,e')$ experimental cross sections and the predictions for the QE process within RMF, SuSA and SuSAv2 models. As mentioned, data correspond to the total inclusive cross section which includes contributions from several channels, mainly: QE scattering, inelastic scattering, many-nucleon emission, *etc.* Here we only focus on the QE process, whereas a more detailed analysis of the inclusive cross section including inelastic processes and 2p-2h MEC contributions will be addressed in Chapter 6. Therefore, one expects that the models do not reproduce the total inclusive experimental data corresponding to kinematical situations in which non-QE contributions play some role. Thus, the main interest of the systematic analysis presented in this section is the comparison between SuSAv2 predictions and those from the SuSA and RMF models. Full analyses of the inclusive (e,e') cross section (including descriptions of QE and non-QE contributions) have been presented with some success in the past [84, 85] within the context of the semiphenomelogical SuSA. Our aim in the following is to complete the description of the inclusive process within the context of SuSAv2 model, via the inclusion of the inelastic spectrum and 2p-2h contributions. This will be detailed in the next chapters.

In Figs. 3.18-3.20 we present the comparison of the (e,e') experimental data and models. Due to the large amount of available data on $^{12}C(e,e')$ at different kinematics (see [100, 101]) in these three figures we only show some representative examples. A more detailed analysis will be drawn in Chapter 7. Each figure is labeled by the incident electron energy, ε_i (in MeV), the scattering angle, θ_e, and the transferred momentum corresponding to the center of the quasielastic peak, q (in MeV/c). Pauli Blocking has been included in the SuSA and SuSAv2 models following the procedure described in [96, 97] and detailed in Section 3.5.1.

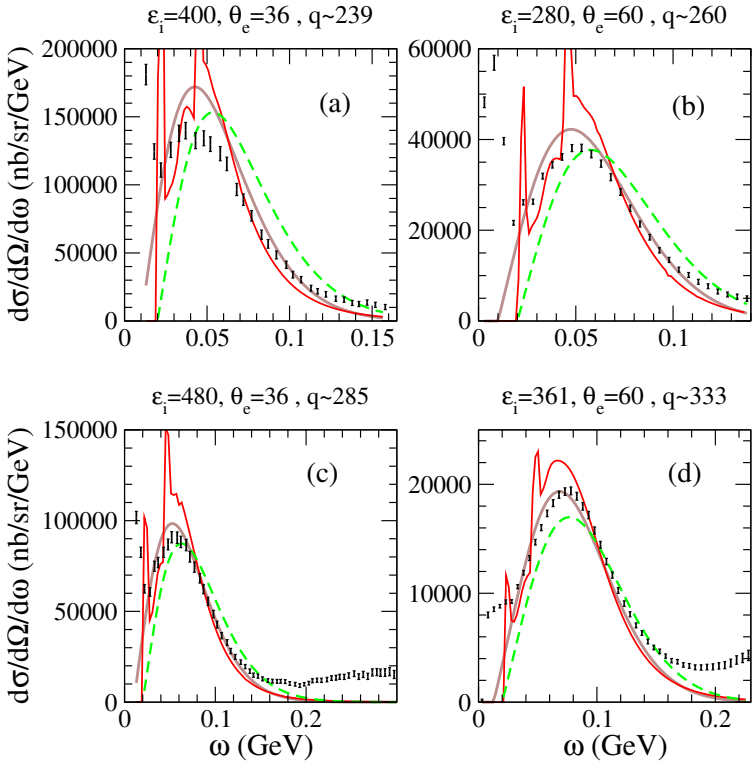

Figure 3.18: Comparison of inclusive $^{12}C(e,e')$ cross sections and predictions of the RMF (red), SuSA (green-dashed) and SuSAv2 (brown) models (see text for details). Set of panels corresponding to low-q values. Data are taken from [100, 101].

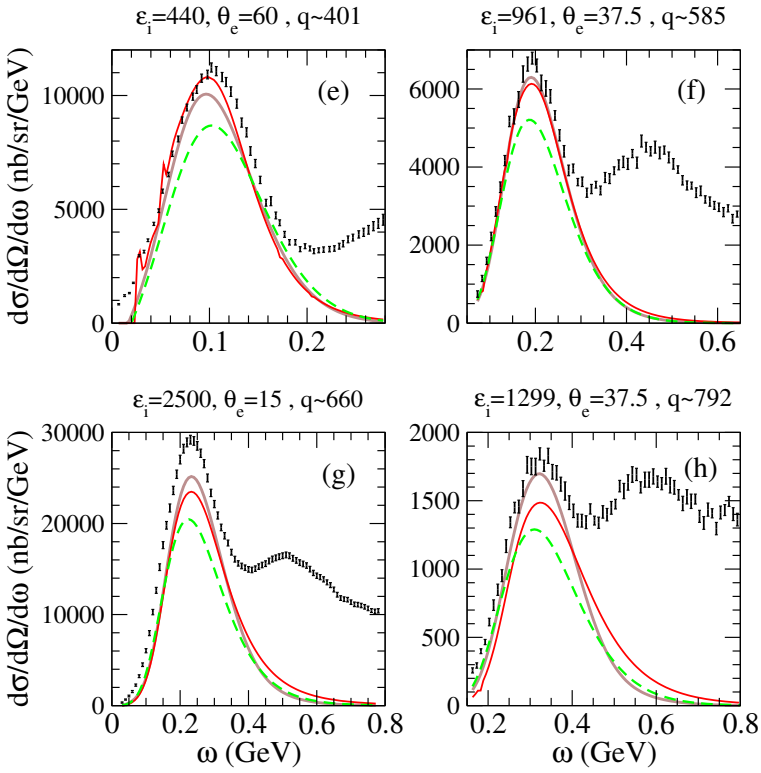

Figure 3.19: Continuation of Fig. 3.18. Set of panels corresponding to medium-q values. Data are taken from [100, 101].

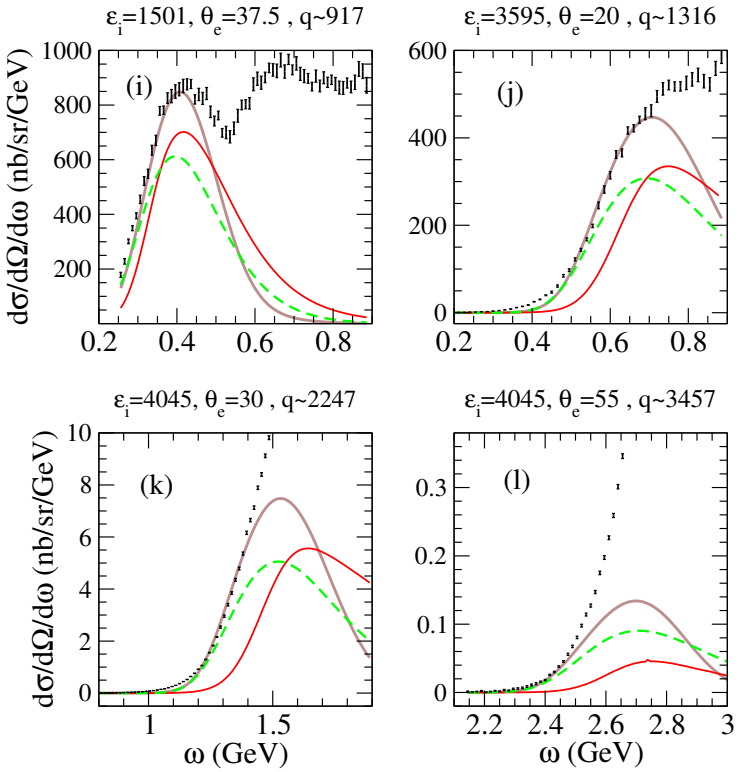

Figure 3.20: Continuation of Fig. 3.18. Set of panels corresponding to high-q values. Data are taken from [100, 101].

The panels in Figs. 3.18-3.20 are organized according to the value of the transferred momentum (at the center of the QE peak) in three sets: low-q (from $q = 238$ to $q = 333$ MeV/c) in Fig. 3.18, medium-q (from $q = 401$ to $q = 792$ MeV/c) in Fig. 3.19 and, high-q (from $q = 917$ to $q = 3457$ MeV/c) in Fig. 3.20. The only phenomenological parameters entering in the calculation are the Fermi momentum k_F and the energy shift E_{shift}. For these we use $k_F = 228$ MeV/c (see [37]) in both SuSA and SuSAv2 models. A constant energy shift of 20 MeV is employed in SuSA [37] while a q-dependent function, the one described in Sect. 3.5, is used for E_{shift} in the SuSAv2 model. Preliminary values for the SuSAv2 transition parameters of $q_0 = 800$ MeV/c and $\omega_0 = 200$ MeV have been applied.

We begin commenting on the low-q panels presented in Fig. 3.18. The main contributions to the cross section from non-QE processes such as inelastic processes contributions (Δ-resonance) and MEC, are very small, even negligible, in this low-q region. In spite of that, when the transferred energy is small ($\omega \lesssim 50 - 60$ MeV) other processes such as collective effects contribute to the cross section making questionable the treatment of the scattering process in terms of IA-based models. This could explain, in part, the general disagreement between models and data in that ω region in (a), (b) and (c) panels. Moreover, we can observe that the SuSA model seems to be shifted to high ω values with regard to the experimental data whereas the SuSAv2 model matches with the experimental QE peak position. At the same time, the SuSAv2 results are higher than the SuSA ones, which is mainly due to the natural enhancement on the RMF transverse scaling function.

Some clarifications are called for regarding the RMF results in Fig. 3.18, where sharp resonances appear at very low ω values. These correspond to 1p-1h excitations with the phase shift of a given partial wave going through 90 degrees. With more complicated many-body descriptions these sharp features are smeared out.

In summary, in order to test the goodness of the models in the kinematical situation of Fig. 3.18, one should focus on the study of the tails of the cross sections where large enough ω-values ($\omega \gtrsim 50 - 60$ MeV) are involved. There, one observes that SuSA predictions are clearly overshifted to high ω-values while RMF and SuSAv2 models fit the data reasonably well. In addition, as expected, SuSA results are systematically below SuSAv2 and RMF ones at the QEP.

We now discuss the results for medium-q values presented in Fig. 3.19. First of all, one should mention that for the kinematics of this figure, in addition to the QE process, non-QE contributions are essential to describe the experimental cross sections. For instance, in panels (f), (g) and (h) the Δ-peak appears clearly defined at ω values above the QE peak. In panel (e) one sees that in the region around the center of the QE-peak, the RMF prediction is slightly above the SuSAv2 one, being closer to the experimental data. This is consistent with the behavior of the RMF scaling function studied in Sect. 3.4.3 (see Fig. 3.8), namely, the peak-height of the RMF scaling functions increases for decreasing q-values.

If the main non-QE contributions are not included in the modeling it is hard to conclude which model is better to reproduce the purely QE cross section. However, it seems reasonable to conclude that SuSAv2 improves the agreement with data compared to SuSA. For instance, in the situation of panel (e), it would be needed that non-QE processes would contribute more than 20% around the QE-peak in order to SuSA fits the height of the data. A 20% fraction of the cross section linked to Δ-resonance and MEC contributions is probably too much for that kinematics. Similar comments and conclusions apply to the results in panel (d) of Fig. 3.18.

For q-values close to 650 MeV/c (panels (f) and (g)) RMF and SuSAv2 produce very similar results because of the way in which SuSAv2 has been defined (see Sect. 3.5). For higher q-values, $q \gtrsim 792$ MeV/c ((h) panel), SuSAv2 and RMF predictions begin to depart from each other. In particular, RMF results tend to shift the peak to higher ω values and to place more strength in the tail while SuSAv2 cross sections tend to be more symmetrical due to the increasing dominance of the RPWIA scaling behavior (see Sect. 3.5).

This difference is more evident for higher q-values, as observed in panels (j)-(l) of Fig. 3.20. It is important to point out that for the kinematics presented in Fig. 3.20 the non-QE contributions are not only important but they become dominant in the cross sections. This is the case presented in panels (k) and (l) where the QE-peak is not even visible in the data.

Next, we summarize the main conclusions from the present comparison of the SuSA and SuSAv2 models in the QE regime with the inclusive (e,e') data:

- Regarding the enhancement of the transverse response, R_T, in SuSAv2 compared with SuSA: prior to the addition of non-QE contributions (which will be addressed in Chapter 6), the most clear indications that support the SuSAv2 assumptions arise from the comparison with data at kinematical situations in which non-QE effects are supposed to be small (panels (e) and (d) in Figs. 3.18 and 3.19, respectively).

- Regarding the energy-shift analysis: within the SuSA model we have used a constant energy shift of 20 MeV/c. From the comparison with the low-q set of experimental data, Fig. 3.18, one concludes that 20 MeV is a too large shift. On the contrary, the comparison with the high-q set of data, Fig. 3.20, suggests that 20 MeV is probably too small. Then, one is led to conclude that a constant energy shift is not the best option to reproduce (e,e') data. These results support the idea of introducing a q-dependent energy shift such as we made in the SuSAv2 model. The theoretical justification of this assumption was already discussed in Sect. 3.5.

In Chapter 7 we will show that the SuSAv2 model describes more accurately the neutrino induced reactions than the semiphenomelogical SuSA aproach. This result mainly comes from the q-dependence on the energy shift, the enhancement on the transverse response via RMF prescriptions as well as the possibility of separating scaling functions into isoscalar and isovector contributions.

Finally, we should add a remark concerning the RMF/RPWIA transition parameters, q_0 and ω_0, appearing in Eq. 3.91. In the previous results (Figs. 3.18-3.20), we have applied a fixed value of these parameters which have shown a reasonable agreement with some experimental data at the QE peak. However, the transition between the RMF and RPWIA models depends on the particular kinematics involved, namely on the momentum transfer q. Accordingly, the transition parameter, q_0, is expected to increase with q in such a way that the RMF contribution will be dominant at low kinematics where FSI effects are of high relevance, whereas the RPWIA description is needed at higher kinematics. Therefore we introduce a dependence on the momentum transfer q that determines explicitly the relative RMF and RPWIA contributions at different kinematics. This analysis is carried out together with the extension of the SuSAv2 formalism to the inelastic spectrum and applied to the study of the (e,e') data in Chapter 6.

Chapter 4

2p-2h MEC contributions for electroweak reactions

In this Chapter, we evaluate and discuss the impact of two-particle two-hole meson-exchange currents (2p-2h MEC) on electron- and neutrino-nucleus cross sections. The 2p-2h MEC responses are calculated within the RFG model in which a fully Lorentz and transitionally invariant calculation can be developed. In order to reduce the computational time, we make use of an accurate parametrization of these responses.

4.1 Introduction

As shown in Fig. 4.1, the 2p-2h MEC process takes place when a weak or electromagnetic boson from the leptonic current is exchanged by a pair of nucleons (2-body current) leading to the emission of two nucleons from the primary vertex. These states, where two nucleons are promoted above the Fermi level leaving two holes inside the Fermi sea, are known to give a large contribution in the so-called "dip region", corresponding to excitation energies lying between the quasielastic (QE) and $\Delta(1232)$ excitation peaks. These contributions are essential for a correct interpretation of

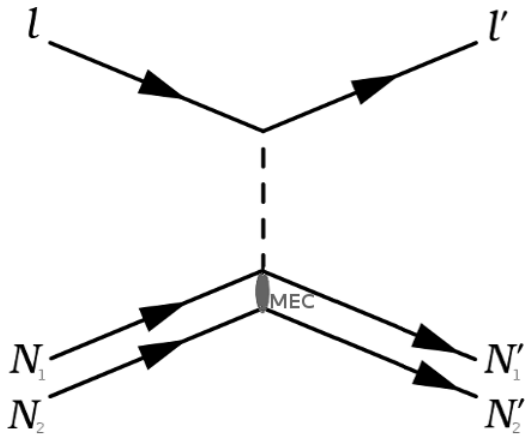

Figure 4.1: Schematic view of the 2p-2h MEC process for lepton-nucleus interactions.

current and forthcoming neutrino oscillation experiments, which strongly relies on our understanding of neutrino-nucleus scattering at intermediate energies (from 0.5 to 10 GeV) and in particular

of the nuclear-structure effects involved. At these kinematics, it has been proved that processes beyond the IA, in which MEC play a major role, give a significant positive contribution to the cross section which helps to account for the discrepancy observed in (e,e') processes between theory and experiment in the "dip" region as well as for the discrepancies between some recent neutrino CCQE measurements (*e.g.,* MiniBooNE, NOMAD, MINERνA, T2K) [20, 21, 24, 46, 47, 56]. Indeed, the inclusion of 2p-2h MEC contributions has allowed to explain these data without modifying any effective parameter (such as the axial mass M_A) [30, 31, 39, 102, 103]. All this supports the need to consider mechanisms such as final-state interactions (included in our QE description via RMF theory), nuclear correlations or MEC, in particular through their contribution to multinucleon knock-out around and beyond the QE peak as suggested by explicit modeling [30, 31, 104, 105].

As commented in Chapter 3, the 2p-2h MEC processes together with inelastic contributions and, in particular, meson production via baryon resonances such as the Δ, are responsible of scaling violations in (e,e') reactions, which are more prominent in the transverse [84, 85]. However, even below the meson production threshold there are scaling violations in the transverse response [36], one source of which is clearly the MEC contributions, again predominantly transverse. These two-body currents can excite both one-particle one-hole (1p-1h) and two-particle two-hole (2p-2h) states. Most studies of electromagnetic (e,e') processes performed for low-to-intermediate momentum transfers with MEC in the 1p-1h sector (see, *e.g.,* [106–109]) have shown a small reduction of the total response at the QE peak, mainly due to diagrams involving the electroexcitation of the Δ resonance. Nevertheless, they are roughly compensated by the positive contributions of correlation diagrams, where the virtual boson couples to a correlated pair of nucleons. In this work we shall therefore neglect them and restrict our attention to 2p-2h final states, computed in a fully relativistic way. As discussed in previous works [105, 110–113], relativity is an essential ingredient in the analysis of 2p-2h processes at momentum transfers above 400-500 MeV/c. At these kinematics, the non-relativistic reduction can lower the resulting 2p-2h MEC cross section around a $\sim 40\%$ or more [105]. This statement is in connection with the kinematical regions of interest for neutrino oscillation experiments which extend to relativistic domains. At these q-values, the static approximation used for the Δ propagator in the non-relativistic calculations of 2p-2h transverse response function [114] fails to explain the "dip" region.

Moreover, the presence of nucleon-nucleon correlation interactions involving the one-nucleon current may lead to the excitation of 2p-2h final states, and interference between these processes and those involving MEC should be analyzed to assess their relevance. These effects, taken into account in the RFG-based descriptions of 2p-2h provided by Nieves *et al.* [31] and Martini [30], are not included explicitly in our RFG MEC model, that relies on a hybrid description where the one-particle emission already contains contributions of nuclear ejections due to nuclear correlations — via scaling functions from the SuSAv2 model. Explicit calculations of the correlation-MEC interference terms are still in progress and their contributions will be presented in further works.

The contributions considered in this thesis englobe the 2p-2h states excited by the action of meson-exchange currents within a fully relativistic framework (see [110, 112, 113, 115] for details), involving virtual Δ resonances as well as the seagull (contact) and pion-in-flight currents obtained in previous works [110, 111]. Deviations from the Fermi gas model 2p-2h responses produced by ingredients such as final-state interactions, finite nuclear effects or nuclear correlations are expected to be moderate, which would result in small corrections in the impulsive cross section as the MEC contributions are also moderate. The previous assumption is based on previous works at low-to-intermediate momentum transfers for ^{12}C and ^{40}Ca within the framework of the continuum shell model [114, 116] as well as in other analyses [117–119].

4.2 General formalism

The evaluation of the 2p-2h MEC contributions is performed within an exact microscopic calculation, where the two-body current is the sum of seagull, pion-in-flight, pion-pole and Δ-pole operators and the basis wave functions are non-interacting Dirac spinors. The features of the RFG model allows for a fully Lorentz covariant calculation of the MEC. In Refs. [110, 113, 115] it has been calculated for the first time the fully relativistic weak (with *vector* and *axial* components) charged meson-exchange currents for neutrino-nucleus interaction in both longitudinal and transverse channels as well as a complete analysis for electromagnetic reactions. The numerical integration method is described in [105, 113, 120] where the 2p-2h MEC hadronic tensor is calculated considering two particles $\mathbf{p}'_1$ and $\mathbf{p}'_2$ above the Fermi momentum in the final state, $p'_i > k_F$, and two holes $\mathbf{h}_1$ and $\mathbf{h}_2$ below the Fermi momentum, $h_i < k_F$,

$$W^{\mu\nu}_{2p-2h} = \frac{V}{(2\pi)^9}\int d^3p'_1 d^3h_1 d^3h_2 \frac{M^4}{E_1E_2E'_1E'_2}\Theta(p'_1,p'_2,h_1,h_2) \\ r^{\mu\nu}(\mathbf{p}'_1,\mathbf{p}'_2,\mathbf{h}_1,\mathbf{h}_2)\delta(E'_1+E'_2-E_1-E_2-\omega)\,, \tag{4.1}$$

where by momentum conservation, $\mathbf{p}'_\mathbf{2} = \mathbf{h_1} + \mathbf{h_2} + \mathbf{q} - \mathbf{p}'_\mathbf{1}$ and E_i and E'_i are the on-shell energies of the holes and particles. The only two parameters in the description are the Fermi momentum k_F associated to the nuclear species and the separation energy, *i.e.*, E_{shift}. Pauli-blocking effects are also considered through the step function

$$\Theta(p'_1,p'_2,h_1,h_2) = \theta(p'_2-k_F)\theta(p'_1-k_F)\theta(k_F-h_1)\theta(k_F-h_2)\,. \tag{4.2}$$

The elementary 2p-2h hadronic tensor $r^{\mu\nu}$ is defined in terms of the two-body MEC antisymmetrized matrix element $j^\mu(1',2',1,2)_A$,

$$r^{\mu\nu}(\mathbf{p}'_1,\mathbf{p}'_2,\mathbf{h}_1,\mathbf{h}_2) = \frac{1}{4}\sum_{s_1s_2s'_1s'_2}\sum_{t_1t_2t'_1t'_2} j^\mu(1',2',1,2)^*_A j^\nu(1',2',1,2)_A\,. \tag{4.3}$$

The MEC operator is written as the sum of four contributions, seagull (a,b), pion-in-flight (c), pion-pole (d,e), and Δ pole (f–i), as shown in Fig. 4.2,

$$j^\mu_{\rm MEC} = j^\mu_{\rm sea} + j^\mu_\pi + j^\mu_{\rm pole} + j^\mu_\Delta\,. \tag{4.4}$$

The different contributions are characterized in terms of how the virtual boson is attached to the hadronic vertex. The seagull or contact terms are associated to the attachment of the virtual boson to the $NN\pi$ vertex whereas the pion-in-fligh operator is referred to the direct interaction of the boson with the virtual pion. At variance with the pion-in-flight current, the pion-pole terms has only the axial component and therefore it is absent in the electromagnetic case. This contribution could be considered as the "axial counterpart" of the pion-in-flight term, in the sense that it contains two pion propagators. MEC contributions involving the virtual Δ resonance (Δ-pole terms) are also of relevance for the description. For completeness, it is worth pointing out that those diagrams that correspond to the excitation of a $2p2h + \pi$ state, hence to pion production [121], are implicitly included in the phenomenological inelastic scaling function described in Chapter **??**.

The exact evaluation of the 2p-2h hadronic tensor (4.1) in a fully relativistic way involves numerical seven-dimensional integrations of a huge number of terms. This makes the computation, exactly performed in [105, 110, 113, 120], highly non-trivial. In order to reduce the computational time as well as to ease the implementation of the results in Monte Carlo generators used in the

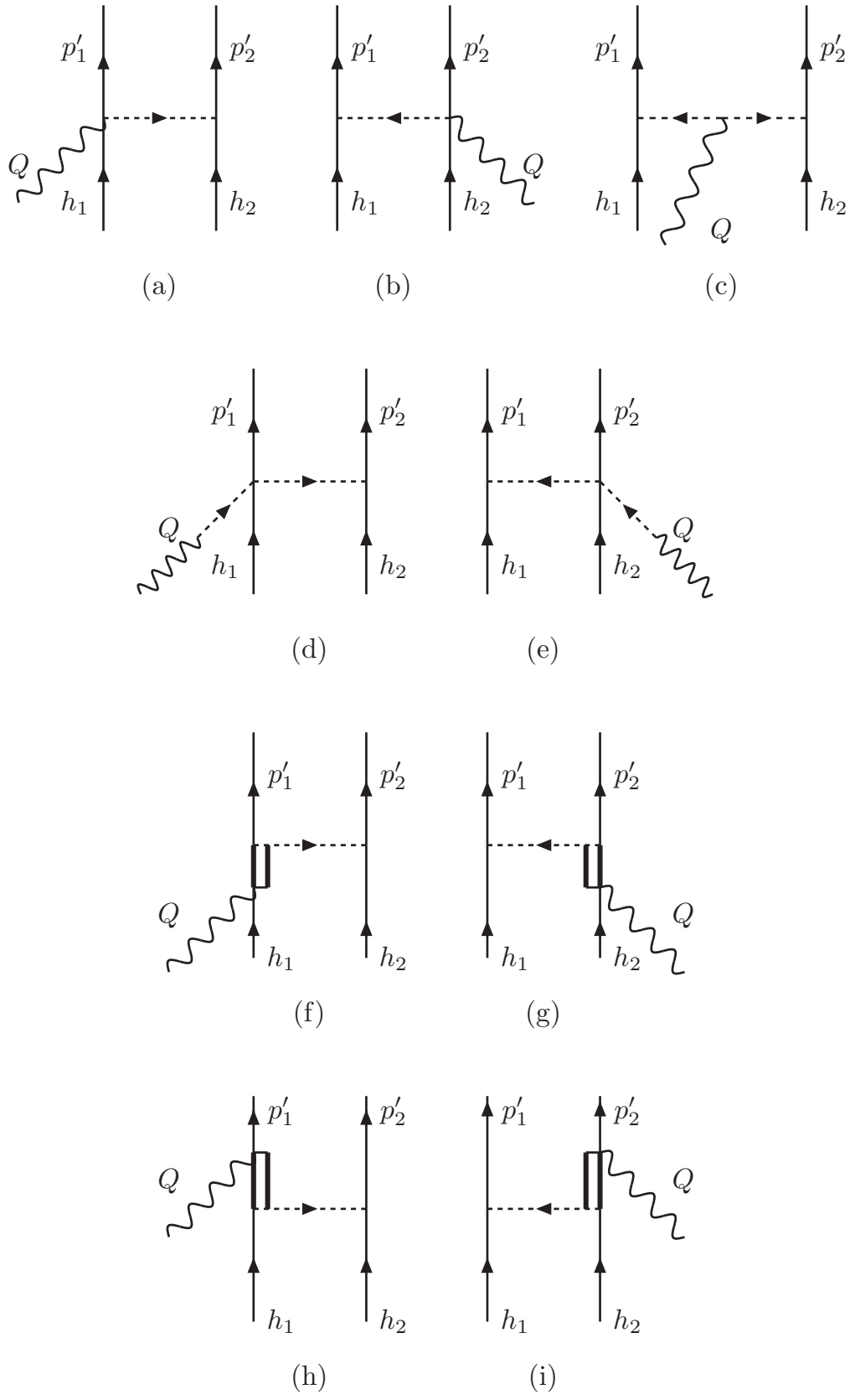

Figure 4.2: Feynman diagrams of the MEC considered in the present analysis, including the seagull (a,b), pion-in-flight (c), pion-pole (d,e), and Δ pole (f-i) contributions. Taken from [105].

analysis of neutrino experiments, where a wide range of kinematic conditions — momentum and energy transfers — are involved, we make use of a parametrization of the MEC responses that can be applied from low to very high momentum and energy transfers. The parametrization form employed for the different electromagnetic and weak responses is a function of the momentum and energy transfers, or equivalently, of the momentum and the scaling variable, and reads

$$R_X^{2p-2hMEC}(\psi',q) = \frac{2a_{3,X}e^{-\frac{(\psi'-a_{4,X})^2}{a_{5,X}}}}{1+e^{-\frac{(\psi'-a_{1,X})^2}{a_{2,X}}}} + \sum_{k=0}^{2} b_{k,X}\cdot(\psi')^k\,, \tag{4.5}$$

where $X = L,T(=T_{VV})$ for electromagnetic reactions and $X = CC,CL,LL,T(=T_{VV},T_{AA}),T'_{VA}$ for neutrino reactions. The parameters $a_{i,X}(q), b_{k,X}(q)$ are q-dependent and are defined for each reaction channel. The ψ' scaling variable is the same as defined in Chapter 3,

$$\psi' = \frac{1}{\sqrt{\xi_F}}\frac{\lambda'-\tau'}{\sqrt{(1+\lambda')\,\tau' + \kappa\,\sqrt{\tau'\,(1+\tau')}}}\,, \tag{4.6}$$

where ξ_F is the dimensionless Fermi kinetic energy and the following dimensionless transfer variables have been also previously defined: $\lambda = \omega/2M_N$, $\kappa = q/2M_N$, $\tau = \kappa^2 - \lambda^2$. Primed variables contain the energy transfer shift, $\omega' = \omega - E_{shift}$, which accounts for the binding energy of the ejected nucleon, which is usually determined phenomenologically. With this parametrization, the evaluation of the 2p-2h MEC cross sections for electromagnetic and weak reactions is similar to the quasielastic case, just replacing the QE response functions in Eqs. (**??**) and (**??**) by the corresponding 2p-2h MEC ones.

In the following sections, we analyze the 2p-2h MEC responses for electromagnetic (Section 4.3) and charged-current weak (Section 4.4) reactions on ^{12}C, also detailing the different parametrization forms. The extension to other nuclei will be addressed in Section 4.5.

4.3 2p-2h MEC responses for (e,e') reactions

Next, we consider the purely isovector nuclear longitudinal and transverse response arising from electromagnetic 2p-2h MEC states on ^{12}C, based on the work by De Pace et al. [110] and Amaro et al. [105, 113]. An accurate parametrization of these responses as a function of the momentum and energy transfers involved is presented.

Although MEC clearly dominate in the transverse channel, the study of Refs. [105, 113] includes also for the first time MEC contributions in the longitudinal sector. In Fig. 4.3 we present the separate 2p-2h MEC responses in the two channels for different q values. As shown, the transverse sector clearly dominates up to $q \sim 1800$ MeV/c, while the L and T contributions are of the same order for larger values of the momentum transfer. However, note that the kinematics where the MEC give the largest contribution to the cross section corresponds to $q \lesssim 1000-1500$ MeV/c, as stated in [115] and will be discussed later.

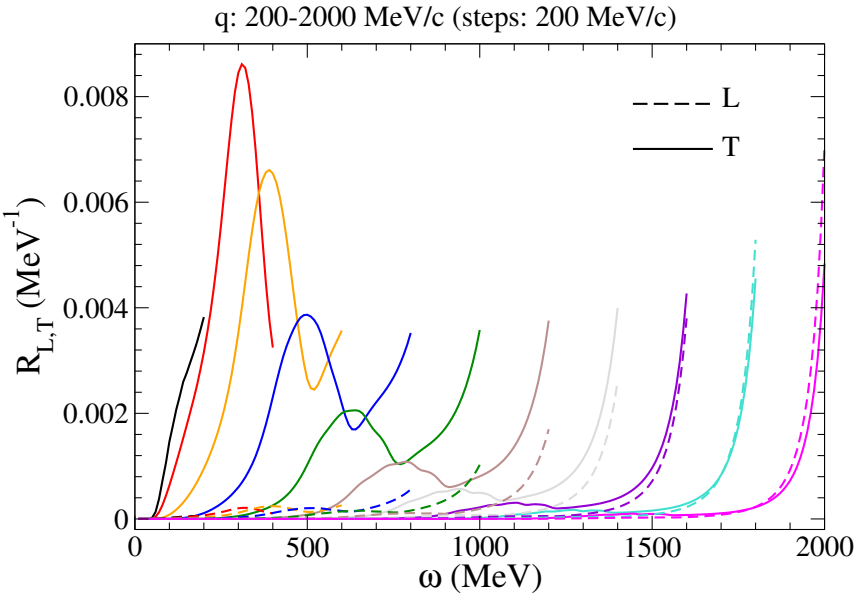

Figure 4.3: Comparison between 2p-2h MEC R_L and R_T response functions versus ω. The curves are displayed from left to right in steps of q =200 MeV/c.

The electromagnetic MEC response functions for $q \geq 400$ MeV/c exhibit a peak that decreases with q together with a tail that rises with ψ' and q. In order to parameterize these functions we applied an expression with two terms, the first one mainly fitting the peak of the response[1] and the second fitting the tail at larger ψ':

$$R^{MEC}_{L(T)_{VV}}(\psi') = \frac{2a_{3,L(T)}e^{-\frac{(\psi'-a_{4,L(T)})^2}{a_{5,L(T)}}}}{1+e^{-\frac{(\psi'-a_{1,L(T)})^2}{a_{2,L(T)}}}} + \sum_{k=0}^{2} b_{k,L(T)} \cdot (\psi')^k \,. \tag{4.7}$$

In this expression the parameters $a_{i,L(T)}$, $b_{k,L(T)}$ are q-dependent, and they are used to fit the original $R^{MEC}_{L(T)_{VV}}$ responses shown in Fig. 4.3. We first fit each response for a given q to get the values of the a_i, b_k parameters for that specific q-value, ensuring a smooth dependence on q for each of them. The q-dependent values of the fitting parameters are shown in Fig. 4.4. We then parametrize the q-dependence of the parameters themselves using a polynomial in q. The responses in Eq. (4.7) then become explicitly dependent on the momentum transfer, $R^{MEC}_{L(T)_{VV}}(\psi', q)$, through the dependence in the parameters, $a_{i.L(T)}(q)$, $b_{k,L(T)}(q)$.

In order to fit the responses above q = 2000 MeV/c, which show almost no peak but a tail-like shape, we keep only the second term in Eq. (4.7), namely $a_{3,L(T)} = 0$; since these responses are very similar in the large-q region under consideration (up to 3500 MeV/c), we use the same parametrization for all of them, namely $b_{k,L(T)}(q > 2000) = b_{k,L(T)}(q = 2000)$. As it will be discussed later, there are no significant MEC contributions for q >2000 MeV/c and the same is true for large $\omega > 1000$ MeV [115]. For the responses below q = 300 MeV/c we use again a polynomial to fit the results ($a_3 = 0$),

$$R^{MEC}_{T,VV}(\psi', q_{<300}) = \sum_{k=0}^{3} c_{k,L(T)}(q) \cdot (\psi')^k \,. \tag{4.8}$$

[1]Note that the functional form for the first term is similar to the one employed for the SuSAv2 scaling functions (see Appendix B for details).

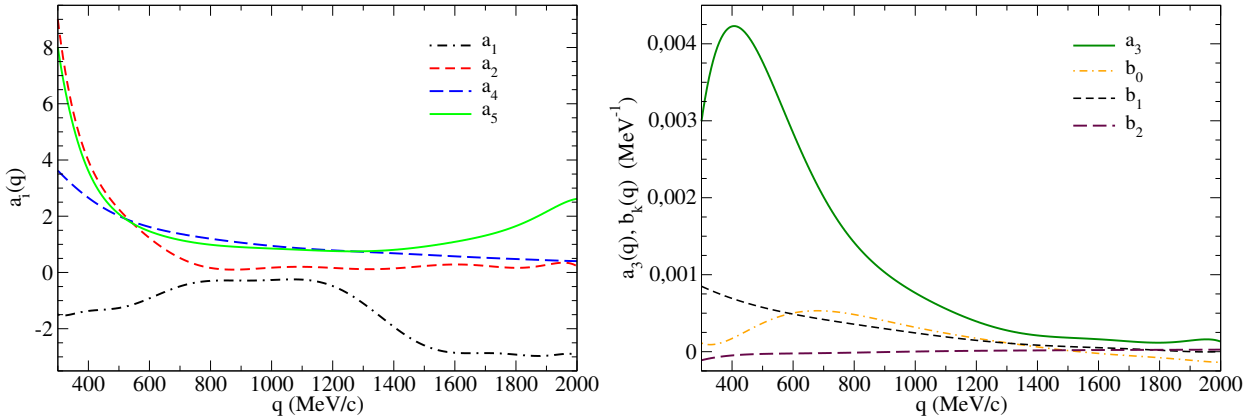

Figure 4.4: Dependence on q of the fitting parameters $\{a_i, b_k\}$ for the electromagnetic 2p-2h MEC transverse response.

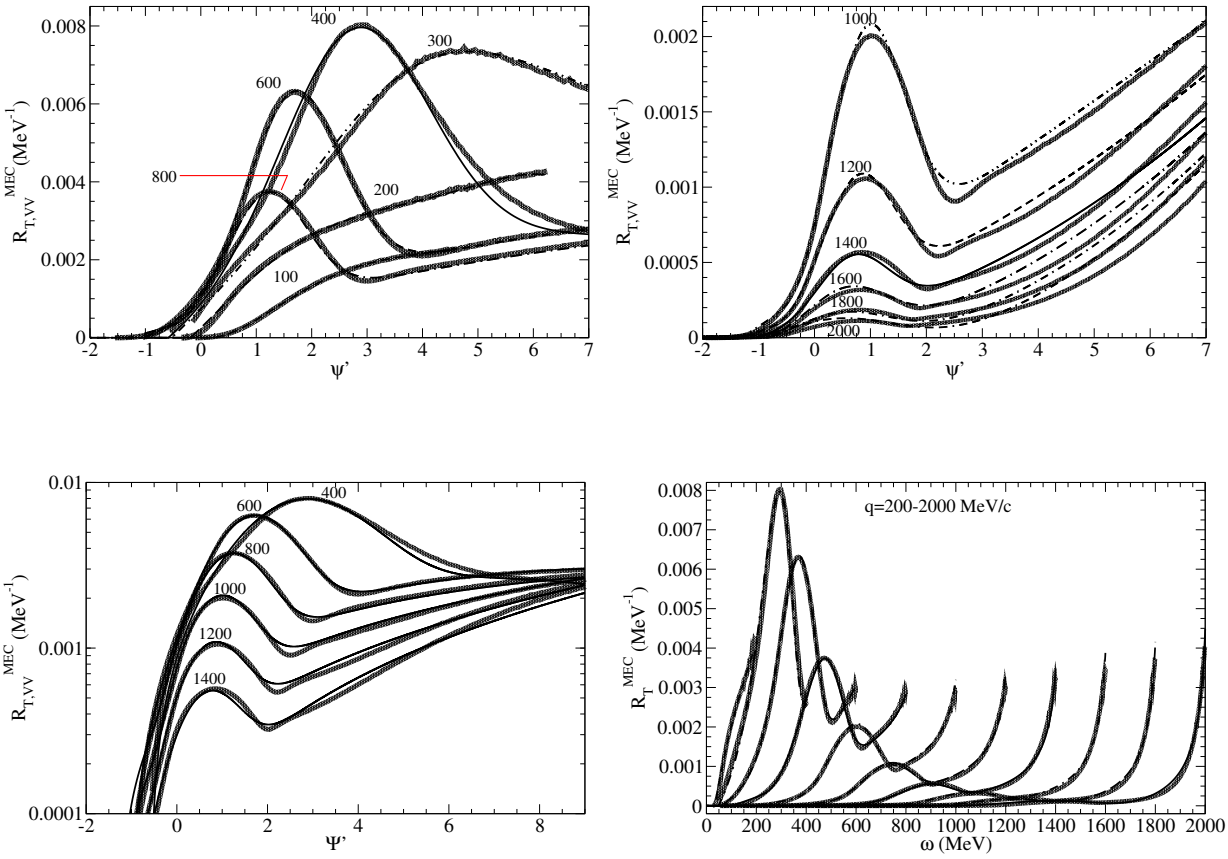

Figure 4.5: $R^{MEC}_{T,VV}$ (MeV^{-1}) versus ψ' from q=100-2000 MeV/c (top panels) and versus ω (right bottom panel), where for the last one the curves are displayed from left to right in steps of q =200 MeV/c. The parameterized responses are shown as black lines. Comparisons with microscopic calculations (coloured thick lines) are also displayed. Note that the y-axis in the left bottom panel is shown as a logarithmic scale to stress the accuracy of the fit.

The results of the above parametrization for the transverse MEC responses are presented as a function of the scaling variable ψ' in Fig. 4.5 where it is shown that it gives an excellent representation of the exact results in the full region of q and ψ' explored. Going into detail, some minor differences between the microscopic calculations and the parametrization can be observed at the highest ψ' values, above $\psi' = 2$, which corresponds to $\omega \rightarrow q$. When comparing them versus the energy transfer, ω, we can observe how these small discrepancies roughly dissapear for all cases. Additionally, a succesful comparison with the 2p-2h MEC calculations at very low-q values is shown in Fig. 4.6. For completeness, we show in Fig. 4.7 the Q^2-dependence of the transverse MEC response in terms of the energy transfer. The 2p-2h MEC responses decrease and are shifted to large ω-values as $|Q^2|$ increases. We also notice that the increase observed in the tail of the MEC responses for fixed q-values at $\omega \rightarrow q$ (see Fig. 4.5) does not appear in Fig. 4.7 as $|Q^2|$-values below 0.1 GeV^2 are neglected.

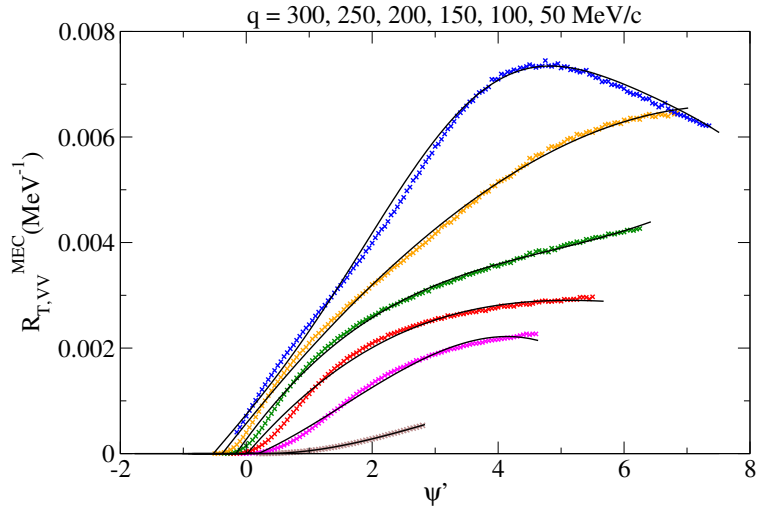

Figure 4.6: $R^{MEC}_{T,VV}$ (MeV^{-1}) versus ψ' for the lowest q values. The curves are displayed from top to bottom in steps of q =50 MeV/c. The parameterized responses are shown as black lines. Comparisons with microscopic calculations (coloured cross points) are also displayed.

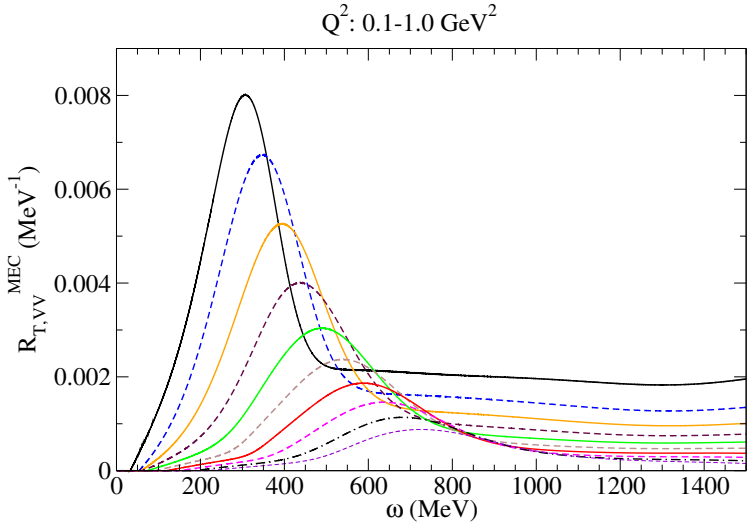

Figure 4.7: Transverse vector 2p-2h MEC response versus ω for different values of Q^2. The curves are displayed from left to right in steps of 0.1 GeV^2.

Similarly to the transverse channel, a high accuracy is achieved for the parametrization of the 2p-2h MEC longitudinal response functions, as reproduced in Fig. 4.8. Notice that no approximations are involved in the present calculations for the longitudinal and transverse functions. The MEC parametrizations considered here takes care of the complete relativistic calculation, making it suitable to be applied at very high values of the momentum and energy transfers.

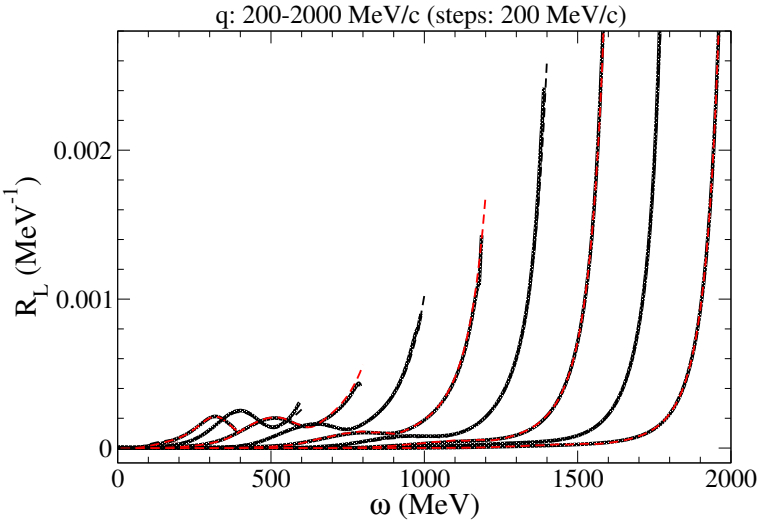

Figure 4.8: 2p-2h MEC R_L responses (dashed lines) compared with the parameterized ones (thick solid lines) versus ω. The curves are displayed from left to right in steps of $q = 200$ MeV/c.

4.4 2p-2h MEC responses for (ν_l, l) reactions

In this section, we consider the fully relativistic weak charged meson-exchange currents on ^{12}C, in both longitudinal and transverse channels and for the *vector* and *axial* components. These have been evaluated in [105, 113, 120] from an exact microscopic calculation based on the RFG model. The procedure to obtain the weak 2p-2h MEC response functions has been previously detailed in Section 4.2 and is similar to the one for electromagnetic reactions.

We use the same functional form (Eq. 4.5) employed for the parametrization of the electromagnetic MEC responses (Section 4.3) but extending it to the different axial and vector components involved in the analysis of CC neutrino reactions. As for (e, e') reactions, the parametrization yields an excellent representation of the microscopic calculations in the same region of q and ψ'. In Fig. 4.9 we compare the contributions of the different 2p-2h MEC responses as functions of the energy transferred to the nucleus for three values of the momentum, $q = 200$, 600 and 1000 MeV/c. Note that in general the 5 weak responses $(CC, CL, LL, T(= T_{VV} + T_{AA})$ and $T'_{VA})$ are comparable in size, depending on the specific kinematics. We also show the contributions of the vector-vector (T_{VV}) and axial-axial (T_{AA}) responses, which are closer to the interference vector-axial term (T'_{VA}). The electromagnetic responses are also shown as reference, where it can be observed the negligible contribution of the vector longitudinal contribution whereas it is recognized the factor 2 between the weak vector contribution (T_{VV}) and the purely-vector electromagnetic one (T_{EM}) as a consequence of the isovector nature of the CC weak interaction considered[2].

[2]The electromagnetic 2p-2h MEC responses and the ones for charged-current neutrino reactions corresponding to the T_{VV} channel are related through $R^{\nu}_{T,VV} = 2R^{EM}_{T,VV}$. The factor 2 arises from the transition between the isovector+isoscalar electromagnetic contributions, where the isoscalar term is negligible, and the purely isovector one for CC neutrino scattering.

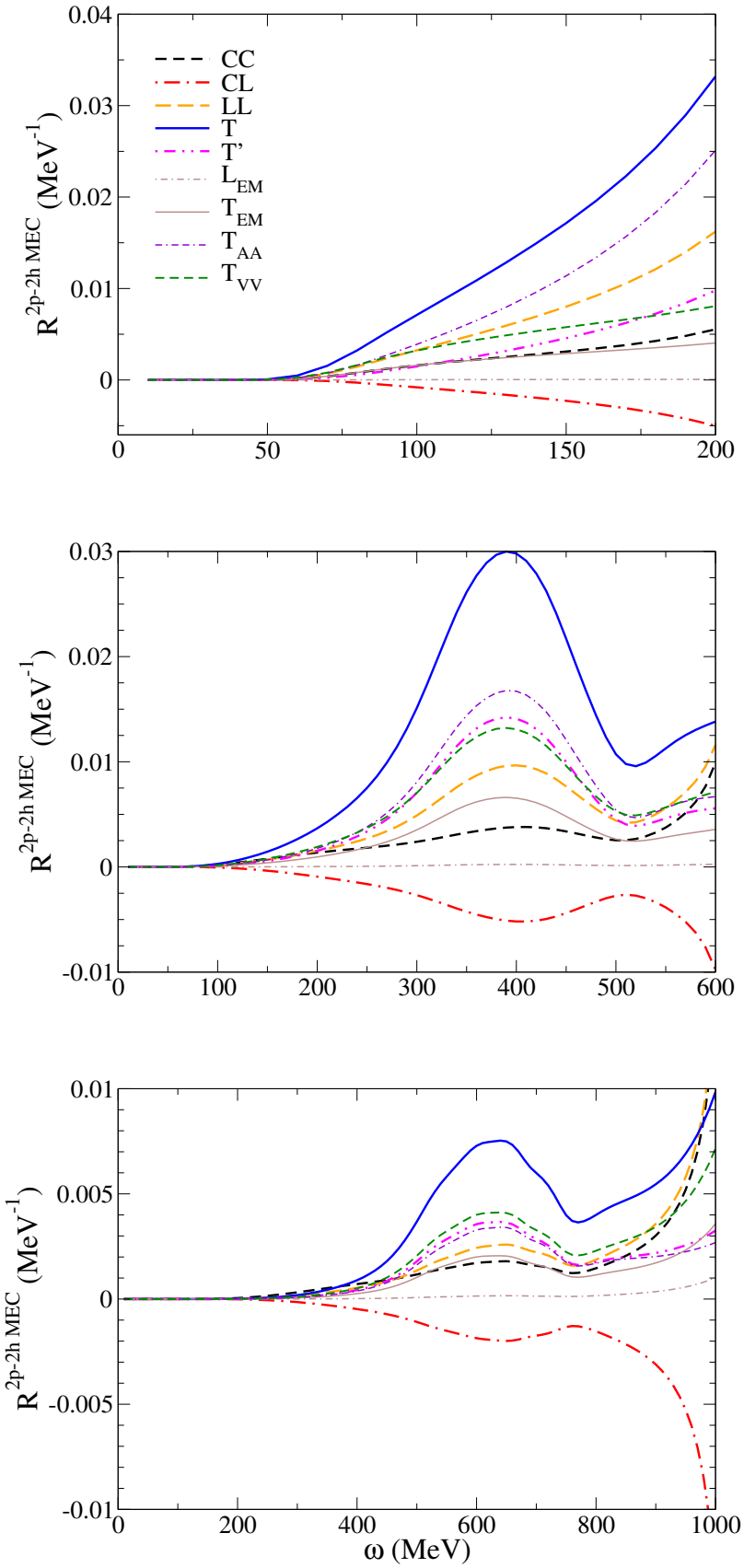

Figure 4.9: Comparison between 2p-2h MEC transverse ($T = T_{VV} + T_{AA}$ and $T' = T'_{VA}$) response functions and the longitudinal ones (CC, CL and LL) at $q = 200$ MeV/c (top panel), $q = 600$ MeV/c (mid panel) and $q = 1000$ MeV/c (bottom panel).

We can also notice a larger relevance of the weak longitudinal contributions with respect to the electromagnetic case. Nevertheless, when computing the total MEC neutrino cross section, the contribution of the CC and LL channels is roughly compensated by that of the negative CL response, so that for neutrino energies below $\sim$ 1 GeV the net longitudinal contribution plays a minor role in the total MEC response. This is illustrated in Fig. 4.10, where the L, T and T' contributions to the 2p-2h MEC cross section are displayed versus the neutrino energy. At higher energies the L and T' contributions become comparable, both being much smaller that the dominant T one. The balance between the longitudinal and transverse 2p-2h channel discussed above is somehow different from the one emerging in the electromagnetic case. As described in Section 4.3, the longitudinal electromagnetic MEC response is indeed negligible with regard to the transverse one. However, as illustrated in Fig. 4.10, we notice that when computing the total 2p-2h MEC weak cross section the longitudinal contribution is dominated by the axial channel and thus it plays a more relevant role compared with the purely-vector electromagnetic case. Concerning the transverse responses, it is noticeable that the magnitude of the pure axial and vector channels to the cross section is very similar. Moreover, the vector-axial interference contribution reaches its maximum around E_ν $\sim$1 GeV and decreases at higher energies as a consequence of the behavior of the leptonic factor $V_{T'}$ and the axial form factor $G_A(Q^2)$, which vanish as $|Q^2|$ increases (see Chapter 2 for details).

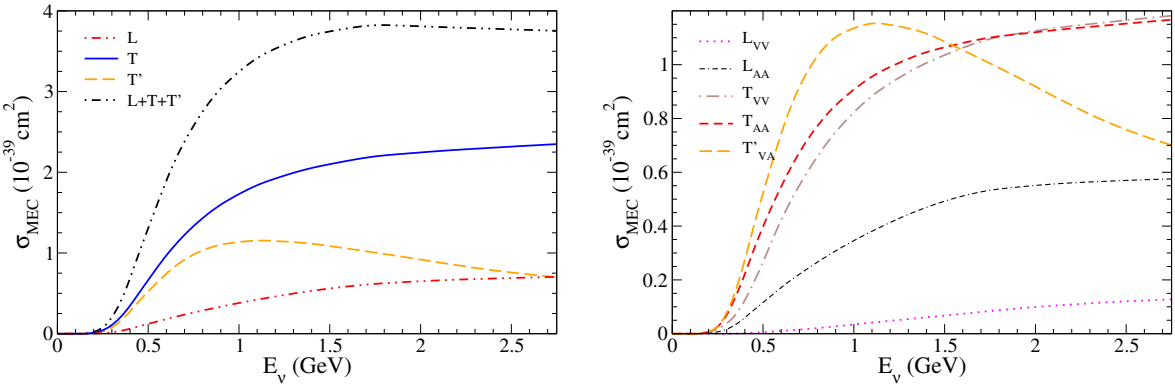

Figure 4.10: Separation into components of the total 2p-2h MEC ν_μ cross section displayed versus neutrino energy E_ν. The total longitudinal (L), transverse (T) and transverse interference (T') contributions are shown (left panel) as well as the net cotnribution ($L + T + T'$). Longitudinal and transverse channels are decomposed into vector and axial contributions (right panel).

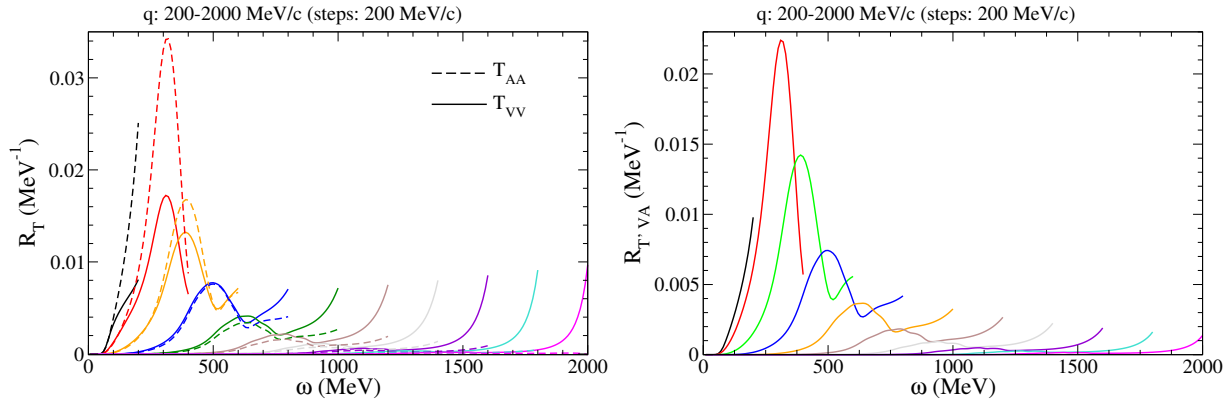

Figure 4.11: Comparison between 2p-2h MEC axial transverse (T_{AA}) response functions and the vector ones (T_{VV}) versus ω (left panel). The transverse vector-axial interference term (T'_{VA}) is also shown (right panel). The curves are displayed from left to right in steps of q = 200 MeV/c.

The analysis of the evolution with q of the individual transverse components (see Fig. 4.11) shows that the axial term is larger than the vector one at low-intermediate kinematics ($q < 800$ MeV/c) whereas the opposite occurs at higher kinematics. The interference vector-axial response functions yield an intermediate result between the axial and vector responses.

The present evaluation of the 2p-2h MEC responses and their corresponding fits also have the merit of covering a very wide q range, including the tail of the responses at high ψ' and ω values. In general, (e,e') data are rarely available when $\omega \to q$ and hence the high-ω region was ignored in some prescriptions. In contrast, for CCQE reactions one must integrate over a broad neutrino spectrum and hence, potentially, the high-ω region may be relevant. This has motivated us to make an accurate description of the MEC contributions also for these kinematics. In Fig. 4.5, the analysis of the $R^{MEC}_{T,VV}$ results versus ω shows a small contribution below $q < 300$ MeV/c as well as the relevance of the tail in the response at $q > 800$ MeV/c. On the other hand, the tail of the MEC responses at high q ($q > 1000$ MeV/c) which appears at $\omega \gtrsim 1000$ MeV does not contribute significantly to the cross section at lower kinematics, as can be deduced from Fig. 4.12. In fact, if we neglect the tail of the MEC response in our parametrization, no significant differences emerge except at neutrino energies above 1 GeV where the complete approach yields somewhat larger contributions, as seen in Fig. 4.13. It can also be deduced from Fig. 4.12 that no significant MEC contributions appear for $q >$2000 MeV/c, and the same is true for large $\omega > 1000$ MeV, showing that the kinematics where the MEC give the largest contribution to the cross section corresponds to $q \sim 500 - 1500$ MeV/c and $\omega \sim 250 - 1000$ MeV, as also stated in [115]. A more detailed analysis of the relevant kinematic regions for the entire 2p-2h MEC contribution will be shown in Chapter 7. Moreover, the comparison between the electromagnetic 2p-2h MEC calculations and the (e,e') data will be addressed in Chapter 6 together with the QE and inelastic contributions.

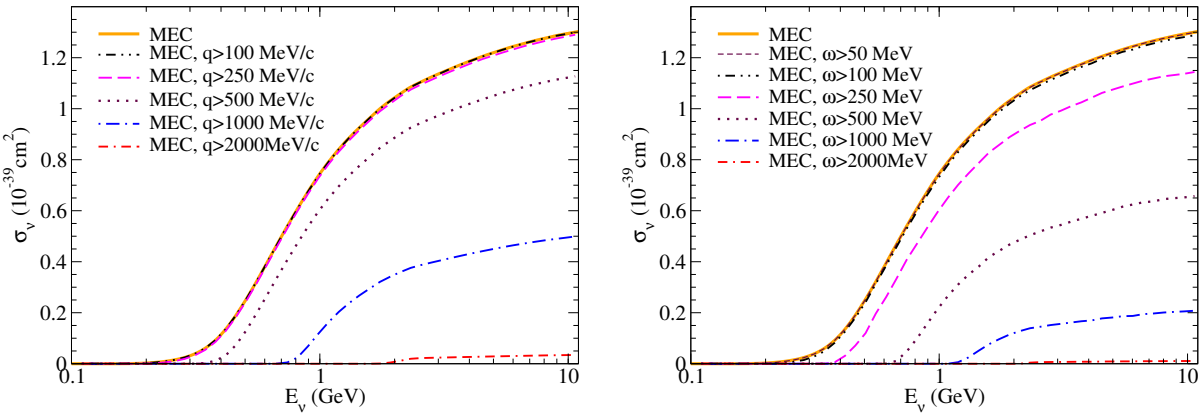

Figure 4.12: Total 2p-2h MEC ν_μ cross section for the T_{VV} channel per target nucleon evaluated excluding all contributions coming from transferred momentum (upper panel) and energy (lower panel) below some selected values, as indicated in the figure.

The main merit of the parametrization provided here for 2p-2h MEC electromagnetic and weak reactions on ^{12}C is that it translates a sophisticated and computationally demanding microscopic calculation into a smooth parametrization which depends on the values of the transfer variables of the process, easing its implementation into Monte Carlo neutrino event simulations used in the analysis of experiments. In the following section, we study the extension of this parametrization to other nuclei.

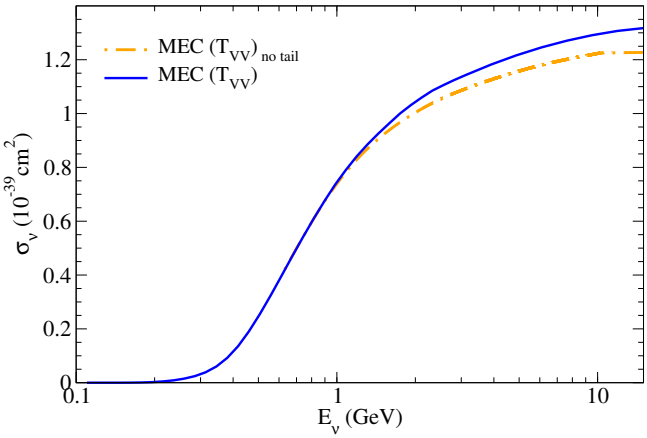

Figure 4.13: Comparison between the total 2p-2h MEC ν_μ cross section per target nucleon for the T_{VV} channel with and without considering the tail contribution in the responses.

4.5 Density dependence of 2p-2h meson-exchange currents

In this section, we analyze the density dependence of the 2p-2h MEC contributions in lepton-nucleus interactions in order to extend the above parametrization on ^{12}C to other nuclei. This is connected to the growing interest in the extension to heavier nuclei, such as ^{16}O, ^{40}Ar, ^{56}Fe and ^{208}Pb, used in ongoing and future neutrino experiments. Therefore, an estimation of the density dependence of the 2p-2h MEC responses would be extremely useful to extrapolate the results from the current parametrization on ^{12}C to other nuclei.

In Chapter 3, the "superscaling" behavior of the inclusive electron scattering data was analyzed for various nuclei (see Figs. 3.2 and 3.3), showing that, below the quasielastic peak, these data were independent on the momentum transfer (scaling of first kind) and on the mass number (scaling of second kind). On the contrary, some scaling violation emerged for energy transfer around and above the QE peak, mainly in the transverse channel and ascribed to reaction mechanisms different from one-nucleon knockout, such as 2p-2h MEC contributions. This superscaling behavior was also reproduced through the SuSAv2 scaling functions arising from the RMF theory. More specifically, it is worth mentioning that the reduced QE cross section, *i.e.* the QE cross section divided by the appropriate single-nucleon one, scales as $\sim A/k_F$, k_F being the Fermi momentum. This can be deduced by simple inspection of the equations described in Sections 3.2-3.4. The Fermi momentum of most nuclei belongs to the range 200-300 MeV/c (see Table 3.1 for a detailed comparison). In what follows we explore the density dependence of the 2p-2h nuclear responses.

Since the behavior with density of the nuclear response is not expected to depend very much on the specific channel or on the nature of the probe, for simplicity we focus on the electromagnetic 2p-2h transverse response, which largely dominates over the longitudinal one. Our starting point is therefore the electromagnetic transverse response for $Z = N$ nuclei, R_T^{MEC}, associated with meson-exchange currents carried by the pion and by the Δ-resonance, evaluated within the model of [110].

In a previous work [117] based on the non-relativistic Fermi gas, it has been suggested that the nuclear dependence of the 2p-2h MEC responses scales as Ak_F^2. Thus, in order to test this scaling

rule within our relativistic approach, we remove the single-nucleon physics from the problem by defining the following reduced response (per nucleon)

$$\widetilde{F}_T^{MEC}(q,\omega) \equiv \frac{1}{\eta_F^2}\frac{R_T^{MEC}(q,\omega)}{G_T^{ee'}(\tau)}\,, \tag{4.9}$$

where the single-nucleon term $G_T^{ee'}$ was previously defined in Section 3.2.3 and depends on the proton (G_{Mp}) and neutron (G_{Mn}) magnetic form factors. For simplicity here we neglect in the single-nucleon dividing factor small contributions coming from the motion of the nucleons ($W_2^{ee'}\Delta$ term), where the electric form factor contributes, which depend on the Fermi momentum (see Section 3.2.3). Note that the reduced response $\widetilde{F}_T^{MEC}$ is divided by $\eta_F^2 = (k_F/m_N)^2$, together with the single-nucleon factor $G_T^{ee'}$ in the search for the Ak_F^2 scaling. We can also introduce a 2p-2h MEC scaling function, f_T^{MEC}, defined analogously to the transverse scaling function coming from the one-body response,

$$f_T^{MEC}(q,\omega) = \frac{R_T^{MEC}(q,\omega)}{G_T^{ee'}(\tau)} = \eta_F^2 k_F \widetilde{F}_T^{MEC}\,. \tag{4.10}$$

The particular case of asymmetric nuclei, $Z \neq N$ requires more involved formalism and will be addressed in future work, although preliminary studies indicate that the qualitative behavior with k_F does not change significantly unless $N - Z$ is very large.

4.5.1 Analysis of results

In Fig. 4.14 we show the dependence on q of the above described 2p-2h MEC scaling function, f_T^{MEC}, for ^{12}C. Unlike the QE case, where the scaling functions for the RFG and RMF models "collapse" into a single one for all q values, the MEC scaling functions depend largely on q and spread far beyond the QE region ($-1 \leq \psi' \leq +1$ within the RFG model). This behavior is more pronounced for $q: \ 400-600$ MeV/c. As q increases, the MEC scaling functions are more similar and their maxima tend to lower ψ' values, getting closer to the QE peak ($\psi' = 0$). Furthermore, we can also notice that at very high momentum transfers the 2p-2h MEC contributions are very significant in the deep scaling region (large negative ψ' values), to the extent that they may even provide a contribution similar to the QE one at very low ω. Nevertheless, the QE and 2p-2h MEC contributions for low ω and high q are very small. In general, the observed trend with q of the 2p-2h MEC responses is consistent with the violation of first-kind scaling exhibited by the MEC in [111].

In Fig. 4.15 we display R_T^{MEC} as a function of the energy transfer ω for momentum transfers q ranging from 200 to 2000 MeV/c and three values of the Fermi momentum k_F from 200 to 300 MeV/c. Unlike the 1-body quasielastic case, it clearly appears that the 2p-2h response functions increase with k_F, *i.e.* with the mass number of the nuclear species. This motivates the search for a second-kind scaling behavior in the 2p-2h MEC regime. In order to study the k_F-dependence of the responses, we fix the momentum transfer to a specific value in Fig.4.16, where we show the response R_T^{MEC} for q=800 MeV/c (upper panels) and the same three values of k_F used above. In the lower panels of Fig. 4.16 we display the scaled 2p-2h MEC response, $\widetilde{F}_T^{MEC}$, as a function of the MEC scaling variable $\psi'_{MEC}(q,\omega,k_F)$ and of the quasielatic one $\psi' \equiv \psi'_{QE}(q,\omega,k_F)$. The MEC scaling variable is defined in the Appendix C, in analogy with the usual QE scaling variable, to adjust the maximum of the 2p-2h results at $\psi'_{MEC} \approx 0$.

The results show that the reduced 2p-2h response roughly scales as k_F^2 when represented as a function of ψ'_{MEC}, *i.e.*, the scaled 2p-2h MEC responses shown blend at the peak into a universal result. This scaling law is very accurate at the peak of the 2p-2h response, while it is violated to some extent at large negative values of the scaling variable. These effects in the "deep scaling" region are reduced when considering the usual scaling variable ψ'_{QE} devised for quasielastic scattering.

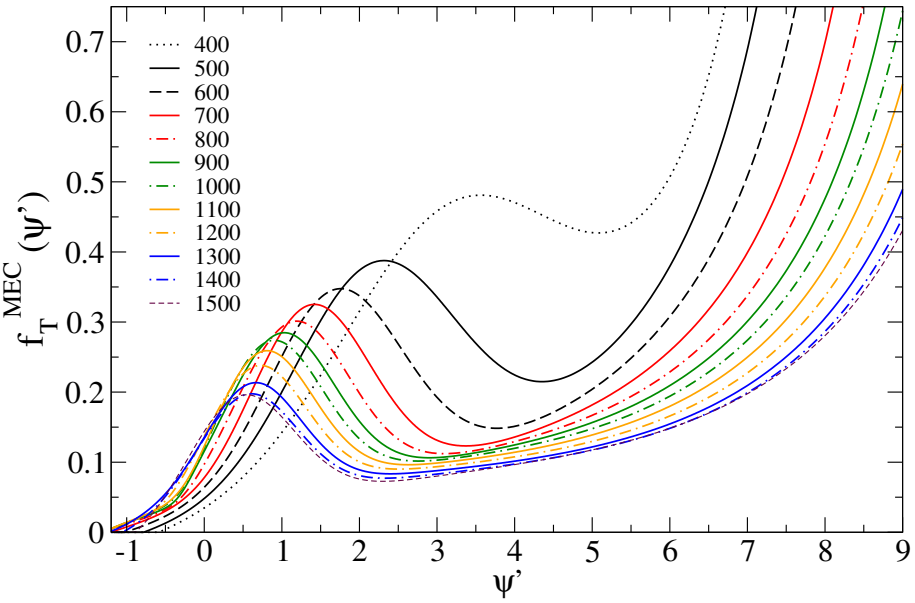

Figure 4.14: Transverse 2p-2h MEC scaling functions f_T^{MEC} for ^{12}C versus the usual QE scaling variable ψ'_{QE} from q = 400 MeV/c to 1500 MeV/c.

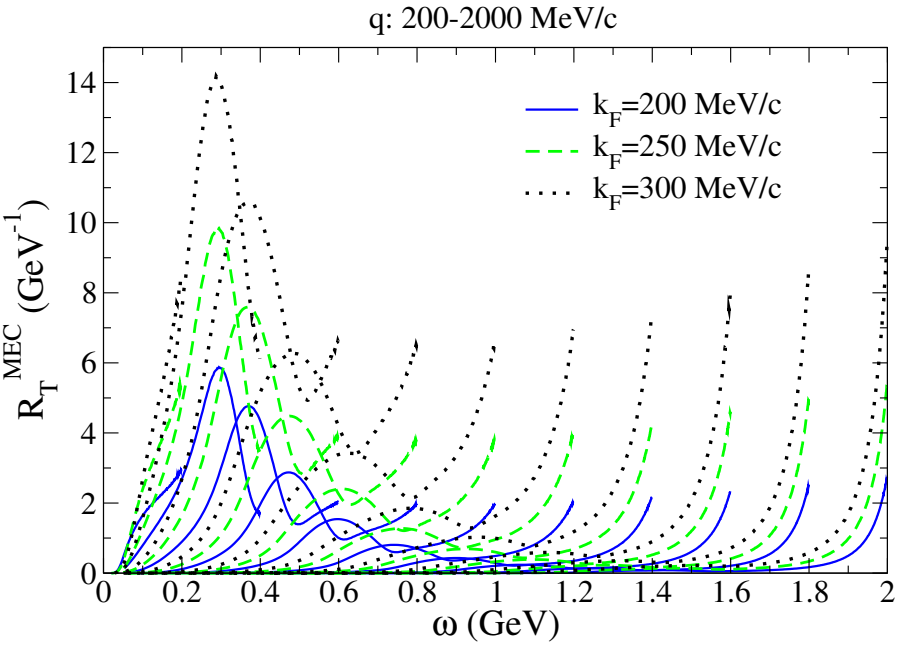

Figure 4.15: The 2p-2h MEC response plotted versus ω for three values of the Fermi momentum k_F and for different values of the momentum transfer. The curves are displayed from left to right in steps of q = 200 MeV/c.

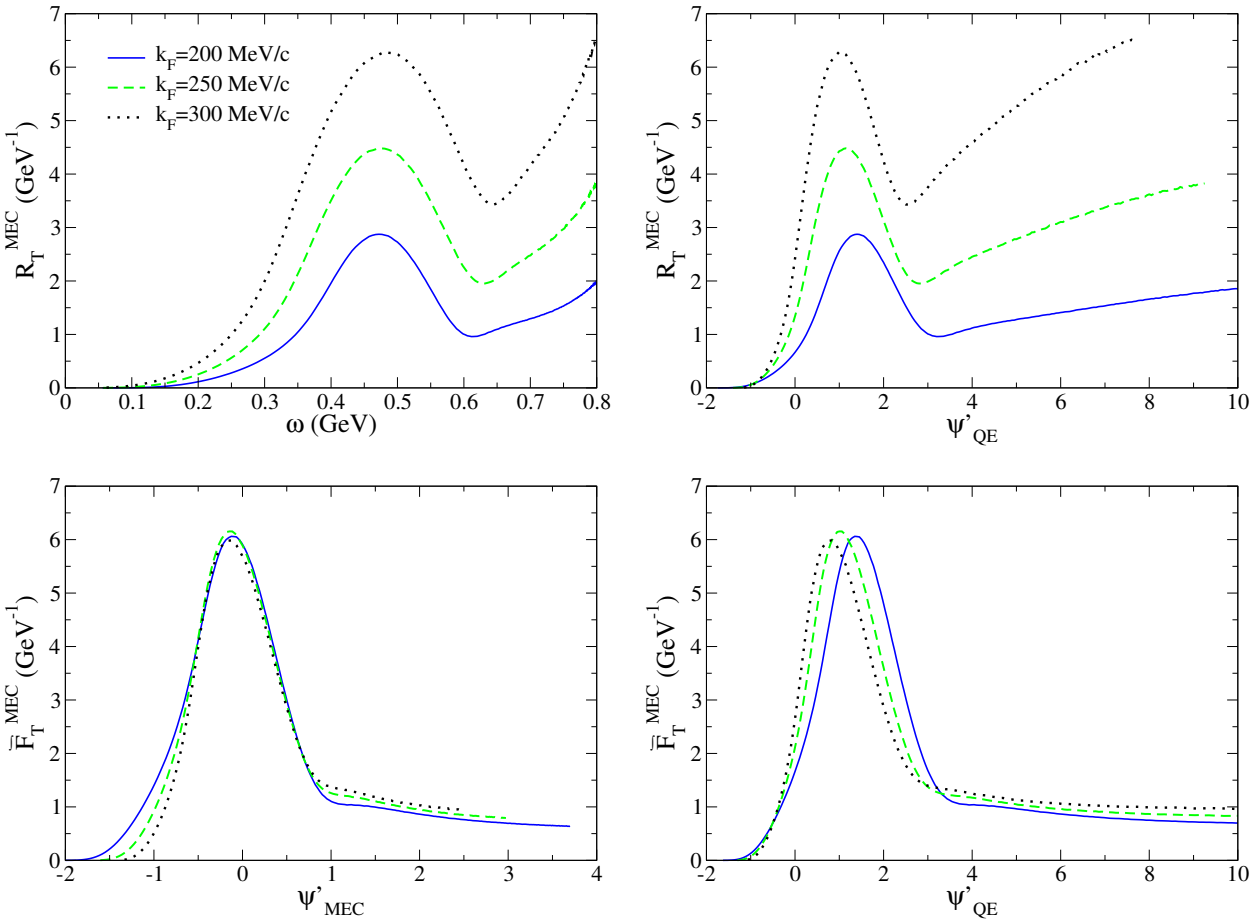

Figure 4.16: Upper panels: the 2p-2h MEC response plotted versus ω (left panel) and ψ'_{QE} (right panel) for $q = 800$ MeV/c and Fermi momentum k_F varying between 200 and 300 MeV/c. Lower panels: the corresponding scaled 2p-2h MEC response $\widetilde{F}_T^{MEC}$ plotted versus the scaling variables ψ'_{MEC} (left panel) and ψ'_{QE} (right panel).

In Fig. 4.17 the scaled 2p-2h MEC response is now plotted versus $\psi'_{\rm MEC}$ for four values of q and k_F. In particular, we have considered the cases of ^{12}C ($k_F = 228$ MeV/c) and ^{40}Ca ($k_F = 241$ MeV/c). The first is clearly relevant for ongoing neutrino oscillation studies whereas the second is a symmetric nucleus lying close to the important case of ^{40}Ar for upcoming neutrino experiments. Here we see that the same k_F-dependence is valid for different values of q as long as Pauli blocking is not active, namely $q > 2k_F$. At lower q and in the deep scaling region this type of scaling is mildly broken. In particular, this corresponds to $q \lesssim 500$ MeV/c and the lowest ω values. Nevertheless, this is not a relevant kinematic region for the analysis of 2p-2h MEC cross sections on neutrino reactions as shown in Fig. 4.12 ensuring an accurate extension of the ^{12}C-parametrization to other nuclei.

For completeness, we compare in Fig. 4.18 the scaled responses $\widetilde{F}_T^{MEC}$ for different powers of η_F for $q = 1000$ MeV/c, which reinforces the idea of the Ak_F^2 scaling behavior observed in Fig. 4.17 also for the same value of q. In particular, no scaling behavior is observed in terms of Ak_F (left panel) even though some agreement between different k_F values appears in the deep scaling region. On the contrary, the analysis of the Ak_F^3 dependence (right panel) only produces similar results for high ψ'_{MEC} values which corresponds to high energy transfers.

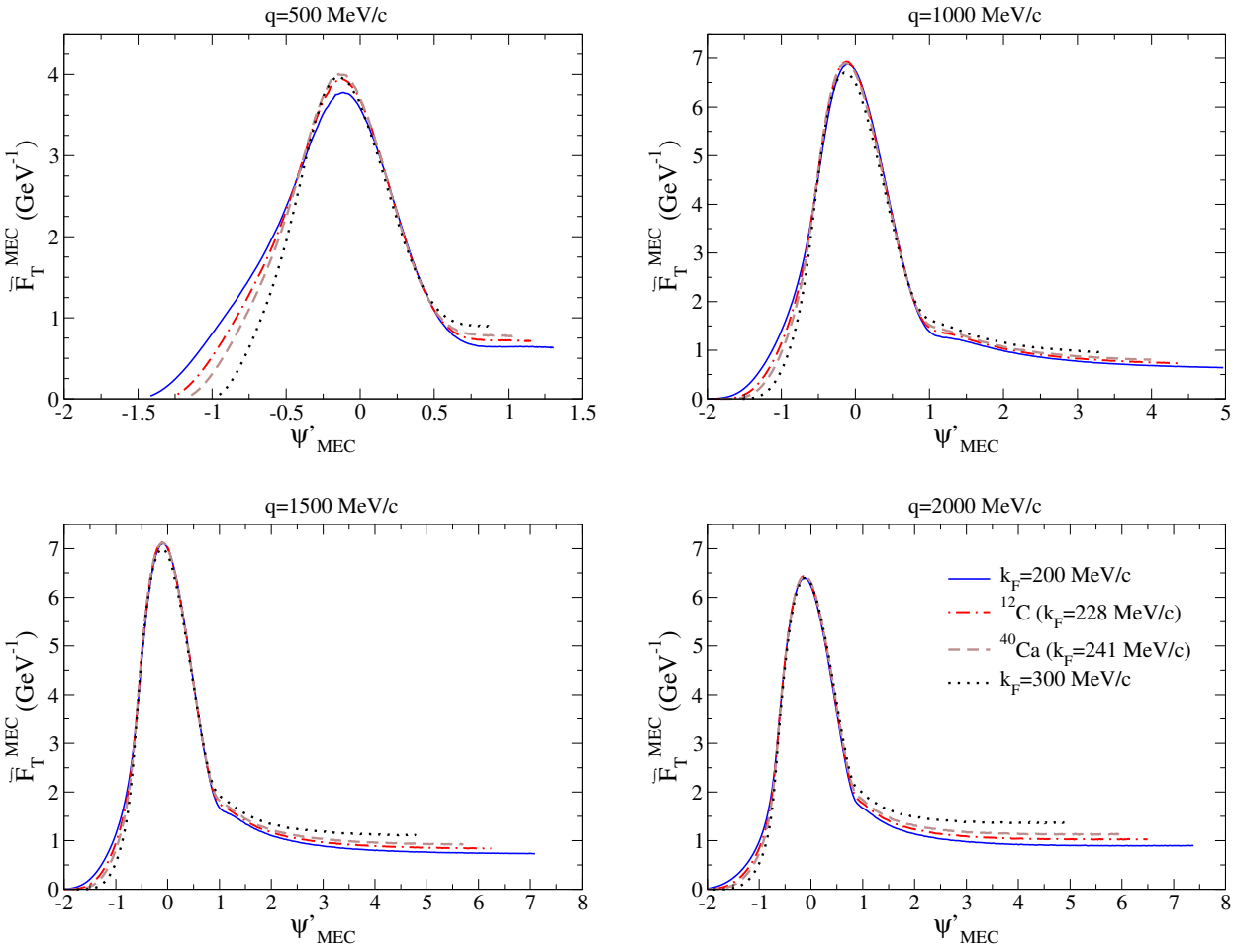

Figure 4.17: The scaled 2p-2h MEC response $\widetilde{F}_T^{MEC}$ plotted versus the scaling variable ψ'_{MEC} for different values of q varying from 500 to 2000 MeV/c and Fermi momentum k_F between 200 and 300 MeV/c. The particular cases of ^{12}C and ^{40}Ca are shown.

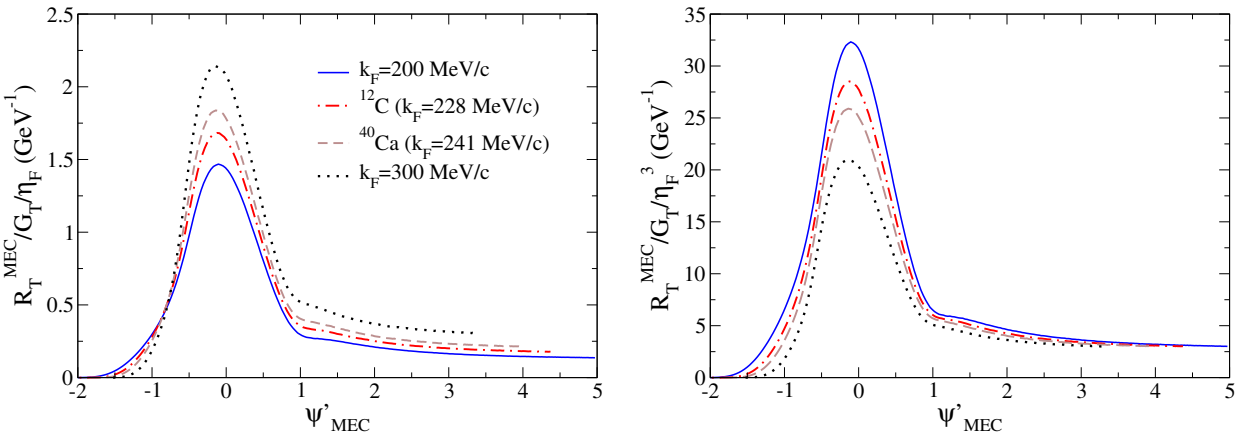

Figure 4.18: The scaled 2p-2h MEC response $\widetilde{F}_T^{MEC}$ for different powers of $\eta_F^n \equiv (k_F/m_N)^n$, $n = 1$ (left panel) and $n = 3$ (right panel) plotted versus the scaling variable ψ'_{MEC} for $q = 1000$ MeV/c and Fermi momentum k_F varying between 200 and 300 MeV/c.

After analyzing the k_F^2 dependence of the MEC responses as well as the $1/k_F$ dependence for the QE regime in terms of the superscaling behavior, we can draw out some conclusions about the relative importance of both contributions. Regarding the k_F dependence for different nuclei shown in Table 3.1, we can deduce that for lighter nuclei, where k_F is changing more rapidly with increasing A, the size of the MEC relative to the QE peak changes noticeably as A becomes larger. As A increases toward heavier nuclei, the nuclear density saturates, causing k_F to slowly approach the nuclear matter value of $k_F \sim 250 - 260$ MeV/c. This implies that for heavier nuclei all contributions will scale approximately as A. Therefore, while the relative MEC contribution will be largest for heavy nuclei, it changes most rapidly when comparing cross sections for light nuclei. This is also observed in the analysis of (e, e') inclusive data shown in Chapter 6 for different nuclei.

4.5.2 Neutrino-Oxygen 2p-2h MEC responses

Finally, we focus on the 2p-2h MEC responses for ^{16}O, which is relevant for recent neutrino experiments [122]. In particular, in the T2K experiment the far detector may have different nuclear targets, mineral oil and water, and it is then crucial to understand how to extrapolate the results from one target to another.

In Fig. 4.19 we analyze the 2p-2h MEC responses for neutrino interactions on ^{16}O compared with ^{12}C for two of the most relevant contributions (T_{VV} and T'_{VA}), based on microscopic calculations by Amaro *et al.* [105]. As previously mentioned, the 2p-2h MEC responses are evaluated within the RFG model in a fully relativistic framework, for which the values of the Fermi momentum and energy shift used are, $k_F = 228$ MeV/c, $E_{shift} = 20$ MeV for ^{12}C and $k_F = 230$ MeV/c, $E_{shift} = 16$ MeV for ^{16}O. The k_F and E_{shift} values corresponding to ^{16}O are consistent with the analysis of electron scattering data, as detailed in Chapter 6.

We observe in Fig. 4.19 (upper panels) that the results for ^{16}O are larger than the ^{12}C ones, which is mainly due to the different A numbers as the k_F values are very similar. At the same time, the ^{16}O responses are slightly shifted to lower ω values with respect to the ^{12}C ones as a consequence of the smaller E_{shift} for oxygen. Using now the previous result that the 2p-2h MEC contributions scale as Ak_F^2 we can multiply the ^{12}C results (which are parametrized) by the ratio between the A numbers and the k_F^2 values for both nuclei,

$$\frac{A(^{16}O)k_F^2(^{16}O)}{A(^{12}C)k_F^2(^{12}C)} \approx 1.35\,, \tag{4.11}$$

in order to reproduce the ^{16}O ones. This is presented in the lower panels of Fig. 4.19 for the T_{VV} and T'_{VA} channels, showing the high degree of accuracy of the scaling law for extrapolating the 2p-2h responses from carbon to oxygen for all values of q and leading to the conclusion that the Ak_F^2 dependence is also widely fulfilled by the 2p-2h weak reactions. Note also that the different energy shifts have been corrected by shifting the carbon results 8 MeV to the left.[3]. Similar comments also apply to all the remaining weak 2p-2h MEC responses. The comparison of our theoretical prescription with ^{16}O (e, e') and (ν_μ, μ^-) data will be addresed in Chapters 6 and 7.

[3]Although the shift difference between ^{12}C and ^{16}O is, $\Delta E_{shift} = E_{shift}(^{12}\mathrm{C}) - E_{shift}(^{16}\mathrm{O}) = 4$ MeV, we have to double this value when considering two-nucleon emission.

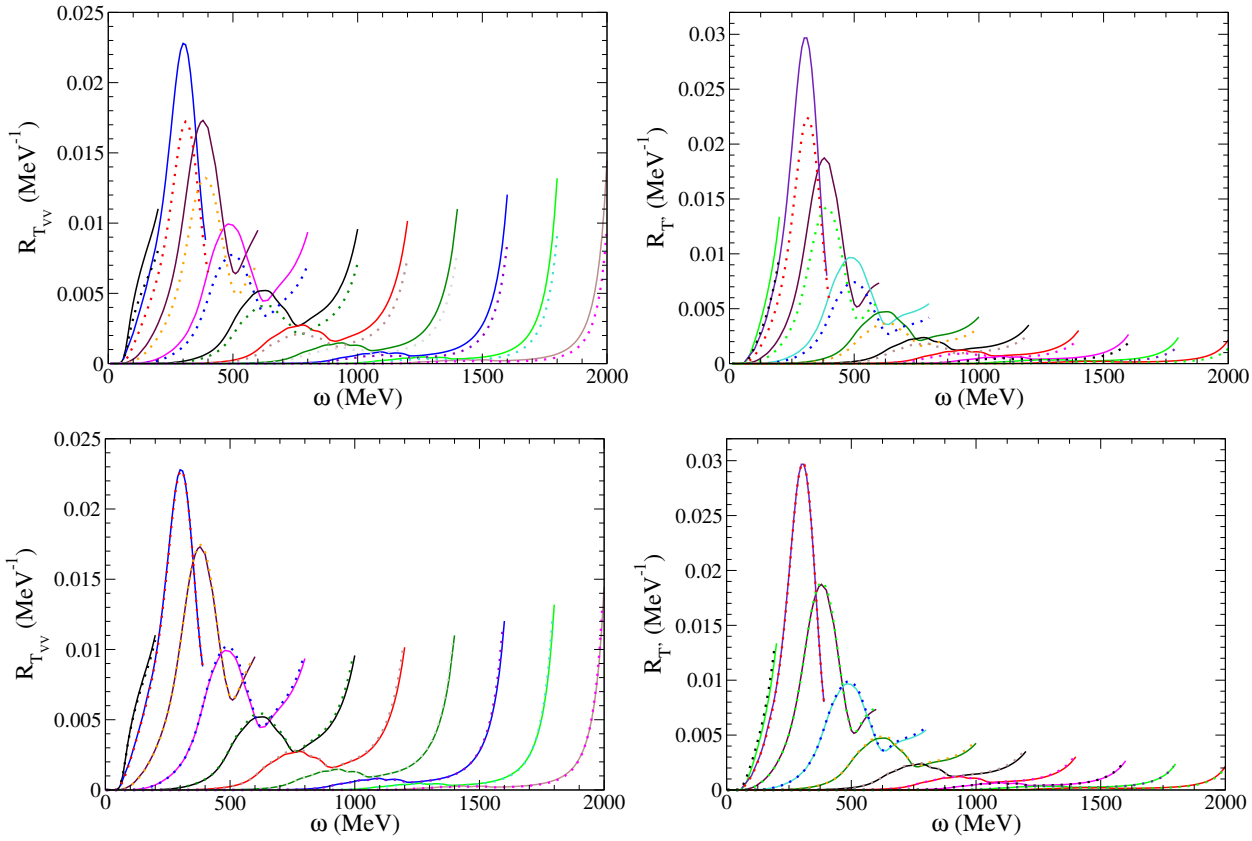

Figure 4.19: 2p-2h MEC vector-vector transverse (T_{VV}) response and the axial-vector interference (T'_{VA}) one. Upper panels: Comparison between the results for ^{12}C (dots) and ^{16}O (solid). Bottom panels: comparison by re-scaling the ^{12}C results with a factor 1.35 (see text). The curves are displayed from left to right in steps of q = 200 MeV/c from q = 200 MeV/c up to 2000 MeV/c.

Summarizing, we have shown that the 2p-2h electromagnetic and weak MEC response functions roughly grow as Ak_F^2 for Fermi momentum varying from 200 to 300 MeV/c. This scaling law is excellent around the MEC peak for intermediate and high values of q whereas it starts to break down around the Pauli-blocking region ($q = 2k_F$), where 2p-2h MEC do not contribute significanly to the neutrino cross sections. Compared to the behavior of the 1-body response, which scales as A/k_F, the relative importance of the 2p-2h contribution grows as k_F^3. This result allows one to get an estimate of the relevance of these contributions for a variety of nuclei, of interest in ongoing and future neutrino scattering experiments, and should facilitate the implementation of 2p-2h effects in Monte Carlo generators.

Chapter 5

Deep Inelastic Scattering in electron-nucleus reactions and its extension to neutrino reactions

In this Chapter we analyze the inelastic regime for electrons and neutrinos extending the previous SuSAv2-formalism for the QE regime to the complete inelastic spectrum – resonant, nonresonant and deep inelastic scattering (DIS). This description is achieved in terms of the inelastic single-nucleon structure functions for protons and neutrons whereas the nuclear medium effects are implemented by means of the SuSAv2 approach.

5.1 Introduction

Nuclear effects for the case of Deep Inelastic Scattering with neutrinos have not been studied at depth in the past. A first step is to make use of the results of DIS with electrons that can be extremely useful for neutrino scattering. Thus, we have taken advantage of high precision measurements for electromagnetic DIS on protons, deuteron and light nuclei to test our model, with the final goal of extending it to (anti)neutrino scattering. The inelastic structure functions arising from DIS with electrons are of interest and can be used to extend the electromagnetic description of the inelastic spectrum to the weak sector. Moreover, the analysis of inelastic processes on lepton-nucleus reactions is an important tool in the study of nucleon structure. At the same time an accurate description of neutrino inelastic cross sections at low energies is essential for precise neutrino oscillations experiments. In the analysis that follows we assume the Impulse Approximation as already done within the QE regime, where only one nucleon interacts with the lepton. An schematic view of the process is shown in Fig. 5.1.

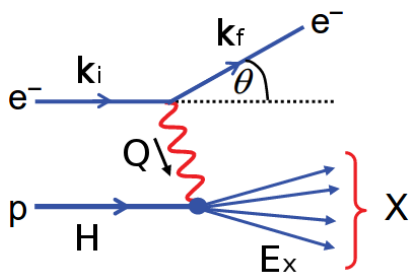

Figure 5.1: Schematic view of the DIS process for electromagnetic *e-p* reactions.

This interacting nucleon must be off the mass shell in order to conserve energy and momentum in the scattering process. The mass of the final state hadronic system is no longer the proton mass, M. The final state hadronic system must contain at least one baryon which implies the final state invariant mass $W_X > M$.

The inelastic structure functions for protons and neutrons are described in terms of phenomenological fits for electron-proton and electron-deuteron reactions. The extension of this formalism to the nuclear regime is addressed by means of the superscaling functions arising from the SuSAv2 model.

5.2 General formalism for (e, e') and (ν_l, l^-) DIS reactions

Following the notation employed for the kinematical description in Chapter 2, the double differential cross section for the reaction of deep inelastic scattering of a lepton from an unpolarized nucleon in the Born approximation,

$$l + N \to l' + X \qquad (l = e, \mu, \tau) \qquad \text{EM interaction} \tag{5.1}$$

$$\nu_l(\overline{\nu}_l) + N \to l^-(l^+) + X \qquad \text{CC weak interaction} \tag{5.2}$$

is given, in terms of the Bjorken variables x and y [123], by

$$\begin{aligned}\frac{d^2\sigma^{EM}}{dxdy} &= \frac{8M\varepsilon_f\pi\alpha^2}{Q^4}\left[\left(y^2x + \frac{m_l^2 y}{2\varepsilon_f M_N}\right)F_1^{eN}(x,Q^2)\right.\\ &+ \left.\left\{\left(1 - \frac{m_l^2}{4\varepsilon_f^2}\right) - \left(1 + \frac{M_N x}{2\varepsilon_f}\right)y\right\}F_2^{eN}(x,Q^2)\right],\end{aligned} \tag{5.3}$$

$$\begin{aligned}\frac{d^2\sigma^{\nu_l(\overline{\nu}_l)}}{dxdy} &= \frac{G_F^2 M_N E_{\nu(\overline{\nu})}}{\pi(1+Q^2/M_W^2)^2}\left[\left(y^2x + \frac{m_l^2 y}{2E_{\nu(\overline{\nu})}M_N}\right)F_1^{\nu N}(x,Q^2)\right.\\ &+ \left\{\left(1 - \frac{m_l^2}{4E_{\nu(\overline{\nu})}^2}\right) - \left(1 + \frac{M_N x}{2E_{\nu(\overline{\nu})}}\right)y\right\}F_2^{\nu N}(x,Q^2)\\ &\pm \left.\left\{xy\left(1 - \frac{y}{2}\right) - \frac{m_l^2 y}{4M_N E_{\nu(\overline{\nu})}}\right\}F_3^{\nu N}(x,Q^2)\right],\end{aligned} \tag{5.4}$$

where F_i^{eN} are the inelastic structure functions associated to the EM interaction and $F_i^{\nu N}$ are the ones related to CC weak interactions. In the latter, the $+(-)$ sign related to $F_3^{\nu N}$ corresponds to the neutrino (antineutrino) case. The x and y Bjorken variables are Lorentz invariant and are defined as

$$x \equiv \frac{\left|Q^2\right|}{2H \cdot Q}, \tag{5.5}$$

hence $x = 1$ corresponds to elastic scattering and $0 < x < 1$ to inelastic processes, and

$$y \equiv \frac{H \cdot Q}{H \cdot k_i} \xrightarrow[\text{in the lab. frame}]{} y = 1 - \frac{\varepsilon_f}{\varepsilon_i} \quad \text{(EM interaction)} \tag{5.6}$$

$$y \equiv \frac{H\cdot Q}{H\cdot k_{\nu(\overline{\nu})}} \xrightarrow[\text{in the lab. frame}]{} y = 1 - \frac{E_l}{E_{\nu(\overline{\nu})}} \quad \text{(weak interaction)}\,, \tag{5.7}$$

being $\varepsilon_i(E_{\nu(\overline{\nu})})$ and $\varepsilon_f(E_l)$ the initial and final lepton energies for the electromagnetic (weak) case and y the fractional energy loss of the incoming particle ($0 < y < 1$). The 4-momentum $H^\mu = (\overline{E}_h, \mathbf{h})$ is referred to the on-shell nucleon, where $\overline{E}_h$ and $\mathbf{h}$ are the on-shell energy and momentum.

With the aim of expressing the nuclear responses in terms of the longitudinal and transverse channels, the inelastic double differential cross section can also be expressed for the electromagnetic and weak interactions as

$$\frac{d\sigma^{EM}}{d\Omega_f d\varepsilon_f} = \frac{2\alpha^2}{Q^4}\frac{\varepsilon_f}{\varepsilon_i}\eta_{\mu\nu}W^{\mu\nu}\,, \tag{5.8}$$

$$\frac{d\sigma^{\nu_l(\overline{\nu}_l)}}{d\Omega_l dE_l} = \frac{k_l}{E_{\nu(\overline{\nu})}}\frac{G_F^2}{4\pi^2}\widetilde{\eta}_{\mu\nu}\widetilde{W}^{\mu\nu}\,, \tag{5.9}$$

where α is the fine structure constant, $\widetilde{\eta}_{\mu\nu}(\eta_{\mu\nu})$ is the leptonic tensor for the weak (electromagnetic) case as for the QE regime, and $\widetilde{W}^{\mu\nu}(W^{\mu\nu})$ is the inelastic hadronic tensor containing all of the nuclear structure and dynamics information.

Within the context of the RFG model, the inelastic nuclear tensor, integrating over the Fermi sea, can be written in the form

$$W^{\mu\nu}(\boldsymbol{q},\omega) = \frac{3\mathcal{N}}{4\pi k_F^3}\int dE_X \int_F d\boldsymbol{h}\frac{M_N}{\overline{E}_h}U^{\mu\nu}(H,Q,E_X)\delta(\omega + \overline{E}_h - E_X)\,, \tag{5.10}$$

where $\mathcal{N}$ is the number of nucleons and $\int_F d\boldsymbol{h} \equiv \int d\boldsymbol{h}\theta(k_F - h)$, k_F being the Fermi momentum. The symbol $\int dE_X$ stands for the integral over the energy of the inelastic final state ($E_X = \sqrt{\boldsymbol{p}_X^2 + W_X^2}$), having a total momentum $\boldsymbol{p}_X = \boldsymbol{h} + \boldsymbol{q}$. The most general expression for the inelastic single-nucleon hadronic tensor ($U^{\mu\nu}$) can be written as:

$$U^{\mu\nu} = -\left(g^{\mu\nu} + \frac{\kappa^\mu\kappa^\nu}{\kappa^2}\right)W_1 + \left(\eta^\mu - \frac{\eta\cdot\kappa}{\kappa^2}\kappa^\mu\right)\left(\eta^\nu - \frac{\eta\cdot\kappa}{\kappa^2}\kappa^\nu\right)W_2 \mp i\varepsilon^{\mu\nu\alpha\beta}\eta_\alpha\kappa_\beta W_3\,, \tag{5.11}$$

where we have employed the dimensionless variables

$$\begin{aligned}\kappa^\mu = \frac{Q^\mu}{2M_N} &= (\lambda,\boldsymbol{\kappa}) = \left(\frac{\omega}{2M_N},\frac{\boldsymbol{q}}{2M_N}\right), \quad \tau = \boldsymbol{q}^2 - \lambda^2 \\ \eta^\mu &= (\overline{\epsilon},\boldsymbol{\eta}) = \left(\frac{\overline{E}_h}{M_N},\frac{\boldsymbol{h}}{M_N}\right)\end{aligned} \tag{5.12}$$

and W_i are related to the generic inelastic structure functions F_i as:

$$M_N W_1 = F_1 \quad ; \quad \nu W_2 = F_2 \quad ; \quad x\nu W_3 = F_3\,, \tag{5.13}$$

where ν is a Lorentz invariant related to the energy lost by the incoming particle in the laboratory frame,

$$\nu = \frac{H\cdot Q}{M_N} \xrightarrow[\text{in the lab. frame}]{} \varepsilon_f - \varepsilon_i \equiv \omega\,. \tag{5.14}$$

We also define the dimensionless invariant mass as $\mu_X = \dfrac{W_X}{M_N}$. So we can express (5.10) as

$$W^{\mu\nu}(\kappa,\lambda) = \frac{3\mathcal{N}}{4\pi\eta_F^3}\int d\mu_X \int d\boldsymbol{\eta}\frac{\mu_X}{\overline{\epsilon}\epsilon_X}U^{\mu\nu}(\boldsymbol{\eta},\mu_X;\kappa,\lambda)\delta(2\lambda+\overline{\epsilon}-\epsilon_X)\theta(\eta_F-\eta)\,. \tag{5.15}$$

For on-shell nucleons, the structure functions W_i depend on two variables, the four-momentum transfer Q^2 and the invariant mass W_X of the final state reached by the nucleon, or, equivalently, the single-nucleon Bjorken variable

$$x = \frac{|Q^2|}{2H\cdot Q} = \frac{|Q^2|}{W_X^2 - M_N^2 - Q^2} = \frac{\tau}{\eta\cdot\kappa}\,. \tag{5.16}$$

In the formalism employed, it is necessary to introduce the inelasticity parameter ρ

$$\rho \equiv 1 + \frac{1}{4\tau}(\mu_X^2 - 1)\,, \tag{5.17}$$

where $\rho = 1$ corresponds to elastic scattering. Note that this parameter is related to the Bjorken scaling variable by the relation $\rho = 1/x$. In the following we will use ρ as argument of the inelastic structure functions.

Coming back to the expression (5.15) and performing the polar angular integration by means of the energy conserving δ function one gets

$$W^{\mu\nu}(\kappa,\lambda) = \frac{3\mathcal{N}\tau}{2\eta_F^3\kappa}\int_0^{2\pi}\frac{d\phi}{2\pi}\int_{\rho_1(\kappa,\lambda)}^{\rho_2(\kappa,\lambda)}d\rho\int_{\epsilon_0(\rho)}^{\epsilon_F}d\overline{\epsilon}\,U^{\mu\nu}(\overline{\epsilon},\theta_0,\rho;\kappa,\lambda)\,, \tag{5.18}$$

where

$$\cos\theta_0 = \frac{1}{\kappa\eta}(\lambda\overline{\epsilon} - \tau\rho)\,. \tag{5.19}$$

The condition $|\cos\theta_0| \le 1$ fixes the integration limit over $\overline{\epsilon}$,

$$\overline{\epsilon} \ge \epsilon_0(\rho) \equiv \kappa\sqrt{\frac{1}{\tau}+\rho^2} - \lambda\rho. \tag{5.20}$$

To evaluate the above integral is convenient to expand the four-vector η^μ (which is normalized to $\eta_\mu\eta^\mu = 1$) in the basis $a^\mu = (\kappa,0,0,\lambda)$, $\kappa^\mu = (\lambda,0,0,\kappa)$, $t_x^\mu = (0,1,0,0)$ and $t_y^\mu = (0,0,1,0)$, namely

$$\eta^\mu = \eta_k\kappa^\mu + \eta_a a^\mu + \eta_x t_x^\mu + \eta_y t_y^\mu\,, \tag{5.21}$$

with

$$\eta_k = \eta\cos\theta_0 = -\rho\,, \tag{5.22}$$

$$\eta_a = \frac{1}{\kappa}(\overline{\epsilon} + \lambda\rho)\,, \tag{5.23}$$

$$\eta_x = \eta\sin\theta_0\cos\phi\,, \tag{5.24}$$

$$\eta_y = \eta\sin\theta_0\sin\phi\,, \tag{5.25}$$

where the hadronic tensor can be written as follows:

$$\begin{aligned} W^{\mu\nu}(\kappa,\lambda) &= \frac{3\mathcal{N}\tau}{2\pi\eta_F^3\kappa}\int_0^{2\pi}\frac{d\phi}{2\pi}\int_{\rho_1(\kappa,\lambda)}^{\rho_2(\kappa,\lambda)}d\rho\int_{\epsilon_0(\rho)}^{\epsilon_F}d\overline{\epsilon}\Big[-W_1(\tau,\rho)\left(g^{\mu\nu}+\frac{\kappa^\mu\kappa^\nu}{\kappa^2}\right)\\ &+ W_2(\tau,\rho)(\kappa^\mu\kappa^\nu\rho^2 + X^{\mu\nu}) \mp W_3(\tau,\rho)i\varepsilon^{\mu\nu\alpha\beta}\eta_\alpha\kappa_\beta\Big]\,. \end{aligned} \tag{5.26}$$

Moreover, by requiring that $\epsilon_0(\rho) \leq \epsilon_F$ and that the resonance mass W_X is above the pion-production threshold, we obtain the following limits for the integration on μ_X and, subsequently, on ρ:

$$M_N + m_\pi \leq W_X \leq M_N + \omega - E_S\,, \tag{5.27}$$

$$\mu_X^{min} = 1 + \frac{m_\pi}{M_N}\,, \tag{5.28}$$

$$\mu_X^{max} = 1 + 2\lambda - \frac{E_S}{M_N}\,, \tag{5.29}$$

where E_S is the separation energy, that coincides with the previously defined energy shift (E_{shift}). Next, after integrating the tensor in Eq. (5.26) over ϕ and $\overline{\epsilon}$, we obtain

$$W_{inel}^{\mu\nu}(\kappa,\lambda) = \frac{3\mathcal{N}\tau}{2\eta_F^3\kappa}\int_{\rho_1(\kappa,\lambda)}^{\rho_2(\kappa,\lambda)} d\rho\,(\epsilon_F-\epsilon_0)\,\theta\,(\epsilon_F-\epsilon_0)\,U^{\mu\nu}(\kappa,\tau,\rho) \tag{5.30}$$

with

$$\begin{aligned} U^{\mu\nu}(\kappa,\tau,\rho) &= -\left[W_1(\tau,\rho)+\frac{1}{2}W_2(\tau,\rho)\mathcal{D}(\kappa,\tau,\rho)\right]\left(g^{\mu\nu}+\frac{\kappa^\mu\kappa^\nu}{\tau}\right) \\ &+ W_2(\tau,\rho)\left[1+\tau\rho^2+\frac{3}{2}\mathcal{D}(\kappa,\tau,\rho)\right]\frac{a^\mu a^\nu}{\tau} \\ &\mp W_3(\tau,\rho)\epsilon^{\mu\nu\alpha\beta}\left[\left(\frac{1}{2}(\epsilon_F+\epsilon_0)+\lambda\rho\right)\frac{a_\alpha\kappa_\beta}{\kappa}-\rho\kappa_\alpha\kappa_\beta\right]\,. \end{aligned} \tag{5.31}$$

Similarly to the QE case, we can also define an inelastic scaling variable dependent on the value of ρ (and hence μ_X)

$$\psi_X \equiv \frac{1}{\sqrt{\xi_F}}\frac{\lambda-\tau\rho}{\sqrt{(1+\lambda\rho)\tau+\kappa\sqrt{\tau(\tau\rho^2+1)}}}\,, \tag{5.32}$$

or, equivalently,

$$\psi_X \equiv (\lambda-\tau\rho)\sqrt{\frac{\epsilon_0(\rho)-1}{\epsilon_F-1}}\,. \tag{5.33}$$

In the previous expression we can introduce the relation

$$\epsilon_F - \epsilon_0 = \xi_F\,(1-\psi_X)^2 \tag{5.34}$$

and express the inelastic hadronic tensor as

$$W_{inel}^{\mu\nu}(\kappa,\lambda) = \frac{3\mathcal{N}\tau}{2\eta_F^3\kappa}\xi_F\int_{\rho_1(\kappa,\lambda)}^{\rho_2(\kappa,\lambda)} d\rho\left(1-\psi_X^2\right)\theta\left(1-\psi_X^2\right)U^{\mu\nu}(\kappa,\tau,\rho)\,. \tag{5.35}$$

Therefore, we can also estimate the different inelastic nuclear responses for electromagnetic (L and T) and weak interactions (CC, CL, LL, T and T') using the following relation

$$R_{inel}^{K}(\kappa,\tau) = \frac{3\mathcal{N}\tau}{2\eta_F^3\kappa}\xi_F\int_{\rho_1(\kappa,\lambda)}^{\rho_2(\kappa,\lambda)} d\rho\left(1-\psi_X^2\right)\theta\left(1-\psi_X^2\right)U^{K}(\kappa,\tau,\rho(\psi_X))\,, \tag{5.36}$$

where, similarly to the QE regime, we can define:

$$U^{L} = U^{CC} = U^{00} = \frac{\kappa^2}{\tau}\left[\left(1+\tau\rho^2\right)W_2(\tau,\rho) - W_1(\tau,\rho) + W_2(\tau,\rho)\mathcal{D}(\kappa,\tau,\rho)\right] \quad (5.37)$$

$$U^{LL} = U^{33} = \frac{\lambda^2}{\kappa^2}U^{00} \quad (5.38)$$

$$U^{CL} = -\frac{1}{2}\left(U^{03}+U^{30}\right) = -\frac{\lambda\kappa}{\kappa^2}U^{00} \quad (5.39)$$

$$U^{T} = U^{11}+U^{22} = 2W_1(\tau,\rho) + W_2(\tau,\rho)\mathcal{D}(\kappa,\tau,\rho) \quad (5.40)$$

$$U^{T'} = -\frac{i}{2}\left(U^{12}-U^{21}\right) = \pm\frac{\tau}{\kappa}\left[\frac{1}{2}(\epsilon_F+\epsilon_0)+\lambda\rho\right]W_3(\tau,\rho)\,, \quad (5.41)$$

where $\mathcal{D}$ is defined as:

$$\begin{aligned}\mathcal{D}(\kappa,\tau,\rho) &= \frac{1}{\epsilon_F-\epsilon_0(\rho)}\int_{\epsilon_0(\rho)}^{\epsilon_F} d\overline{\epsilon}\int_0^{2\pi}\frac{d\Phi}{2\pi}\left(\boldsymbol{\eta}\times\widehat{\boldsymbol{\kappa}}\right)^2 \\ &= \frac{\tau}{\kappa^2}\left\{\frac{1}{3}\left[\epsilon_F^2+\epsilon_F\epsilon_0(\rho)+\epsilon_0(\rho)^2\right]+\lambda\left[\epsilon_F+\epsilon_0(\rho)\right]+\lambda^2\right\}-(1+\tau) \\ &+ (\rho-1)\frac{\tau}{\kappa^2}\left\{\lambda\left[\epsilon_F+\epsilon_0(\rho)\right]-\tau(\rho+1)\right\} \\ &= \xi_F\left(1-\psi_X^2\right)\left[1+\xi_F\psi_X^2-\frac{\lambda}{\kappa}\psi_X\sqrt{\xi_F\left(2+\xi_F\psi_X^2\right)}+\frac{\tau}{3\kappa^2}\xi_F\left(1-\psi_X^2\right)\right]\,.\end{aligned} \quad (5.42)$$

As previously discussed, and for a fixed value of the invariant mass μ_X, the RFG yields a scaling function

$$f^{RFG}(\psi'_X) = f_L^{RFG}(\psi'_X) = f_T^{RFG}(\psi'_X) = \frac{3}{4}(1-\psi'^2_X)\theta(1-\psi'^2_X)\,. \quad (5.43)$$

where ψ'_X also contains the corresponding energy shift, E_{shift}, as for the QE regime,

$$\psi'_X \equiv \frac{1}{\sqrt{\xi_F}}\frac{\lambda'-\tau'\rho'}{\sqrt{(1+\lambda'\rho')\tau'+\kappa\sqrt{\tau'(\tau'\rho'^2+1)}}}\,, \quad (5.44)$$

with ρ' defined as

$$\rho' \equiv \frac{2H\cdot Q}{|Q^2|} = 1+\frac{1}{4\tau'}\left({\mu'_X}^2-1\right) \quad ; \quad \mu'_X = \frac{W'_X}{M_N} = \frac{1}{M_N}\left(\omega'+\overline{E}_h\right)^2-\mathbf{p}_X^2\,. \quad (5.45)$$

Then, we can indentify in Eq. (5.36), the term which englobes all the nuclear dependence of the interaction, f^{RFG}, and replace it by the one arising from the SuSA or SuSAv2 models (f^{model}), in a similar way as done for the QE regime in Chapter 3. Therefore, we calculate the inelastic nuclear responses for each specific model (RFG, SuSA or SuSAv2) as

$$R^K_{inel}(\kappa,\tau) = \frac{\mathcal{N}}{\eta_F^3\kappa}\xi_F\int_{\mu_X^{min}}^{\mu_X^{max}} d\mu_X\,\mu_X\,f^{model}(\psi'_X)U^K\,. \quad (5.46)$$

The previous formalism allows for a complete description of the inelastic cross sections on lepton-nucleus interactions where the nuclear effects are included by means of the SuSAv2 model.

The procedure is similar to that applied for the QE regime (see Chapter 3), keeping the same functional form for the RMF and RPWIA scaling functions (3.89) but using a different scaling variable (ψ'_X) and a different q_0 transition parameter for the blending function (3.91). The specific details about the application of the SuSAv2 model for the inelastic spectrum as well as the estimation of the q_0 transition parameter between the RMF and RPWIA prescriptions for both quasielastic and inelastic regimes will be presented in Chapter 6, where a detailed analysis of the existing (e,e') data and the 2p-2h MEC contributions is also provided.

5.3 Inelastic structure functions

In this Section, the properties of single-nucleon inelastic structure functions for protons and neutrons are analyzed. The specific details about the existing parametrizations and empirical models are detailed in Section 5.4.

As defined in Section 5.2, the inelastic structure functions F_1, F_2 and F_3 depend on two variables Q^2 and x, or, equivalently, τ and ρ. To determine these inelastic functions for given Q^2 and x, measurements of the differential cross section at different scattering angles and incoming electron beam energies are needed. This will help in obtaining phenomenological fits of the single-nucleon inelastic structure functions for protons and neutrons. Specific information on the proton inelastic form factors can be obtained from the analysis of electron-proton (ep) and electron-deuteron (eD) scattering processes. On the contrary, the neutron case is much harder as no spedific electron-neutron (en) processes are available. Thus, information on neutron inelastic form factors relies directly on the joint analysis of the two scattering processes mentioned above, namely, ep and eD. Experimentally it is observed that both F_1 and F_2 are almost independent of Q^2 in the limit of high Q^2 and ν. This is known as Bjorken x-scaling [123]

$$F_{1,2}(x, Q^2) \to F_{1,2}(x)\,. \tag{5.47}$$

Under the previous kinematical conditions, a relationship between F_1 and F_2 is given by the Callan-Gross relation [124]

$$F_2(x) = 2xF_1(x)\,, \tag{5.48}$$

originally based on the parton model. Some violation effects on the Callan-Gross relation are related to second order QCD corrections [125, 126], which appear at x approaching zero, *i.e.* in the highly deep-inelastic region, as well as to mesonic contributions in the nuclear medium. The violation due to mesonic and other nuclear effects are shown to be noticeable only in the region of low x and Q^2 [127] where the inelastic structure functions are very reduced. Violation of Callan-Gross relation in nuclei is of current interest in ongoing experiments at JLab [128, 129], where the measurements of F_1 and F_2 on nuclear targets will provide important information on this subject [130]. Both the Bjorken Scaling and the Callan-Gross relationship can be explained assuming that DIS is dominated by the scattering of a single virtual photon (boson) from a point-like quark within the proton (see Fig. 5.2).

At very high kinematics where nucleon resonance structures are not substantially relevant, the parton distribution functions arising from pQCD (perturbative QCD) provide a proper representation of the inelastic structure functions. The range of validity of this approach will be discussed in Section 5.4.4.

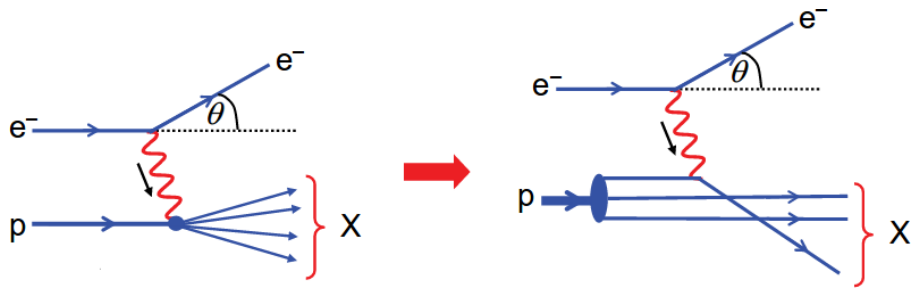

Figure 5.2: DIS process for electromagnetic e-p reactions described in terms of inelastic structure functions (left panel) and of the quark-parton model (right panel).

5.3.1 Extension to the weak sector

The description of the deep-inelastic regime for weak interactions implies the analysis of an additional structure function, $F_3(W_3)$, related to the parity violating contribution associated to the $V-A$ interference. An accurate determination of this weak function is hard to achieve from neutrino experiments as well as from parity-violating electron scattering [131, 132] due to the large uncertainties associated to the cross section measurements. Nevertheless, within the quark-parton model, we can establish a relationship among the electromagnetic and weak structure functions and between F_2 and F_3 [74, 133, 134]. This is based on the assumption that the corresponding structure functions W_i can be written in terms of quark Q and antiquark $\overline{Q}$ distributions [135, 136]

$$F_2 = \nu W_2 = Q + \overline{Q} \tag{5.49}$$

$$F_3 = x\nu W_3 = Q - \overline{Q} \tag{5.50}$$

and, hence,

$$x\nu W_3 = \nu W_2 - 2\overline{Q}\,. \tag{5.51}$$

For electron scattering, the isoscalar F_2 structure function of the nucleon, defined as the average of the proton and neutron structure functions, is given (at leading order in α_s and for three flavors) by

$$F_2^{eN} = \frac{1}{2}\left(F_2^{ep} + F_2^{en}\right) = \frac{5x}{18}\left(u + \overline{u} + d + \overline{d}\right) + \frac{x}{9}\left(s + \overline{s}\right)\,, \tag{5.52}$$

where $u(\overline{u}), d(\overline{d})$ and $s(\overline{s})$ are the distributions for the up, down and strange quarks (antiquarks), respectively. The quark distributions are defined to be those in the proton and the factors 5/18 and 1/9 arise from the squares of the quark charges. For neutrino scattering, the corresponding F_2 structure function is given by

$$F_2^{\nu N} = x(u + \overline{u} + d + \overline{d} + s + \overline{s})\,, \tag{5.53}$$

where quark charges are not considered. In the moderate and large-x region, where strange quarks are suppressed, the weak and electromagnetic F_2 structure functions approximately satisfy,

$$F_2^{eN} \approx \frac{5x}{18}\left(u + \overline{u} + d + \overline{d}\right) \approx \frac{5}{18}F_2^{\nu N}\,. \tag{5.54}$$

Under this assumption, which has been analyzed in connection with experimental results [135, 137–139], one can readily obtain the weak structure functions from the existing parametrization of the electromagnetic structure functions and the antiquark distribution.[1]

[1] In this work, the inelastic cross sections are only calculated and compared with data for electromagnetic reactions. Their extension to the weak sector and the construction of the appropriate isoscalar and isovector contributions needed for CC and NC neutrino reactions will be accounted for in further works.

5.4 Parametrization of the inelastic structure functions

In this section, we analyze two different parametrizations of the inelastic structure functions and a Parton Distribution Function (PDF) model, showing their capability to reproduce (e,e') data at intermediate kinematics for the inelastic regime.

5.4.1 Bodek-Ritchie parametrization

This approach is based on phenomenological fits of the single-nucleon inelastic structure functions W_1 and W_2 for ep and en, being the latter extracted from deuteron data. The Bodek-Ritchie parametrization is a general fit of Refs. [133, 134, 140, 141], which describes both the deep inelastic and resonance regions, covering the entire inelastic spectrum. The parametrization fits the SLAC data published in [140], covering a $|Q^2|$ range from 0.1 to 30 GeV^2, and including scaling violations in terms of a modified scaling variable ω_w. The structure function W_2 is described by

$$\nu W_2^{ep(en)}(\nu,Q^2) = B(W_X,Q^2)g(\omega_w)\omega_w/\omega\,, \tag{5.55}$$

$$g(\omega_w) = \sum_{n=3}^{7} C_n(1-1/\omega_w)^n\,, \tag{5.56}$$

$$\omega_w = \frac{2M_N\nu + a^2}{Q^2+b^2}\,. \tag{5.57}$$

The modulating function $B(W_X,Q)$ contains 12 parameters representing the masses, widths, and amplitudes of the cross section for electroproduction of the four most prominent nucleon resonances, and eight parameters representing the W_X dependence of the low-W_X nonresonant contribution and single-pion production threshold. The modulating function is close to unity in the deep-inelastic region ($W_X > 2$ GeV). The rest of parameters are defined in [133] where a and b are the same for proton (W_2^{ep}) and neutron (W_2^{en}) and the C_n coefficients are different for protons and neutrons. The W_1^{ep} and W_1^{en} structure functions can be deduced from the Callan-Gross relation (5.48). The W_3 functions, related to VA interference, are obtained using the relation (5.51) with the antiquark distribution, $\overline{Q}$, given by

$$\overline{Q}(x,Q^2) = \frac{1}{2}\left(1-\frac{1}{\omega_w}\right)^7 B(W_X,Q^2)g(0)\frac{\omega_w}{\omega}\,. \tag{5.58}$$

The different W_i functions for protons and neutrons within the Bodek-Ritchie parametrization will be shown in 5.4.4 in comparison with other parametrizations.

5.4.2 Bosted-Christy parametrization

Although the Bodek-Ritchie [133] parametrization has been widely used for the analysis of the highly-inelastic scattering region [142], in recent years new studies, both theoretical and experimental, of the nucleon structure functions in the resonance region have been performed, indicating the need for more sophisticated parametrizations. The kinematical region where nucleon resonances contribute is essential for the analysis of (e,e') data and pion production results from inclusive neutrino measurements. Therefore, it is more convenient to employ more actual expressions for $W_{1,2}^{ep(en)}$. In this sense, the Bosted-Christy (B-C) parametrization for the proton [143] and neutron [144] structure functions seems to reproduce better the electromagnetic behavior in the resonance region.

This approach is based on an empirical fit to describe the measurements of inclusive inelastic electron-proton and electron-deuteron cross sections in the kinematic range of four-momentum transfer $0 \leq |Q^2| < 8$ GeV^2 and final state invariant mass $1.1 < W_X < 3.1$ GeV, thus starting roughly from the pion production region to the highly-inelastic region. The fit is constrained by the high precision longitudinal and transverse (L/T) separated cross section measurements from JLab Hall C [145].

Compared to previous fits, it covers a wider kinematic range, fits both transverse and longitudinal cross sections, and features smooth transitions to the photoproduction data at $Q^2 = 0$ and DIS data at high $|Q^2|$ and W_X. At the same time, it provides an excellent description of the resonant structures seen in inclusive (e, e') cross sections. As it will be shown in 5.4.4, its agreement with data in the region of the Δ-peak within the SuSAv2 model is better than using the previous Bodek-Ritchie parametrization.

5.4.3 PDF model: GRV98

The Glück-Reya-Vogt GRV98 model [146] employs effective leading order (LO) Parton Distribution Functions for quarks and antiquarks to get the inelastic structure functions F_1, F_2 and F_3. In this thesis, we use a recent update [147] designed for both inelastic neutrino- and electron-nucleon scattering cross sections. The model describes existing inelastic neutrino-nucleon scattering measurements and has been developed to analyze neutrino oscillation experiments in the few GeV region. The PDFs are extracted from global fits to various sets of deep inelastic scattering data at high energies and high $|Q^2|$, where non-perturbative QCD effects are negligible. These effects are relevant for lower kinematic regions. In this sense, an scaling variable $(\xi_w(x, Q^2))$ is employed to construct effective LO PDFs that account for the contributions from target mass corrections, non-perturbative QCD effects, and higher order QCD terms. The non-perturbative effects from spectator quarks are required to be considered for $|Q^2| < 1$ GeV^2. These corrections together with effects from low energy scattering data are parametrized and included in the description. This model also accounts for nucleonic resonances and includes photoproducion data above the $\Delta(1232)$.

In general, the model gives a reasonable average cross section in the resonance region and beyond as shown in [147] but it seems to be inadequate to describe inelastic (e, e') data at low-intermediate kinematics, below $|Q^2| < 1$ GeV^2. Regarding this, we show in Section 5.4.4 that the GRV98 prescription only matches the empirical Bosted-Christy and Bodek-Ritchie structure functions, based on fits of electron scattering data, at $|Q^2| \gtrsim 5$ GeV^2.

5.4.4 Comparison of the different parametrizations

Next, we present a comparison of the different parametrizations for the single-nucleon inelastic structure functions described above, also confronting them with (e, e') experimental data in the inelastic regime.

The electromagnetic inelastic structure functions for protons and neutrons $W_{1,2}^{ep(en)}$ are displayed versus the Bjorken scaling variable x in Figure 5.3. The comparison is carried out for the Bodek-Ritchie and Bosted-Christy parametrizations as well as for the GRV98 PDFs prescription from low to high-Q^2 values. As observed, the GRV98 PDFs produces an average of the inelastic structure functions through the parton distribution functions whereas the Bodek-Ritchie and

Bosted-Christy parametrizations, based on phenomenological fits of the structure functions, reproduce in a more realistic way the resonance structures observed in *ep* and *ed* reactions.

The three models appear to be similar at $|Q^2|$ above 5 GeV^2 for low x values where DIS processes dominate whereas some minor differences appear as x gets closer to 1, *i.e.*, where resonance effects are more significant. On the contrary, the differences among these parametrizations increase when moving to lower $|Q^2|$ values where resonant contributions are more relevant in the entire x range, even at low x values. Indeed, at $|Q^2| = 1$ GeV^2, the GRV98 is roughly an average of the empirical Bodek-Ritchie and Bosted-Christy fits but does not reproduce the resonant structures at all. The comparison at the lowest $|Q^2|$ values produces the most diverging picture between the empirical fits and the GRV98 PDFs model. Therefore, its applicability at energies of relevance for current neutrino experiments is rather questionable.

Focusing on the empirical fits, we can observe small differences between the proton structure functions $W_{1,2}^{ep}$ for the Bodek-Ritchie and Bosted-Christy parametrizations (see Fig. 5.3), being the latter a bit larger at low $|Q^2|$ and high x. Concerning the neutron structure functions, $W_{1,2}^{en}$, they are significantly greater at lower $|Q^2|$ and large x for the Bosted-Christy fit. Although, in general, the neutron structure functions remain below the proton ones, the opposite occurs for the Bosted-Christy parametrization at the lowest $|Q^2|$ values. All these differences between both parametrizations may be due to the more accurate analysis of the resonances included in the Bosted-Christy fit as well as to the different procedures to disentangle the neutron structure functions from the proton and deuteron ones.

Similar comments also apply to Fig. 5.4, where the sum of proton and neutron contributions are shown for F_2^{eN} and F_3^{eN} within the Bosted-Christy and Bodek-Ritchie fits. The antiquark distribution ($\overline{Q}$) obtained through the procedure described in Section 5.4.1 (see also Ref. [133]), is also displayed. As can be noticed, the antiquark distribution is more relevant at $|Q^2|$<1 GeV^2 and low x values, thus implying that the main differences between the F_3 and F_2 functions appear at these kinematics. In Fig. 5.4, the ω dependence with x is also displayed, showing how ω increases as x tends to lower values. Regarding the Bosted-Christy approach, some divergences appear at very low x for higher $|Q^2|$ values. Nevertheless, they correspond to the highly-inelastic regime and extremely high ω, which, in general, corresponds to kinematically forbidden regions.

The comparison of the three parametrizations with (e, e') data is shown in Fig. 5.5 for two representative cases at intermediate kinematics where the QE and Δ peaks are easily recognizable. At the beginning of the highly-inelastic region, *i.e.* large ω values, where inelastic structure functions are more similar (see Fig. 5.3), the three models tend to be closer. It can be also noticed that the GRV98 PDFs overstimate the experimental data in the Δ-resonance region. At the same time, its contribution in the "dip" region between the QE and the Δ peaks is too large in such a way that the total result, after considering QE and 2p-2h MEC contributions, would clearly overestimate the data. On the contrary, the Bodek-Ritchie parametrization underestimates the Δ region as well as the beginning of the highly-inelastic regime which may be in connection with its poorer description of the resonance structures with respect to the Bosted-Christy one. As commented for Figs. 5.3 and 5.4, the larger Bosted-Christy structure functions result here in an increased inelastic cross section. At the same time, the accurate inclusion of resonances in this parametrization allows for a better description of the (e, e') data in the Δ-peak region without contributing remarkably to the "dip" region. As can be deduced from Fig. 5.4, the differences between the empirical fits decrease as going deeper into the inelastic regime, *i.e.*, larger ω values.

Therefore, on the basis of the previous analysis, the Bosted-Christy parametrization emerges as the most appropriate approach for the analysis of the inelastic regime. In this sense, the reference inelastic structure functions F_i to be employed in our theoretical description are shown in Fig. 5.6.

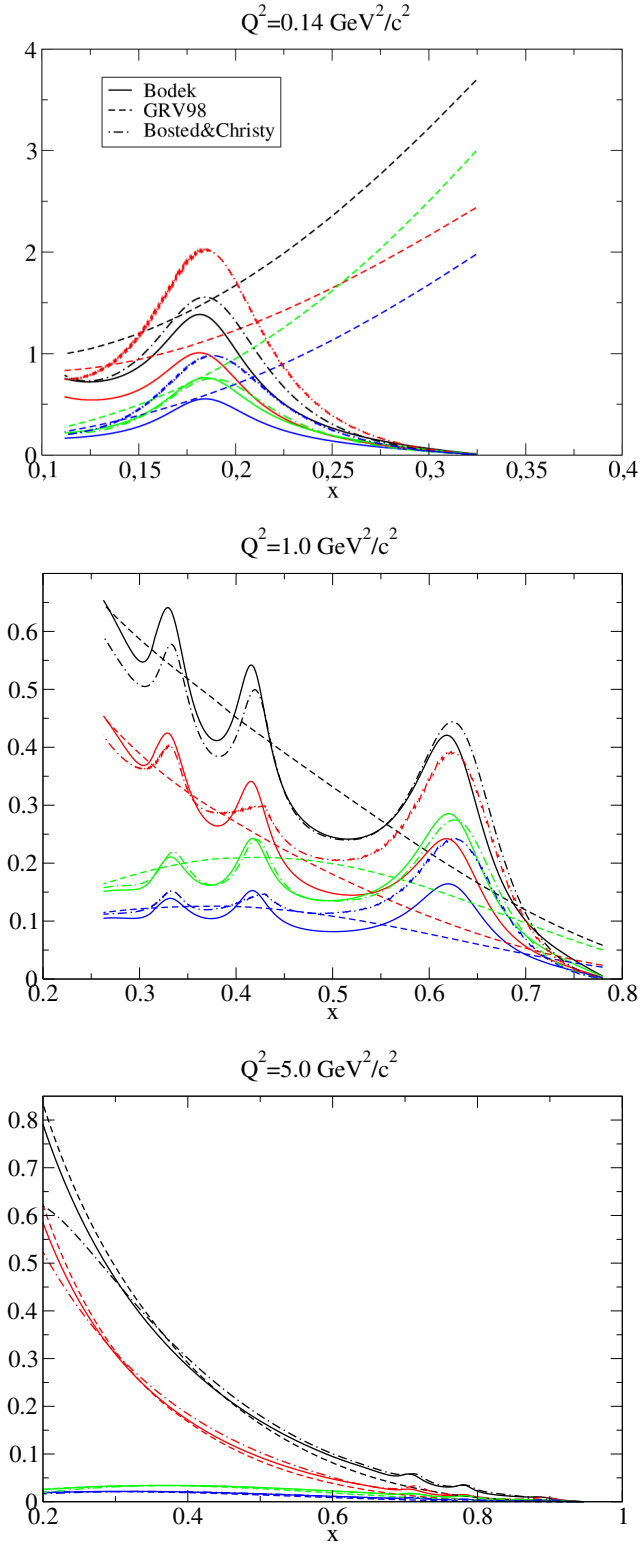

Figure 5.3: Inelastic structure functions W_1^{ep} (black lines), W_1^{en} (red lines), W_2^{ep} (green lines), W_2^{en} (blue lines) in terms of x for the Bodek-Ritchie parametrization (solid lines), Bosted-Christy parametrization (dot-dashed lines) and GRV98 PDFs (dashed lines) at $Q^2 = 0.14, 1.0$ and 5.0 GeV^2.

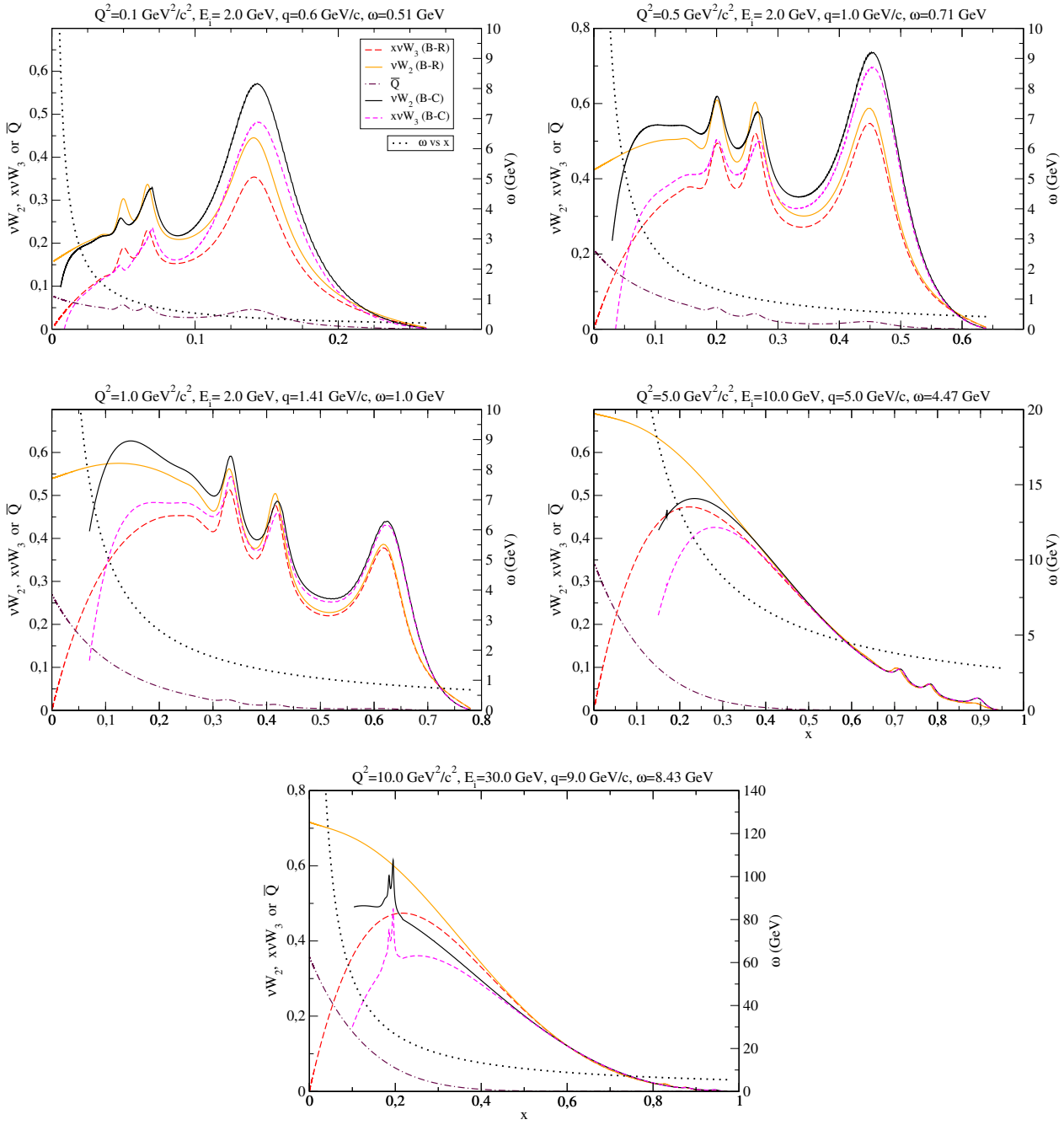

Figure 5.4: Comparison of the inelastic structure functions $F_2^{eN} = \nu W_2^{eN} = \nu W_2^{en} + \nu W_2^{ep}$ and $F_3^{eN} = x\nu W_3^{eN} = x\nu W_3^{en} + x\nu W_3^{ep}$ for the Bodek-Ritchie (B-R) and Bosted-Chisty (B-C) parametrizations. The antiquark distribution, $\overline{Q}^{eN} = \overline{Q}^{en} + \overline{Q}^{ep}$, is also shown. The ω dependence with x is also displayed.

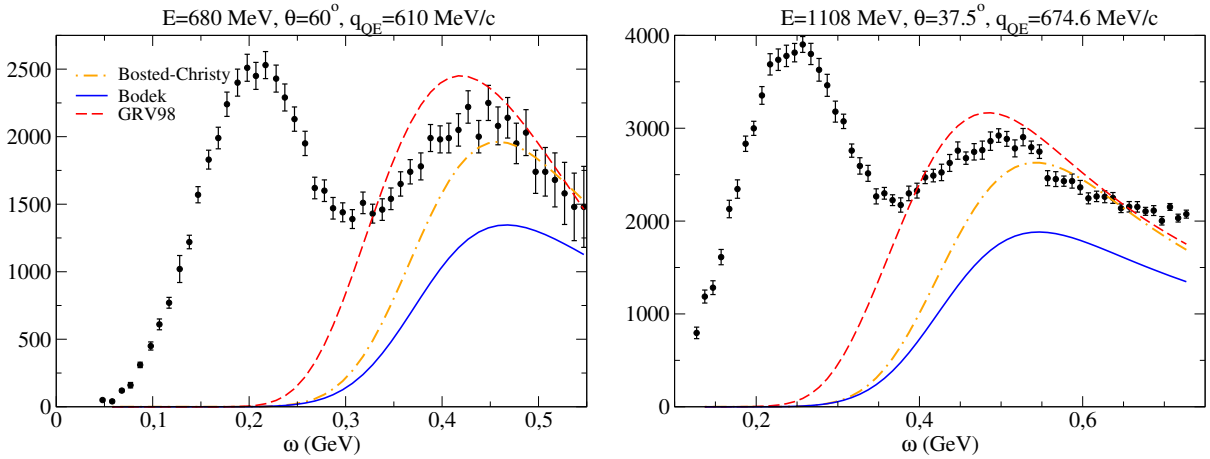

Figure 5.5: Comparison of inclusive $^{12}C(e,e')$ double differential cross sections and predictions for the inelastic regime of the Bodek-Ritchie parametrization (solid lines), Bosted-Christy parametrization (dot-dashed lines) and GRV98 PDFs (dashed lines) at different kinematics (incident electron beam and scattering angle) in terms of the energy transferred to the nucleus (ω). Experimental data taken from [100, 101]. The y-axis represents $d^2\sigma/d\Omega/d\omega$ in nb/GeV/sr. The value of q at the QE peak (q_{QE}) is shown as reference.

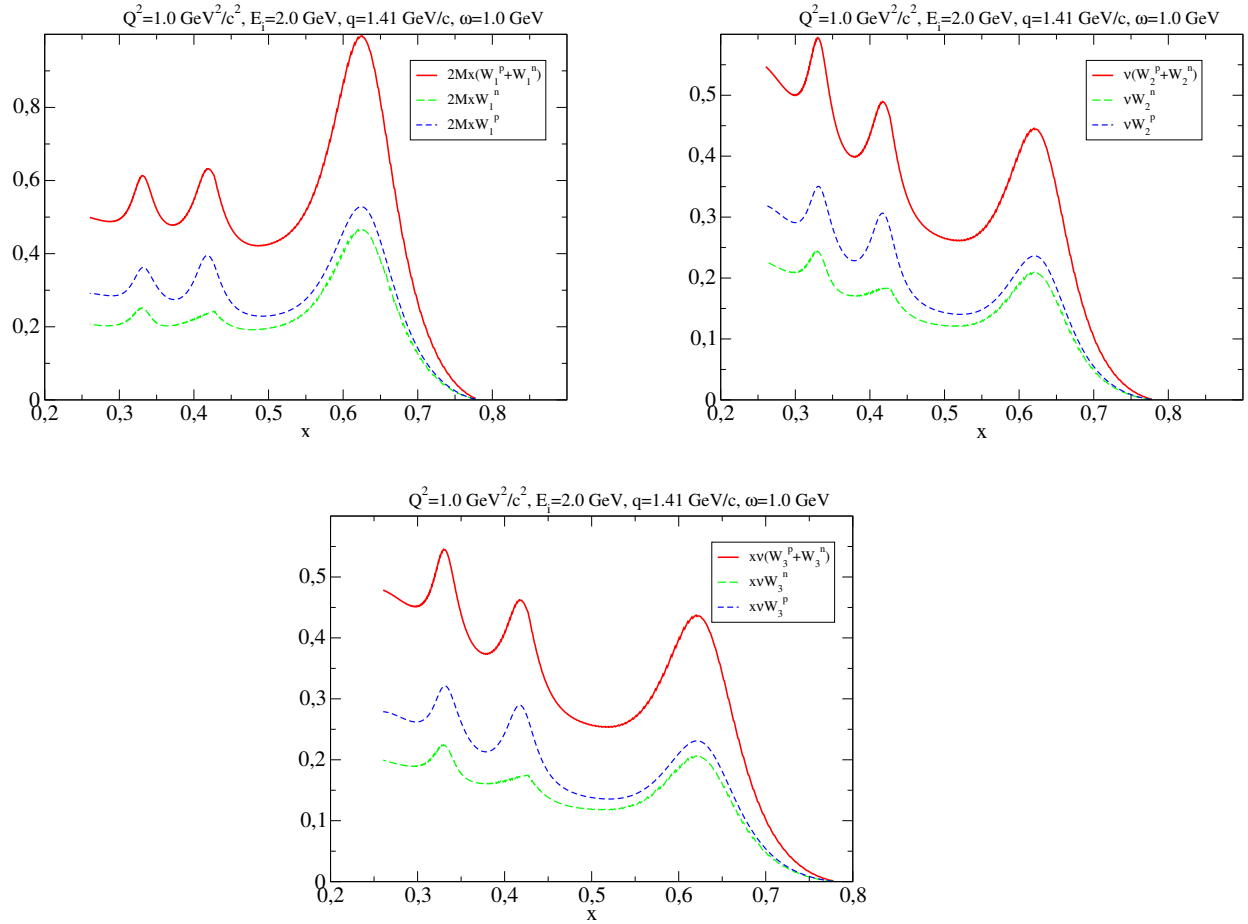

Figure 5.6: Reference inelastic structure functions $F_1 = 2MxW_1$ (top panel), $F_2 = \nu W_2$ (mid panel) and $F_3 = x\nu W_3$ (bottom panel) for protons and neutrons and the sum of both contributions at $Q^2 = 1$ GeV^2. The calculations are performed within the Bosted-Christy parametrization.

Chapter 6

Analysis of inclusive electron scattering within the SuSAv2-MEC model

Although the focus in this PhD thesis concerns the study of CC neutrno-nucleus scattering processes, it is essential first to test our theoretical predictions against the available inclusive electron scattering data. This was already shown in Chapter 3 but restricting ourselves to the pure QE regime. In this chapter the SuSAv2 model is extended to include the complete inelastic spectrum — resonant, nonresonant and deep inelastic scattering — described in Chapter 5. We also consider the impact of 2p-2h meson-exchange currents following the procedure detailed in Chapter 4. The predictions of the full SuSAv2-MEC model are first compared with the existing inclusive ^{12}C(e,e') data and later also applied to other nuclei. The capability of the model to describe electron scattering data with accuracy gives us confidence in its subsequent extension, and validity, when applied to recent neutrino oscillation experiments. This subject will be addressed in Chapter **??**.

6.1 SuSAv2 model for quasielastic and inelastic regimes

In Chapter 3 a very detailed description of the SuSAv2 model was given, that, as known, incorporates the predictions from the RMF theory and a transition to the RPWIA model at high values of the momentum transfer. This transition between both RMF and RPWIA regimes is governed by a blending function whose explicit expression is also given in Chapter 3 (see Eqs. 3.89—3.91 for details). Here our interest is to extend the SuSAv2 model to the inelastic regime so its predictions can be compared with data covering the entire energy spectrum. This requires to have a good control of the transition parameters (q_0, ω_0) that determine the relative strength of the RMF and RPWIA responses, and how the transition between them evolves as the transfer momentum varies. Accordingly, the transition parameter, q_0, is expected to increase with q in such a way that the RMF contribution will be dominant at low kinematics whereas the RPWIA one starts to be relevant at higher energies. Therefore we introduce a dependence of the parameter q_0 on the momentum transfer q that determines the relative RMF and RPWIA contributions at different kinematics. Moreover, this transition occurs in a region of width ω_0, which is fixed at 200 MeV.

The particular procedure to determine the q_0-behavior with q is in accordance to the best fit to a large amount of (e,e') experimental data on ^{12}C in a wide kinematical region, covering from low to high q-values (q: 239 − 3432 MeV/c). For this analysis, ^{12}C is employed as target reference due to the ample variety of existing data for electron scattering as well as its relevance for neutrino oscillation experiments. The method applied to determine the RMF/RPWIA transition in the SuSAv2 model in both QE and inelastic regimes is based on a reduced-χ^2 analysis of the data sets.

As previously mentioned, the transition parameter, q_0, must exhibit a dependence on the particular kinematics involved in such a way that at higher energies, which imply higher momentum transfers, the RPWIA contribution is more relevant than the RMF one, whereas the opposite occurs at lower energies. With these assumptions, we perform a χ^2 analysis of the electron-nucleus experimental data which is first focused on the QE region (q_0^{QE}) and after that extended to the inelastic domain (q_0^{inel}). In the whole analysis we take into account the so-called "SuSAv2-MEC" model for both QE and inelastic regimes as well as the 2p-2h MEC calculations. After analyzing the experimental data set, we get the q_0^{QE} and q_0^{inel} parameters as functions of q. Figure 6.1 illustrates the behavior of both parameters, q_0^{QE} (top and middle panels) and q_0^{inel} (bottom). The data points and their error bands represent the values of the parameters that best fit the data at different kinematics (within a $\sim 20\%$ in the χ^2 minimum). Each data point is referred to a particular set of data for a fixed incident energy (E_i) and scattering angle (θ_e) and is characterized in terms of the respective momentum transfer at the QE peak (q_{QE}) and an averaged value of q in the inelastic region. As shown, q_0^{QE} increases moderately with q at low to intermediate values whereas the slope goes up significantly at higher kinematics ($q \gtrsim 700$ MeV/c). This implies that the RMF contribution, even being reduced at these high kinematics, is still necessary to describe data satisfactorily.

This suggests the following parametrization:

$$q_0^{QE}(q) = \begin{cases} A + Bq, & q < q_1 \\ C + Dq, & q > q_1 \end{cases} \tag{6.1}$$

with $q_1 = 700$ MeV/c, $A = 377.629$ MeV/c, $B = 0.407$, $C = -5.322$ MeV/c and $D = 0.968$. Imposing continuity of the above function we are left with three free parameters, A, B and C.

A similar parametrization is found for $q_0^{inel}(q)$, but in this case only one linear function is used for the whole region of q explored,

$$q_0^{inel}(q) = A' + B'q \tag{6.2}$$

with $A' = 494.439$ MeV/c and $B' = 0.706$.

Finally, it is also worth mentioning that an even better agreement with the (e, e') data could be achieved by employing a non-linear fit of the q_0 parameters as well as including a dependence on the incident energy (E_i) or the scattering angle (θ_e) in the transition parameters (q_0, ω_0); however, the simpler assumptions made in this work are felt to be adequate for our purposes.

6.2 Analysis of (e, e') experimental data

In this section we present the SuSAv2-MEC results for ^{12}C(e, e') cross sections. We adopt the Bosted and Christy parametrization for the single-nucleon inelastic structure functions [143, 144] which describes DIS, resonant and non-resonant regions as detailed in Chapter 5. For the QE regime, we employ the electromagnetic form factors of the extended Gari-Krumpelmann (GKex) model [148–150] which improves the commonly used Galster parametrization for $|Q^2| > 1$ GeV^2 (see Chapter 2 for details). The sensitivity of the QE results to the different parametrizations of the nucleon form factors has been discussed in [19] and it will be addressed in Chapter 7. Additionally, for the Fermi momentum we employ the values shown in Table 3.1, namely $k_F = 228$ MeV/c for ^{12}C.

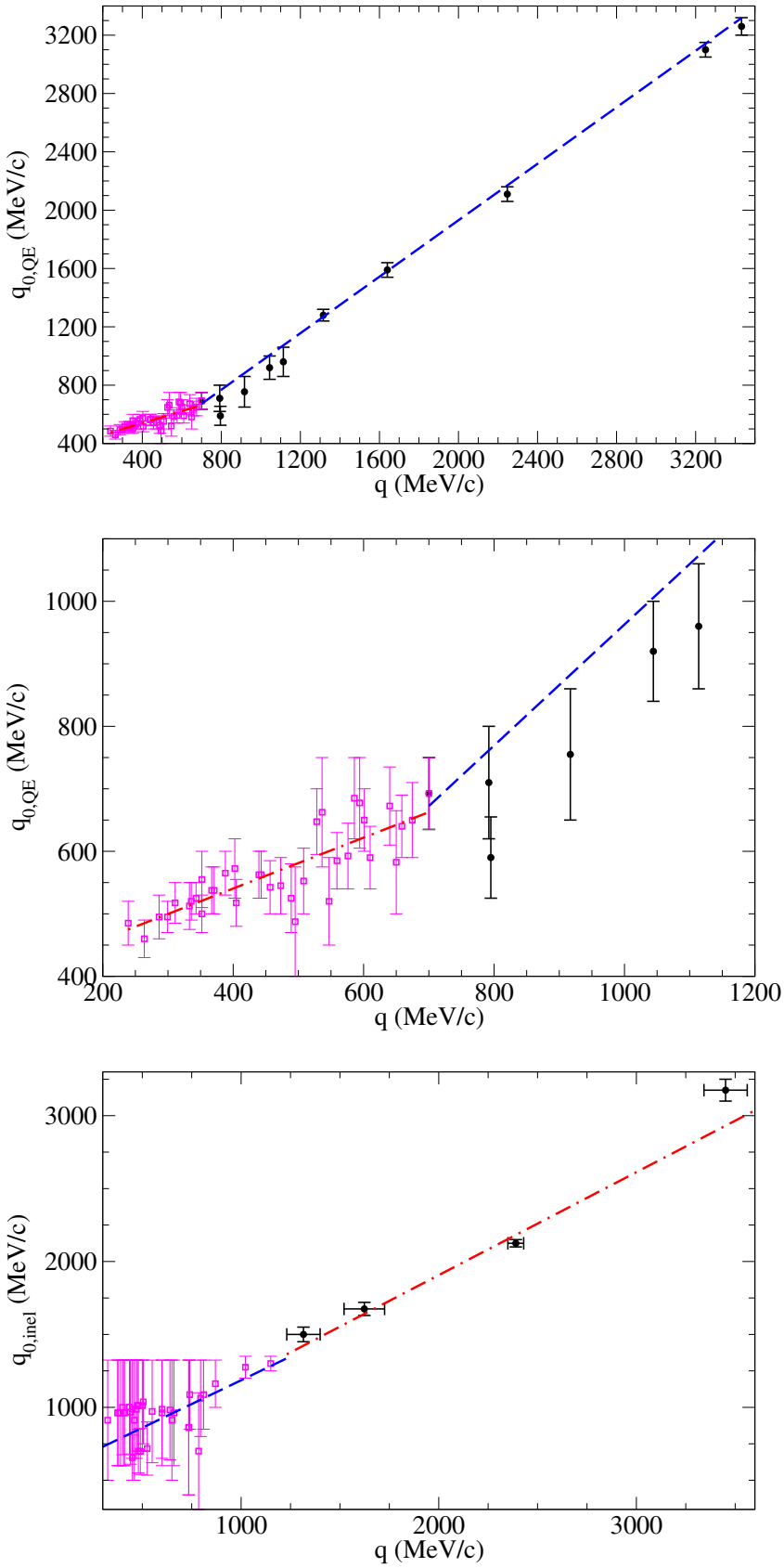

Figure 6.1: Parametrization of q_0^{QE} in terms of q (top and middle panels). Parametrization of q_0^{inel} in terms of q (bottom panel). Data points represent the q_0 values that best fit each case where the momentum transfer at the QE peak (q_{QE}) is considered for q_0^{QE} and an averaged value of q in the inelastic region is considered for q_0^{inel}.

6.2.1 Experimental (e, e') cross sections on ^{12}C

In this section we present the double differential inclusive ^{12}C(e, e') cross section versus the energy transferred to the nucleus (ω), confronting our predictions with the available experimental data [100, 101]. Results are shown in Figs. 6.2, 6.3 and 6.4: in each panel we show the three separate contributions to the inclusive cross section, namely, QE, 2p-2h MEC and inelastic.

The comparisons are carried out for a very wide range of kinematics from low-intermediate energies to the highly-inelastic regime. Each panel corresponds to fixed values of the incident electron energy (E_i) and the scattering angle (θ_e): E_i : 280 – 4045 MeV and θ_e : 12^o – 145^o. To make it easier to discuss the results to follow, the ordering of the panels has been done according to the corresponding value for the momentum transfer at the quasielastic peak, denoted as q_{QE}. This gives us the value of q where the maximum in the QE peak appears. However, it is important to point out that as ω varies, q also varies. This is of relevance to estimate the value of the RMF/RPWIA transition parameter q_0 in both regimes, QE and inelastic. Hence we also include in each panel a curve that shows how the momentum transfer changes with ω. Results illustrate that at very forward angles the value of q increases with the energy transfer, whereas this trend tends to reverse at backward angles. Thus for electrons scattered backwards, the q-values corresponding to the inelastic process are smaller than those ascribed to the QE regime. However, in this situation the cross section is clearly dominated by the QE peak. On the contrary, at very forward kinematics the inelastic process takes place at larger values of q. Thus, the two regimes, QE and inelastic, overlap strongly, the inelastic processes being the main ones responsible for the large cross sections observed at increasing values of ω. Finally, for intermediate scattering angles the behavior of q exhibits a region where it decreases (QE-dominated process), whereas for higher ω (inelastic regime) the behavior of q reverses and starts to go up. In these situations the QE peak, although significantly overlapped with the inelastic contributions, is clearly visible even for very high electron energies.

The systematic analysis presented in Figs. 6.2, 6.3 and 6.4 demonstrates that the present SuSAv2-MEC model provides a very successful description of the whole set of (e, e') data, validating the reliability of our predictions. The positions, widths and heights of the QE peak are nicely reproduced by the model taking into account not only the QE domain but also the contributions given by the 2p-2h MEC terms (around $\sim 10 - 15\%$). Only at very particular kinematics, *i.e.,* $\theta_e = 145^o$ and $E_i = 320$ (360) MeV (Fig. 6.3) and 440 MeV (Fig. 6.4), does the model clearly underpredict data at the QE peak as also observed in [151]. However, notice that the dip region is successfully reproduced by the theory. Moreover, the remaining kinematics corresponding to very backward angles, $E_i = 560$ MeV, $\theta_e = 145^o$ (Fig. 6.4), is well described by the model with a very high tail ascribed to the inelastic processes. Another kinematical situation whose discussion can be of interest concerns the scattering angle $\theta_e = 37.5^o$. Four cases are shown, one in Fig. 6.3 and three in Fig. 6.4. As noted, the model does very well for the lower values of q_{QE} starting to depart from data as q_{QE} goes up. Note that this is the case at $q_{QE} = 792$ MeV/c and, particularly, at $q_{QE} = 917$ MeV/c where the theoretical predictions overestimate data by 5% and 10%, respectively, at the QE peak as well as in the dip region where the QE and inelastic contributions overlap and 2p-2h MEC are sizeable. This overestimation of cross section occurs only for the set of data of [152], while a good agreement is observed at similar scattering angles, but for lower momentum transfers, namely, $q_{QE} = 402.5$ MeV/c (Fig. 6.2) and $q_{QE} = 443$ MeV/c (Fig. 6.3), which correspond to different experimental setups.

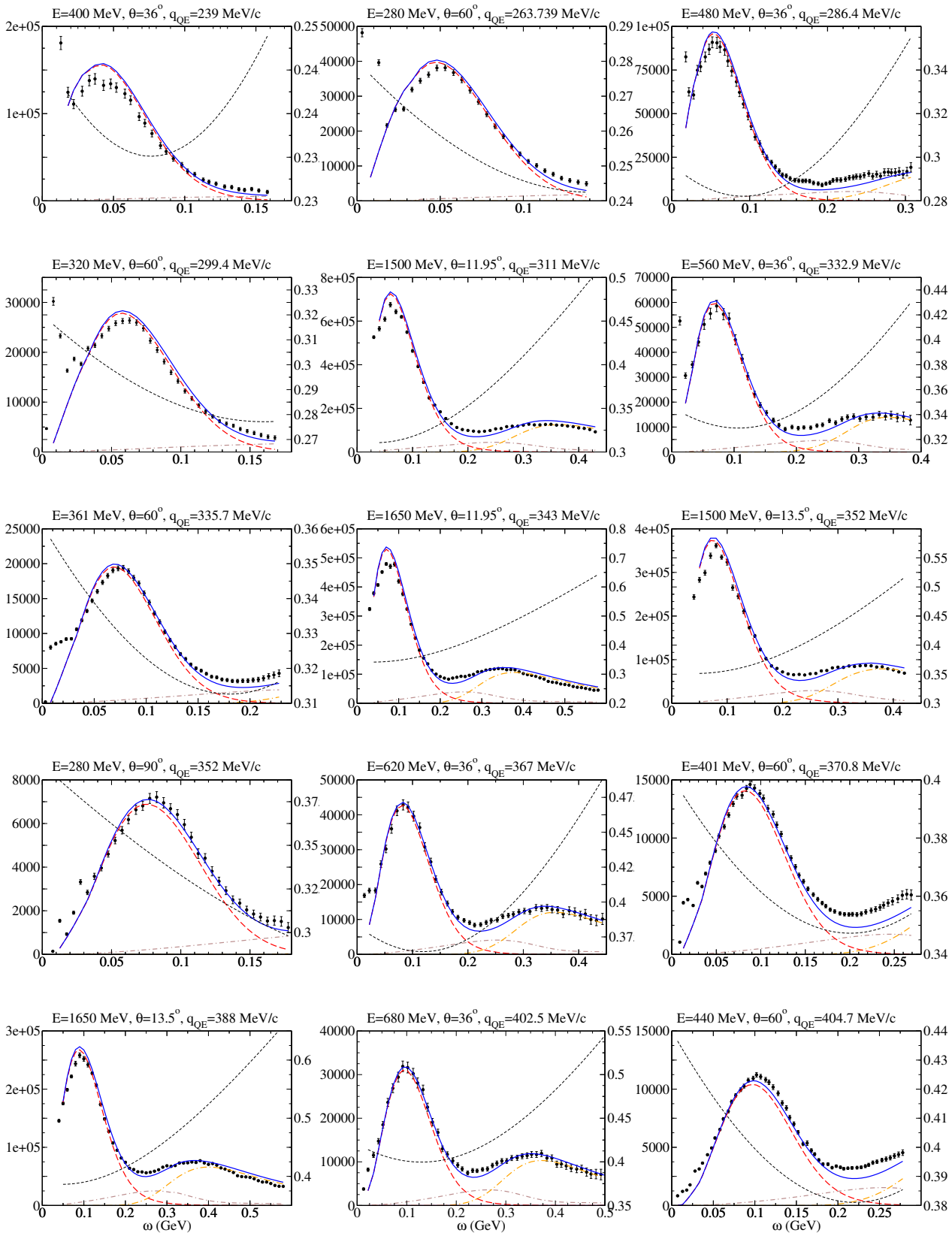

Figure 6.2: Comparison of inclusive ^{12}C(e,e') cross sections and predictions of the QE-SuSAv2 model (long-dashed red line), 2p-2h MEC model (dot-dashed brown line) and inelastic-SuSAv2 model (long dot-dashed orange line). The sum of the three contributions is represented with a solid blue line. The q-dependence with ω is also shown (short-dashed black line). The y-axis on the left represents $d^2\sigma/d\Omega/d\omega$ in nb/GeV/sr, whereas the one on the right represents the q value in GeV/c.

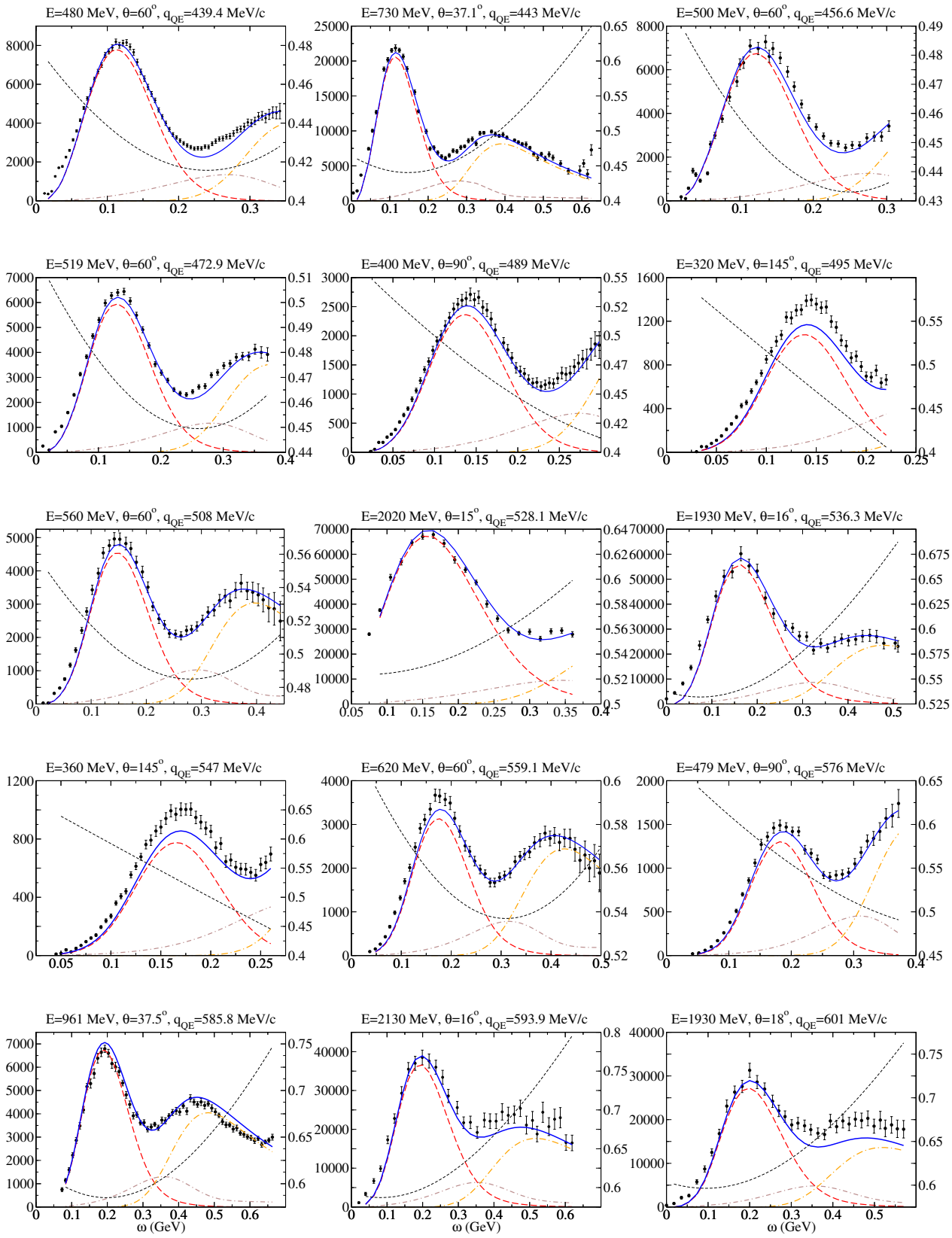

Figure 6.3: As for Fig. 6.2, but now for kinematics corresponding to higher q_{QE}-values.

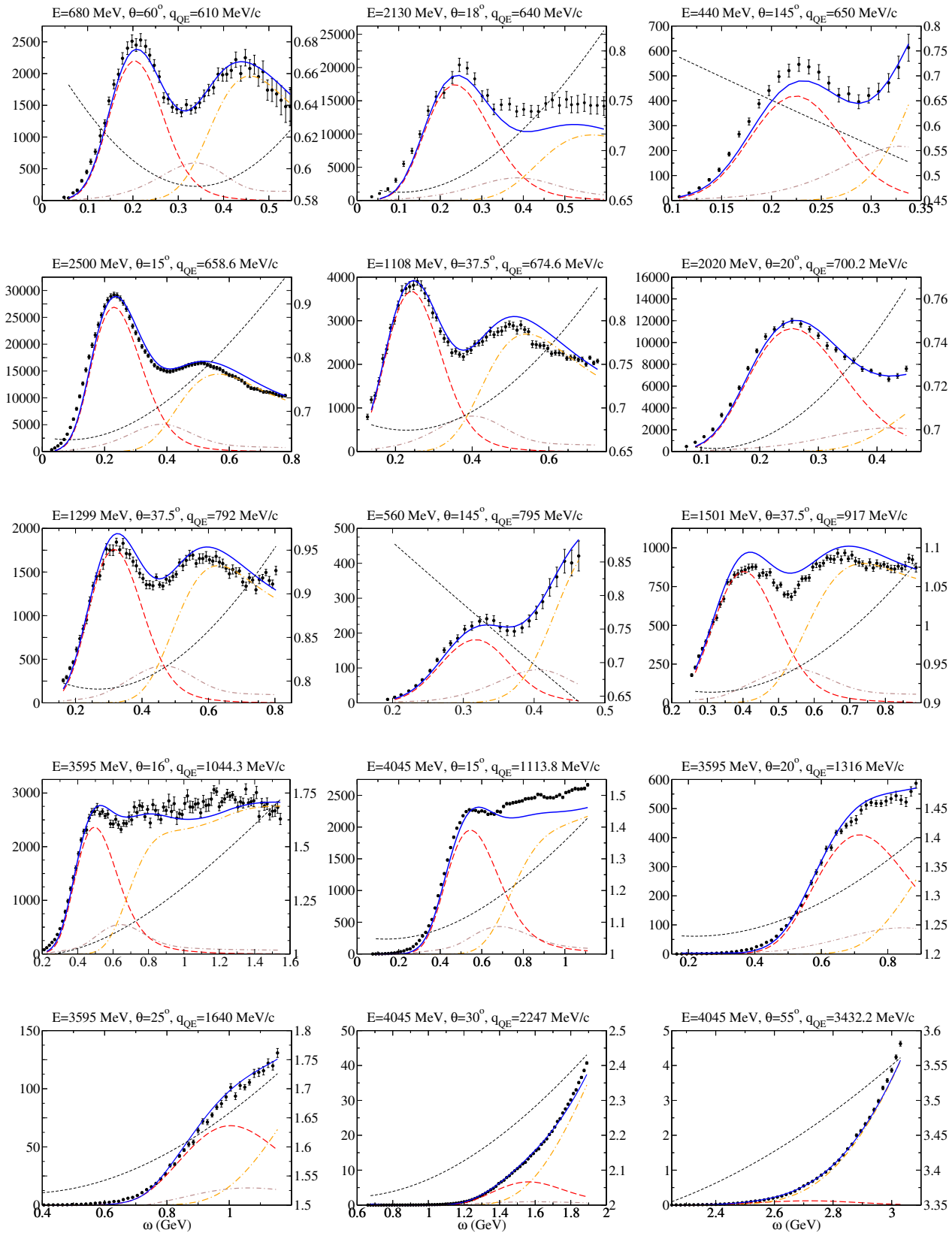

Figure 6.4: As for Fig. 6.2, but now for kinematics corresponding to the highest q_{QE}-values considered.

Some comments concerning the "dip" region between the QE and the Δ peaks are also in order. This is the region where the QE and the inelastic contributions overlap the most and where FSI effects that modify in a significant way the tail of the QE curve at large ω-values can introduce an important impact. Moreover, the role of the 2p-2h MEC effects is essential because its maximum contribution occurs in this region. Thus, only a realistic calculation of these ingredients beyond the IA can describe successfully the behavior of the cross section.

To conclude, the accordance between theory and data in the inelastic regime, where a wide variety of effects are taken into account, also gives us a great confidence in the reliability of our calculations. The inelastic part of the cross section is dominated by the Δ-peak that mainly contributes to the transverse response function. At low electron scattering angles the longitudinal QE response function dominates the cross section and the inelastic contribution is smaller (as will be shown in Section 6.2.4). The opposite holds at large scattering angles, where the Δ-peak contribution is important. On the other hand, for increasing values of the transferred momentum the peaks corresponding to the Δ and QE domains become closer, and their overlap increases significantly. This general behaviour is clearly shown by our predictions compared with data. In those kinematical situations where inelastic processes are expected to be important, our results for the QE peak are clearly below the data which is compensated by the larger inelastic contribution. On the contrary, when the inelastic contributions are expected to be small, the QE theoretical predictions get closer to data. Note also the excellent agreement in some situations (bottom panels on Fig. 6.4) even being aware of the limitations and particular difficulties in order to obtain phenomenological fits of the inelastic structure functions, and the reduced cross sections at these kinematics.

6.2.2 Sensitivity of the model

It is important to point out the novelties introduced in this PhD thesis compared with some previous studies. With regards to the original "SuSA" results shown in [84], that were based only on the superscaling function extracted from the analysis of the longitudinal (e,e') data and assuming the transverse function to be equal (scaling of zeroth kind), in the SuSAv2 approach the enhancement in the transverse channel introduced by the RMF model is incorporated. Moreover, the role of FSI is carefully examined by making use of the evolution of the scaling function from the RMF responses to the RPWIA ones as the momentum transfer goes up. This explains why the present analysis provides a much more accurate description of the data. Notice that the SuSAv2 model makes both QE and inelastic results higher than the SuSA ones. A similar outcome can be also observed in Sections 3.5.2 and 3.5.1 (see also [153]) where the study was restricted to the QE region and a fixed value of q_0 that can be appropriate for the specific kinematics considered was used. On the contrary, here the aim is to provide a model capable of reproducing (e,e') cross sections for a very wide selection of kinematics and including in each case the whole energy spectrum. This is consistent with the q-dependence shown by q_0 in both regimes, QE and inelastic. We have also tested the sensitivity of our results to different choices in the values of ω_0, q_0 and E_{shift} for two representative kinematical situations (see Fig. 6.5).

Concerning the ω_0 parameter, a variation of ±100 MeV leads to negligible effects, hence the value of χ^2 is basically the same (upper panels in Fig. 6.5). In the case of q_0 and E_{shift}, variations of the order of ±100 MeV/c (in q_0) and ±5 MeV (E_{shift}) lead to differences within ∼ 20% on χ^2, but still providing a very good representation of the data (see results presented in the middle and bottom panels of Fig. 6.5). Note however that q_0 is a dynamical parameter running with q, whereas the value of E_{shift} is determined by the right location of the maxima in the scaling functions. Hence a significant variation of these three values does not imply a worsening in the agreement with data.

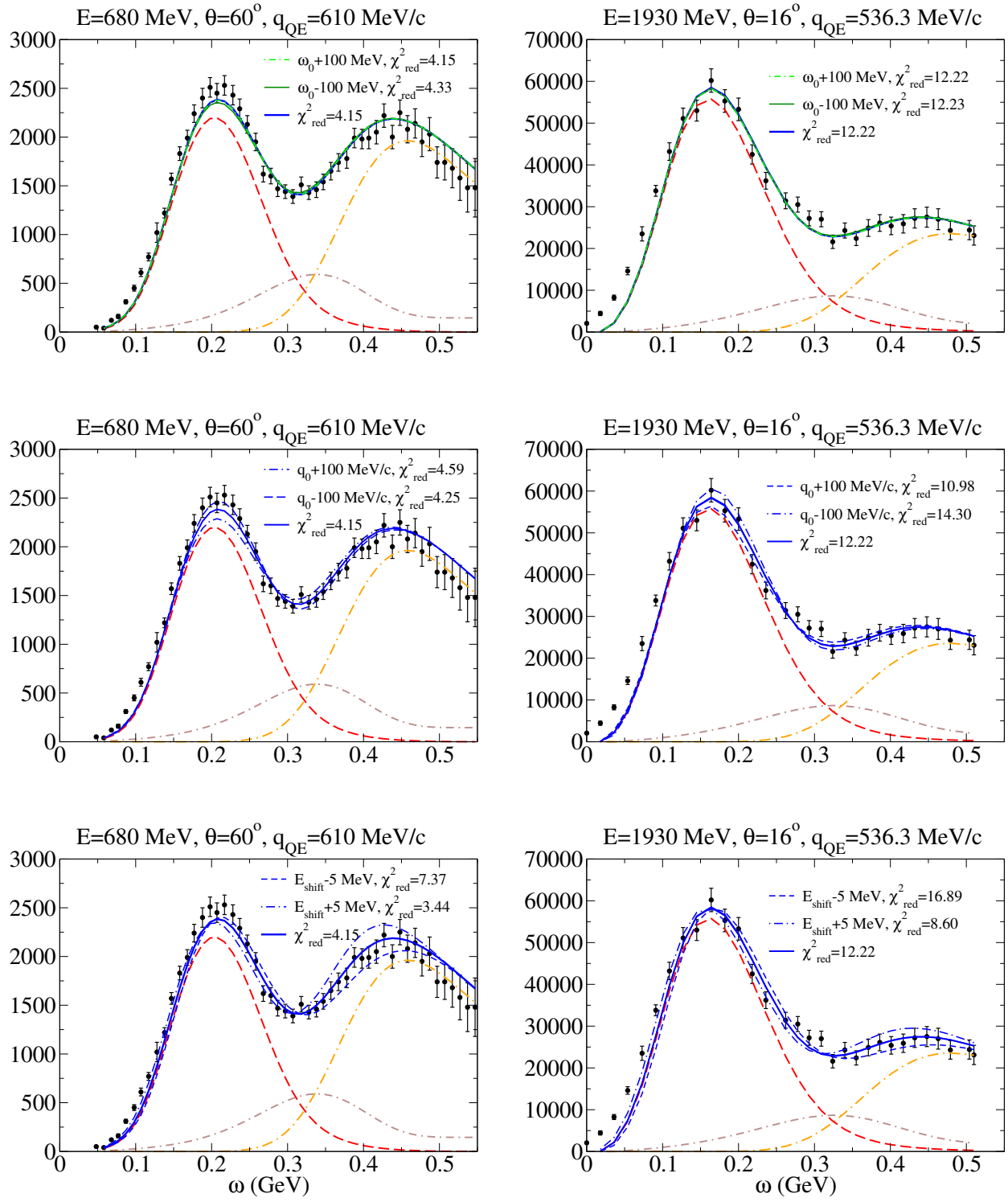

Figure 6.5: Comparison of inclusive ^{12}C(e,e') cross sections and predictions of the QE-SuSAv2 model (long-dashed red line), 2p-2h MEC model (dot-dashed brown line) and inelastic-SuSAv2 model (long dot-dashed orange line). The sum of the three contributions is represented with a solid blue line. It is also shown the total contribution by shifting ω_0 (top panels), q_0 (middle panels) and E_{shift} (bottom panels). The y-axis represents $d^2\sigma/d\Omega/d\omega$ in nb/GeV/sr, whereas the x-axis represents ω in GeV.

6.2.3 Relevance of the RMF/RPWIA effects

Next, we discuss the relevance of the RMF and RPWIA approaches in the SuSAv2 model. Whereas the RMF provides an excellent description of the experimental longitudinal scaling function extracted from data taken at intermediate q-values, producing the required asymmetry and the enhancement of the transverse response, the RPWIA approach yields much more suitable results at higher values of the momentum transfer where FSI effects are significantly reduced. In Fig. 6.6 we present the cross sections for a set of kinematical situations showing the isolated contributions emerging from the two models in the case of the QE regime. Notice that we consider the effects introduced by the blending function and the q_0 parameters in the RMF and RPWIA results. The percentage of the two contributions is given in each panel. As shown, for those kinematics that correspond to the lower values of q_{QE} (top panels) the RMF response contributes the most. As q_{QE} increases, the RPWIA contribution becomes relatively more important, approaching the RMF one (see panels in the middle). Finally, for the higher q_{QE}-values (bottom panels) the behavior reverses with the RPWIA result being the main one responsible for the QE response.

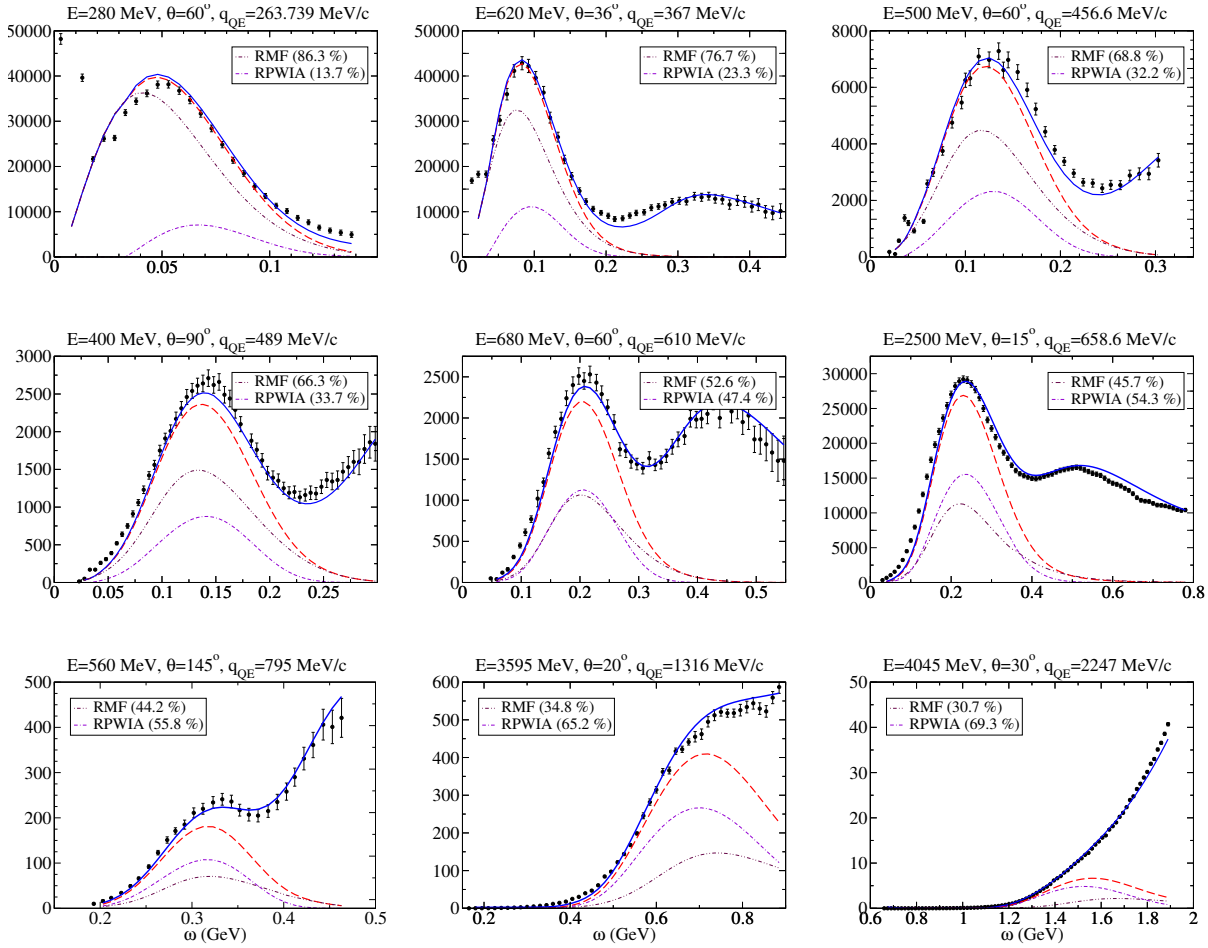

Figure 6.6: Comparison of RMF and RPWIA contributions in the QE regime. Also shown for reference the predictions of the total QE-SuSAv2 model (long-dashed red line) and the total inclusive contribution (solid blue line). The y-axis represents $d^2\sigma/d\Omega/d\omega$ in nb/GeV/sr.

To make clearer how both RMF and RPWIA approaches contribute within the SuSAv2 model, in Fig. 6.7 we present the specific percentages ascribed to the two contributions and how they vary with q_{QE}. The main variation in the two cases is produced in the region of intermediate

q_{QE}-values, namely, $250 \lesssim q_{QE} \lesssim 700$ MeV/c. Here, the relative RMF contribution quickly diminishes as q_{QE} increases whereas the opposite occurs for the RPWIA. Note that at $q_{QE} \sim 700$ MeV/c both models produce basically the same answer ($\sim 50\%$) crossing each other, whereas for $q_{QE} \lesssim 500$ MeV/c RPWIA gives a very minor contribution, that is, FSI are essential to describe data at these kinematics. Finally, at higher q_{QE} the RPWIA increases slowly, whereas the RMF decreases, although in both cases some kind of saturation seems to emerge approaching the RPWIA percentage to $\sim 60-70\%$ ($\sim 30-40\%$ for the RMF). Although not presented here for simplicity, similar conclusions arise for the RMF and RPWIA contributions in the inelastic regime.

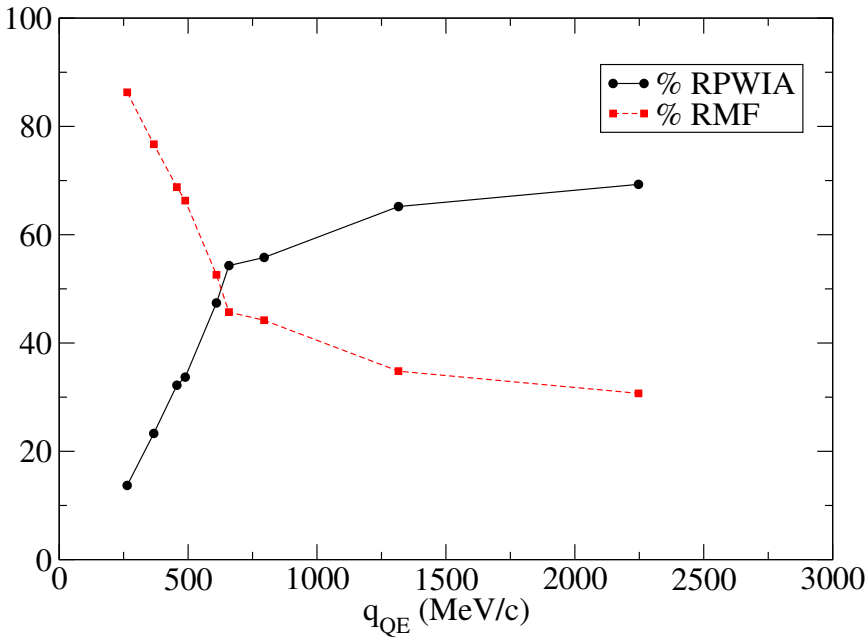

Figure 6.7: Comparison of percentages corresponding to the RMF and RPWIA contributions in the QE regime as a function of q_{QE}.

6.2.4 Separate L/T analysis

The separate analysis of the longitudinal and transverse response functions of ^{12}C is presented in Fig. 6.8. We compare our predictions with data taken from Jourdan [82] based on a Rosenbluth separation of the (e,e') world data. In each case we isolate the contributions corresponding to the QE, inelastic and 2p-2h MEC sectors. Three kinematical situations corresponding to fixed values of the momentum transfer have been considered in Fig. 6.8: $q = 300$ MeV/c (top panel), 380 MeV/c (middle) and 570 MeV/c (bottom). As observed, the longitudinal channel is totally dominated by the QE contribution. Only at very large values of ω does the inelastic process enter giving rise to a minor response, whereas the effects due to 2p-2h MEC are negligible. This result is in accordance with previous work [82, 93, 151, 154], and it clearly shows that the longitudinal response is basically due to the IA. On the contrary, the transverse sector shows an important sensitivity to MEC and inelastic processes. Note that the inelastic transverse response gives rise to the high tail shown by data at large ω-values, whereas the 2p-2h MEC can modify significantly the transverse response in the dip region as well as in the maximum of the QE peak. It is also worth mentioning that the natural enhancement in the transverse response arising from the RMF model is necessary in order to reproduce the separate L/T data, rejecting the idea of 0-th kind scaling.

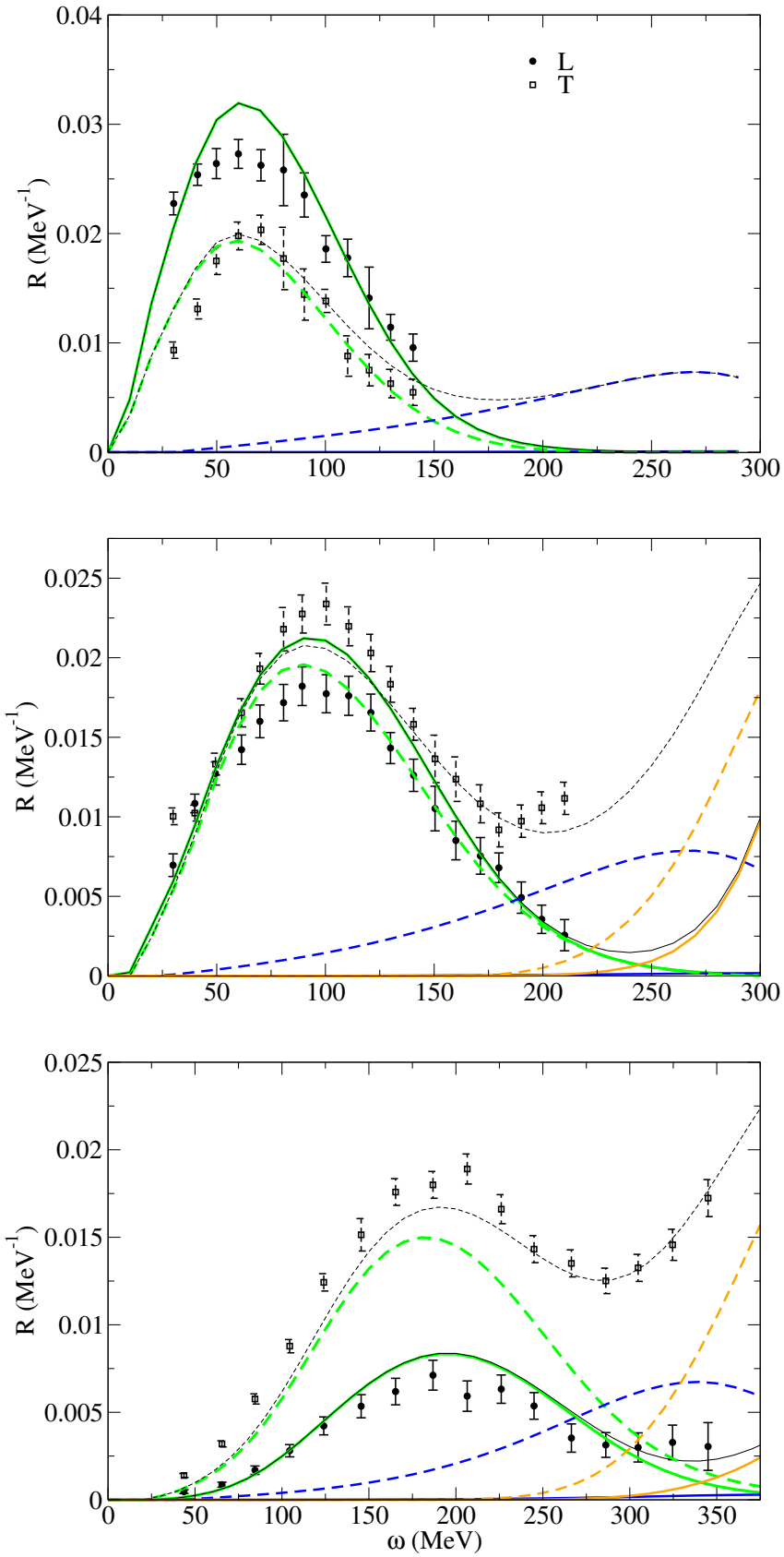

Figure 6.8: Analysis of the longitudinal (solid lines) and transverse responses (dashed lines) in (e,e') scaterring at q = 300 MeV/c (top panel), q = 380 MeV/c (middle panel) and q = 570 MeV/c (bottom panel). QE, MEC and inelastic contributions are shown, respectively, as green, blue and orange lines. The total response is shown by the black lines. Data taken from [82].

From results in Fig. 6.8 we observe that the model leads to a reasonable agreement with data in both channels, although some discrepancies also emerge. Notice that the longitudinal prediction at $q = 300$ MeV/c ($q = 380$ MeV/c) overstimates data by $\sim 12\%$ ($\sim 15\%$). It is important to point out that SuSAv2 is based on the existence of the scaling phenomenon for (e,e') data, and this is completely fulfilled when the value of q is large enough ($q \geq 400$ MeV/c). Therefore, the extension of the superscaling approach to low q-values is not well established even though a good agreement at low kinematics has been achieved in the previous section. Furthermore, the minor discrepancies observed may also be due to the specific Rosenbluth separation method used in [82], which introduces some level of model dependence through y-scaling assumptions and the treatment of radiative corrections.

6.3 Extension of the SuSAv2-MEC model to other nuclei

Once analyzed the capability of the SuSAv2 model to reproduce the ^{12}C(e,e') data, we extend the previous formalism to the analysis of electron scattering data on other nuclei. For this purpose, no differences in the scaling functions are assumed for the different nuclei except for the values used for the Fermi momentum and energy shift (see Table 3.1 for details). The use of the same scaling functions for different nuclear systems is consistent with the property of scaling of second type, *i.e*, independence of the scaling function with the nucleus, and it also follows from the theoretical predictions provided by the RMF and RPWIA models on which SuSAv2 relies. This has been studied in detail in previous works (see [32, 86–88, 155]) where the electromagnetic and weak scaling functions evaluated with the RMF and RPWIA approaches have been compared for ^{12}C, ^{16}O and ^{40}Ca. In Figure 6.9 we compare the general RMF scaling functions for these nuclei, which exhibit no remarkable differences in terms of the nuclear species. In this sense, we apply the reference scaling functions for ^{12}C to the analysis of QE and inelastic regimes in other nuclei. The extension of the 2p-2h MEC contributions to other targets was previously described in Section 4.5.

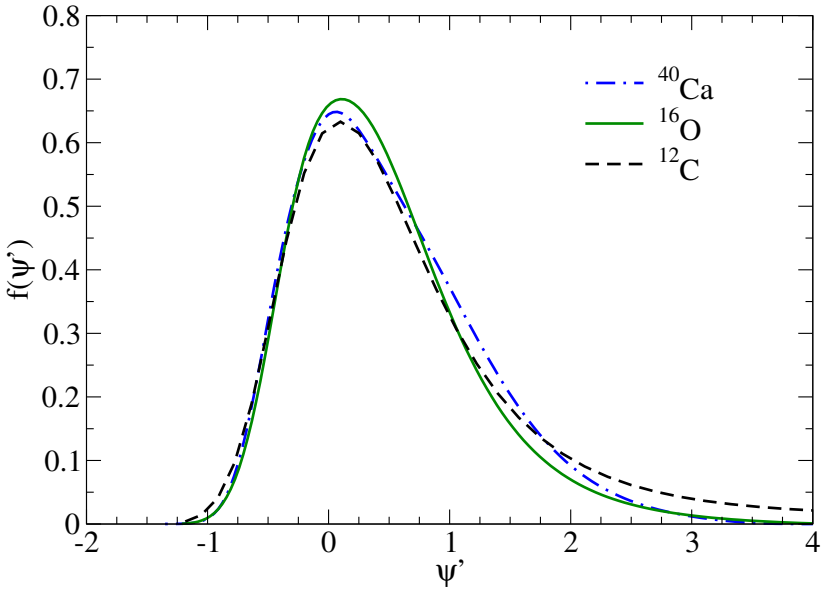

Figure 6.9: Analysis of second kind scaling within the RMF model for ^{12}C, ^{16}O and ^{40}Ca.

In the case of ^{16}O, the k_F and E_{shift}-values selected ($k_F = 230$ MeV/c, $E_{shift} = 16$ MeV/c) are also consistent with the general trend observed in [37], *i.e.*, an increase of the Fermi momentum

with the nuclear density. This is at variance with some previous works [85–87, 91] where ^{16}O was described by using k_F = 216 MeV/c and E_{shift} = 25 MeV. Although both sets of values lead to small differences in the cross sections, the present choice does provide a more consistent analysis of the superscaling behavior in the deep scaling region, and more importantly, it also improves the comparison with electron scattering data. In particular, the analysis of the scaling behavior of the ^{16}O(e,e') data in the deep scaling region below the QE peak ($\psi' = 0$), where no scaling violations are expected, leads to the conclusion that the present choice of k_F and E_{shift}-values works better when comparing with other nuclei (see Figure 6.10).

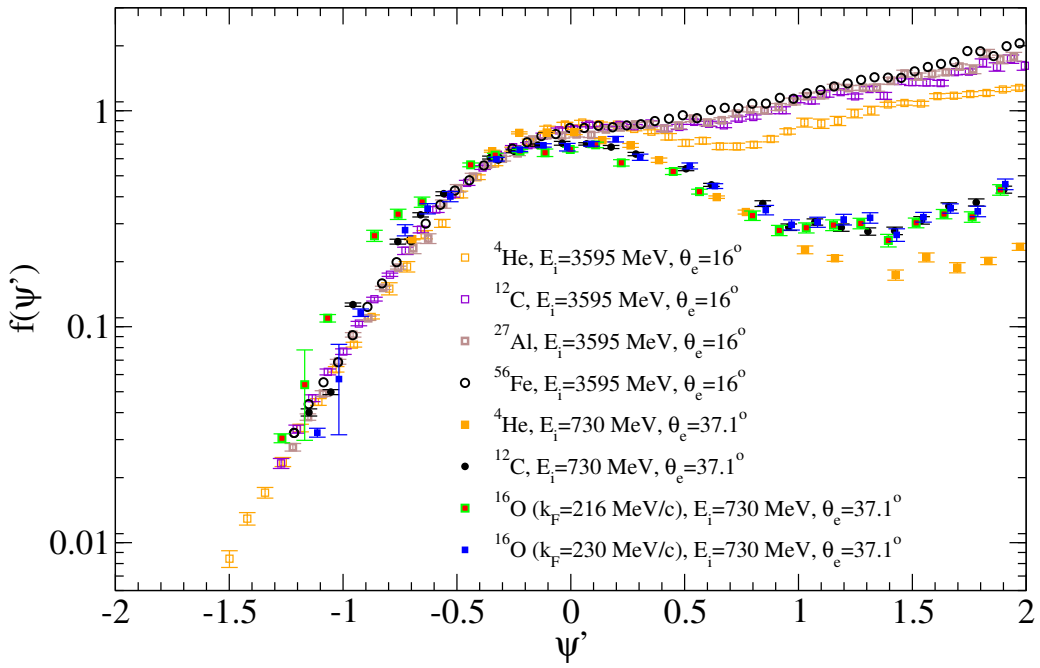

Figure 6.10: Experimental scaling data for various nuclei and for different values of the incident energy (E_i) and scattering angle (θ_e). The ^{16}O data are show for two different values of k_F. The k_F-values for other nuclei are described in Table 3.1.

In accordance with the previous analysis, we show in Fig. 6.11 the predictions of the SuSAv2-MEC model for six different kinematical situations, corresponding to the available (e,e') data on ^{16}O. In all the cases we present the separate contributions for the QE, 2p-2h MEC and inelastic regimes. The 2p-2h MEC responses are extrapolated from the exact calculation performed for ^{12}C assuming the scaling law $R_{2p2h} \sim Ak_F^2$ deduced in Ref. [156] as well as in Section 4.5. The inclusive cross sections are given versus the transferred energy (ω), and each panel corresponds to fixed values of the incident electron energy (E_i) and the scattering angle (θ). Whereas the latter is fixed to 32^0 [157] except for one case (center panel on the top, i.e, $\theta = 37.1^0$) [158], the electron energy values run from 700 MeV (left-top panel), where the QE peak dominates, to 1500 MeV (right-bottom) with the inelastic channel giving a very significant contribution. This is due to the values of the transferred momentum q involved in each situation. Although q is not fixed in each of the panels, *i.e.*, it varies as ω also varies, the range of q-values allowed by the kinematics increases very significantly as the electron energy grows up (for fixed scattering angles). Thus, for higher E_i the two regimes, QE and inelastic, overlap strongly, the inelastic processes being responsible for the large cross sections at increasing values of ω. This different range of q-values spanned in each panel also explains the relative role played by the RMF versus the RPWIA approaches.

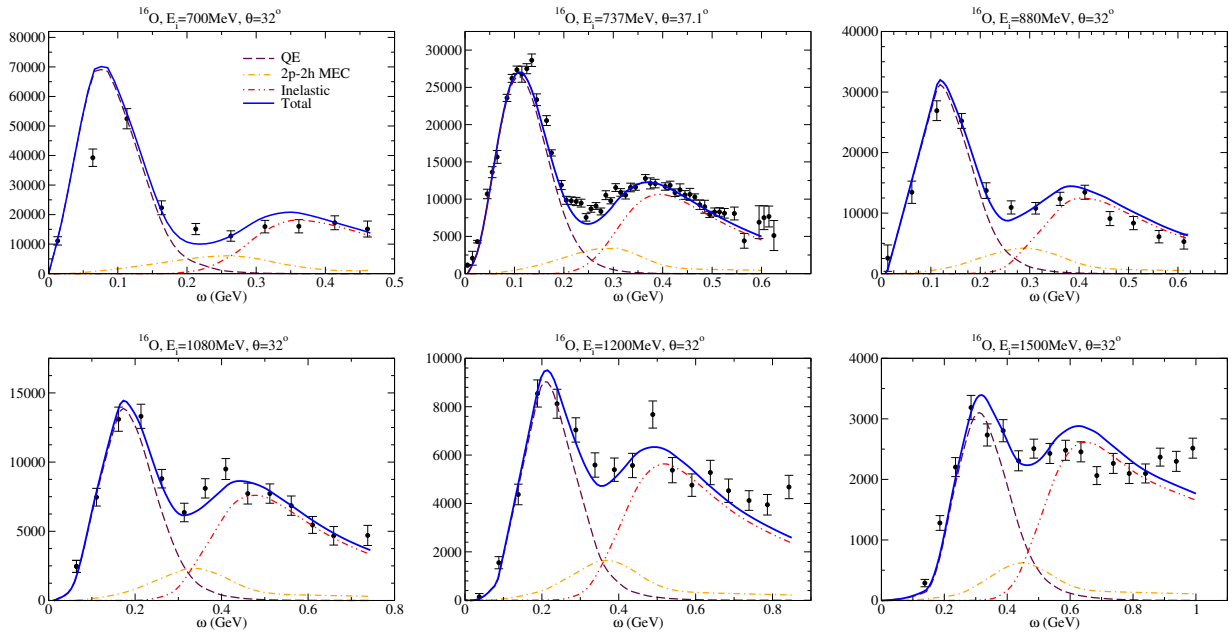

Figure 6.11: Comparison of inclusive ^{16}O(e,e') cross sections and predictions of the SuSAv2-MEC model. The separate contributions of the pure QE response (dashed line), the 2p-2h MEC (dot-dashed), inelastic (double-dot dashed) are displayed. The sum of the three contributions is represented with a solid blue line. The y axis represents $d^2\sigma/d\Omega/d\omega$ in nb/GeV/sr. Data from Refs. [157] and [158].

Although not shown in the figure for simplicity, whereas the RMF response dominates at lower E_i-values (panels from left to right on the top), the reverse occurs, that is, the scaling function is essentially given by the RPWIA prediction, as E_i increases together with q (panels on the bottom).

As observed, the SuSAv2-MEC predictions are in very good accordance with data for all kinematical situations. Although the relative role of the 2p2h-MEC effects is rather modest compared with the QE and inelastic contributions, at the peak of the 2p2h response the three contributions are comparable in size, as also observed for ^{12}C.

For completeness, we also present in Figure 6.12 the calculations for the heavier target ^{40}Ca (k_F = 241 MeV/c, E_{shift} = 28 MeV) where the comparison with data is again very precise from forward to very backward angles. The analysis of these results is relevant because of the similarity with ^{40}Ar, a target of interest for recent and forthcoming neutrino oscillation experiments. Note also that the 2p-2h MEC contributions are more prominent for ^{40}Ca than for ^{12}C and ^{16}O with respect to the QE regime due to the different k_F dependence of the QE and 2p-2h MEC contributions, A/k_F and Ak_F^2, respectively [156].

To conclude, the comparison with a very light nucleus as ^{4}He (k_F = 200 MeV/c, E_{shift} = 15 MeV) is displayed in Fig. 6.13. In this situation, the SuSAv2 model underestimates the QE peak which may be a consequence of the strong vector and scalar potentials arising from the RMF prescription. Therefore, the applicability of the SuSAv2 model and, specifically, the ^{12}C RMF scaling functions and their associated FSI effects may be questionable for very light nuclei, *i.e.* for very low Fermi momentum. We can also observe, in accordance with the density dependence shown in Section 4.5, that the 2p-2h MEC relative contribution is significantly smaller than the one observed for heavier nuclei.

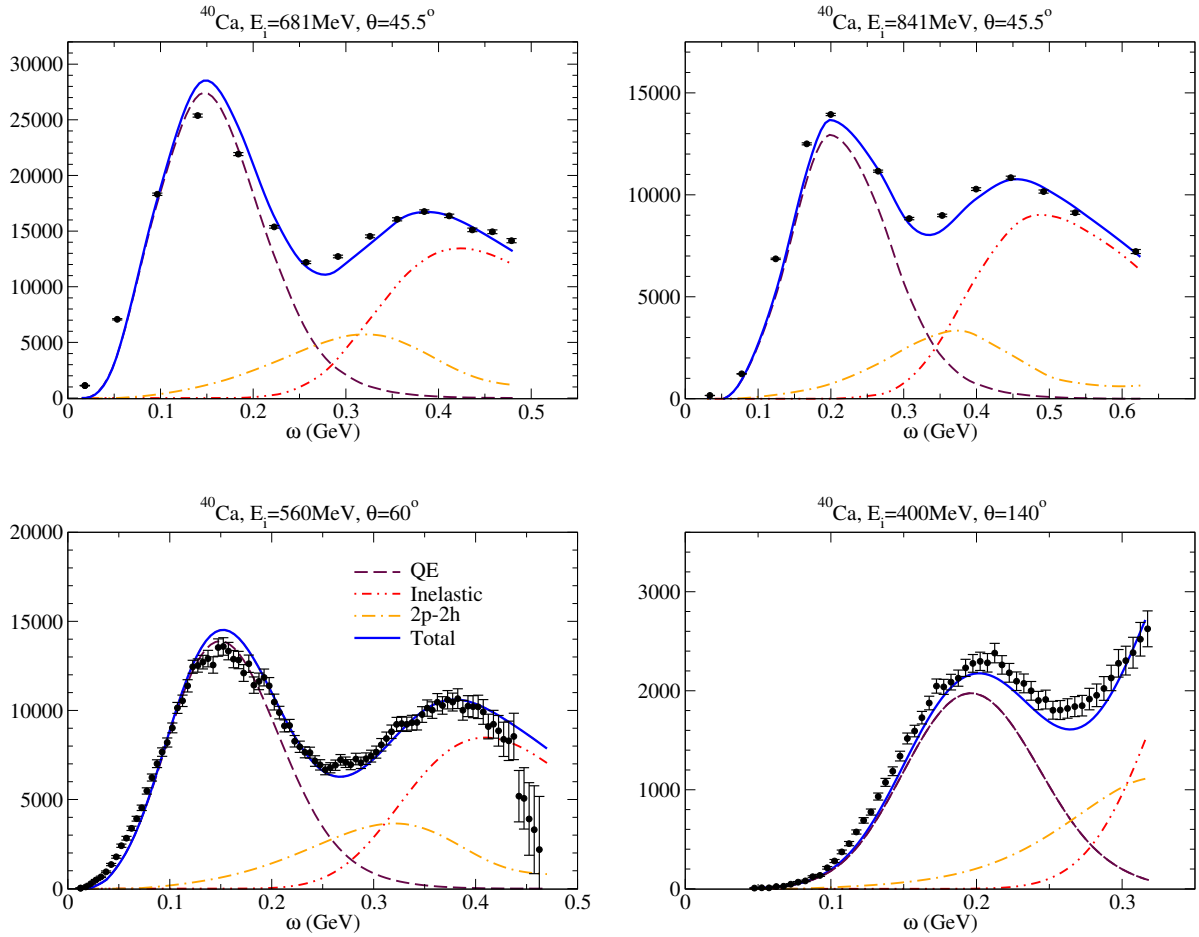

Figure 6.12: Comparison of inclusive ^{40}Ca(e,e') cross sections and predictions of the SuSAv2-MEC model. The separate contributions of the pure QE response (dashed line), the 2p-2h MEC (dot-dashed), inelastic (double-dot dashed) are displayed. The sum of the three contributions is represented with a solid blue line. The y axis represents $d^2\sigma/d\Omega/d\omega$ in nb/GeV/sr. Data from Refs. [159] and [160].

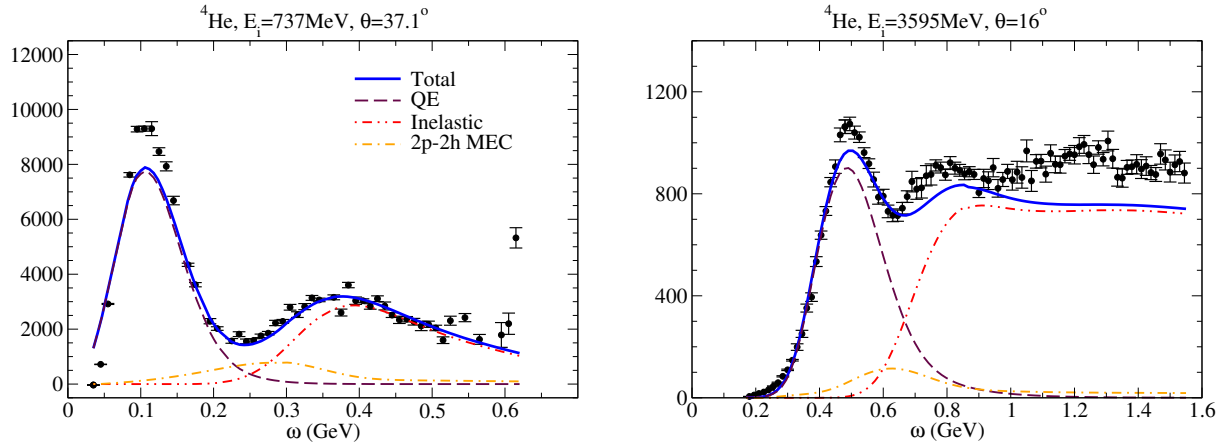

Figure 6.13: Comparison of inclusive ^{4}He(e,e') cross sections and predictions of the SuSAv2-MEC model (solid blue line). The separate contributions of the pure QE response (dashed line), the 2p-2h MEC (dot-dashed), inelastic (double-dot dashed) are displayed. The y axis represents $d^2\sigma/d\Omega/d\omega$ in nb/GeV/sr. Data from Refs. [158] and [161].

6.4 Conclusions

In this Chapter the SuSAv2-MEC model applied to electron scattering is extended to the whole energy spectrum, incorporating the contributions coming from the QE, inelastic and two-body meson exchange currents. Within this framework a general "blending" function is introduced to make the transition between the RMF and RPWIA responses. This function is constructed in terms of a parametrization of the optimized blending region given by a transition parameter, q_0, and it has been applied consistently to the QE as well as to the inelastic regimes, using the same scaling functions with an analogous RMF-RPWIA transition. Although the use of more free parameters, as ω_0 and/or the shift energy, leads to an even better agreement with data in some particular cases, the specific parametrization assumed is not critical, and indeed, the present model is capable of reproducing very successfully the whole energy spectrum of ^{12}C(e,e') data at very different kinematics. In particular, the SuSAv2 model reproduces accurately the position, width and maximum of the QE peak for all kinematics, whereas the use of the single-nucleon inelastic structure functions together with the SuSAv2 scaling functions has led to a precise description of the Δ-resonance region and the entire inelastic regime. Accordingly, the application of the phenomenological SuSA approach to the inclusive (e,e') reactions would clearly result in an underprediction of the data, as it was previously suggested in Section 3.5.2.

Remarkably, we have also shown that the SuSAv2-MEC model gives a reasonably good description not only of the cross sections but also of the separate longitudinal and transverse response functions. This is a very important test for models used in neutrino scattering studies, since in this case the balance between the L and T channels is different from the (e,e') case. All this gives us a great confidence in the reliability of the model, providing a solid benchmark to assess its validity when extended to the description of neutrino- nucleus scattering. In this case, not only new responses contribute, but also the wide neutrino energy band implied by the typical accelerator-based neutrino fluxes makes it difficult to reconstruct the neutrino energy. Thus, ingredients beyond the ones usually assumed within the IA can have a significant impact on the analysis of data.

A basic feature of our present study, apart from the appliance of the SuSAv2 model to the QE and inelastic regions, concerns the evaluation of the two-body meson exchange currents in both longitudinal and transverse channels. This fully relativistic calculation has allowed for a consistent evaluation of high energies/momenta experimental data. Furthermore, the parametrization of the exact results for the 2p-2h MEC responses has allowed us to avoid the computationally demanding microscopic calculation for the entire set of kinematics required for the experimental data presented here.

Additionally, this analysis has been extended to other nuclear species leading to an accurate description of the experimental data for nuclei of relevance in forthcoming neutrino experiments. Despite the smaller amount of available (e,e') experimental data for some nuclei with respect to ^{12}C, the growing interest of experimental collaborations on (e,e') measurements, together with the extension of neutrino experiments to other nuclear targets, is expected to shed light on their nuclear effects and the associated parameters that play a role in most theoretical description for both electron and neutrino reactions.

To conclude, we emphasize the importance of scaling arguments that provide a proper description of electron scattering data before the analysis be extended to neutrino reactions. In this sense, the fully relativistic analysis presented in this chapter for the entire energy spectrum and the different nuclear responses is of crucial importance for the analysis of neutrino reactions.

Chapter 7

Analysis of charged-current neutrino induced reactions

In this Chapter we present our theoretical predictions compared with CC neutrino scattering data from different collaborations: MiniBooNE, NOMAD, MINERνA, T2K and SciBooNE, whose main features were analyzed in Chapter 1. The SuSAv2-MEC model, that has already proven to describe accurately (e, e') data in Chapter 6, is now applied to the analysis of neutrino experiments. Our study is mainly restricted to the "quasielastic-like" regime where the impulse approximation used to describe the one-nucleon knockout process in addition to the effects linked to the 2p-2h meson-exchange currents play a major role. However, some results that incorporate the contribution of the Δ-excitation are also compared with data.

In the case of the QE regime, our study includes the analysis of muonic neutrino and antineutrino scattering reactions on carbon corresponding to MiniBooNE, NOMAD and MINERνA experiments. In the latter we also consider electron neutrinos. Furthermore, results for the T2K Collaboration are analyzed in detail, also accounting for the recent measurements on ^{16}O. In this case, we first restrict ourselves to the QE domain, and we extend the discussion later to the T2K inclusive charged-current neutrino reactions where high inelasticities are of significance. Other studies regarding low-energy effects as well as the relevance of the different reaction channels to neutrino reactions are also addressed. Therefore, our main interest is to show the capability of the present model, SuSAv2-MEC, to analyze and describe successfully a large variety of neutrino scattering data corresponding to different experiments with a wide range of kinematics explored.

7.1 CCQE neutrino and antineutrino reactions at MiniBooNE and NOMAD kinematics

In recent years a significant amount of charge-changing quasielastic (CCQE) neutrino and antineutrino cross section data have been presented in the literature. In this section we compare the results of the SuSAv2-MEC model with the measurements of CCQE ν_μ and $\overline{\nu}_\mu$ reactions on ^{12}C from the MiniBooNE [20, 21] and NOMAD [24] experiments.

The MiniBooNE Collaboration has measured CCQE muonic neutrino and antineutrino cross sections on ^{12}C for neutrino energies in the 1 GeV region, the neutrino and antineutrino fluxes peaking at 0.79 GeV and 0.66 GeV, respectively, and going from 0 to about 7 GeV with the most important contributions coming from below 3 GeV. These measurements have provided CCQE cross sections that are higher than most predictions based on IA. This excess, at relatively low

energy ($\langle E_\nu \rangle \sim 0.7$ GeV), has been interpreted as an evidence that non-QE processes may play an important role at that kinematics (see Section 1.5 in Chapter 1 for further details). It is important to point out that in the experimental context of MiniBooNE as well as in other experiments such as MINERνA or T2K, "quasielastic" or, equivalently, *CCQE-like* events are defined as those from processes or channels containing no mesons in the final state. This is a direct consequence of the lack of experimental sensitivity to the outgoing hadrons in the final state. Thus, in addition to the purely QE process, which in this work refers exclusively to processes induced by one-body currents (IA), multi-nucleon excitations and, in particular, two-particle emission induced by MEC should also be taken into account for a proper interpretation of data. These have been evaluated in [30, 31, 39] provinding a very good agreement with the MiniBooNE data in spite of being rather different in their basic ingredients. On the contrary, the NOMAD experiment involves an incident neutrino (antineutrino) beam energy much larger, with a flux extending from $E_\nu = 3$ to 100 GeV. In this case, one finds that data are in reasonable agreement with predictions from IA models [19, 39, 83, 115].

On this basis, it is worth mentioning that the unfolding procedure to obtain the total integrated cross sections from the measured differential ones largely depends on model assumptions, being detailed in [20, 21]. Within this procedure, the true (anti)neutrino energy $E_{\nu(\overline{\nu})}$ is obtained in terms of the reconstructed four-momentum Q^2_{QE} and neutrino energy E_ν^{QE}. These reconstructed magnitudes are obtained assuming an initial-state nucleon at rest with a constant binding energy, E_b, set to 34 MeV (30 MeV) in the neutrino (antineutrino) case,

$$E_\nu^{QE} = \frac{M_p^2 - (M_n - E_b)^2 - m_\mu^2 + 2(M_n - E_b)E_\mu}{2(M_n - E_b - E_\mu + k_\mu \cos\theta_\mu)} \tag{7.1}$$

$$E_{\overline{\nu}}^{QE} = \frac{M_n^2 - (M_p - E_b)^2 - m_\mu^2 + 2(M_p - E_b)E_\mu}{2(M_p - E_b - E_\mu + k_\mu \cos\theta_\mu)} \tag{7.2}$$

$$Q^2_{QE} = 2E^{QE}_{\nu,\overline{\nu}}(E_\mu - k_\mu \cos\theta_\mu) - m_\mu^2, \tag{7.3}$$

where E_μ, k_μ and θ_μ are the corresponding muon energy, momentum and angle, and m_n, m_p and m_μ are the masses of the neutron, proton and muon, respectively. While these quantities certainly differ from the underlying true quantities, they are unambiguously defined and and easily reproducible by other experiments. In this regard, we include in Appendix F some preliminary results for the analysis of the energy reconstruction effects in neutrino oscillation experiments which are essential for determining the oscillation parameters.

Thus, in Fig. 7.1 we present the total flux-unfolded integrated cross section per nucleon for muonic neutrino (top panel) and antineutrino (bottom panel) reactions within the SuSAv2-MEC model. The energy range has been extended to 100 GeV and data are shown for the MiniBooNE and NOMAD experiments. Whereas 2p-2h MEC contributions are needed in order to reproduce MiniBooNE data (in consistency with the previous discussion), the NOMAD experiment seems to be in accordance with the pure QE response. As observed, the role of 2p-2h MEC is very significant at all neutrino (antineutrino) energies, getting an almost constant value for E_ν ($E_{\overline{\nu}}$) greater than 1 – 2 GeV. At these values the pure QE cross section is increased by $\sim 30 - 35\%$ due to 2p-2h MEC. Moreover, the large error bars of the MiniBooNE and NOMAD data do not allow to draw definite conclusions.

It is also important to point out that, in spite of the very large neutrino (antineutrino) energies involved in NOMAD experiment, the main contribution to the cross section, about $\sim 90\%$, comes

from momentum and energy transfers below $\sim$ 1 GeV/c and $\sim$ 0.5 GeV, respectively. An analysis of the relevant kinematic regions for neutrino reactions will be addressed in Section 7.3.

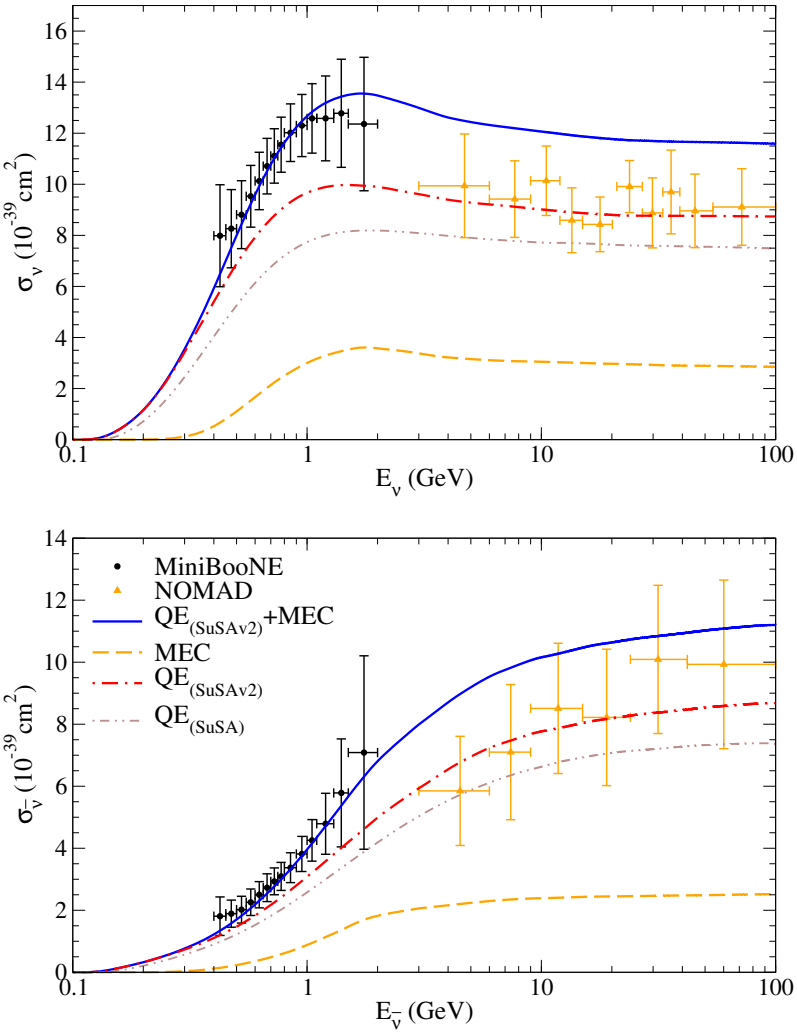

Figure 7.1: MiniBooNE CCQE ν_μ-^{12}C ($\bar{\nu}_\mu$-^{12}C) total cross section per nucleon as a function of the neutrino energy. The top panel corresponds to neutrino cross sections and the bottom one to antineutrino reactions. Data are from [20, 21, 24].

The difference between MiniBooNE and NOMAD measurements can roughly be explained by different definitions of the CCQE signal. In the case of MiniBooNE a sample of 2-subevents (Cherenkov light from muon and from decay electron) is analyzed and ejected protons are not detected. In the case of NOMAD 1-track (muon) and 2-tracks (muon and proton) samples of events are analyzed simulateously. This can prevent one from including multi-nucleon emission events in the NOMAD results, thus leading to an agreement with the purely QE response without the need of significant contributions from multi-nucleon excitations.

For completeness, we also show the comparison with the phenomenological SuSA approach in Fig. 7.1. As commented in Chapter 3, the SuSA model assumes that the longitudinal and transverse scaling function are identical. On the contrary, the SuSAv2 model, based on the RMF predictions leads to a natural enhancement on the transverse response. As also noticed in the analysis of electron scattering data in Chapter 3, the SuSAv2 improves the agreement with the experimental data in comparison with the SuSA model, being the former closer to the center of the NOMAD bins.

At MiniBooNE kinematics, the addition of MEC effects to the SuSA approach would also underestimate the data. Although not shown here for brevity/simplicity, the same conclusions can be drawn for the comparison of the SuSA model with the MiniBooNE double differential cross sections. This comparison is shown in Ref. [153] where a clear underestimation of data is observed. Moreover, the difference between SuSA and SuSAv2 is larger for neutrino than for antineutrino results. This occurs because of the cancellation between R_T (positive) and $R_{T'}$ (negative) responses in antineutrino cross sections. Notice that the transverse responses are substantially enhanced in SuSAv2 compared with SuSA. This cancellation due to the different sign on the T'_{VA} responses also affects the total 2p-2h MEC cross section.

At this point, it is worth mentioning that, as for the (e,e') case, we adopt the electromagnetic nucleon form factors of the extended Gari-Krumpelmann (GKeX) model [148–150] for the vector CC current entering into neutrino cross sections. As described in Chapter 2, this prescription improves the commonly used Galster parametrization at $|Q^2| > 1$ GeV^2. For completeness, we show in Figure 7.2 the sensitivity of the total CCQE neutrino cross section within the SuSA model for the different up-to-date parametrizations of the nucleon form factors (see Refs. [19, 71] for details) where all of them are essentially equivalent for the kinematics that are relevant for neutrino scattering experiments. Similar comments also apply to the SuSAv2 model.

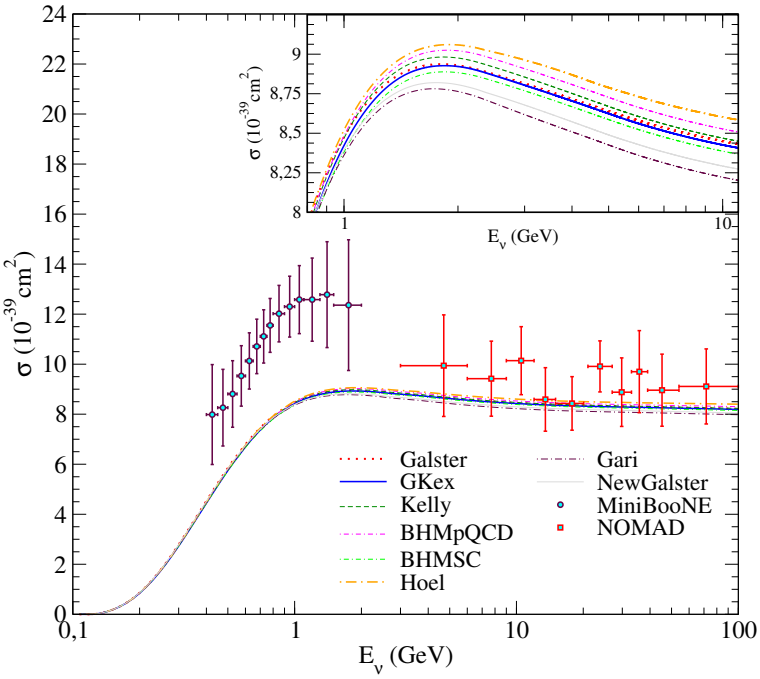

Figure 7.2: CCQE ν_μ–^{12}C cross section per nucleon evaluated in the SuSA model for various parametrizations of the nucleon electromagnetic form factors [19]. A sub-panel zooming in on the region near the maximum is inserted on the top.

Regarding the axial contributions, we employ the commonly used dipole axial nucleon form factor described in Chapter 2. A comparison between dipole and monopole axial form factor is shown in Appendix D together with a discussion on the quenching of the axial coupling g_A parameter in Appendix E.

In what follows, we mainly focus on the directly-measured differential cross sections for the MiniBooNE experiment. This, in contrast, with the total flux-unfolded total cross section leads to a more meaningful analysis of the experimental results.

7.1.1 MiniBooNE flux-integrated cross sections

In this section, we apply the SuSAv2-MEC model to the study of neutrino and antineutrino CCQE MiniBooNE double-differential cross sections. Unlike the total flux-unfolded cross section that is not measured directly and largely depends on model assumptions, the flux-integrated double differential cross section implies minimal model dependence although requires the convolution of the cross section over the energy spectrum of the neutrino flux. This is obtained through the following procedure:

$$\frac{d^2\sigma}{dT_\mu d\cos\theta_\mu} = \frac{1}{\Phi_{tot}} \int \left[\frac{d^2\sigma}{dT_\mu d\cos\theta_\mu}\right]_{E_\nu} \Phi(E_\nu) dE_\nu \,, \tag{7.4}$$

where $\left[\frac{d^2\sigma}{dT_\mu d\cos\theta_\mu}\right]_{E_\nu}$ is the double differential cross section for a given neutrino energy E_ν and Φ_{tot} is the neutrino flux integrated over all neutrino energies. A similar expression also applies to the antineutrino case.

In Figs. 7.3 – 7.5 we show the double differential cross section averaged over the neutrino (antineutrino) energy flux against the kinetic energy of the final muon. We represent a large variety of kinematical situations where each panel refers to results averaged over a particular muon angular bin. Notice that the mean energy of the MiniBooNE ν_μ ($\bar{\nu}_\mu$) flux is 788 (665) MeV which requires a relativistic treatment of the process. In Figs. 7.3 – 7.5 we show results for the pure QE response (red dot-dashed line) and the total contribution of the 2p-2h MEC (orange dashed line), *i.e.,* including vector and axial terms in the three responses, L, T and T'. Finally, the total response (QE+2p-2h MEC) is represented by the solid blue line.

As observed, the model tends to overpredict the data for the most forward angles, *i.e.,* $0.9 \leq \cos\theta_\mu \leq 1$. This corresponds to very small energy and momentum transfers, a kinematic situation where “quasi-free" scattering is highly questionable. However, note how well the pure QE response fits the data, in particular, for neutrinos. As the scattering angle increases, the theoretical prediction including both the QE and the 2p-2h MEC effects agrees well with the data. This is the case for neutrinos and antineutrinos (Fig. 7.3 and Fig. 7.5) at angles below 90°. On the contrary, the discrepancy between theory and data tends to increase as θ_μ gets larger (Fig. 7.4 and bottom panels in Fig. 7.5). Notice, however, that in these situations only a small number of data points with large uncertainties exist and the cross section is much smaller. A possible explanation for these results at very backward kinematics, *i.e* higher q values, particularly for neutrino scattering, might be due to the lack of MEC-correlations interference in our description. Nevertheless, similar results can also be found in [162] where MEC-correlation interferences are considered but including some approximations in the relativistic treatment of the 2p-2h MEC contributions. In this sense, effects of relevance at backward kinematics beyond IA and 2p-2h MEC contributions in the analysis of the MiniBooNE experimental data are not excluded.

Results in Figs. 7.3 – 7.5 clearly show the relevant role played by effects beyond the impulse approximation. In particular, 2p-2h MEC contributions are essential to describe data. Their relative percentage at the maximum, compared with the pure QE response, being of order 25 – 35%. The relative strength associated with 2p-2h MEC gets larger for increasing values of the angle, particularly, in the case of antineutrinos. Note that, in spite of the quite different neutrino and

antineutrino energy fluxes, the quality of the agreement with data is rather similar in the two cases.

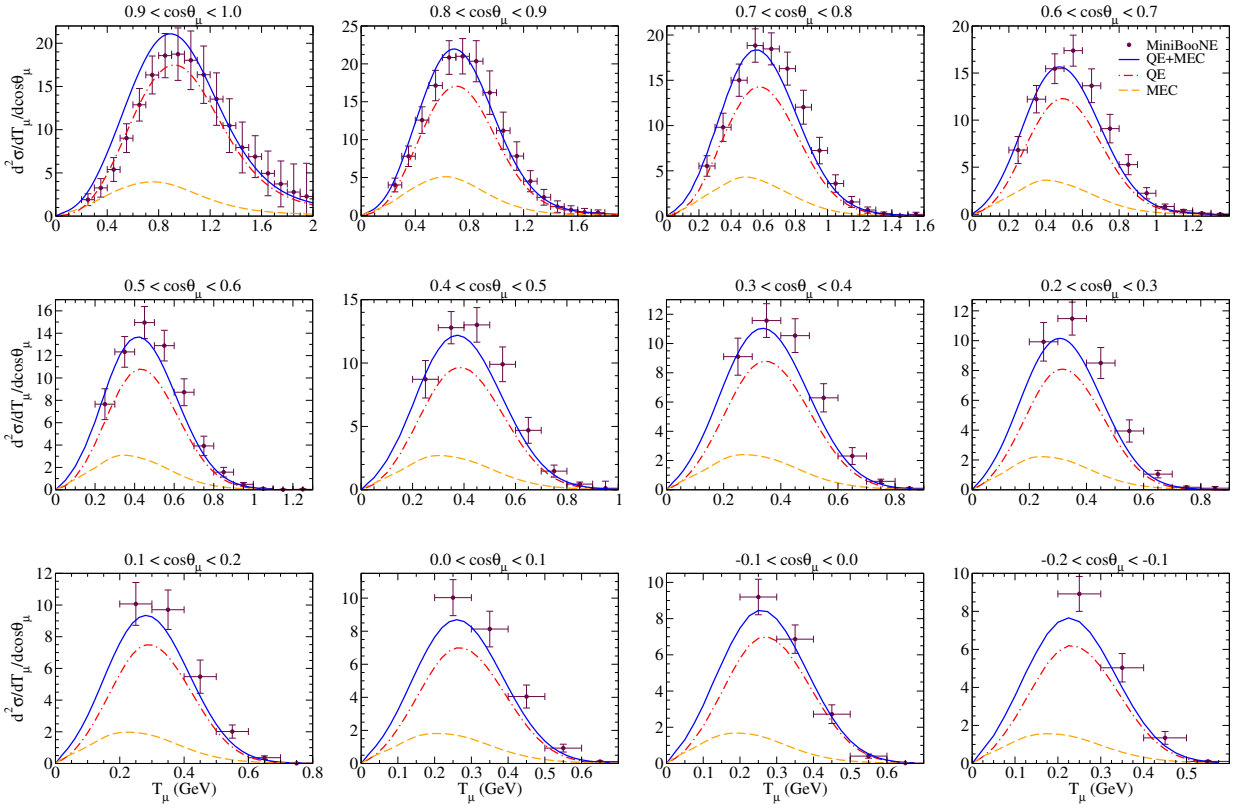

Figure 7.3: MiniBoone flux-folded double differential cross section per target nucleon for the ν_μ CCQE process on ^{12}C. Results are given in 10^{-39} cm^2/GeV and displayed versus the μ^- kinetic energy T_μ for various bins of $\cos\theta_\mu$ obtained within the SuSAv2-MEC approach. QE and 2p-2h MEC results are also shown separately. Data are from [20].

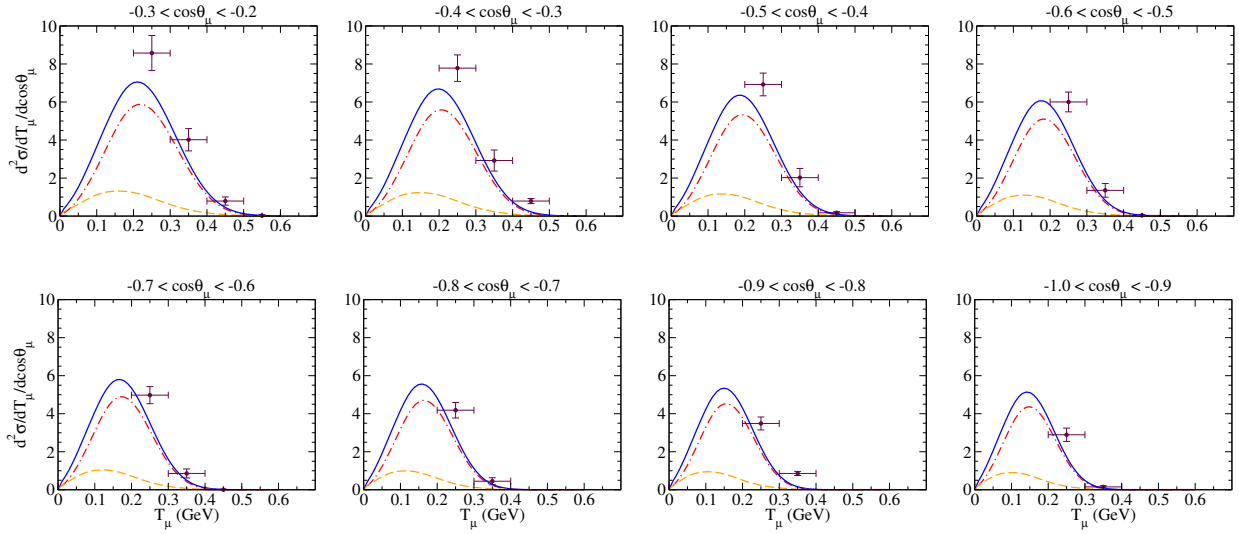

Figure 7.4: As for Fig. 7.3 but considering more backward kinematics. Data are from [20].

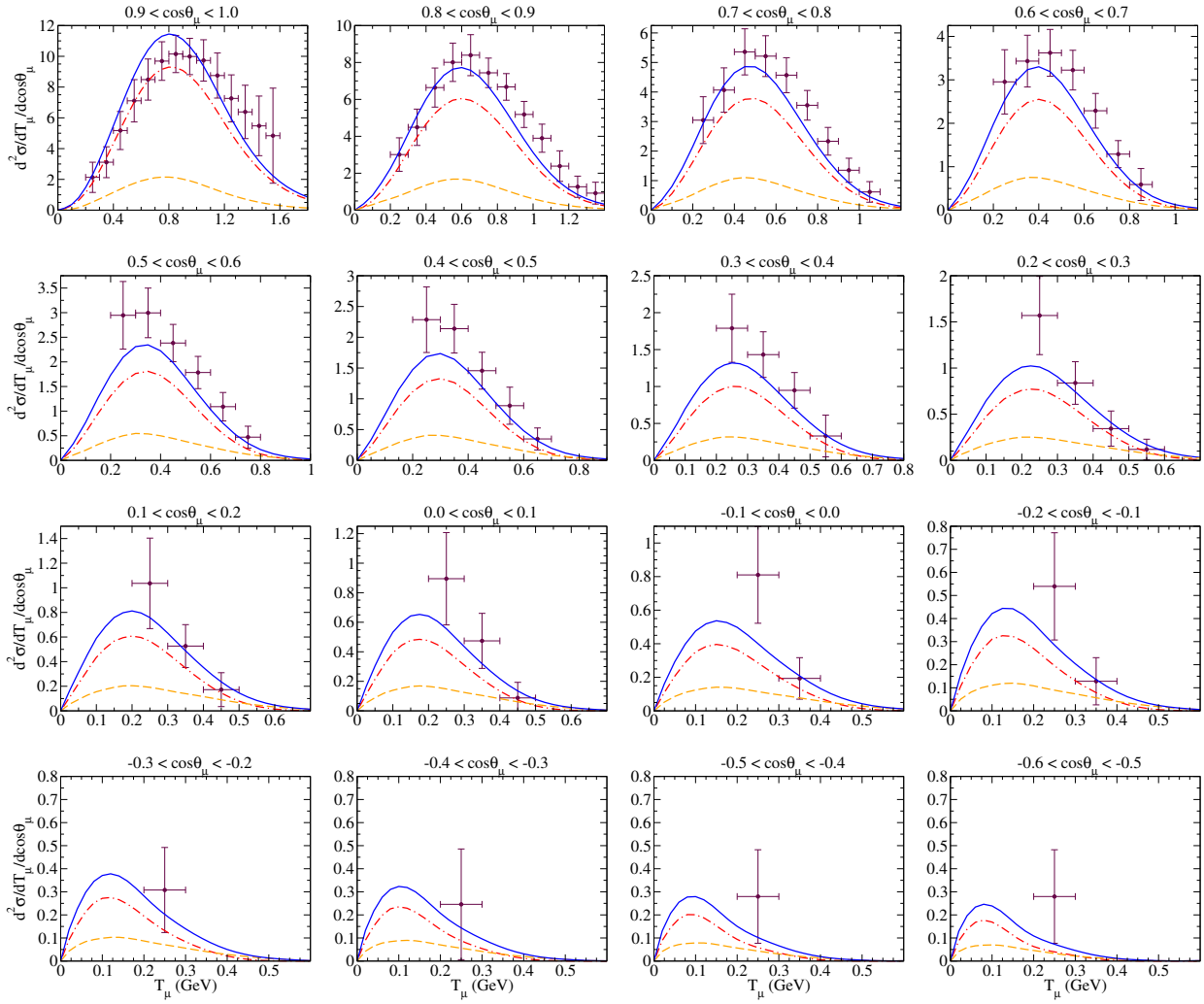

Figure 7.5: As for Fig. 7.3 but considering now the $\bar{\nu}_\mu$ CCQE process on ^{12}C. Data are from [21].

A further general comment on the previous results from Figs. 7.3—7.5 is in order: the RMF predictions (shown in [163]) produce almost identical results to the ones from the SuSAv2 model at MiniBooNE kinematics. A similar comparison was also shown in Chapter 3 for the analysis of (e,e') data at intermediate q-values.

To complete the previous discussion on the double differential cross sections, we present in Figs. 7.6 and 7.7 the results averaged over the muon kinetic energy bins as functions of the muon scattering angle for neutrinos and antineutrinos, respectively. These graphs complement the previous ones, and prove the capability of the model to reproduce the data for a large variety of kinematic situations. The 2p-2h MEC contributions increase the pure QE response by $\sim 25-35\%$ (depending on the particular region explored) and are shown to be essential in order to describe the data. As observed, the total model tends to overpredict the data measured at angles close to zero and T_μ in the vicinity of $\sim 0.8-1$ GeV. This is consistent with results in previous figures and the inability of the model to describe properly data at very small angles. However, the largest discrepancy between theory and data occurs at the smallest muon kinetic energy bins considered, *i.e.*, $0.2 < T_\mu < 0.4$, in particular, for neutrinos (Fig. 7.6) and angles bigger than 90^0 ($\cos\theta_\mu < 0$). As seen, the data are higher by $\sim 25-30\%$ than theoretical predictions. This outcome is consistent with the results shown in the panels on the bottom in Figs. 7.3-7.5.

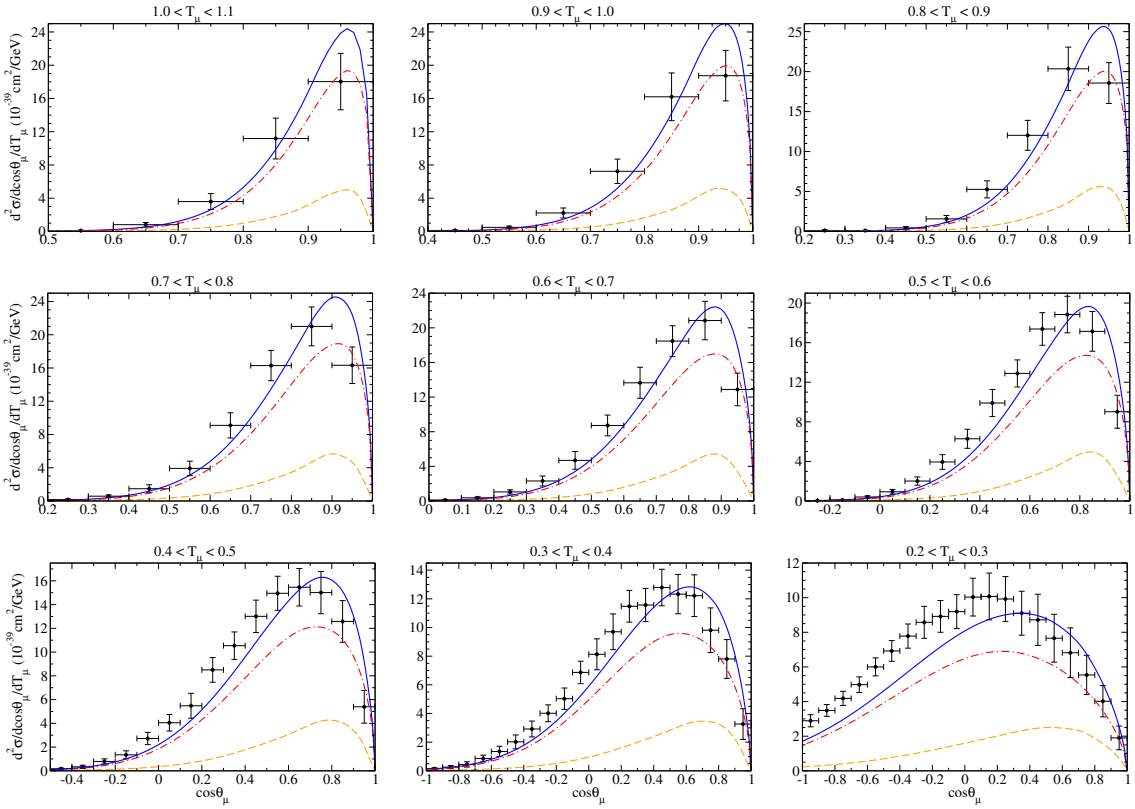

Figure 7.6: MiniBoone flux-folded double differential cross section per target nucleon for the ν_μ-^{12}C CCQE process displayed versus $\cos\theta_\mu$ for various bins of T_μ obtained within the SuSAv2-MEC approach. QE and 2p-2h MEC results are also shown separately. Data are from [20].

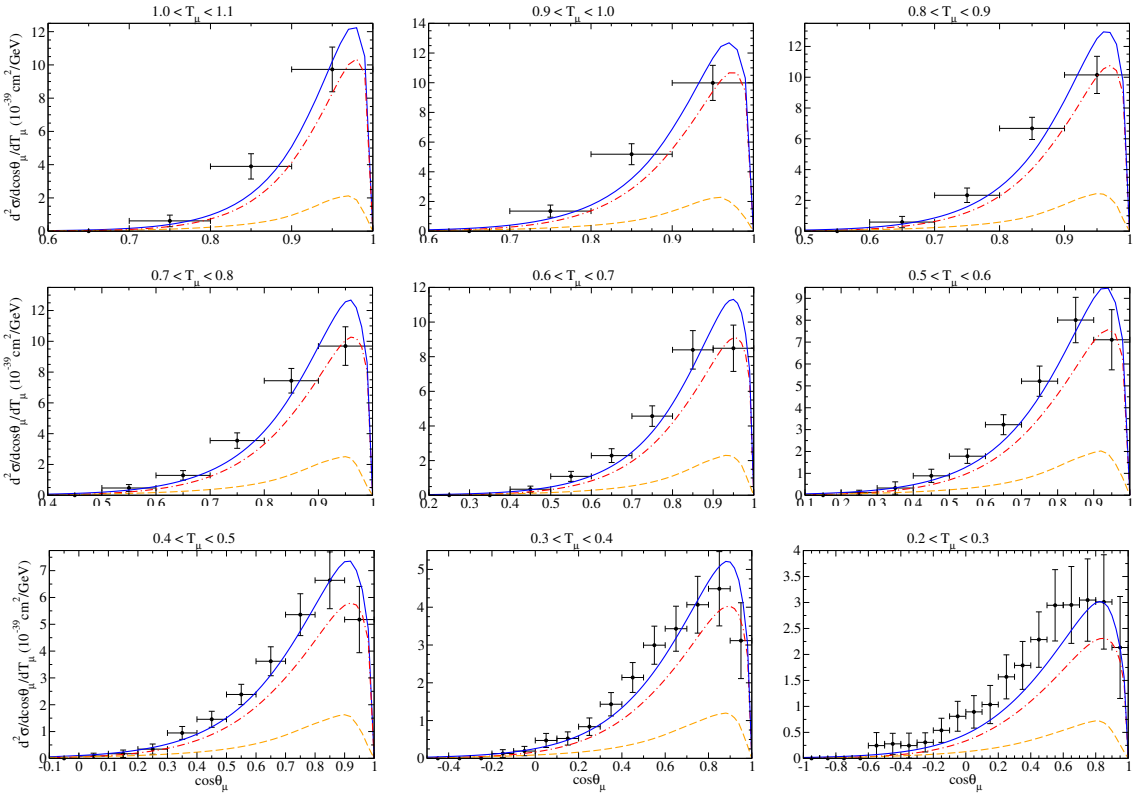

Figure 7.7: As for Fig. 7.6, but now for the $\overline{\nu}_\mu$ CCQE process on ^{12}C. Data are from [21].

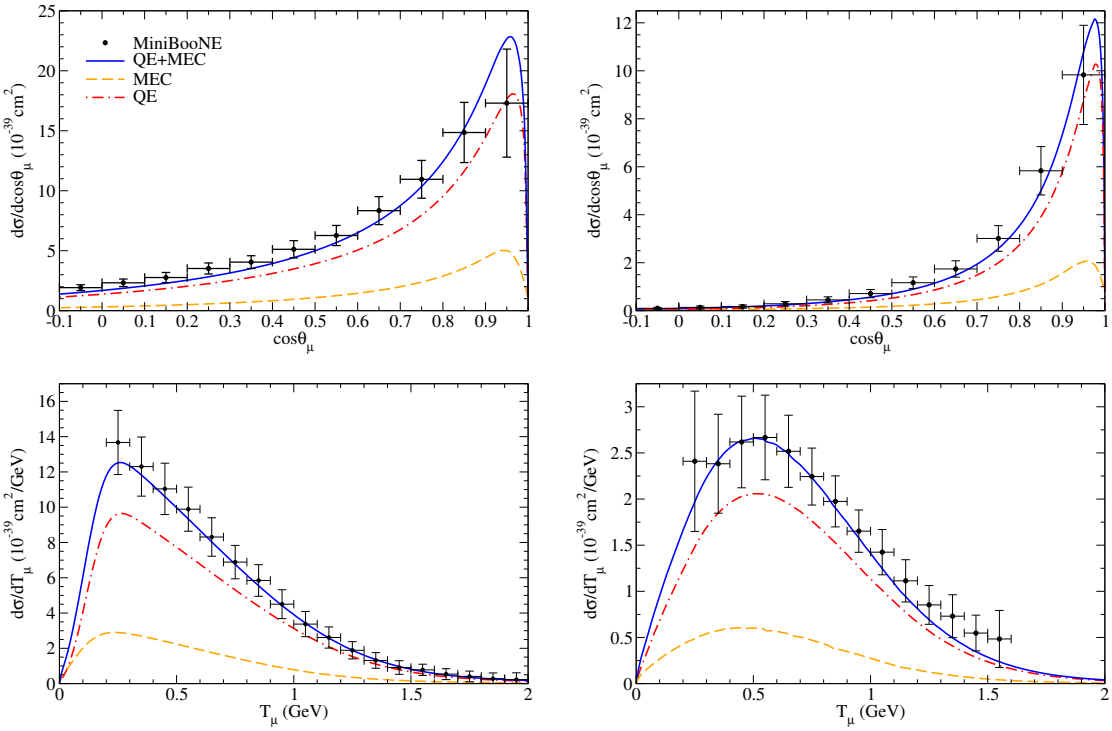

Figure 7.8: MiniBooNE flux-averaged CCQE ν_μ-^{12}C ($\bar{\nu}_\mu$-^{12}C) differential cross section per nucleon as a function of the muon scattering angle (top panels) and of the muon kinetic energy (bottom panels). The left panels correspond to neutrino cross sections and the right ones to antineutrino reactions. Data are from [20, 21].

In Fig. 7.8 results are presented for the MiniBooNE flux averaged CCQE $\nu_\mu(\overline{\nu}_\mu)-^{12}$C differential cross section per nucleon as a function of the muon scattering angle (top panels) and the muon kinetic energy (bottom panels). The integration over the muon kinetic energy has been performed in the range 0.2 GeV $< T_\mu <$ 2.0 GeV. Panels on the left (right) correspond to neutrinos (antineutrinos). As shown, and in consistency with previous results, the SuSAv2-MEC model is capable of reproducing the magnitude as well as the shape of the experimental cross section in all of the cases.

7.1.2 Analysis of longitudinal/transverse channels for neutrino reactions

In this section we study in detail the relevance of the different longitudinal and transverse channels that contribute to the QE and 2p-2h MEC MiniBooNE cross sections, also accounting for the corresponding axial and vector contributions which arise from the hadronic currents.

An analysis on the different channels for the 2p-2h MEC nuclear responses and the total cross section was addressed in Chapter 4 (see Figs. 4.9, 4.10 and 4.11), showing a predominance of the transverse over the longitudinal ones, whereas for the latter the contributions arising from vector currents were negligible in comparison with the axial ones. Moreover, the separate transverse channels, T_{VV}, T_{AA} and T'_{VA}, whereas showing some remarkable differences for different q values, contribute in a similar way to the total cross section. This is due to the relevant kinematic regions (see Section 7.3 for details). Here we explore the relevance of the different channels in the specific kinematics of the MiniBooNE experiment. In Fig. 7.9 the separate 2p-2h MEC contributions to the different channels (L, T_{VV}, T_{AA} and T'_{VA}) corresponding to the MiniBooNE double differential cross section at different bins of the muon scattering angle.

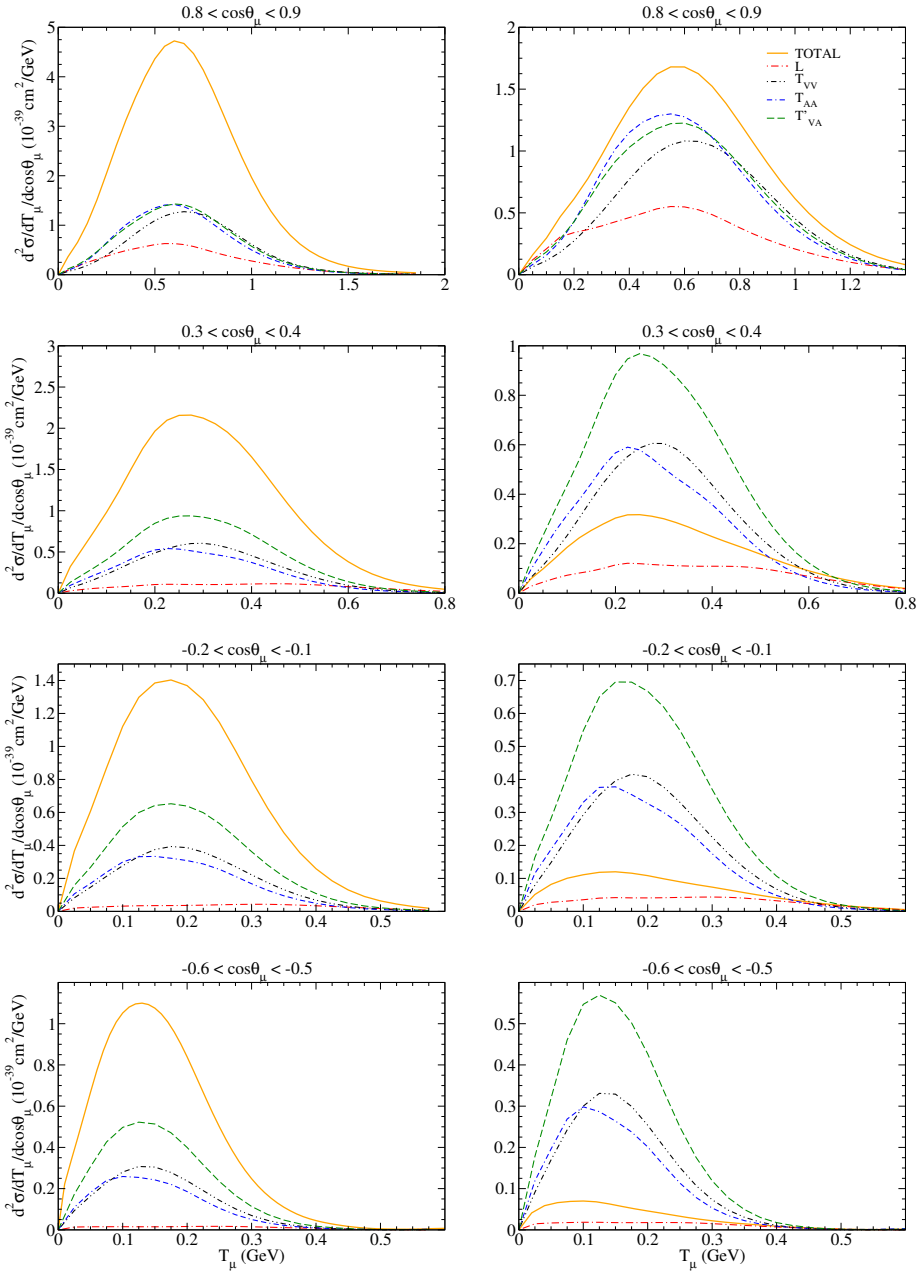

Figure 7.9: Comparison of the different 2p-2h MEC channels for the ν_μ (left panels) and $\overline{\nu}_\mu$ (right panels) MiniBooNE double differential cross section.

Results in Fig. 7.9 show the differences between the T_{AA} and T_{VV} contributions, the latter being shifted to higher T_μ values by about 50 MeV for all angular bins. At very forward angles, *i.e.*, lower q-values, the global magnitude of the AA channel is greater than the VV one, in accordance with the results observed in Fig. 4.11. This figure also shows clearly that at q of the order of 400 MeV/c the T_{VV} and T_{AA} responses differ roughly by a factor 2 at the maximum. This difference decreases for higher q-values. Concerning the interference T'_{VA} component, its magnitude is not so different from the VV and AA ones at very forward angles, being on the contrary the most relevant contribution at larger angles. Finally, although the longitudinal channel gives the smallest global contribution, its role is essential in order to interpret antineutrino scattering at backward angles. This is a consequence of the negative T'_{VA} term for antineutrino reactions that almost cancels out the $T_{VV} + T_{AA}$ contribution.

The conclusions extracted from the previous analysis on the 2p-2h MEC cross section also apply for the separate QE contributions to neutrino and antineutrino cross sections. The different QE channels are analyzed for the MiniBooNE double differential cross sections in Fig. 7.10, where the transverse contribution predominate at all kinematics whilst the net longitudinal channel, even being a very small contribution, is essential to describe antineutrino data at backward kinematics together with the 2p-2h longitudinal one.

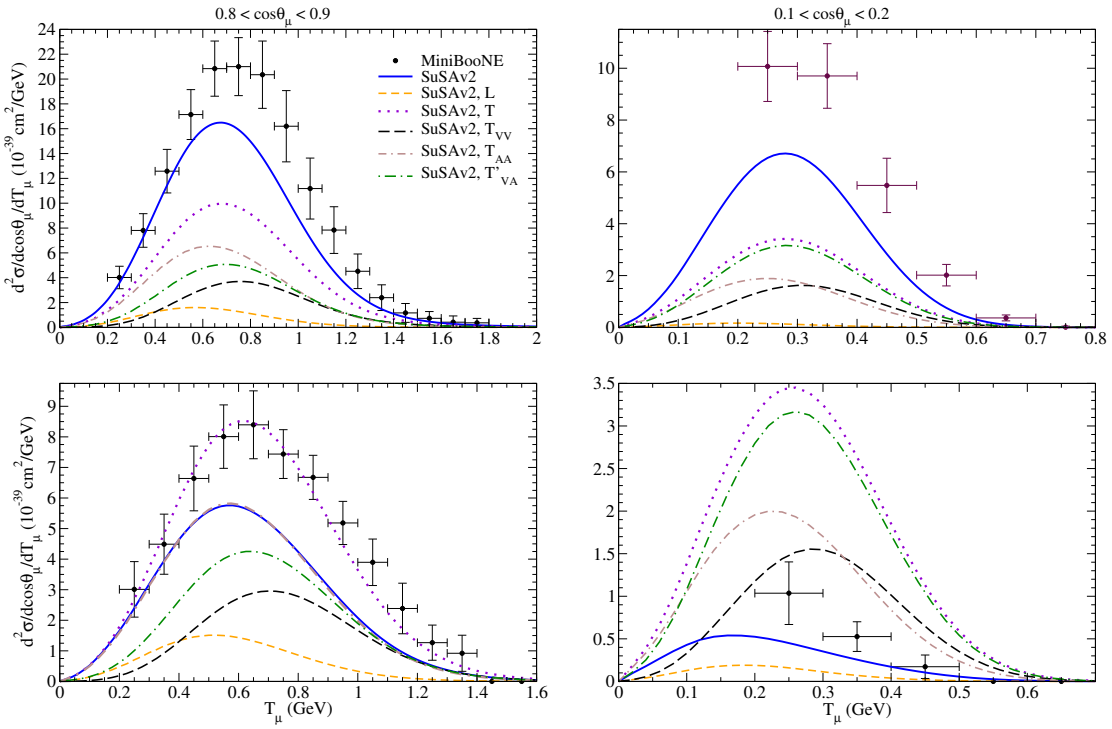

Figure 7.10: Separation into components of the MiniBooNE CCQE ν_μ (top panel) and $\bar{\nu}_\mu$ (botoom panel) double-differential cross section per nucleon displayed versus T_μ for various bins of $\cos\theta_\mu$ within the SuSAv2 approach. The MiniBooNE data [20, 21] are also shown for reference.

In Fig. 7.11 we show the breakdown of the total neutrino cross sections into individual $L(= L_{VV} + L_{AA})$, $T(= T_{VV} + T_{AA})$, T_{VV}, T_{AA} and T'_{VA} contributions, with the last occurring as a positive (constructive) term in the neutrino cross section and a negative (destructive) term in the antineutrino one. The sign of the T'_{VA} channel represents the main difference between the total neutrino and antineutrino cross sections (see also Fig. 7.1). Apart from the opposite sign in the VA response, some minor differences between neutrino and antineutrino cross sections arise from the different Coulomb distortions of the emitted lepton (see Section 7.3.2 for details) and the final nuclei involved in the CC neutrino (nitrogen) and antineutrino (boron) scattering processes on carbon. We also notice that below 1 GeV the T'_{VA} response is higher than the T_{VV} one and of the same order as the T_{AA} one. Note that the maximum of the VA contribution is around the peak of the MiniBooNE neutrino flux. On the contrary, the effects of VA contributions to the cross sections are negligible at energies above 10 GeV as a consequence of the small axial form factor G_A and leptonic factor $V_{T'}$ at high E_ν and Q^2 values (see Chapter 2 for details). This is also in agreement with some previous QE results [19]. As a consequence, for very high ν_μ ($\bar{\nu}_\mu$) energies (above $\sim$ 10 GeV) the total cross section for neutrinos and antineutrinos is very similar. Only the L and T channels contribute for the higher values explored by NOMAD experiment. On the contrary, in the region explored by the MiniBooNE collaboration, the main contributions come from the two transverse T, T' channels.

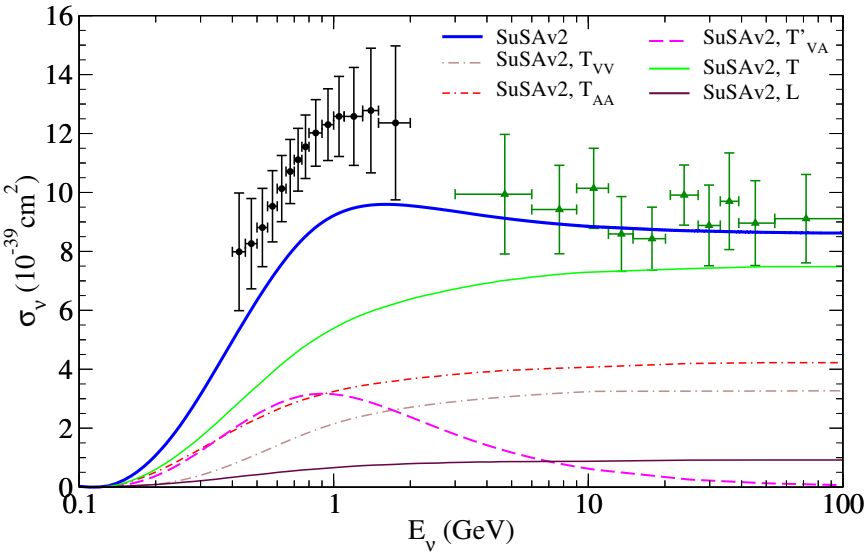

Figure 7.11: Separation into components of the CCQE ν_μ cross section per nucleon on ^{12}C displayed versus neutrino energy E_ν within the SuSAv2 approach. The MiniBooNE [20] and NOMAD [24] data are also shown for reference.

The asymmetry between neutrino and antineutrino cross sections introduced by the VA interference is analyzed in Fig. 7.12 where we show the experimental difference $(\sigma_{\nu_\mu} - \sigma_{\overline{\nu}_\mu})_{exp}$ from MiniBooNE, together with the corresponding theoretical prediction from the SuSAv2-MEC model. This difference is approximately equal to $2\,(\sigma_{\nu_\mu})^{SuSAv2}_{T'_{VA}} + 2\,(\sigma_{\nu_\mu})^{MEC}_{T'_{VA}}$, apart from the minor differences between neutrino and antineutrino reactions described above. The result from the purely QE responses is also shown, reinforcing the importance of the 2p-2h MEC contributions for the analysis of the MiniBooNE experiment and their relevance in the interference channel.

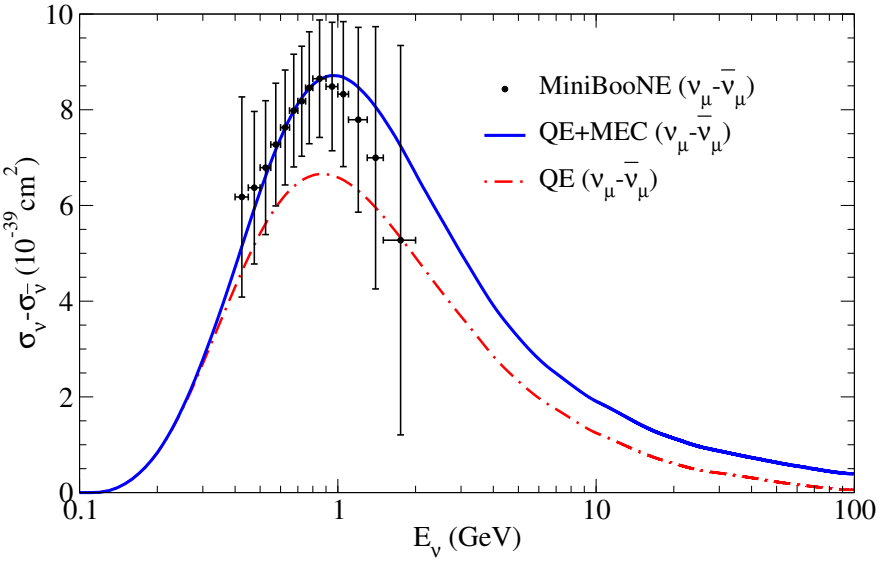

Figure 7.12: Experimental difference between neutrino and antineutrino cross sections $(\sigma_{\nu_\mu} - \sigma_{\overline{\nu}_\mu})$ from MiniBooNE, together with the corresponding theoretical prediction from SuSAv2+MEC. The purely QE response is also shown. MiniBooNE data are from [20, 21].

The asymmetry of the nuclear effects for neutrino and antineutrino is important for CP violation studies and it has been analyzed in previous works [3, 115, 164]. However, the inherent difficulties related to the different neutrino and antineutrino fluxes result in a potential obstacle for the interpretation of experiments aimed at the measurement of the CP violation angle. In this context, some preliminary studies on the CP asymmetry from the MINERνA Collaboration have been recently published [165]. Moreover, CP violation effects in the lepton sector related to the ν_μ and ν_e cross sections will be addressed in following sections.

7.2 CCQE-like scattering in the MINERνA experiment

In this section we apply the SuSAv2-MEC model to the analysis of the MINERνA experiment. The MINERνA Collaboration has recently measured differential cross sections for muonic and electron neutrino and antineutrino charged-current quasielastic scattering on a hydrocarbon target [46, 47]. The "quasielastic" events are defined, in this case, as containing no mesons in the final state (*CCQE-like*) thus also including contributions from multi-nucleon excitations. The energy flux extends up to 10 GeV and is peaked at $E_\nu \sim 3$ GeV for both neutrinos and antineutrinos, *i.e.,* in between MiniBooNE and NOMAD energy ranges. Therefore, its analysis can provide valuable information on the role played by 2p-2h meson-exchange currents in the nuclear dynamics [110, 166, 167].

7.2.1 Analysis of charged-current muonic neutrino results

In previous studies of the MINERνA Collaboration [46, 47], the RMF, SuSA and SuSAv2 models [97,153] as well as other theoretical approaches [168–170] were able to reproduce the MINERνA data without the inclusion of np-nh excitations, unlike the MiniBooNE results. It is important to point out that the MINERνA kinematics, larger than the MiniBooNE one, extends into the pion production region and hence the experimental subtraction of these effects to isolate CCQE-like events is more critical. Note that in these experiments only the information related to muon variables is considered. Moreover, the recently improved analysis of the MINERνA flux results [171] leads to an increase of the MINERνA CCQE-like experimental cross sections.

Considering the reevaluation of the MINERνA flux [171, 172], we present in Fig. 7.13 the flux averaged CCQE $\nu_\mu(\overline{\nu}_\mu)$ differential cross section per nucleon as a function of the reconstructed four-momentum Q^2_{QE}. This reconstructed magnitude is obtained following the procedure introduced in Section 7.1 and also detailed in [46, 47].

The top panel in Fig. 7.13 refers to ν_μ–^{12}C whereas the bottom panel contains predictions and data for $\overline{\nu}_\mu$–CH. The mean energy of the MINERνA muonic flux is much higher than the MiniBooNE one, about 3.5 GeV for both ν_μ and $\overline{\nu}_\mu$. As observed, significant contributions of the 2p-2h MEC, of the order of $\sim 35-40\%$ ($\sim 25\%$) at the maxima for ν_μ ($\overline{\nu}_\mu$), are needed in order to reproduce the experimental data that correspond to a new analysis performed by the MINERνA collaboration [171, 172]. These data exceed by $\sim 20\%$ the ones already presented in previous publications [46, 47] (using the uncorrected MINERνA flux) that, on the other hand, were consistent with calculations based exclusively on the impulse approximation (see [97]).

Thus, the new MINERνA analysis shows major consistency with the MiniBooNE data and invalidates the previous conclusion [97] that the MINERνA results can be reproduced without the

inclusion of 2p-2h contributions. In spite of the very different muon neutrino (antineutrino) energy fluxes between MiniBooNE and MINERνA, 2p-2h MEC effects remain very significant (on average, 25 – 35%) being their contribution essential in order to reproduce the data.

For completeness, it is worth mentioning that in the specific conditions of MINERνA, it clearly appears that, even if the neutrino energy is as large as 3 GeV, the process is largely dominated by relatively small energy and momentum transfer, namely, $\omega < 500$ MeV, $q < 1000$ MeV, whereas contributions below $\omega < 50$ MeV, $q < 200$ MeV govern the lowest Q^2_{QE} region. More specific details can be found in Section 7.3 and, additionally, in Ref. [97].

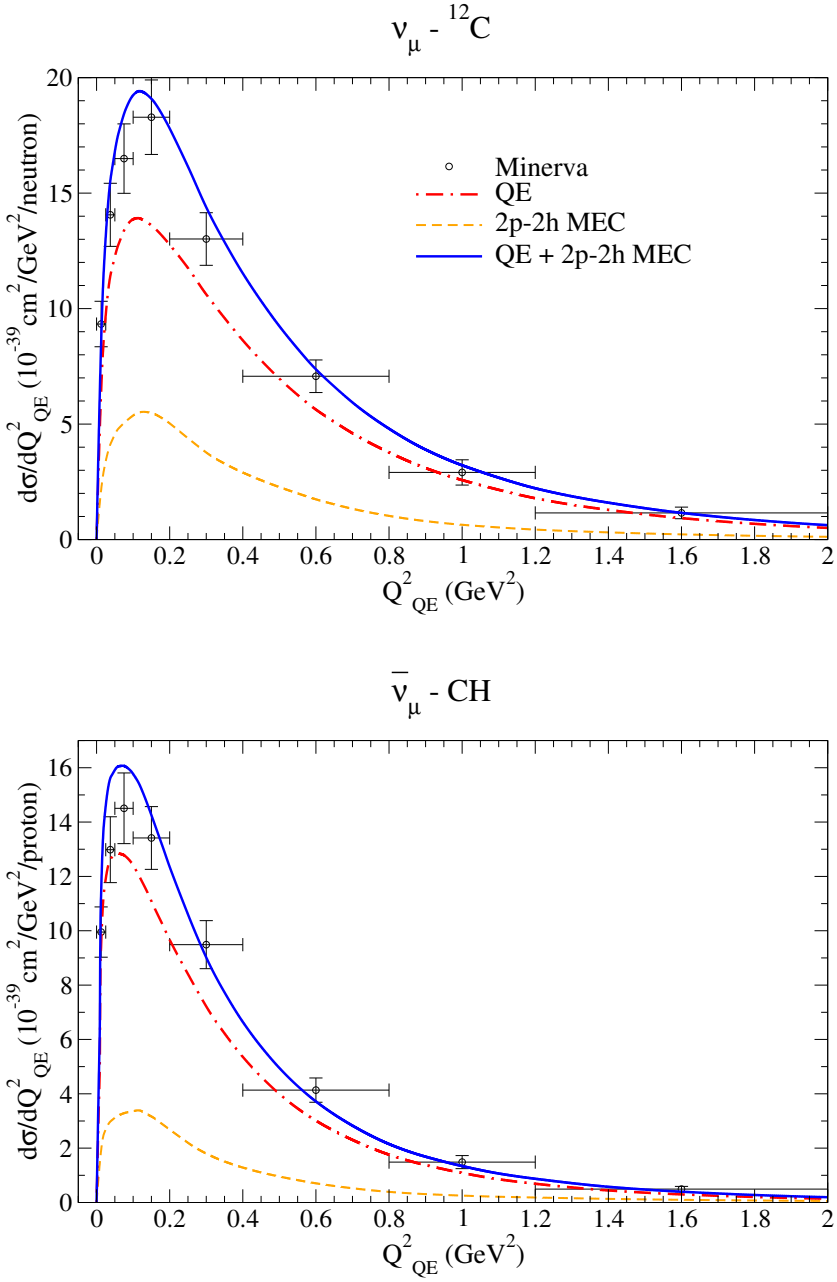

Figure 7.13: Flux-folded ν_μ–^{12}C CCQE (upper panel) and $\bar{\nu}_\mu$–CH (lower panel) scattering cross section per target nucleon as a function of Q^2_{QE} and evaluated in the SuSAv2 and SuSAv2-MEC models. MINERνA data are from [172].

7.2.2 Analysis of charged-current electron neutrino results

The previous conclusion holds also for the ν_e CCQE-like differential cross sections on hydrocarbon published by MINERνA in [53]. These results are presented in Fig. 7.14 as a function of the electron energy (top-left panel), electron angle (top-right) and reconstructed four-momentum (bottom-left). Compared to the ν_μ ($\overline{\nu}_\mu$) fluxes, the ν_e and $\overline{\nu}_e$ ones have roughly the same shape in the region of the peak but the tail region at large energies is significantly higher in the electronic case which softly increases the average ν_e energy up to 3.6 GeV. A detailed comparison of the ν_e versus ν_μ cross sections is addressed in Section 7.4.

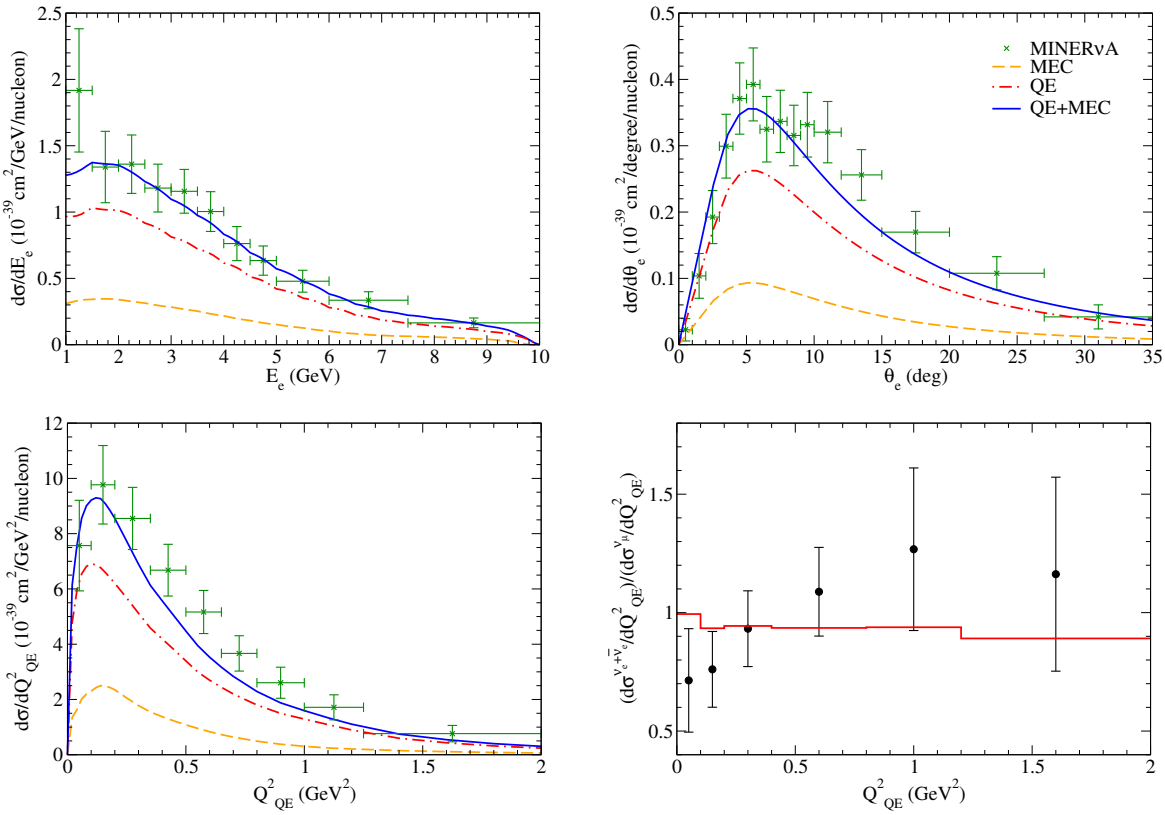

Figure 7.14: MINERνA flux-integrated differential ν_e-^{12}C CCQE-like cross section per nucleon vs. electron energy (top left) and electron angle (top right). The bottom panels show the ν_e differential cross section vs. Q^2_{QE} (bottom left) and the ratio between the flux averaged CCQE $\nu_e+\overline{\nu}_e$ and ν_μ cross sections versus Q^2_{QE} (bottom right) compared with the SuSAv2-MEC prediction (solid red line). Data are from [53].

In Fig. 7.14, results are shown for the pure QE response based on the IA, the 2p-2h MEC contribution and the total response. In all the cases the contribution at the maximum coming from the 2p-2h MEC is roughly 30 – 35% compared with the pure QE response. These results are similar to the ones already presented for muon neutrinos (antineutrinos), and they show the importance of 2p-2h effects in order to explain the behavior of data. As observed, the model is capable of reproducing successfully the data. For completeness, we present in the right-bottom panel the results corresponding to the ratio between the flux averaged CCQE $\nu_e + \overline{\nu}_e$ and ν_μ cross sections versus the reconstructed four-momentum. We compare the predictions of the model (red curve) with the data, leading to a similar result as when compared with GENIE predictions [53], *i.e.*, the SuSAv2-model predicts a rather flat ratio while the experimental data seem to grow up to $Q^2_{QE} \approx 1$ GeV^2. Taking into account that the $\overline{\nu}_e$ flux is negligible in comparison with the ν_e

one, the main differences in the ratio comes mainly from the shape differences between the ν_e and ν_μ fluxes. In addition, some differences also emerge from the diverse phase-space of the ν_e-ν_μ-^{12}C interactions which is due to the different final-lepton masses, being more prominent at low kinematics (see Section 7.4 for further discussions). However, the large error bars presented by the data make it hard to extract definite conclusions.

7.3 Relevant kinematical regions

In this section, the relevant kinematical regions for the description of neutrino-nucleus reactions are analyzed within the SuSAv2-MEC model at kinematics of relevance for the MiniBooNE, T2K and MINERνA experiments. We also inspect other contributions that may play a significant role at low kinematics such as the mass of the residual nuclei or the influence of Pauli-blocking effects.

For a proper understanding of the neutrino experimental results as well as to assess the appropriate description of the nuclear dynamics in theoretical models, it is important to identify the kinematical region where the QE and 2p-2h MEC responses attain their maximum values. This is clearly illustrated in the density plot of Fig. 7.15, which represents the double differential cross section in terms of ω and q at $E_\nu = 3.0$ GeV, that corresponds to the peak energy flux of MINERνA [171]; here the left (right) panel corresponds to the 2p-2h MEC (pure QE) contributions. As shown in the figure, the main contribution to the MEC cross section comes from $q \in (0.3, 1.0)$ GeV/c and $\omega \in (0.3, 0.8)$ GeV. On the contrary, the QE peak is moved to lower values of ω. Both the one-body and two-body responses decrease with the momentum transfer q, but their ratio is rather constant (see [105] for details). Although results in Fig. 7.15 correspond to a fixed incident neutrino energy, 3 GeV, similar results are obtained for larger E_ν values. It is important to point out the differences between our predictions and those based on the model of Nieves [168] that show the 2p-2h MEC contribution to be shifted to slightly bigger values of the energy and momentum transfer.

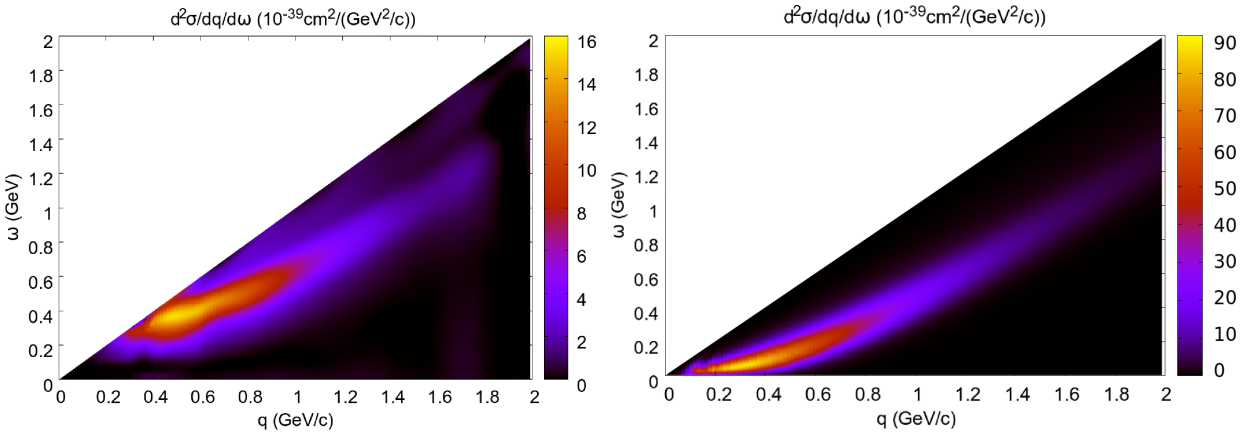

Figure 7.15: 2p-2h MEC (left panel) and QE (right panel) density plots of the double-differential cross section per neutron of ^{12}C versus ω and q at $E_\nu = 3$ GeV.

For completeness, we also show in Fig. 7.16 the density plots for the 2p-2h MEC contributions in terms of the values of the muon kinetic energy and the scattering angle for three values of neutrino energy: 1 GeV (top panel), 3 GeV (middle) and 10 GeV (bottom). It is worth mentioning that $E_\nu = 1$ GeV and $E_\nu = 3$ GeV are reference values, respectively, to the mean neutrino energies for MiniBooNE and MINERνA experiments. As observed, the main contribution resides in the

region of very small angles, close to zero, and large T_μ, which correspond to low-intermediate ω values. These effects are maximized as E_ν increases.

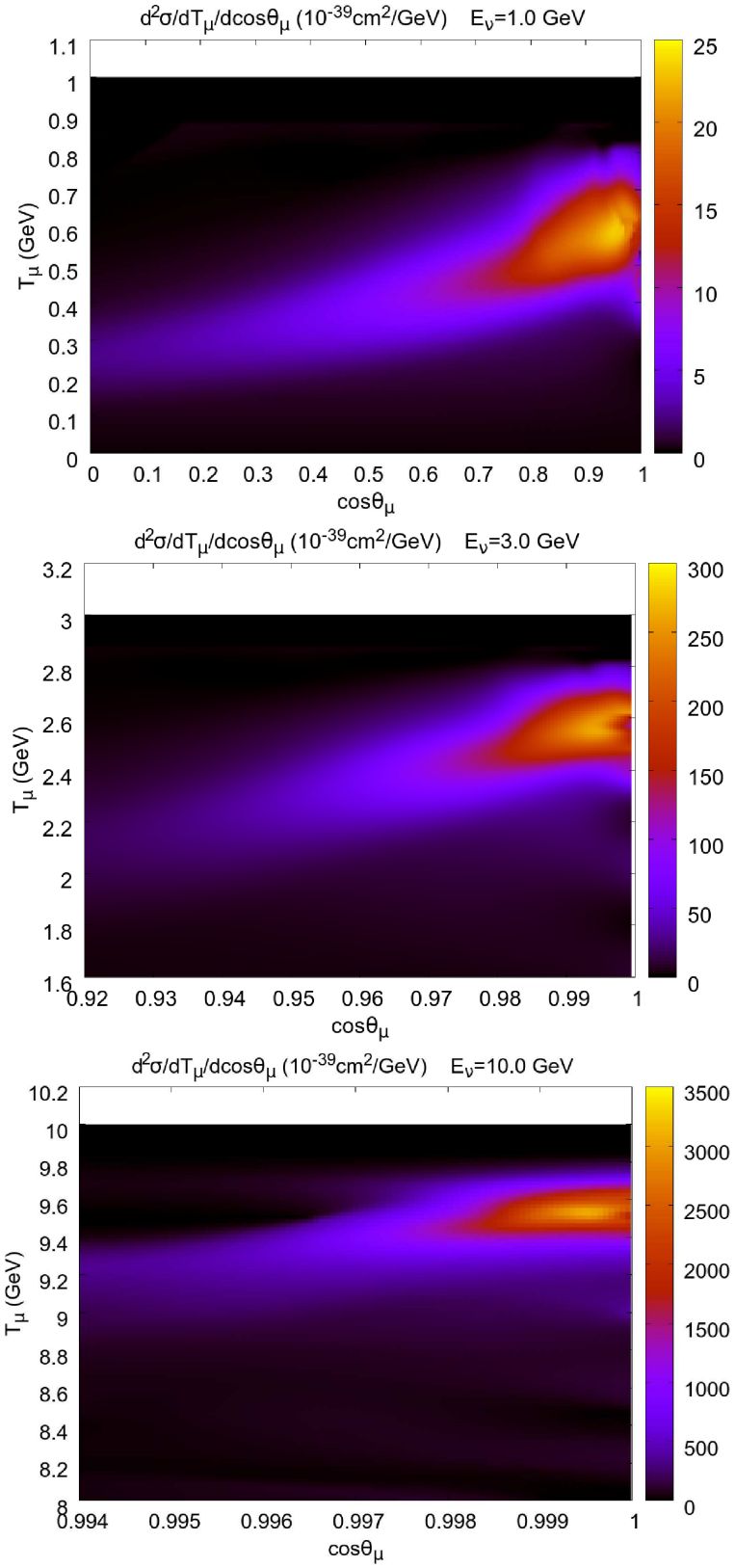

Figure 7.16: 2p-2h MEC density plots of the double-differential cross section per neutron of ^{12}C at three different neutrino energies E_ν versus T_μ and $\cos\theta_\mu$.

Moreover, an analysis of the relevant kinematical regions for the total QE cross section is shown in Fig. 7.17, where it is observed that the main contribution comes from $\omega < 500$ MeV and $q \lesssim 1000$ MeV/c whereas the region of small $\omega < 50$ MeV and $q < 250$ MeV/c, which contributes substantially at very forward angles, is not too significant for the total neutrino cross section ($\sim 8\%$). This is in accordance with some previous works [19, 97]. The same conclusion can be drawn by analyzing the different kinematics in the total MEC cross section (Fig. 7.18), where the low kinematic region ($\omega < 50$ MeV, $q < 250$ MeV/c) is even less important ($< 2\%$) for the 2p-2h channel. We can also notice in Fig. 7.18 that no significant MEC contributions emerge for $q >$2000 MeV/c and the same is true for large $\omega > 1000$ MeV. This analysis leads to the conclusion that relativistic effects cannot be ignored in theoretical models aimed at describing neutrino oscillation experiments.

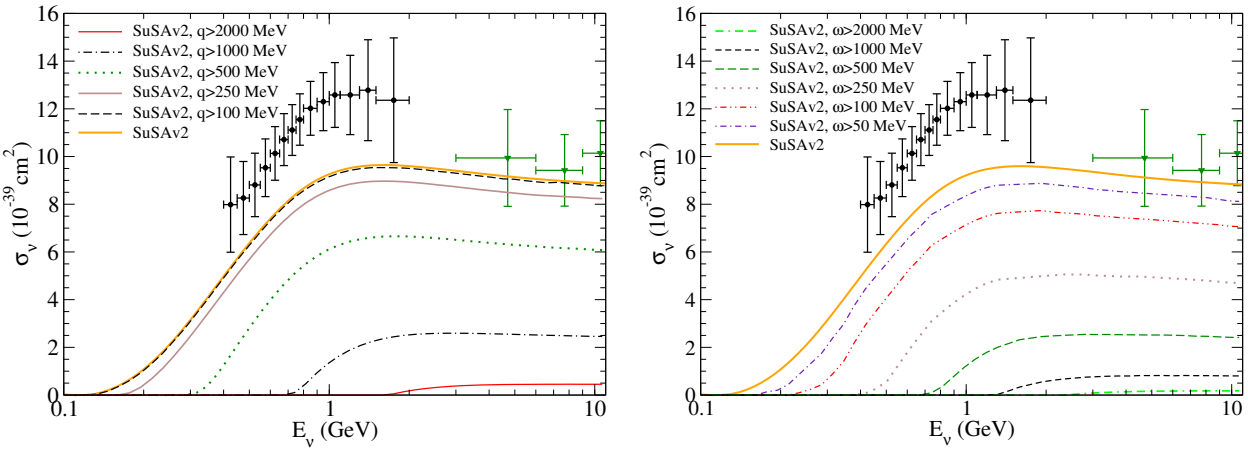

Figure 7.17: SuSAv2 ν_μ-^{12}C total cross section per target nucleon evaluated excluding all contributions coming from transferred momentum (left panel) and energy (right panel) below some selected values, as indicated in the figure. The MiniBooNE [20] and NOMAD [24] data are also shown for reference.

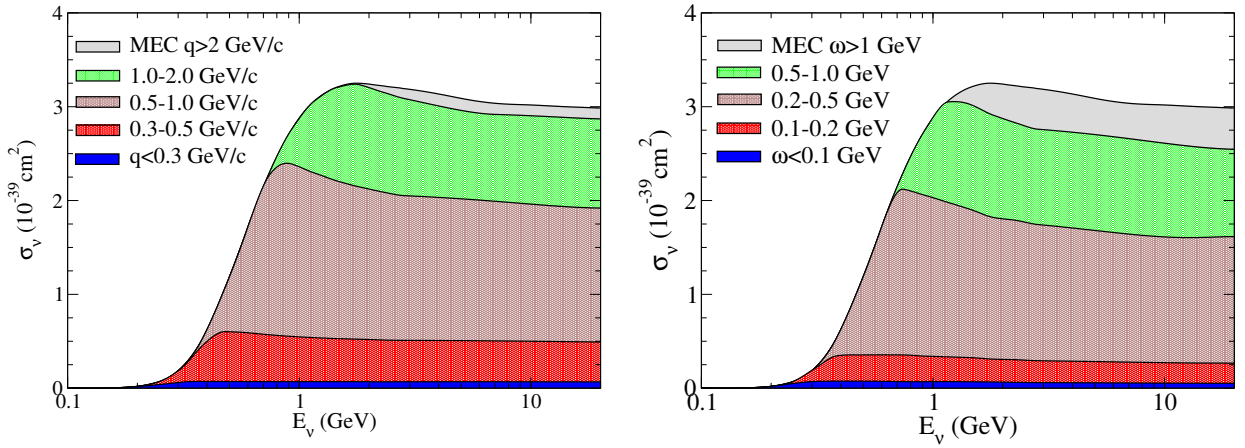

Figure 7.18: 2p-2h MEC ν_μ-^{12}C total cross section per target nucleon evaluated excluding all contributions coming from transferred momentum (left panel) and energy (right panel) below some selected values, as indicated in the figure.

7.3.1 Low-energy effects

Next, it is also important to analyze the relevance of the low-energy effects in our description which englobe Pauli-blocking effects, mass excess of the residual nucleus and the Coulomb distortions of the emitted lepton.

As introduced for (e,e') reactions in Section 3.5.1, the effect of Pauli Blocking (PB) is also of relevance for the analysis of CCQE neutrino cross sections. We concluded from Figs. 3.15—3.17 that these effects are noticeable for $q < 250$ MeV/c and $\omega \lesssim 50$ MeV. Nevertheless, when analyzing flux-folded cross sections, the convolution over a wide range of energy can make these effects being irrelevant in some cases where low-kinematics do not play a major role. In Fig. 7.19, we notice the small contribution of PB effects on the MiniBooNE double differential cross section at forward kinematics. On the contrary, if we focus on the smallest values of Q^2, which are directly related to the low q and ω kinematic region, we would observe a significant increase of the cross section when neglecting Pauli blocking. This is clearly illustrated in Fig. 7.20, where the omission of PB effects would result in an overstimation of the MINERνA data at low Q^2_{QE}, after considering 2p-2h contributions.

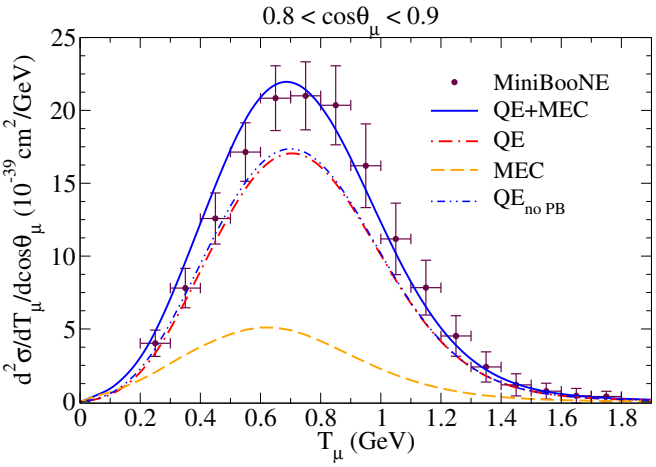

Figure 7.19: Analysis of Pauli-blocking effects ($\text{QE}_{\text{no PB}}$) on the MiniBoone ν_μ–^{12}C flux-folded double differential cross section. The results are displayed versus the μ^- kinetic energy T_μ for various bins of $\cos\theta_\mu$. The QE+MEC results as well as the separated QE and 2p-2h MEC ones are also shown for reference. Data are from [20].

Moreover, there are also other contributions which may play an important role in the low-kinematic region. In Chapter 3, we define a sort of excitation energy ω_0, related to the mass excess of the residual nucleus, which sets a minimum neutrino energy necessary for the interaction (see Eq. 3.6 for details). In the case of neutrino and antineutrino reactions on ^{12}C, the mass excess of the final nuclear system is $\Delta N = 13.88$ MeV (nitrogen) for neutrinos and $\Delta B = 16.83$ MeV (boron) for antineutrinos, which turns into a restriction of a few MeV in the allowed ω values. This apparently minor effect has a large relevance at very forward kinematics, *i.e.*, low ω region. This can be observed in Fig. 7.21 for the MiniBooNE double differential cross section where it is assumed $\Delta N = 0$. This effect at $\cos\theta_\mu \sim 0.95$ would increase the cross section around 15%.

We also show in Fig. 7.21 the cross section computed excluding contributions coming from $\omega < 50$ MeV to assess the importance of low-energy excitations in the total cross section. Likewise, the most sensitive region corresponds to very forward kinematics. As it was observed in Fig. 7.17, this low-ω region is quite important even for very high neutrino energies (typically amounting to

about 10% of the total cross section). Similar results can also be observed in [173, 174]. In [175] the contribution of the discrete excitations of the final nucleus ^{12}N in CC neutrino scattering from ^{12}C was evaluated in a semi-relativistic shell model. This contribution turned out to be below 2% for potential parameters fitted to reproduce the Q-value of the reaction.

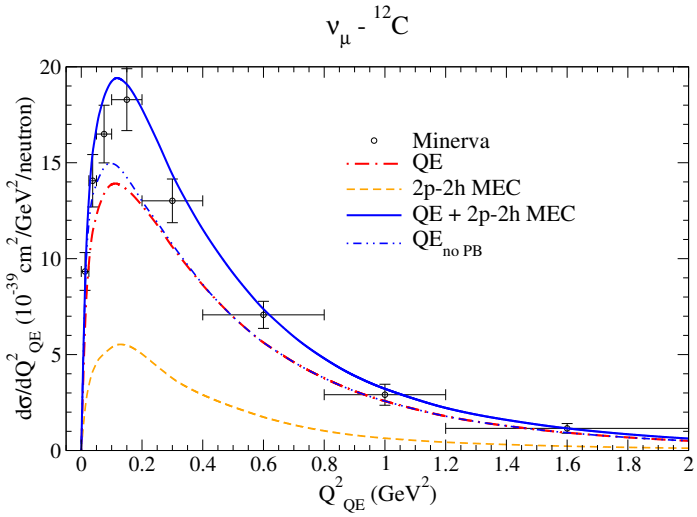

Figure 7.20: Flux-folded ν_μ–^{12}C CCQE scattering cross section per target nucleon as a function of Q^2_{QE} and evaluated in the SuSAv2 and SuSAv2+MEC models. The QE contribution without Pauli Blocking effects is also displayed (dot-dot-dashed line). MINERνA data are from [172].

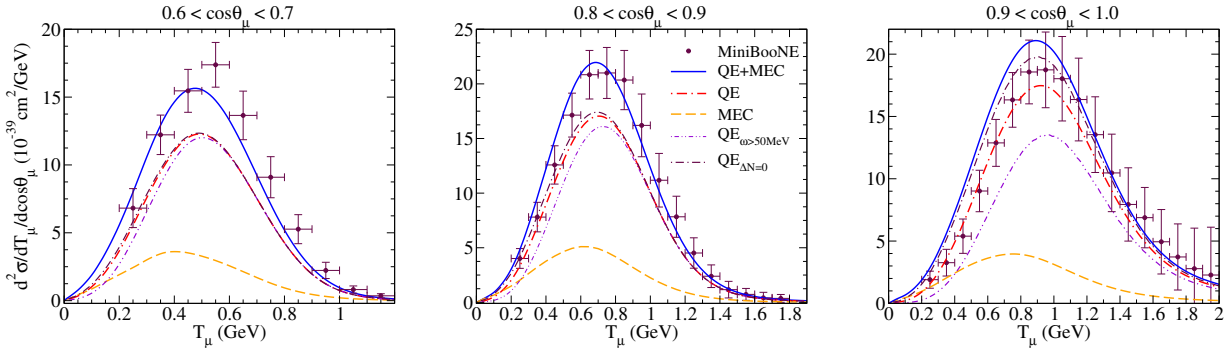

Figure 7.21: Analysis of low-energy effects on the MiniBoone ν_μ–^{12}C flux-folded double differential cross section. The SuSAv2 results for $\omega > 50$ MeV and $\Delta N = 0$ are displayed separatedly versus the μ^- kinetic energy T_μ for various bins of $\cos\theta_\mu$. The QE+MEC results as well as the separated QE and 2p-2h MEC ones are also shown for reference. Data are from [20].

7.3.2 Coulomb corrections on the emitted lepton

Finally, one additional issue arises in computing charged-current neutrino cross sections where charged leptons in the final state are not strictly described by plane waves as they are influenced by the Coulomb potential of the nucleus. These Coulomb distortions of the emitted lepton are accounted for in our theoretical prescription and can significantly alter the momentum and direction of the final-state particles. These effects are present in all neutrino-nucleus interactions, but can largely be ignored at high E_ν where most final-state particles are produced with high momenta. Nevertheless, they can be more important at lower E_ν, where the momentum of the target is of similar magnitude to the neutrino one and, hence, the outgoing lepton can be largely affected by

the nuclear potential. It is important therefore that neutrino interaction experiments are aware of the consequences of these low-energy effects for their analysis.

Following standard procedures (see, for instance, [64, 176]) the Coulomb interaction can be incorporated in our prescription, at least approximately, by shifting from the local lepton variables $(E_l, \vec{k}_l)$ to asymptotic energy-momentum ones $(E_l^\infty, \vec{k}_l^\infty)$:

$$\vec{k}_l^\infty = D(k_l)\vec{k}_l \tag{7.5}$$

$$E_l^\infty = \sqrt{m_l^2 + \left(\vec{k}_l^\infty\right)^2}, \tag{7.6}$$

where

$$D(k_l) = 1 - \chi \frac{3Z\alpha}{2R|\vec{k}_l|} \tag{7.7}$$

with $\chi = +1(-1)$ for neutrinos (antineutrinos) and $R \cong 1.2A^{1/3}$ the effective charge radius of the nucleus considered. Thus, the local calculations must be multiplied by the density-of-states factor $[D(k_l)]^{-1}$ to include these distortion effects.

Therefore, these Coulomb effects depend on the charge properties of the nucleus as well as on the charge of the final lepton, which is negative (positive) for neutrinos (antineutrinos), thus increasing (decreasing) the resulting cross section. Thus, these effects increase slightly the cross section for neutrino reactions whereas the opposite occurs for antineutrinos as shown in Fig. 7.22 for the total cross section within the SuSAv2 model. We also notice that the relevance of this corrections are smaller than 2% for $E_\nu \sim 0.4$ GeV whereas differences of $\sim 10\%$ can be found at the lowest energies where the cross sections are also minor. For completeness, the Coulomb effects are also analyzed at low energies (E_ν) for the double-differential CCQE ν_μ-^{12}C cross section in Fig. 7.23. In this case, Coulomb distortions modify the cross section by a $\sim$ 2% at the lowest ω values. These effects are largely increased for high-ω values where the energy of the emitted lepton is very small. Nevertheless, this kinematic region does not contribute significantly to the cross section.

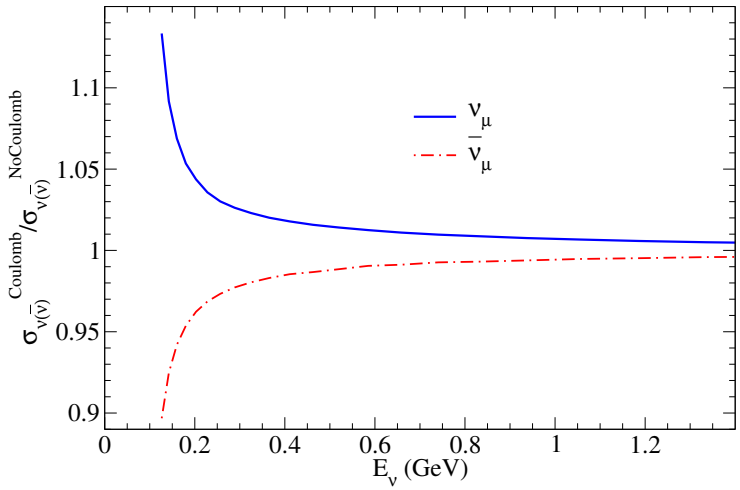

Figure 7.22: Ratio of the CCQE on $(\overline{\nu}_\mu)\nu_\mu$-^{12}C total cross section with and without considering Coulomb distortions of the emitted letpon. Results are shown for neutrino and antineutrino reactions.

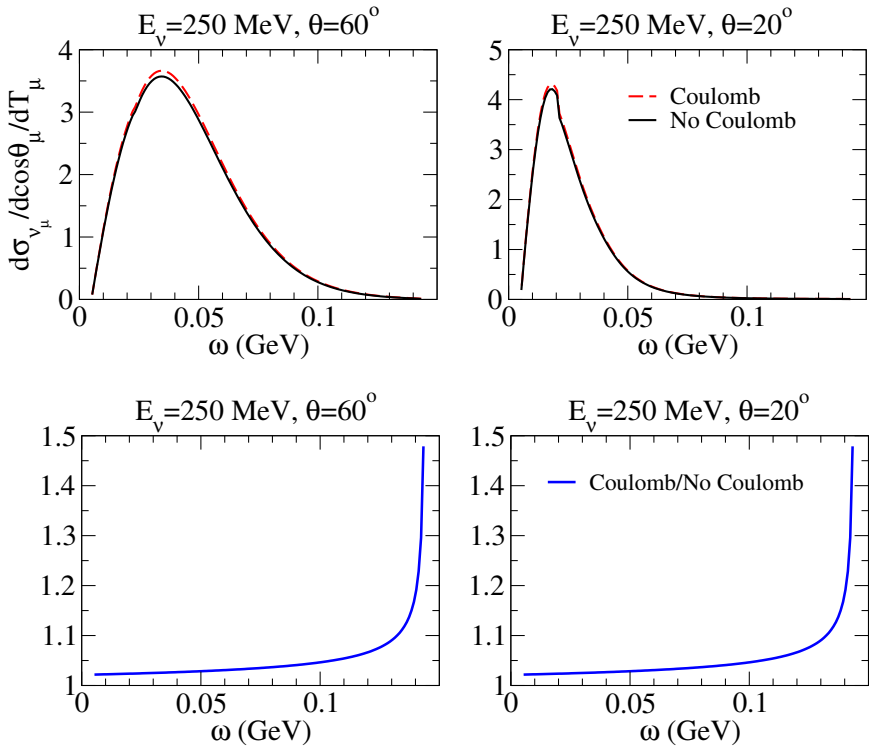

Figure 7.23: Top panels: CCQE ν_μ-^{12}C double differential cross section with and without considering Coulomb distortions of the emitted letpon for two different scattering angles at E_ν = 250 MeV. Results are given in nb/GeV. Bottom panels: Ratio of the CCQE ν_μ-^{12}C double differential cross section with and without considering Coulomb distortions for the above kinematics.

7.4 Electron neutrino versus muon neutrino cross sections

Most of the current neutrino oscillation experiments as well as the theoretical approaches that deal with their description focus on the analysis of ν_μ cross sections in contrast with the few published measurements on ν_e cross sections. The relatively small components of ν_e and $\overline{\nu}_e$ flux in neutrino beams coupled with significant backgrounds arising from the dominant ν_μ interactions have led to a shortage of ν_e and $\overline{\nu}_e$ measurements in the energy range from 0.5 to a few GeV. This turns into a small-statistics measurements for ν_e reactions. Gargamelle [177], NOνA [178] and T2K [45] have published ν_e inclusive cross section results at these energies, but small statistics and the inclusive nature of these measurements limit their usefulness for model comparisons. Nevertheless, a detailed and simultaneous knowledge of ν_μ and ν_e cross sections is decisive in connection to the $\nu_\mu \rightarrow \nu_e$ oscillation experiments aiming at the determination of the neutrino mass hierarchy and the search for CP violation in the leptonic sector. In this sense, the recent measurements of ν_e and $\overline{\nu}_e$ CCQE-like interactions from MINERνA [53] at energies around $\sim$ 3.6 GeV, overlapping the energy range of NOνA [178] and DUNE [60], represent an outstanding exception. As shown in Section 7.2.2, their relatively high statistics allows for a detailed analysis of the flux-integrated differential cross-section measurements for the ν_e CCQE-like process as well as for a comparison of the ν_e and ν_μ quasielastic cross sections as a function of $Q^2_{\rm QE}$. Furthermore, the ArgoNEUT Collaboration has recently presented the first experimental observation of ν_e and $\overline{\nu}_e$ on argon in the energy region of $\sim$ 4 GeV [179].

In this connection, we present here a comparison of ν_e and ν_μ cross sections and their corresponding ratios. These are interesting quantities to analyze the differences between ν_e and ν_μ scattering which are influenced by the kinematical restrictions due to the different final-lepton masses, radiative corrections, Coulomb distortions and to uncertainties in the nucleon form factors. In Fig. 7.24 we compare the ν_e ($\overline{\nu}_e$) and ν_μ ($\overline{\nu}_\mu$) total cross sections in the SuSAv2 model for the kinematics relevant for different ν_e experiments (T2K, NOνA, DUNE or MINERνA) as well as for the proposed facility νSTORM [58, 59], which will provide high quality electron neutrino beams in the energy range $E < 4$ GeV. Although the hadronic interaction is the same for ν_μ and ν_e, the different mass of the outgoing leptons produces a different energy transfer to the nucleus for the same incident neutrino energy. As seen in Fig. 7.24, this results in a small shift for low neutrino energy. For higher energies the small differences due to the lepton mass tend to disappear, yielding a universal curve for the total cross section, independent of the neutrino flavour. This is emphasized in Fig. 7.25, where the ratios ν_e/ν_μ and $\overline{\nu}_e/\overline{\nu}_\mu$ for the total CCQE cross sections are shown, reaching both unity at energies above 1 GeV. For small energies one expects that the different nuclear excitation energy involved and the energy-dependence of the nuclear response functions will emphasize differences between the two cross sections, or between either of these and more sophisticated modeling of the low-lying nuclear excitations. Some theoretical calculations on this line can be found in [180]. A precise measurement of the cross sections in this region might therefore allow one to extract new information concerning the electroweak nuclear matrix elements.

We note that the difference between the two cases is also linked to the Coulomb corrections, *i.e.,* distortions of the final-state charged lepton wave functions in the Coulomb field of the nucleus. These are taken into account using the effective momentum approximation described in Section 7.3.2 (see also [64]). Their effects were found to be negligible in the energy range considered (up to 1 GeV), becoming important only at neutrino energies below 250 MeV, where the cross sections are substantially smaller.

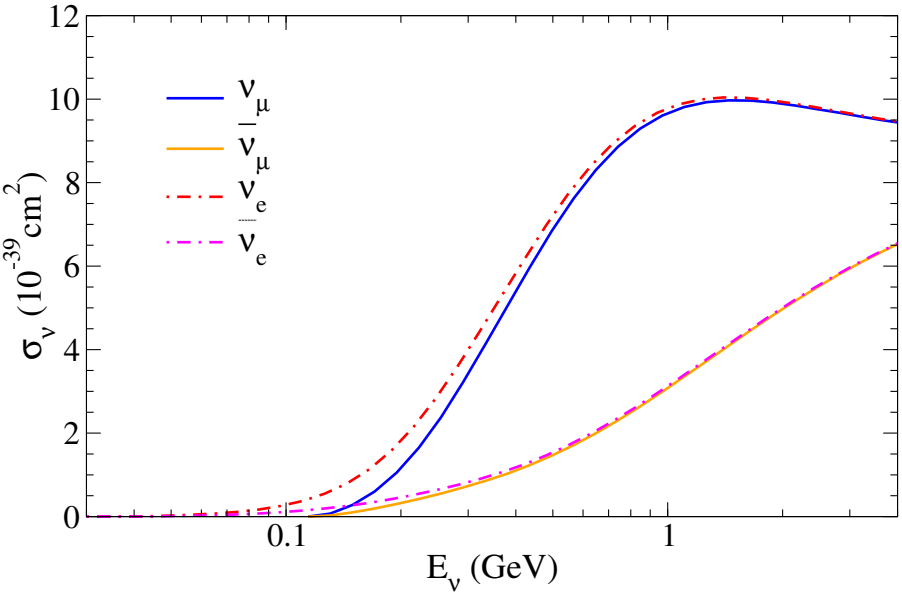

Figure 7.24: SuSAv2 predictions for muon- (solid curves) and electron- (dot-dashed curves) neutrino and antineutrino CCQE cross section per nucleon on ^{12}C.

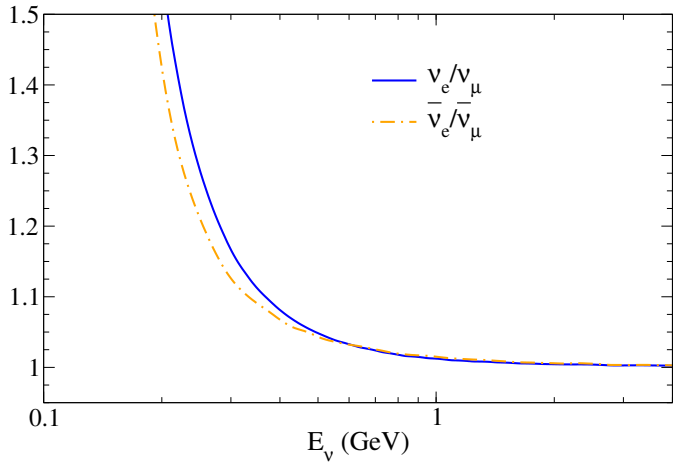

Figure 7.25: Ratio of the SuSAv2 predictions for muon- and electron- neutrino (solid line) and antineutrino (dot-dashed line) CCQE cross section per nucleon on ^{12}C.

For completeness, we present in Fig. 7.26 the ν_e and ν_μ double-differential cross section on ^{12}C within the SuSav2 model at different kinematics, where the effects due to the final-lepton masses are clearly prominent at lower energies (E_ν = 250 MeV), leading to a reduction of $\sim$ 30% for ν_μ at the peak position. Additionally, a small shift to lower ω is observed. These effects roughly disappear at $E_\nu \geq$ 750 MeV. Similar results for the ν_e cross section are found in [180] within the RPA (random phase approximation) and CRPA (continuum random phase approximation) approaches. On the contrary, the RPA and SuSAv2 models are not capable of reproducing the low-lying nuclear excitations below ω = 50 MeV shown by the CRPA calculations.

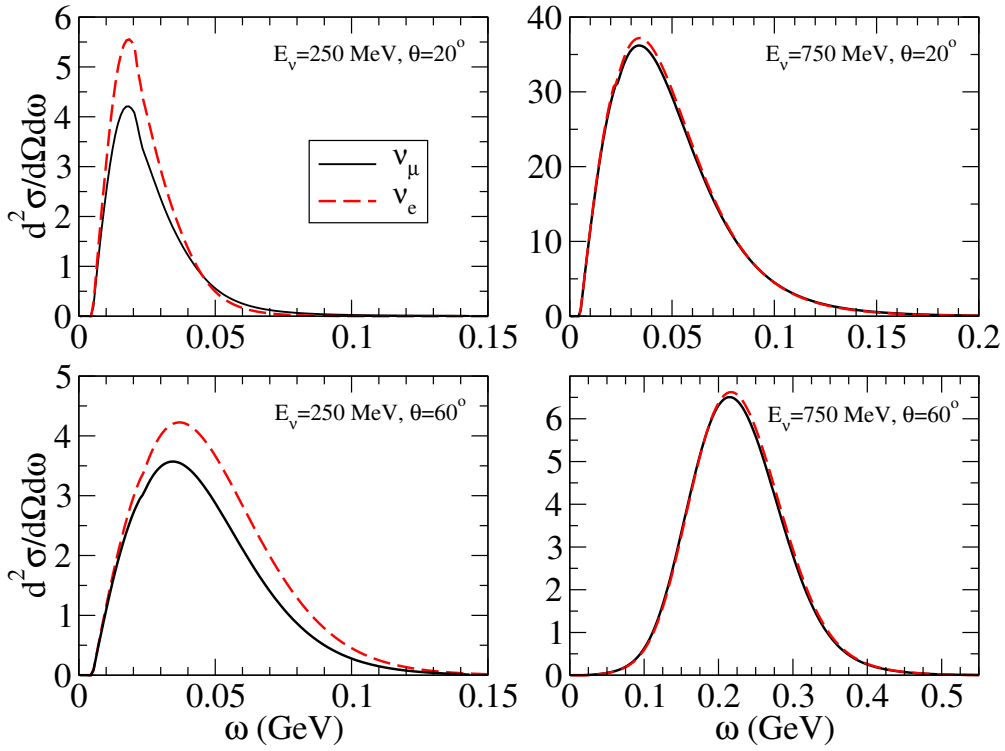

Figure 7.26: SuSAv2 predictions for muon- and electron- neutrino CCQE double-differential cross section per nucleon on ^{12}C for the fixed values of $E\nu$ and θ displayed in the figures.

Finally, in Fig. 7.27 we compare the ν_e and ν_μ single-differential cross sections in terms of the scattering angle for $E_\nu = 250, 500$ and 750 MeV where, apart from the larger results for ν_e, we notice that ν_e and ν_μ cross sections get closer at very forward angles. This is observed in detail in the bottom right panel of Fig. 7.27, where the ratio $\frac{d\sigma_{\nu_e}}{d\cos\theta}/\frac{d\sigma_{\nu_\mu}}{d\cos\theta}$ is shown for the previous E_ν values. As also deduced from Fig. 7.25, the ν_e/ν_μ ratio increases at the lowest energies, while at higher kinematics ($E_\nu = 750$ MeV) it gets closer to 1. Similar results are also obtained within the context of the CRPA approach [180] in the energy range from 200 to 750 MeV. This $\frac{d\sigma_{\nu_e}}{d\cos\theta}/\frac{d\sigma_{\nu_\mu}}{d\cos\theta}$ ratio, expected to be larger than 1 due to the different kinematical limits arising from the different final-lepton masses, experiments a sharp decrease at very forward angles, where differential cross sections approach zero. This a direct consequence of the different phase-space for each case, more pronounced at lower kinematics.

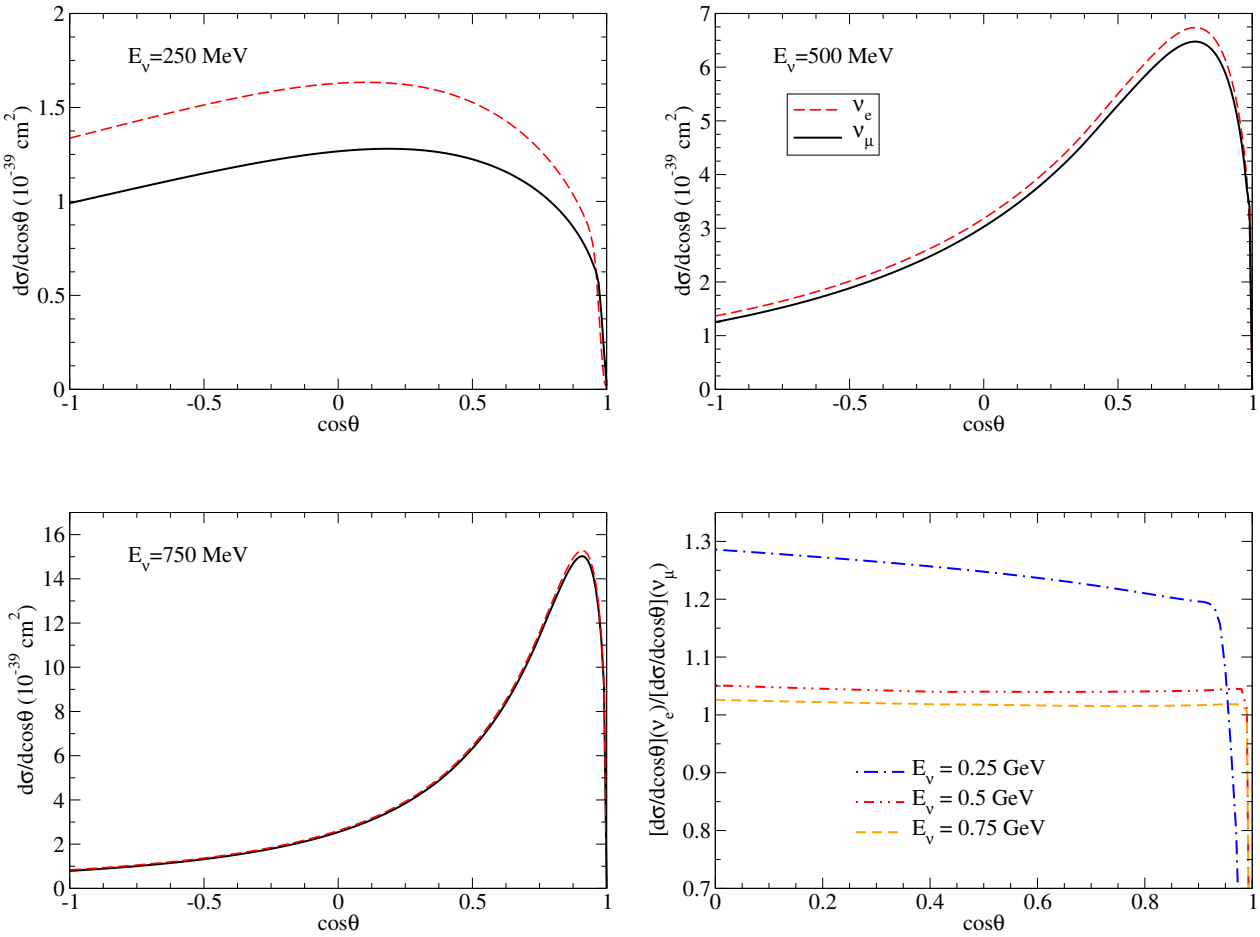

Figure 7.27: SuSAv2 predictions for muon- and electron- neutrino CCQE single-differential cross section per nucleon on ^{12}C for $E_\nu = 250$ (top left panel), 500 (top right panel) and 750 MeV (bottom left panel). The ratio $\frac{d\sigma_{\nu_e}}{d\cos\theta}/\frac{d\sigma_{\nu_\mu}}{d\cos\theta}$ for the previous neutrino energies is also shown (bottom right panel).

7.5 T2K results for ν_μ CC0π interactions

In the previous sections, our analysis has been mainly focused on the scattering of neutrinos and antineutrinos on mineral oil, CH_2 and CH, which has been the most commonly used target in experimental facilities up to now. However, there is an increasing experimental interest in theoretical predictions for cross sections on different targets, specifically ^{40}Ar and ^{16}O, which could shed light on the uncertainties arising from both initial state nuclear effects and final state interactions. In particular, in the T2K experiment the far detector may have different nuclear targets, a polystyrene (C_8H_8) and water (H_2O), and it is then crucial to understand how to extrapolate the results from one target to another.

Therefore, in this section we explore, in the framework of the SuSAv2-MEC model [38, 39, 153], the similarities and differences between the T2K CC0π (anti)neutrino scattering on ^{16}O and ^{12}C. The CC0π scattering is defined, equivalently to the CCQE-like one, as the process where no pions are detected in the final state. This process receives contribution from two different reaction mechanisms: quasielastic (QE) scattering and multi-nucleon excitations dominated by 2p-2h MEC contributions. These two mechanisms have in general a different dependence upon the nuclear species, namely they scale differently with the nuclear density [156], as previously analyzed in Chapters 4 and 6.

In what follows we apply our SuSAv2-MEC model to CC0π ν_μ scattering reactions on ^{12}C and ^{16}O and compare the theoretical predictions with data taken at different kinematics given by the T2K collaboration [56, 122]. The discussion follows closely the analysis already presented in Chapter 6 for (e, e') reactions on ^{12}C and ^{16}O.

7.5.1 T2K ν_μ-^{12}C reactions

In Fig. 7.28 we present the flux-averaged double differential cross sections corresponding to the T2K experiment [56]. The graphs are plotted against the muon momentum, and each panel corresponds to a bin in the scattering angle. As in previous cases, we show the separate contributions of the pure QE, the 2p-2h MEC and the sum of both. Contrary to the MiniBooNE and MINERνA experiments, the T2K data show a larger dispersion with significant error bands. Concerning the theoretical predictions, in the present case the relative contribution of the 2p-2h MEC compared with the pure QE is significantly smaller than in the previous cases; of the order of $\sim$ 10% at the maximum of the peak compared with the $\sim 25-35\%$ in the MiniBooNE case. This can be connected with the T2K neutrino flux [181] that, although averaged at ~ 0.8 GeV similar to MiniBooNE, shows a much narrower distribution around the peak. Hence 2p-2h MEC contribute less to the differential cross section.

As observed, the theoretical model is capable of reproducing the data although, contrary to the MiniBooNE and MINERνA data, the addition of the 2p-2h MEC does not seem to improve significantly the description of the experimental data, except at backward kinematics. Notice that the relative contribution of the 2p-2h channel compared with the QE one is less relevant as for the MiniBooNE case due to the narrower T2K flux. Similar comparisons have also been achieved within the Martini *et al.* and Nieves *et al.* models shown in [56].

Moreover, due to the present level of experimental accuracy and the large error bands shown by T2K data in most of the kinematical situations, both the pure QE as well as the total, QE+2p-2h

MEC, predictions are in accordance with the experiment. It is interesting to point out the results for the most forward angles, *i.e.,* the panel on the right-bottom corner. Notice that the QE and 2p-2h MEC contributions are stabilized to values different from zero for increasing muon momenta as a consequence of the high energy tail of the T2K neutrino flux. This is at variance with all remaining situations where the cross sections decrease significantly as the muon momentum p_μ goes up.

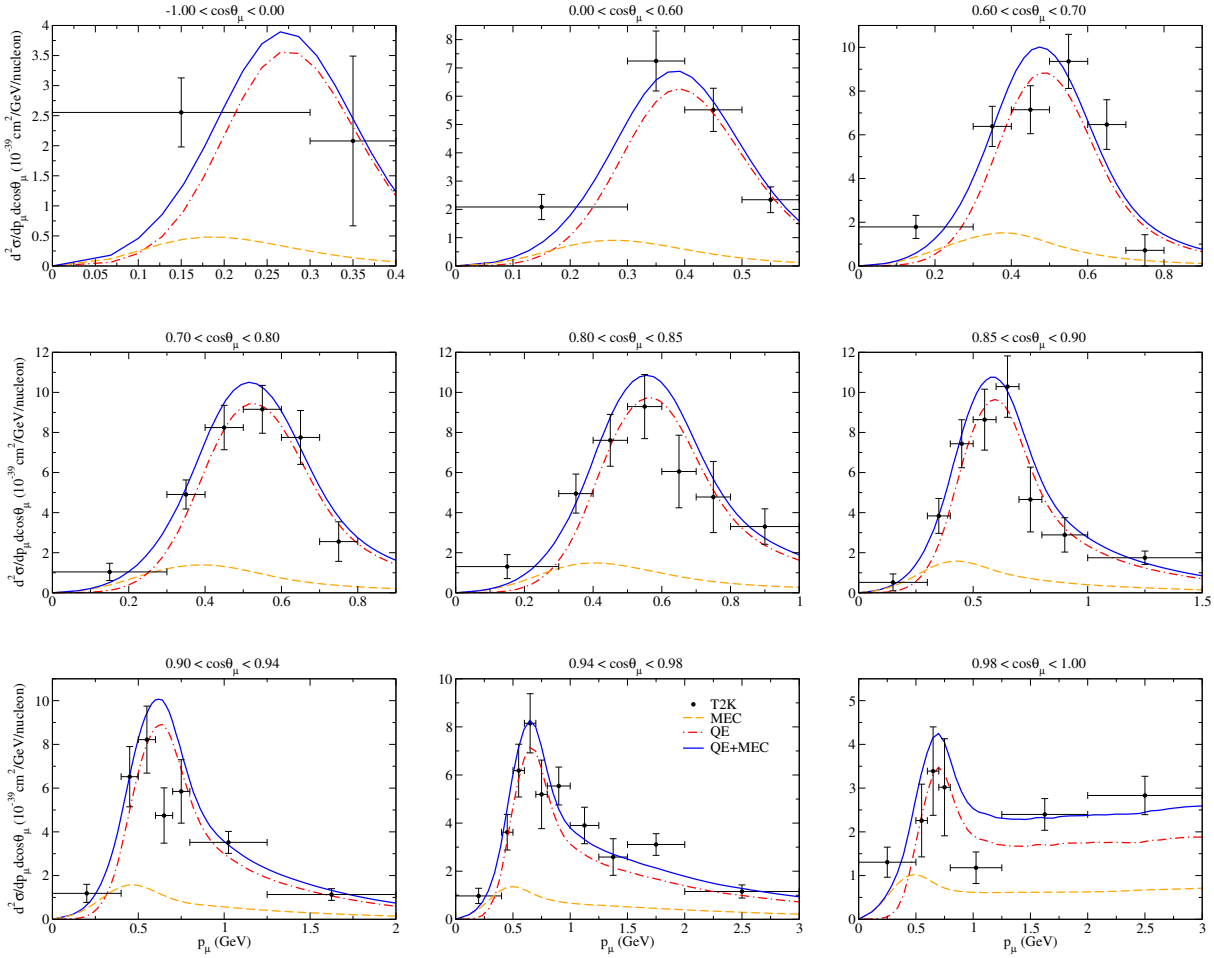

Figure 7.28: T2K flux-folded double differential cross section per target nucleon for the ν_μ CCQE process on ^{12}C displayed versus the muon momentum p_μ for various bins of $\cos\theta_\mu$ obtained within the SuSAv2-MEC model. QE and 2p-2h MEC results are also shown separately. Data are from [56].

7.5.2 T2K ν_μ-^{16}O reactions

In the following, we assume the procedure described in Sections 6.3 and 4.5 for the extension of the SuSAv2-MEC model to other nuclei. In the case of ^{16}O, the k_F and E_{shift}-values used are the ones defined for electron scattering (k_F = 230 MeV/c and E_{shift} = 16 MeV) in Chapter 6, being consistent with the general trend observed in [37]. In previous works [85–87, 91, 182], a different choice (k_F = 216 MeV/c and E_{shift} = 25 MeV) of these parameters was employed. Although both sets of values lead to small differences in the cross sections, the present choice does provide a more consistent analysis, and more importantly, it also improves the comparison with electron scattering data (see Fig. 6.11), thus ensuring its validity to analyze neutrino experimental data on ^{16}O.

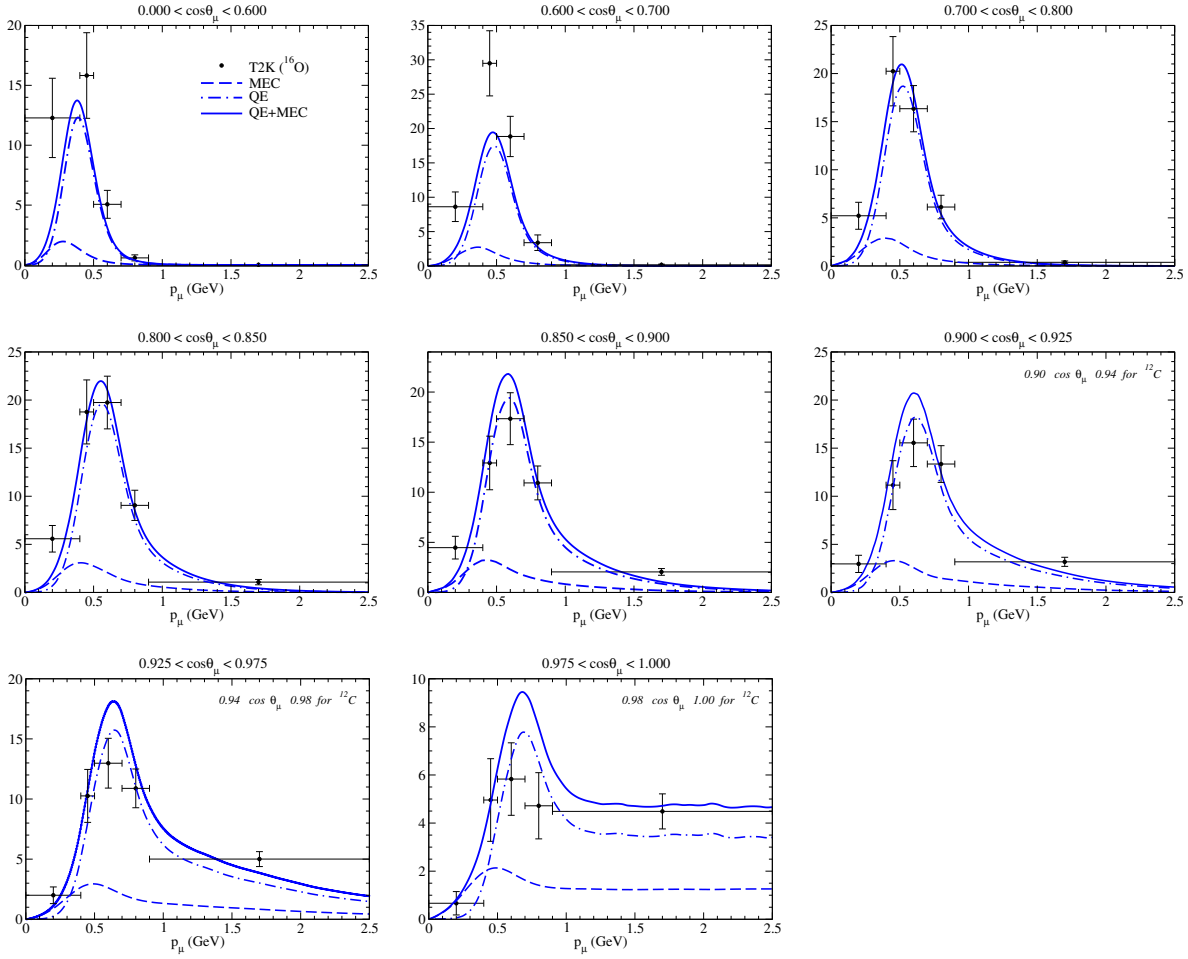

Figure 7.29: T2K flux-folded double differential cross section per target nucleon for the ν_μ CCQE process on ^{16}O displayed versus the muon momentum p_μ for various bins of $\cos\theta_\mu$ obtained within the SuSAv2-MEC model. QE and 2p-2h MEC results are also shown separately. Preliminary T2K data are from [122]. The y-axis represents $d^2\sigma/dp_\mu/d\cos\theta_\mu$ in 10^{-39} cm^2/GeV/nucleon.

Results for CC0π ν_μ-^{16}O reactions within the SuSAv2-MEC model are shown in Fig. 7.29. Each panel presents the double differential cross section averaged over the T2K ν_μ flux versus the muon momentum for fixed bins of the muon scattering angle. We show the separate contributions of the pure QE, the 2p-2h MEC and the sum of both. As for the ^{12}C case, a good agreement with data is achieved in most of the situations, although due to the present level of experimental accuracy it is hard to draw further conclusions. As well, a minor role of the MEC effects compared with the pure QE ones is observed. Furthermore, the MEC peak compared with the QE one is shifted to smaller p_μ-values.

These results, also present in the case of T2K-^{12}C, are in contrast with the analysis of the MiniBooNE and MINERνA experiments, that show 2p-2h MEC relative effects to be larger and the peak location more in accordance with the QE maximum. This is connected with the much narrower distribution of the T2K flux, of little relevance above 1 GeV. Similar comments also apply to the results for CC0π $\bar{\nu}_\mu$-^{16}O reactions shown for completeness in Fig. 7.30. Although the average $\bar{\nu}_\mu$ is sligthly lower ($\sim$ 0.6 GeV), the relative contribution of the 2p-2h MEC compared with the QE one is very similar to the case of neutrinos, also showing the same general shape versus the muon momentum.

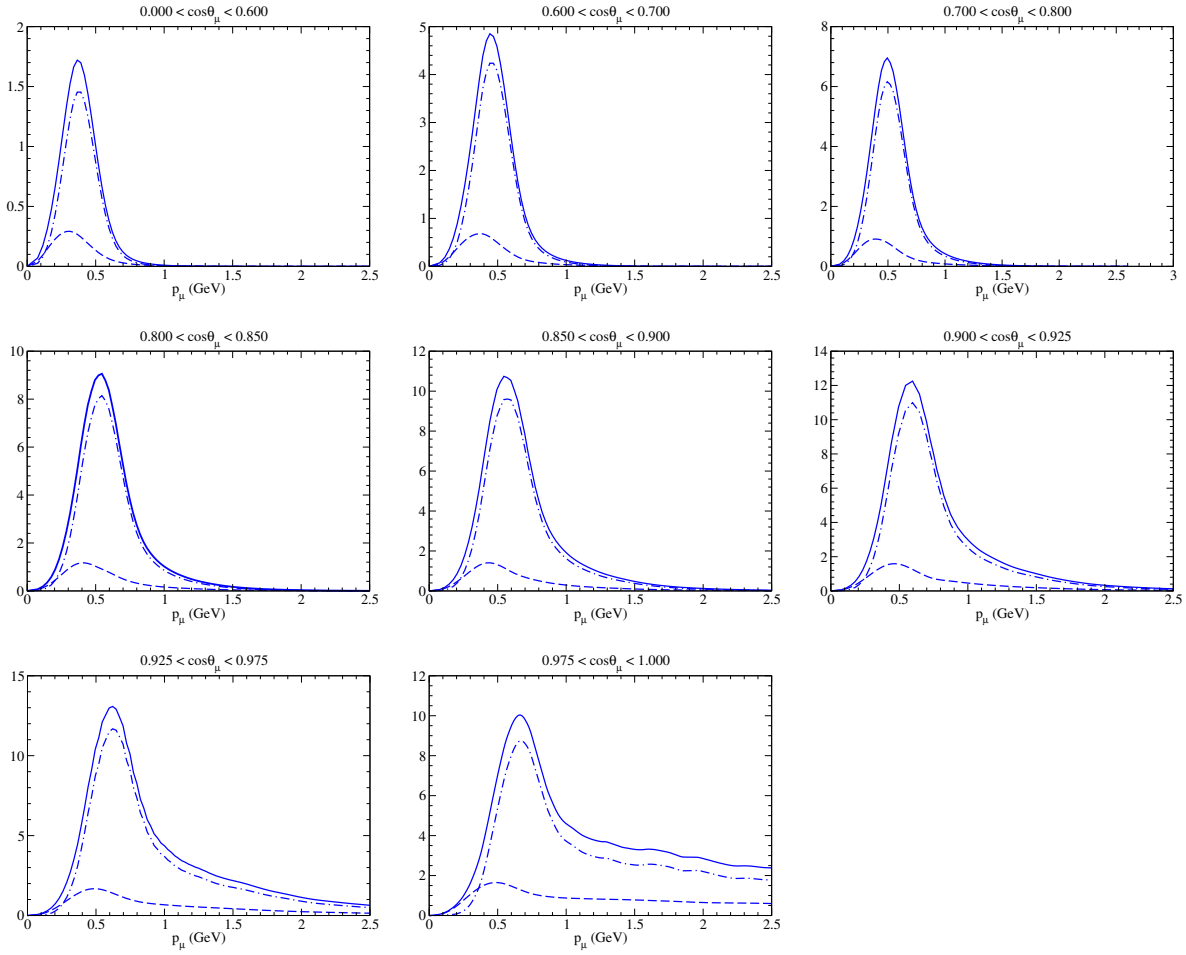

Figure 7.30: As for Fig. 7.29, but now for the $\overline{\nu}_\mu$ CCQE process on ^{16}O.

7.5.3 Oxygen versus Carbon CC0π results

In order to disentangle how nuclear effects enter in the analysis of the T2K experiment, we show in Fig. 7.31 the predictions provided by SuSAv2-MEC for the neutrino-averaged double differential cross sections per nucleon in the cases of ^{12}C (red lines) and ^{16}O (blue lines). The separate contributions of the pure QE (dot-dashed), the 2p-2h MEC (dashed) and the total responses (solid) are presented.

Although the scaling behavior of the QE and the 2p-2h cross section per nucleon is different: while the former goes like k_F^{-1} (scaling of the second kind), the latter increases as k_F^2, the results in Fig. 7.31 are very similar for the two nuclei in most of the kinematical situations. This is a consequence of the very close values of k_F assumed in both cases: 228 MeV/c (230) for ^{12}C (^{16}O). Only at forward angles some discrepancy between the results for ^{12}C and ^{16}O emerges being the latter cross sections larger. The amount of this difference gets higher as the scattering angle approaches zero. This is clearly observed in the bottom panels of Fig. 7.31, where the total cross section for ^{16}O is significantly larger than the one for ^{12}C. Notice that this discrepancy comes essentially from the pure QE response, being the relative difference in the 2p-2h MEC contributions much smaller. This is consistent with the fact that at very forward angles the transferred energy in the process is very small and low-energy effects and Coulomb distortions are of relevance (see Sections 7.3.1 and 7.3.2). However, in spite of these discrepancies, it is important to point out that the model is capable of reproducing the data for ^{12}C and ^{16}O within their error dispersion.

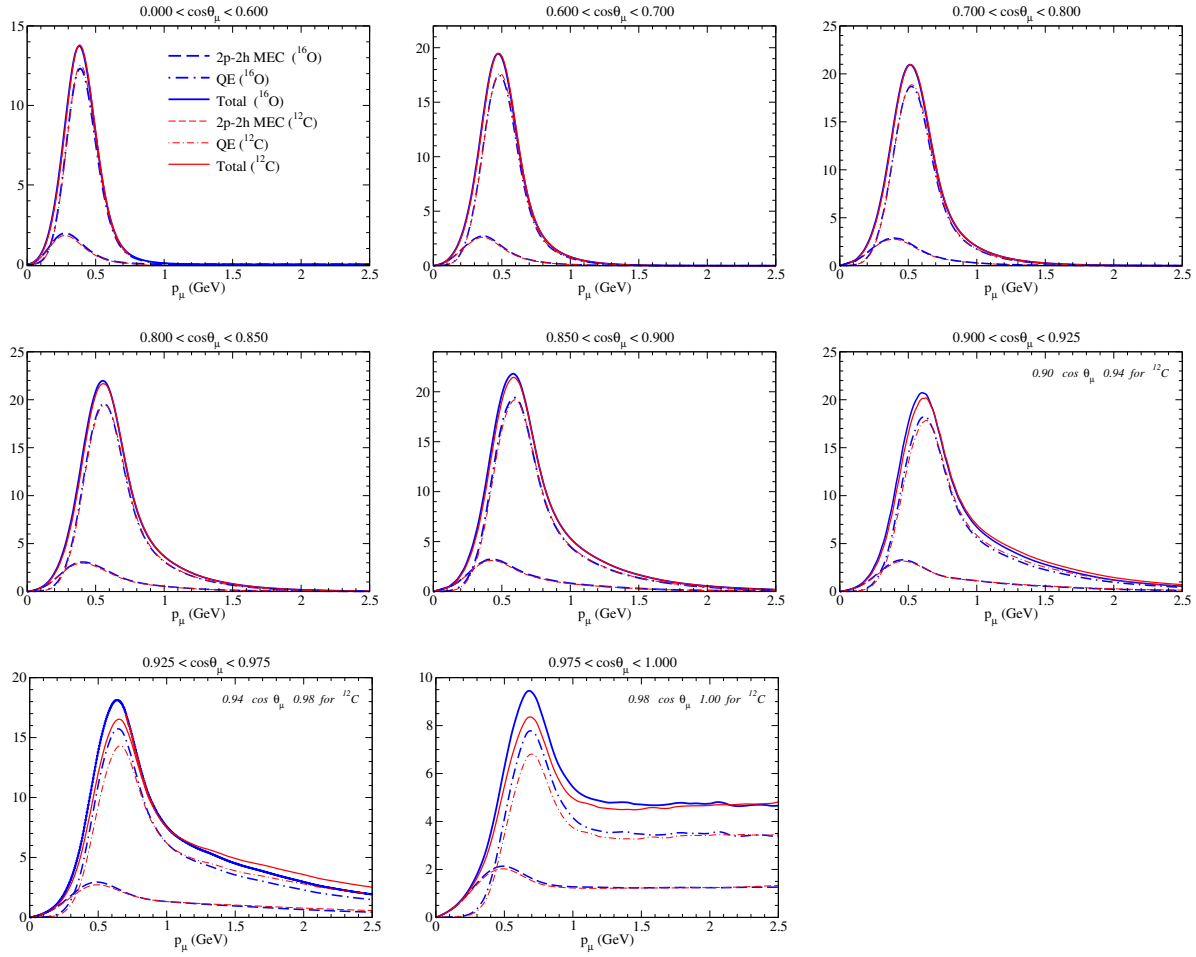

Figure 7.31: The same as Fig. 7.29, but now including also the results corresponding to the T2K-ν_μ CCQE process on ^{12}C.

Next we explore the dependence of the C/O differences upon the neutrino energy. To this scope, we show in Fig. 7.32 the total integrated cross section per nucleon versus the neutrino energy.

Results from the left panel in Fig. 7.32 show that nuclear effects in the total cross section, including both QE and 2p-2h MEC contributions, are very reduced. This minor discrepancy comes from the partial cancellation between the results obtained for the pure QE response (slightly lower for oxygen) and the 2p-2h MEC (a bit larger for oxygen). This is connected with the different scaling behavior shown by the QE and 2p-2h MEC responses with the Fermi momentum, and the very close values of k_F selected for the two nuclei. Although not shown in the left panel of Fig. 7.32, as almost no visible difference appears, the use of a smaller value of k_F for ^{16}O, as the one $k_F = 216$ MeV/c considered in some previous works [85–87], leads to more significant differences in the QE (being larger) and 2p-2h MEC (smaller) contributions. Nevertheless, the total response remains rather similar to the result for ^{12}C. It is important to point out that the use of different k_F-values only leads to significant discrepancies for low energy transfer, *i.e.*, $\omega \leq 50$ MeV, where other ingredients, not explicitly included in the SuSAv2-MEC model, can be relevant. Moreover, the relative contributions coming from transfer energies below 50 MeV are larger as the neutrino energy decreases. This is clearly observed in the right panel of Fig. 7.32 for the ratio ^{16}O/^{12}C corresponding to the two values of the Fermi momentum selected for oxygen, 230 MeV/c

and 216 MeV/c. As shown, for neutrino energies above 500 MeV the cross sections for the two nuclei are almost identical (ratio equal to 1), independently of the particular k_F-value selected for oxygen. On the contrary, the situation clearly differs for smaller neutrino energies, $E_\nu \lesssim 500$ MeV. Here the ratio grows up (goes down) very quickly as E_ν diminishes, leading to differences of the order of $\sim 5-10\%$ at $E_\nu \sim 0.2$ GeV. Notice that in this region 2p-2h MEC contributions (dashed lines in the left panel) are negligible, so the total cross section (solid lines) coincides with the pure QE contributions (dot-dashed) that determine the behavior of the ratio. As already commented, the oxygen response evaluated for $k_F = 216$ MeV/c is significantly larger than the carbon one because of its smaller value for the Fermi momentum. This is in contrast with the oxygen response corresponding to $k_F = 230$ MeV/c. Furthermore, it has been found that both ^{12}C and ^{16}O QE total cross sections collapse into the same result when neglecting $\omega < 50$ MeV (see right panel on Fig. 7.32). Therefore, in this case the ratio would be closer to unity even at very low neutrino energies.

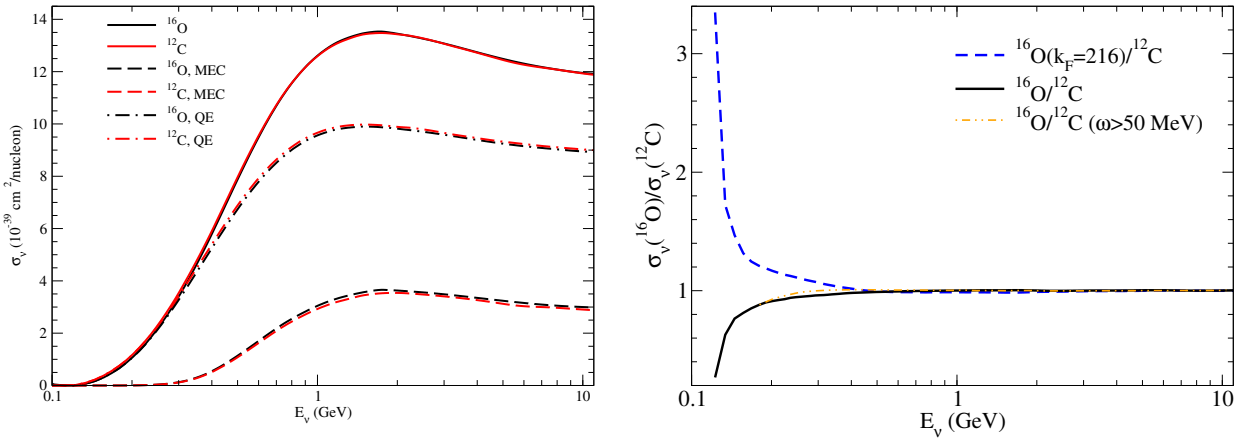

Figure 7.32: Left panel: Total ν_μ cross section per nucleon as a function of the neutrino energy evaluated for ^{12}C and ^{16}O nuclei. Separate contributions of the pure QE (dot-dashed) and 2p-2h MEC (dashed). Right panel: Ratio of total cross sections corresponding to Oxygen and Carbon. Results are presented for two values of the Fermi momentum in ^{16}O: $k_F = 230$ MeV/c (solid line) and $k_F = 216$ MeV/c (dashed line). The Fermi momentum for ^{12}C is fixed to 228 MeV/c.

Another ingredient in the calculation that also affects the O/C results within this low-neutrino energy region concerns the energy shift. As already mentioned, the careful analysis of (e,e') data for both nuclei leads to the use of $k_F = 230$ MeV/c for ^{16}O with an energy shift 4 MeV smaller than the ^{12}C one (see discussion in Section 6.3).

For completeness, the results for the flux-averaged single-differential cross sections per nucleon corresponding to the T2K experiment are presented in the left panels of Fig. 7.33. We show the cross sections versus the scattering angle (top panel) and against the muon momentum (bottom). In both cases a comparison between the carbon and oxygen results is provided using the values of the Fermi momentum given above, namely, 228 MeV/c (^{12}C) and 230 MeV/c (^{16}O). The separate contributions of the pure QE (dot-dashed), 2p-2h MEC (dashed) and the total result (solid) are shown. As noted, the discrepancy between the two nuclei is very small.

In order to provide a more detailed analysis on the role played by the nuclear effects, we present in the right panels of Fig. 7.33 the corresponding ratios between the differential cross sections for

both nuclei. Here, in addition to the two Fermi momenta selected for the cross sections (left panels), we also include the results obtained for ^{16}O with k_F = 216 MeV/c. The shadowed region represents the uncertainty in the total response (QE+MEC) linked to the use of the two values of the Fermi momentum for oxygen: 230 MeV/c (lower limit) and 216 MeV/c (upper limit). In the case of the cross section versus the muon angle (right-top panel) the uncertainty spread is of the order of $\sim 2-3\%$. Notice that only for very forward angles the curves cross each other. This corresponds to very small values of the energy transfer (see discussion above). The tiny $\sim 2-3\%$ uncertainty comes from the significant cancellation between the isolated QE and 2p-2h MEC contributions that show a much wider spread, of the order of $\sim 7-8\%$ (QE) and $\sim 16-18\%$ (MEC), roughly connected with their corresponding k_F dependence.

The results for the ratios of the differential cross section versus the muon momentum are presented in the right-bottom panel. Again, the shadowed region represents the uncertainty linked to the total cross sections. Notice the significant fluctuation of the results at low values of the muon momentum. This is a region where the cross sections increase very quickly with p_μ until reaching their maxima. In fact, the value of the muon momentum where the two curves for the global ratios cross each other is close to the values where the maxima in the cross sections are located. For higher muon momentum p_μ the uncertainty in the total ratios is at most of the order of $\sim 5-6\%$ being reduced to $\sim 2-3\%$ for $p_\mu \geq 1$ GeV/c.

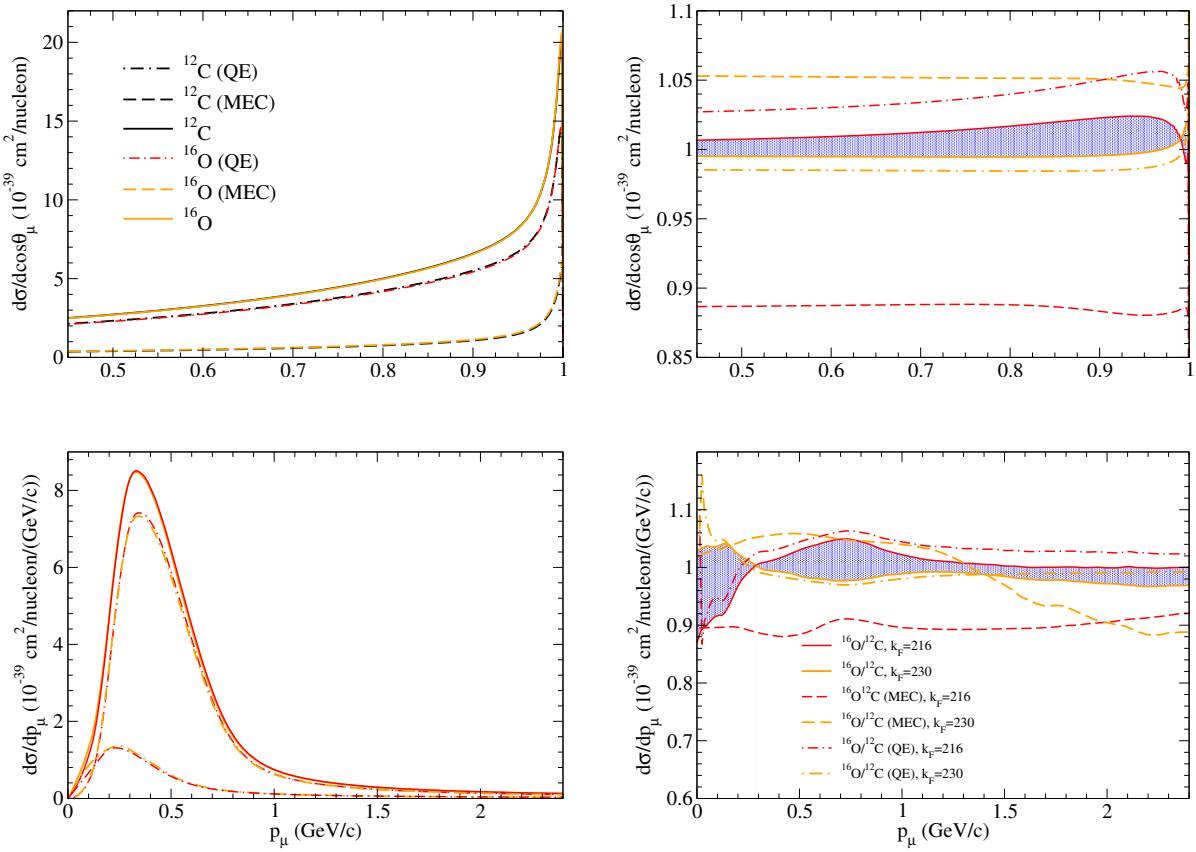

Figure 7.33: Left panels: T2K flux-averaged CCQE neutrino differential cross sections per nucleon for ^{12}C and ^{16}O as a functions of the muon scattering angle (top panel) and of the muon momentum (bottom panel). Right panels: Ratios between the T2K differential cross sections for the two nuclei and diverse values of the Fermi momentum for ^{16}O. The shadowed areas represent the uncertainty between the total responses linked to Fermi momenta.

7.6 Inclusive ν_μ-^{12}C cross sections

In this section, the analysis is extended to the inclusive charged current neutrino-nucleus cross sections which, in this context, requires the addition of resonance production and deep inelastic scattering processes to the QE and MEC multinucleon contributions previously considered. As a consequence of these competing mechanisms, the products of neutrino interactions include a variety of final states from the emission of nucleons to more complex results including pions, kaons and collections of mesons. The CC inclusive cross sections are evaluated within the SuSAv2-MEC model and its extension to the pion production region associated to the Δ-resonance. Note that this implies some limitation for the analysis of very high-energy neutrino experiments where higher inelasticities and DIS contributions can play the main role.

We compare our predictions with the inclusive measurements carried out by the T2K [44, 45, 183] and SciBooNE [41] Collaborations, where only the outgoing lepton is detected. For neutrino energies around 1 GeV (T2K and SciBooNE) the main contributions to the cross sections are associated with quasielastic (QE) scattering, one pion (1π) production and, to a lesser extent, 2p-2h MEC, while at higher neutrino energies (such as the ones from the ArgoNeuT experiment [48, 49]) multiple pion and kaon production, excitation of resonances other than the Δ and deep inelastic channels are necessary to describe the data. In what follows we attempt to provide some insights into how important these last effects may become as the neutrino energy increases.

7.6.1 Δ-scaling in lepton-nucleus interactions

Next, we briefly introduce the extension of the SuSAv2 formalism to the Δ regime for neutrino-nucleus scattering. This approach allows for a description of the QE and Δ resonance regions in a unified framework and can also be applied to high energies due to its relativistic nature.

In previous works [64, 84], it has been shown that the residual strength in the resonance region, obtained by subtracting the QE+MEC contribution from the total cross section, can be accounted for by introducing a new scaling function f^Δ dominated by the $N \to \Delta$ and employing a new scaling variable, ψ_Δ, which is suited to the resonance region, resembling the inelastic scaling variable introduced in Chapter 5 for (e, e') reactions (see Eq. 5.32),

$$\psi_\Delta = \frac{1}{\sqrt{\xi_F}} \frac{\lambda - \tau\rho_\Delta}{\sqrt{(1+\lambda\rho_\Delta)\,\tau + \kappa\sqrt{\tau\left(1+\tau\rho_\Delta^2\right)}}} \tag{7.8}$$

with ρ_Δ defined in terms of the Δ-resonance mass, m_Δ,

$$\rho_\Delta = 1 + \frac{\mu_\Delta^2 - 4\tau}{4\tau} \;\; ; \;\; \mu_\Delta = \frac{m_\Delta}{M_N}\,. \tag{7.9}$$

It is also important to stress that this Δ-scaling approach is expected to be valid only for those kinematical situations where the Δ-resonance excitation is the dominant inelastic process. In this sense, the extension of the SuSAv2-inelastic model (succesfully applied to the analysis of (e, e') data in Chapter 6) to the analysis of CC neutrino interactions would be more suitable to describe the inclusive cross section at higher energies.[1]

[1] The extension of the SuSAv2-inelastic model to CC neutrino reactions is still in progress and will be presented in further works.

Thus, the phenomenological Δ-scaling function employed here for the analysis of the non-quasielastic (non-QE) region, assuming that this is dominated by the Δ-resonance, follows the procedure described in [84, 184]. We first define a non-QE experimental scaling function in this region, $f^{\text{non-QE}} \equiv f_\Delta$. This entails subtracting from the experimental (e,e') double-differential cross section the SuSAv2-QE predictions and the 2p-2h MEC contributions:

$$\left(\frac{d^2\sigma}{d\Omega d\omega}\right)^{\text{non-QE}} = \left(\frac{d^2\sigma}{d\Omega d\omega}\right)^{\text{exp}} - \left(\frac{d^2\sigma}{d\Omega d\omega}\right)^{\text{QE,SuSAv2}}_{\text{1p1h}} - \left(\frac{d^2\sigma}{d\Omega d\omega}\right)^{\text{MEC}}_{\text{2p2h}} . \tag{7.10}$$

Then we define a superscaling function in the region of the Δ peak as follows:

$$f^{\text{non-QE}}(\psi_\Delta) = k_F \frac{\left(\frac{d^2\sigma}{d\Omega d\omega}\right)^{\text{non-QE}}}{\sigma_{Mott}(V_L G_L^\Delta + V_T G_T^\Delta)} , \tag{7.11}$$

where G_L^Δ, G_T^Δ are the single-hadron functions referred to the $N \to \Delta$ transition (see [64, 84, 184] for explicit expressions and details on the form factors employed).

The behavior of $f^{\text{non-QE}}$ is determined by analyzing a large set of high quality (e,e') data for ^{12}C, using similar procedures to those discussed in [64]. The data used are chosen to match, at least roughly, the relevant kinematics for the neutrino experiments under discussion.

From this analysis, illustrated in Fig. 7.34, it appears that scaling in the Δ region works reasonably well up to the center of the Δ peak, $\psi_\Delta = 0$, while it breaks, as expected, at higher energies where other inelastic processes come into play. Nevertheless the quality of scaling is not as good as in the QE-peak region. For this reason the non-QE scaling function is represented with a band, rather than with a function, which accounts for the spread of pseudo-data seen in Fig. 7.34. This band, together with the SuSAv2-MEC model, can now be used to validate the model against electron scattering data and, hence, to extend it to neutrino and antineutrino cross sections.

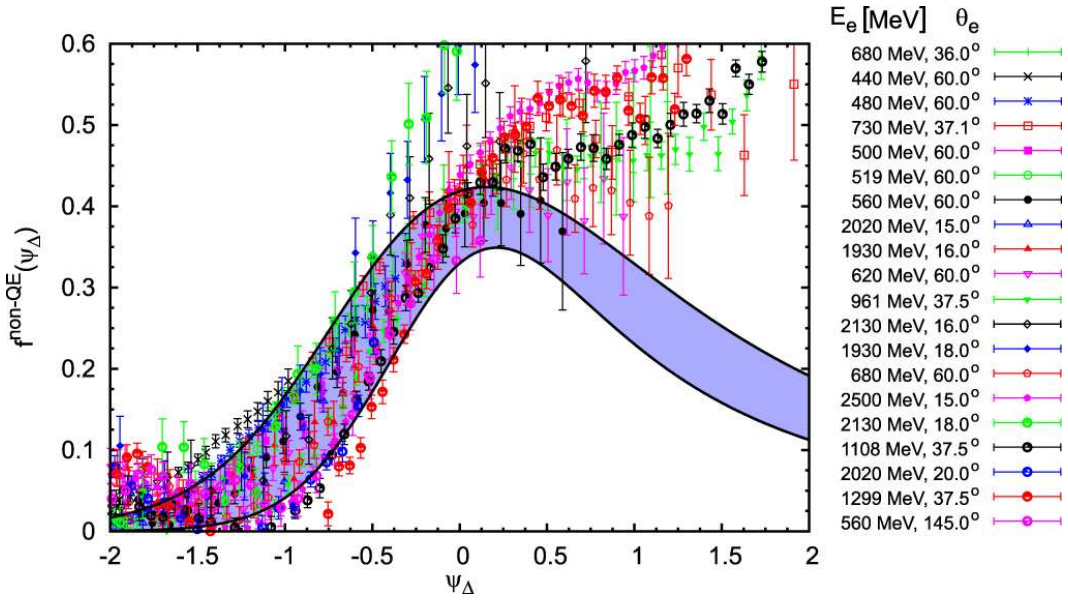

Figure 7.34: Averaged experimental values of $f^{\text{non-QE}}(\psi_\Delta)$ together with a phenomenological fit of the non-QE scaling function. The colored band represents an estimation of the theoretical uncertainty. Data taken from [100, 101].

In Fig. 7.35 we compare the model predictions with inclusive electron scattering data on ^{12}C. Although many high quality electron scattering data exist, here we only show results for a few representative choices of kinematics that are of interest in the neutrino experiments addressed in the following sections.

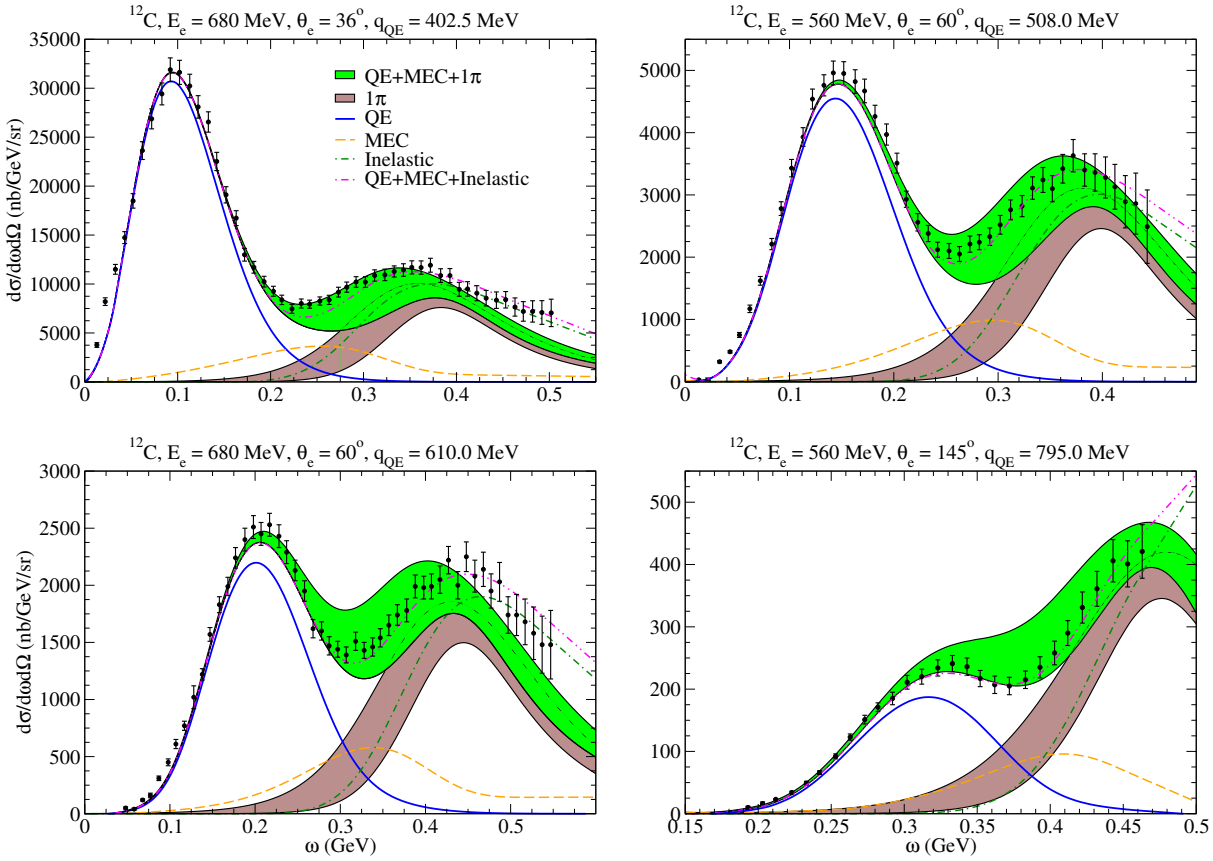

Figure 7.35: Double-differential inclusive electron-carbon cross sections, $d\sigma/d\omega d\Omega$. The panels are labeled according to beam energy, scattering angle, and value of q_{QE} at the quasielastic peak. The results are compared with the experimental data from [185] at the selected kinematics.

As observed, the model gives a good description of the (e,e') data. The band in the final cross section (green region) comes from the uncertainty in the determination of the Δ superscaling function. This explains that the data located in the region close to the Δ-peak are contained within the limits of the above band. Note also the compatibility between the 1π contribution and the SuSAv2-inelastic model except for the highly-inelastic regime, *i.e.* very large ω. More importantly, the model (with its associated uncertainty) is capable of reproducing successfully all data with particular emphasis on the dip region. This result gives us confidence in the reliability of the model and its application to the analysis of neutrino-nucleus scattering reactions.

7.6.2 Analysis of inclusive T2K and SciBooNE cross sections

First, we analyze the predictions corresponding to the T2K flux-averaged inclusive double differential cross sections for muon neutrinos [44]. Results are shown in Fig. 7.36 as function of the muon momentum and averaged over particular muon angular bins (each panel). The separate contribution of the QE, 2p-2h MEC and the Δ resonance (brown band) are presented. The global response is shown by the green band. In spite of the large experimental uncertainties, the model provides a very nice description of data once all contributions are included, *i.e.,* QE, 2p-2h MEC

and pion production. This is consistent with the kinematics implied by the present T2K experiment ($\langle E_{\nu_\mu} \rangle \sim 0.8$ GeV) being the Δ resonance the main response (almost the only one) within the inelastic region. It is also worth mentioning that the effects associated to the Δ-scaling function above $\psi_\Delta = 0.5$, where effects beyond the Δ-resonance are particularly relevant (see Fig. 7.34), are less than $10 - 12\%$ at T2K kinematics. This supports the reliability of our model to be applied to the description ot the T2K μ_ν data at $\langle E_{\nu_\mu} \rangle \sim 0.8$ GeV.

The previous comparison with T2K ν_μ inclusive data has been also addressed in other works [184, 186, 187] where similar results were obtained in the framework of the SuSAv2+vectorMEC, RPA and GiBUU models. On the contrary, some underprediction were found in [173, 188] for the CRPA and RGF approaches, respectively. When comparing with results from [184], the main difference between the two calculations is the inclusion, in the present, of the axial and interference vector-axial 2p-2h contributions. Whereas in [184] the purely vector MEC were found to be negligible at these kinematics, in Fig. 7.36 it is shown that the axial+vector two-body currents give a contribution closer to the one associated with the Δ resonance.

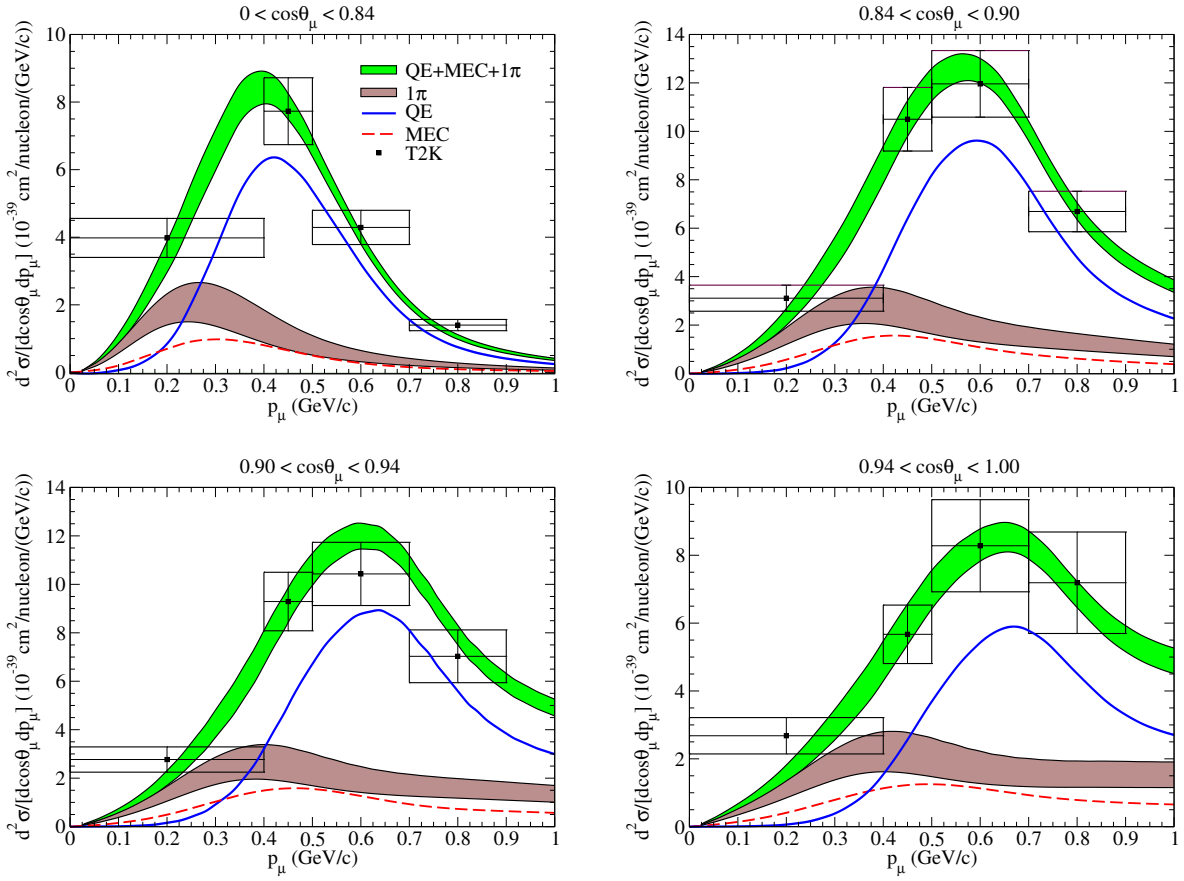

Figure 7.36: The CC-inclusive T2K flux-folded ν_μ–^{12}C double-differential cross section per nucleon evaluated in the SuSAv2+MEC model is displayed as a function of the muon momentum for different bins in the muon angle. The separate contributions of the QE, 1π and 2p-2h MEC are displayed. The data are from [44].

Similar conclusions apply to the inclusive T2K results for electron neutrinos analyzed in Fig. 7.37, where the flux-averaged single differential cross sections are shown. Results are presented against the electron scattering angle (top panel), the electron momentum (middle) and the reconstructed four-momentum (bottom). In the three cases we show the separate contributions corresponding to the QE response, the 2p-2h MEC, pionic and the total response.

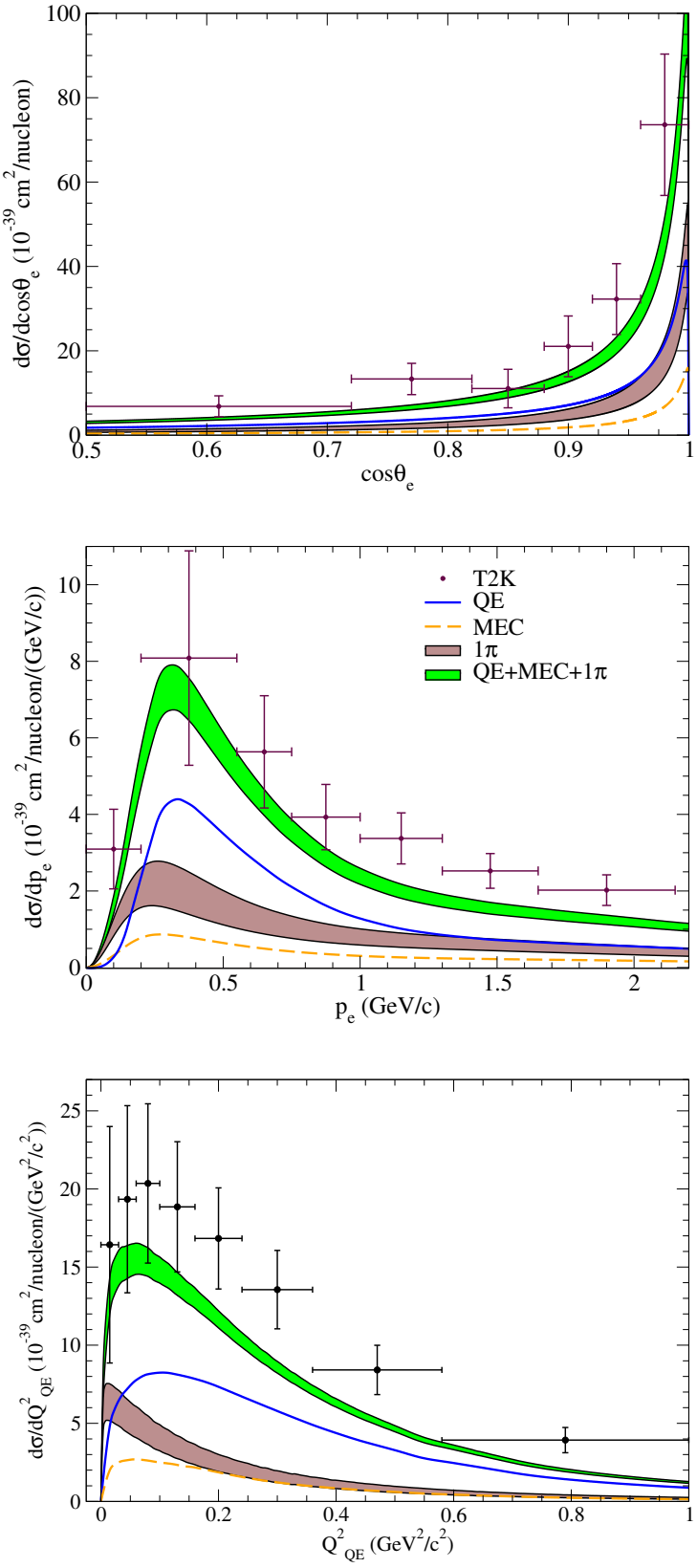

Figure 7.37: The CC-inclusive T2K flux-folded ν_e–^{12}C differential cross section per nucleon evaluated in the SuSAv2+MEC model is displayed as a function of the electron momentum (top), $\cos\theta_e$ (middle) and Q^2_{QE} (bottom). The separate contributions of the QE, 1π and 2p-2h MEC are displayed. The data are from [45].

Although, as noted, the role associated with the Δ resonance is essential, the data in Fig. 7.37 are underpredicted by the model predictions. This implies that other higher nucleon resonances, not taken into account in the present description, may also have a significant role in explaining T2K ν_e data. Note that the averaged ν_e flux is placed at $\sim$ 1.3 GeV, significantly larger than the ν_μ one ($\sim$ 0.8 GeV) and, at the same time, the role ascribed to the 2p-2h MEC effects is of the order of $\sim$ 20% ($\sim$ 15%) for ν_e (ν_μ). The need for higher inelasticities in the theoretical description are clearer for increasing values of the electron momentum (see results in the middle panel) and/or the reconstructed four-momentum transfer (bottom panel). The DIS cross section shown in [187], which is intended to be included in further works, could reduce the underestimation on the T2K-ν_e results displayed here as well as in the ones from Martini *et al.* [180].

To conclude, we present in Fig. 7.38 the results for the SciBooNE experiment [41]. These correspond to CC ν_μ ($\overline{\nu}_\mu$) scattering on a polystyrene target (C_8H_8). The data are presented as a total unfolded integrated cross section as a function of the neutrino energy. Because of the model-dependent unfolding procedure to reconstruct the neutrino energy, one should be very cautious in the comparison between data and theoretical predictions (see discussion in [41]). The case of neutrinos is presented in the left panel of Fig. 7.38 in comparison with available data, including also as reference the T2K total inclusive cross section measurements for ν_μ [183] and ν_e [45] as well as the recent MINERνA inclusive measurements for ν_μ and $\overline{\nu}_\mu$ [165]. The theoretical predictions for antineutrinos are referred to the right panel. Contrary to the analysis in [184] where only vector 2p-2h contributions were considered, here the model reproduces the neutrino data up to 1 GeV. Nevertheless, for higher energies the model still underpredicts the data by a significant amount. This result clearly indicates that new channels and higher nucleon resonances, in addition to the resonant pion production, should be added to the model for the analysis of measurements beyond $E_\nu \sim 1$ GeV.

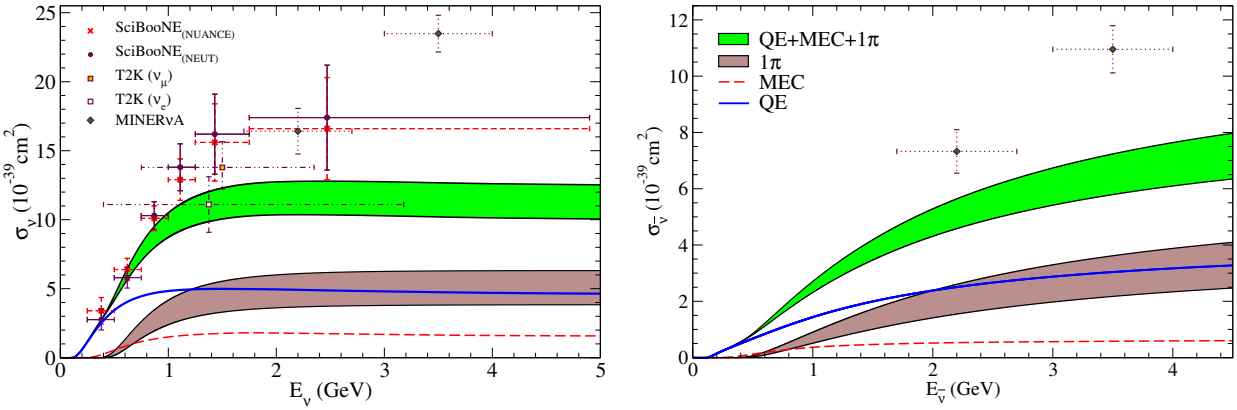

Figure 7.38: The CC-inclusive ν_μ (left) and $\overline{\nu}_\mu$ (right) cross section on a polystyrene target (C_8H_8) per nucleon evaluated in the SuSAv2-MEC model as a function of the neutrino energy. The SciBooNE data are from [41]. The T2K total inclusive data for ν_μ [183] and ν_e [45] as well as the MINERνA inclusive measurements [165] for ν_μ and $\overline{\nu}_\mu$ are also shown as reference.

7.7 Conclusions

In this Chapter, the SuSAv2-MEC model has been succesfully applied to the analysis of charged-current neutrino interactions at intermediate energies, dealing with several aspects of neutrino interactions with nuclei. This has been performed by means of a joint calculation of QE and 2p-2h contribution using the SuSAv2 model for the quasielastic responses and a relativistic Fermi gas model for the 2p-2h meson exchange currents in the weak sector. We have analyzed the published data from the MiniBooNE, T2K, MINERνA, NOMAD and SciBooNE experiments on ^{12}C, spanning an energy range from a few MeV to hundreds of GeV. We have found an overall good agreement with data when considering the QE and 2p-2h contributions. When extended to the analysis of inclusive neutrino reactions, the SuSAv2-MEC approach considering the Δ production region to model resonant pion production leads to an accurate description of the T2K and SciBooNE inclusive data in the region where higher inelasticities are not prominent ($E_\nu < 1$ GeV). On the other hand, the inclusion of the complete inelastic spectrum into the SuSAv2 model for weak interactions will be necessary to account for the higher energies involved in the ArgoNeuT [48, 49] or MINERνA [165] inclusive measurements. We have also concluded that the 2p-2h MEC channel is essential to describe a great amount of CCQE-like and inclusive experimental data, with a contribution relative to the QE response ranging from $15 - 35\%$ depending on the kinematics.

Regarding the analysis of the different L/T and vector/axial channels that contribute to the neutrino-nucleus interactions, we have confirmed a dominance of the traverse channel over the longitudinal one in both the QE and 2p-2h contributions, being the transverse axial and vector terms of similar magnitude. On the contrary, the longitudinal axial contribution has been proved to be essential to interpret properly antineutrino reactions due to the interference V-A cancellation. Moreover, the analysis of the relevant kinematics for CC weak processes has led to the conclusion that the major contribution to both QE and MEC regimes comes from $\omega < 500$ MeV and $q < 1000$ MeV/c even at very high neutrino energies. In addition, a proper description of low-energy effects is essential for the analysis of forward kinematics and the low-$|Q^2|$ region. This low-kinematical region is also responsible for the main differences between ν_e and ν_μ cross sections.

Additionally, the SuSAv2-MEC model has also been extended to the analysis of neutrino-oxygen cross sections, yielding a good representation of the experimental data within the present experimental accuracy. In this connection, the scaling behavior of the RMF scaling functions together with the nuclear dependence of the 2p-2h contributions will allow for a consistent description of forthcoming neutrino experiments on heavier nuclear targets, such as DUNE [60], ArgoNeuT [48, 49] or MINERνA [54]. On this basis, an appropriate analysis of asymmetric nuclei ($Z \neq N$) of interest for these experiments, such as ^{40}Ar or ^{56}Fe, will be provided in further works by the inclusion of the separate neutron and proton scaling functions arising from the RMF theory [86, 87] into the SuSAv2 model as well as supplying the separate 2p-2h charge channel contributions, *pn*, *pp* and *nn* emission [189].

To conclude, the SuSAv2 model as well as the 2p-2h MEC parametrization can be described in a simple way for different nuclei, translating sophisticated and computationally demanding microscopic calculations into a straightforward description and, hence, easing its implementation in MonteCarlo event generators employed in the analysis of neutrino oscillation experiments. Accordingly, the SuSAv2-MEC model constitutes a satisfactory approach for analyzing current and forthcoming neutrino experiments.

Chapter 8

Summary and Conclusions

In this PhD thesis we have explored the charged-current weak interaction on hadronic systems at intermediate energies, spanning from a few MeV to hundreds of GeV. We have focused on different processes of relevance for neutrino oscillation experiments and have compared our predictions with a large variety of experimental results.

Beginning with neutrino reactions off free nucleons, we have described the inner structure of the hadrons and have introduced the general formalism necessary to describe charged-current neutrino-nucleus scattering processes for the different regimes, namely, quasielastic, 2p-2h MEC contributions and inelastic spectrum.

With the aim of achieving a complete theoretical description of the CCQE neutrino-nucleus interaction, we have developed the so-called SuSAv2 model. This model makes use of the predictions given by the relativistic mean field theory and is based on the SuperScaling Approach, which assumes the existence of universal scaling functions for both electromagnetic and weak interactions. The scaling functions implicitly contain the nuclear dynamics of the process, namely, mean-field effects, final-state interactions, nucleon correlations, etc. These nuclear effects can be studied using different approaches. In this thesis, we have offered a possible explanation in terms of the relativistic mean field theory which accounts for the FSI between the outgoing nucleon and the residual nucleus. This model is also consistent with the observed superscaling properties of (e, e') data and includes a natural enhancement of the transverse nuclear response as a genuine relativistic effect, where the latter has shown to be in accordance with the L/T differences suggested by the experimental data.

We have considered in the SuSAv2 model the difference between isoscalar and isovector contributions coming from the RMF theory, as well as the separate vector-vector, axial-axial and vector-axial channels. We have also noticed that whereas the RMF approach works properly at low to intermediate values of the transfer momentum, also providing an accurate description of FSI, results in the high-q regime, where FSI are negligible, are better described by RPWIA. This is a consequence of the strong energy independent scalar and vector potentials involved in the RMF model which, at high values of q, imply a strong energy shift and a long high-energy tail in the scaling functions. Accordingly, a general "blending" function has been introduced in the SuSAv2 model to make a transition between the RMF and RPWIA responses.

Furthermore, we have extended the SuSAv2 model to the whole energy spectrum, incorporating to the QE contributions the ones coming from 2p-2h excitations and the entire inelastic regime. In this connection, a detailed analysis of the inelastic structure functions for protons and neutrons

has been addressed. The present model has shown to be capable of describing very successfully the whole energy spectrum of ^{12}C(e,e') data at very different kinematics. In particular, SuSAv2 has accurately reproduced the position, width and maximum of the QE peak for all kinematics, whereas the use of the single-nucleon inelastic structure functions together with the SuSAv2 scaling functions has led to a precise description of the Δ-resonance region and the complete inelastic regime. The addition of 2p-2h MEC effects has also allowed for a proper interpretation of the "dip" region. Remarkably, the SuSAv2-MEC model has provided a reasonably good description not only of the cross sections but also of the separate longitudinal and transverse response functions. This is a very important test for models used in neutrino scattering studies, since the balance between the L and T channels is different from the (e,e') case.

Accordingly, a basic feature in the present study, apart from the SuSAv2 model applied to the QE and inelastic regimes, has concerned the evaluation of the two-body meson exchange currents that have proven to be essential to describe recent neutrino experiments as well as the "dip" region in (e,e') data. The prescription employed here is based on a fully relativistic model in which a fully Lorentz and translational invariant calculation can be developed and, hence, applied to very high energies/momenta. This is crucial in order to analyze neutrino oscillation experiments. In the present study we have used a fixed, highly accurate parameterization of the 2p-2h MEC vector and axial nuclear responses that allows us to avoid the computationally demanding microscopic calculation for the entire set of kinematics involved in the experimental data. It is also important to remark that whereas the SuSAv2 model has been developed from the original calculations based on the RMF theory, the 2p-2h MEC calculations are linked to the RFG model. The main justification for this hybrid approach resides in the technical difficulties inherent to the calculation of such contributions, which is extremely complex even in the simple RFG basis.

Additionally, the analysis has been extended to other nuclear species in terms of the scaling properties and nuclear density dependence, thus leading to an accurate description of the experimental data for nuclei of relevance in forthcoming neutrino experiments. Despite the smaller amount of available (e,e') data for other nuclei compared to ^{12}C, the growing interest of experimental collaborations on (e,e') measurements, together with the extension of neutrino experiments to other nuclear targets, is expected to shed light on the nuclear effects that play a role in the experimental measurements for both electron and neutrino reactions.

All this complete analysis has given us a great confidence in the reliability of the model, providing a solid benchmark to assess its validity when extended to the description of CCQE neutrino-nucleus scattering. In this case, not only new responses contribute, but also the wide neutrino flux energy spectrum implies that ingredients, such as multinucleon excitations, beyond the ones assumed within the IA can have a significant impact on the data analysis. In this sense, the fully relativistic description presented in electron scattering processes for the entire energy spectrum and the different nuclear regimes is of crucial importance for the study of neutrino reactions.

From this baseline, the SuSAv2-MEC model has been succesfully applied to the analysis of charged-current neutrino interactions at intermediate energies. We have compared our predictions with recent experimental results from different collaborations: MiniBooNE, T2K, MINERνA, NOMAD and SciBooNE, covering an ample energy range from a few MeV to hundreds of GeV. Accordingly, these measurements on CCQE neutrino and antineutrino reactions on ^{12}C have constituted an extensive guide to assess the reliability of our model. In this context, we have found an overall good agreement with data when considering both the QE and 2p-2h MEC contributions, thus verifying the relevance of the 2p-2h excitations for a proper interpretation of the CCQE-like

measurements. When extended to the analysis of inclusive neutrino reactions, the SuSAv2-MEC approach, considering the Δ production region to model resonant pion production, has led to an accurate description of the T2K and SciBooNE inclusive data in the region where higher inelasticities are not prominent ($E_\nu < 1$ GeV). In this connection, the inclusion of the complete inelastic spectrum into the SuSAv2 model for weak interactions, still in phase of analysis, will be necessary to account for the higher energies involved in the ArgoNeuT and MINERνA inclusive measurements.

The conclusions extracted from the analysis of the different L/T and vector/axial channels that contribute to the neutrino-nucleus interactions, have confirmed a dominance of the tranverse channel in both QE and 2p-2h regions, being the transverse axial and vector terms of similar magnitude. On the contrary, the longitudinal axial contribution has been proved to be essential in both QE and 2p-2h MEC regimes in order to interpret properly antineutrino reactions. This is a consequence of the interference V-A cancellation. Moreover, the analysis of the relevant kinematics for CC weak processes has led to the conclusion that the major contribution to both QE and MEC regimes comes from $\omega < 500$ MeV and $q < 1000$ MeV/c even at very high neutrino energies. In addition, a proper description of low-energy effects, including the influence of Pauli blocking and considering the residual nucleus mass, is necessary for the analysis at forward kinematics and low-$|Q^2|$ values. This kinematical region is also responsible for the main differences between ν_e and ν_μ cross sections, mainly related to the final-lepton mass dependence of the momentum transfer and the Coulomb distortions of the emitted lepton.

Concerning the growing interest in neutrino reactions on different targets as a method to disentangle the experimental uncertainties arising from nuclear effects in both initial and final states, the SuSAv2-MEC model has been extended to the analysis of neutrino interactions on water. The comparison within the preliminary T2K CC0π ν_μ-^{16}O results has evidenced a good description of the data within the present experimental accuracy. In this sense, the scaling behavior of the RMF scaling functions together with the nuclear dependence of the 2p-2h contributions analyzed in this thesis will allow for a consistent description of forthcoming neutrino experiments on heavier nuclear targets, such as DUNE, ArgoNeuT or MINERνA. In this connection, an appropriate analysis of asymmetric nuclei ($Z \neq N$) of interest for these experiments, such as ^{40}Ar or ^{56}Fe, will be provided in further works. This will be accounted for by including, into the SuSAv2-MEC model, the individual neutron and proton scaling functions arising from the RMF theory as well as the separate 2p-2h charge channel contributions, *pn*, *pp* and *nn* emission.

Finally, in the ongoing effort to model neutrino-nucleus interactions for precise measurements of neutrino oscillations, the results presented in this thesis within the SuSAv2-MEC model can provide a deeper understanding of these processes. On this basis, the SuSAv2 model as well as the 2p-2h MEC contributions can be described in a simple way for different nuclei, translating sophisticated and demanding microscopic calculations into a straightforward description of the interacting nucleons and, hence, easing its implementation in the MonteCarlo simulations employed in the analysis of neutrino oscillation experiments. All this makes the SuSAv2-MEC model a promising candidate for analyzing current and forthcoming neutrino experiments.

Appendix A

Electromagnetic electron-nucleon elastic scattering

Following the procedure described in Chapter 2 for CC elastic neutrino-nucleon interaction, we introduce in this appendix some remarks on the formalism employed to describe elastic electron-nucleon scattering processes. These interactions are schematically shown in Fig. A.1, where the electromagnetic interaction ($e^- + N \rightarrow e^- + N$) via the exchange of a γ photon is represented. Analogously to Chapter 2, the frame of reference is selected so that the initial and final electrons are contained in the XZ plane. The kinematics of the elastic e-N scattering process is summarized as follows:

- Incident electron e^-:
  - 4-momentum: $k_i = (\varepsilon_i, \vec{k}_i)$
  - Mass: $m_e \neq 0 \rightarrow \varepsilon_i = \sqrt{\vec{k}_i^2 + m_e^2}$
- Final electron e^-:
  - 4-momentum: $k_f = (\varepsilon_f, \vec{k}_f)$
  - Mass: m_e
  - Scattering angle: θ_e
- Initial nucleon N:
  - 4-momentum: $P_i = (M_N, 0)$
  - Mass: M_N
- Final nucleon N:
  - 4-momentum: $P_f = (E_f, \vec{q})$
  - Mass: M_N
- Exchanged boson γ:
  - 4-momentum: $Q_e = (\omega, \vec{q} \equiv \mathbf{q})$

The energy-momentum conservation law in the leptonic and hadronic vertexes implies the following relations:

Leptonic vertex

- Energy conservation: $\varepsilon_i - \varepsilon_f = \omega$
- Momentum conservation: $\vec{k}_i - \vec{k}_f = \vec{q} \Rightarrow q^2 = |\vec{k}_i|^2 + |\vec{k}_f|^2 - 2|\vec{k}_i||\vec{k}_f| \cos\theta_e$

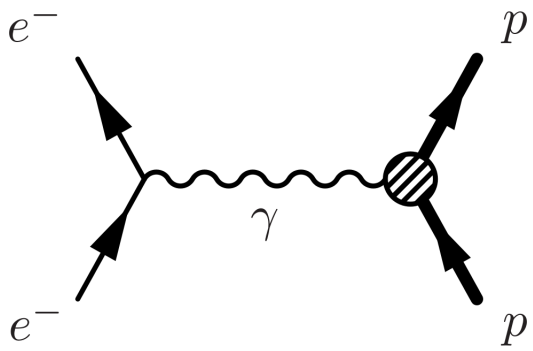

Figure A.1: Feynman diagram for the electromagnetic electron-proton scattering via the exchange of a virtual photon.

Hadronic vertex

- Energy conservation: $E_f = \omega + M_N \Rightarrow \omega^2 + 2M_N\omega = q^2 \Rightarrow -Q^2 \equiv |Q^2| = 2M_N\omega$
- Momentum conservation: $\vec{q} = \vec{P}_i + \vec{P}_f \Rightarrow \vec{q} = \vec{P}_f$

As shown in the previous equations, the kinematical variables ε_i, ε_f and θ_e are not independent so the kinematic of the process are completely defined by determining two of them.

Interaction hamiltonian

The transition ampplitude S_{fi} of the scattering process is obtained from the electromagnetic hamiltonian (H_{EM}):

$$S_{fi} = -i \int d^4X H_{EM}(X)\,, \tag{A.1}$$

$$H_{EM}(X) = eJ_\mu^{(e)\dagger}(X)A_{(N)}^\mu(X) = eJ_\mu^{(e)\dagger}(X)D_{EM}(Q)J_\nu^{(N)}(X)\,, \tag{A.2}$$

where e is the electron charge. The 4-potential $A_{(N)}^\mu(X)$, *i.e.*, the field generated by the nucleon in the interaction with the corresponding lepton can be related to the hadronic current through the electromagnetic propagator, $D_{EM}^{\mu\nu}$:

$$A_{(N)}^\mu(X) = \int d^4Y \overbrace{\int \frac{d^4Q}{(2\pi)^4}\left(\frac{-1}{Q^2+i\varepsilon}\right)e^{iQ\cdot(X-Y)}}^{D_{EM}} J_{(N)}^\mu(Y)\,. \tag{A.3}$$

Next we introduce the leptonic and hadronic currents, used to obtain the electron-nucleon cross section.

Leptonic and hadronic currents

Unlike weak processes where an axial term ($\gamma^\mu\gamma^5$) is also considered for the leptonic current, the analysis of the electromagnetic leptonic current ($j_\mu^{(e)}$) only involves the vector component (γ^μ),

$$j_\mu^{(e)} = \overline{\psi}_e(k_f, s_f)\gamma^\mu\psi_e(k_i, s_i)\,. \tag{A.4}$$

Likewise, only the vector part remains for the hadronic currents,

$$J^{\mu}_{(N)} = \overline{\psi}_{P_f}(P_f, S_f)\widetilde{\Gamma}^{\mu}\psi_{P_i}(P_i, S_i) \tag{A.5}$$

$$\widetilde{\Gamma}^{\mu} = F_1^N \gamma^{\mu} + \frac{iF_2^N}{2M}\sigma^{\mu\nu}Q_{\nu}\,. \tag{A.6}$$

Electromagnetic electron-nucleon cross section

Using the previous definitions and proceeding in a similar way as described in Chapter 2 for CC weak processes (2.21), we obtain the so-called Rosenbluth formula [66] for electromagnetic (e, e') reactions:

$$\frac{d\sigma}{d\Omega_f} = \sigma_{Mott} f_{rec}^{-1}\left[\frac{G_E^2 + \tau G_M^2}{1+\tau} + 2\tau G_M^2 \tan^2\theta_e/2\right], \tag{A.7}$$

where $f_{rec} = \dfrac{\varepsilon_i}{\varepsilon_f}$ is the recoil factor, $\tau = \dfrac{|Q^2|}{4{M_N}^2} = \dfrac{q^2-\omega^2}{4{M_N}^2}$, and the electric and magnetic Sachs form factors are defined, respectively, as $G_E(Q^2) = F_1^N - \tau F_2^N$ and $G_M(Q^2) = F_1^N + F_2^N$. The σ_{Mott} term is the Mott cross section, which is given by

$$\sigma_{Mott} = \frac{\alpha^2 \cos^2\theta_e/2}{4\varepsilon_i^2 \sin^4\theta/2}\,. \tag{A.8}$$

Notice that for electromagnetic interactions, the nucleon responses only contain the purely vector terms, that is, R_L^{VV} and R_T^{VV}. Thus the single differential cross section can be expressed as:

$$\frac{d\sigma}{d\Omega_f} = \sigma_{Mott} f_{rec}^{-1}\mathcal{F}_{EM}^2, \quad \text{with} \quad \mathcal{F}_{EM}^2 = X_L^{VV} + X_T^{VV} \tag{A.9}$$

$$\text{and} \quad X_L^{VV} = v_L R_L^{VV}\,;\; X_T^{VV} = v_T R_T^{VV}\,, \tag{A.10}$$

where the leptonic factors v_L, v_T are given by

$$v_L = \rho^2 = \frac{|Q^2|}{q^2} \tag{A.11}$$

$$v_T = \frac{1}{2}\rho + \tan^2\theta_e/2\,. \tag{A.12}$$

The nucleon responses (R_L^{VV}, R_T^{VV}) are defined as for the CC weak processes (see Eqs. 2.60 and 2.66 in Chapter 2) but considering the purely electric and magnetic Sachs form factors, G_E and G_M, given above.

More information about the formalism of electron-nucleon $(e + N \rightarrow e' + N)$ and electron-nucleus $(e + A \rightarrow e' + N + (A-1))$ reactions can be found in previous works [63, 64, 75].

Appendix B

Parametrization of the reference scaling functions within the SuSAv2 model

In this Appendix we summarize the parameterization of the reference SuSAv2 scaling functions. The RMF scaling functions are given in terms of a skewed-Gumbel (sG) function [190], defined as

$$\widetilde{f}_{sG} = S(\nu_0;\psi) f_G(\psi_0,\sigma,\beta;\psi)\,, \tag{B.1}$$

where

$$S(\nu_0;\psi) = \frac{2}{1+e^{\nu/\nu_0}} \tag{B.2}$$

$$f_G(\psi_0,\sigma,\beta;\psi) = \frac{\beta}{\sigma} e^{\nu} \exp[-e^{\nu}] \tag{B.3}$$

$$\nu = -\left(\frac{\psi-\psi_0}{\sigma}\right). \tag{B.4}$$

In Table B.1, the values of the free parameters that fit the corresponding longitudinal (L) and transverse (T) RMF scaling functions are shown. The differences linked to the isospin effects (τ) are also taken into acccount.

	$\widetilde{f}_{L,T=1}$	$\widetilde{f}_{L,T=0}$	$\widetilde{f}_{T}$
β	0.8923	1.0361	0.9425
σ	0.6572	0.5817	0.7573
ψ_0	0.1708	0.02217	−0.4675
$1/\nu_0$	−0.7501	−0.1163	2.9381

Table B.1: Values of the parameters that characterize the RMF scaling functions.

Moreover, the reference RPWIA scaling functions are described as

$$\widetilde{f}^{RPWIA}_{L,T} = \frac{2(a_3)_{L,T}}{1+\exp\left(\frac{\psi-a_1}{a_2}\right)} \exp\left(-\frac{(\psi-a_4)^2}{a_5}\right), \tag{B.5}$$

with $a_1 = -0.892196$, $a_2 = 0.1792$, $(a_3)_L = 6070.85$, $(a_3)_T = 6475.57$, $a_4 = 1.74049$, $a_5 = 0.64559$. There are no significant differences associated to isospin effects (isovector, isoscalar) on the RPWIA scaling functions.

In order to reproduce the peak position of RMF and RPWIA scaling functions within SuSAv2 we consider a q-dependent energy shift, namely, $E_{shift}(q)$. This quantity modifies the scaling variable $\psi(q,\omega) \longrightarrow \psi'(q,\omega,E_{shift})$ as

$$\psi' = \frac{1}{\sqrt{\xi_F}} \frac{\lambda' - \tau'}{\sqrt{(1+\lambda')\tau' + \kappa\sqrt{\tau'(\tau'+1)}}} \tag{B.6}$$

where $\xi_F = \sqrt{1+(k_F/M_N)^2} - 1$, $\kappa = q/(2M_N)$, $\lambda' = \omega'/(2M_N)$ and $\tau = \kappa^2 - \lambda'^2$. M_N is the nucleon mass and k_F is the Fermi momentum. Additionally, we have introduced the variable $\omega' = \omega - E_{shift}$.

In particular, we build this function $E_{shift}(q)$ from the results of the RMF and RPWIA models presented in Chapter 3 (see also [153]). In the particular case of ^{12}C, the energy shift for the longitudinal and transverse RMF/RPWIA scaling functions is defined (in GeV) as

$$\begin{aligned} E^{RMF}_{shift,L} &= -0.005506 + 0.0548 * q \\ E^{RMF}_{shift,T} &= -0.007687 + 0.0564 * q \\ E^{RPWIA}_{shift,L} &= 0.035164 + 0.0112 * q \\ E^{RPWIA}_{shift,T} &= -0.007687 + 0.0564 * 0.827 \end{aligned} \tag{B.7}$$

The resulting reference-SuSAv2 scaling functions defined above are displayed versus the scaling variable in Fig. B.1.

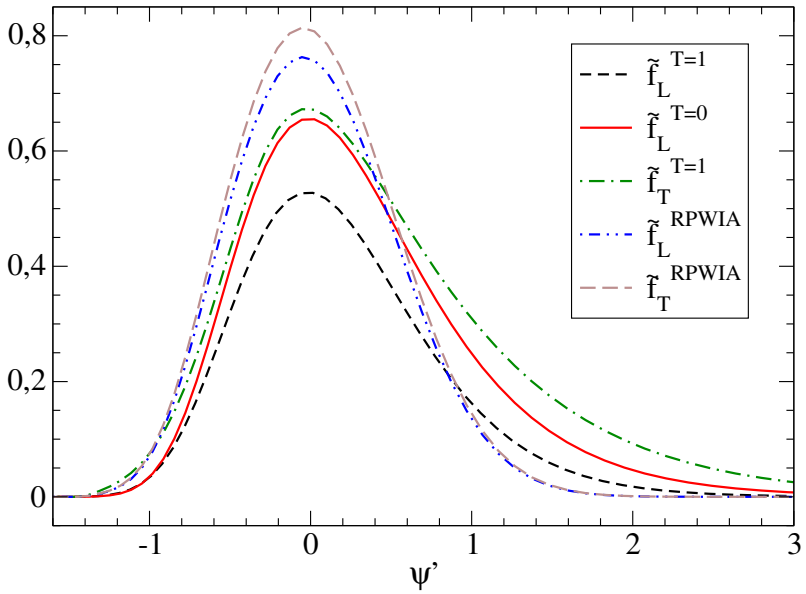

Figure B.1: Reference scaling functions in the SuSAv2 model displayed versus ψ'.

Appendix C

MEC scaling variable

In this Appendix, we describe in detail the 2p-2h MEC scaling variable $\psi'_{MEC}(q,\omega,k_F)$ which bears a resemblance with the usual QE scaling variable $\psi' \equiv \psi'_{QE}(q,\omega)$, and adjusts the maximum of the 2p-2h MEC results at $\psi'_{MEC} \approx 0$. This MEC scaling variable is given by

$$\psi'_{\rm MEC}(q,\omega,k_F) \equiv \frac{1}{\sqrt{\xi_F^{eff}(q)}} \frac{\lambda'_{\rm MEC} - \tau'_{\rm MEC}\rho'_{\rm MEC}}{\sqrt{(1+\lambda'_{\rm MEC}\rho'_{\rm MEC})\tau'_{\rm MEC} + \kappa\sqrt{\tau'_{\rm MEC}\left(1+\tau'_{\rm MEC}\rho'^{\,2}_{\rm MEC}\right)}}}, \quad \text{(C.1)}$$

where

$$\lambda'_{\rm MEC} \equiv \frac{\omega'_{\rm MEC}}{2M_N}, \quad \kappa \equiv \frac{q}{2M_N}, \quad \tau'_{\rm MEC} \equiv \kappa^2 - (\lambda'_{\rm MEC})^2, \quad \text{(C.2)}$$

$$\omega'_{\rm MEC} \equiv \omega - E^{shift}_{\rm MEC}(q), \quad \rho'_{\rm MEC} \equiv 1 + \frac{1}{4\tau'_{\rm MEC}}\left(\frac{m_*^2}{M_N^2} - 1\right). \quad \text{(C.3)}$$

The functions

$$\xi_F^{eff}(q) = \sqrt{1 + \left[\alpha\left(1+\beta e^{-w\gamma}\right)\eta_F\right]^2} - 1 \quad \text{(C.4)}$$

and

$$E^{shift}_{\rm MEC}(q) = E_0 + E_1 t + E_2 t^2, \quad \text{(C.5)}$$

where $w = q/1000$ and $t = (q-500)/1000$ with q in MeV/c are chosen in such a way that the maxima of the 2p-2h responses at different values of q align at $\psi'_{\rm MEC} = 0$. The values of the parameters for the case of ^{12}C are given in Table 1.The same values are used for all the choices of k_F and the results shown in Figs. 4.16 and 4.17 indicate that this procedure is successful.

m_*(MeV/c^2)	α	β	γ	E_0(MeV)	E_1(MeV)	E_2(MeV)
1170	1.3345	30.73	0.85	42.718	-70.0	37.0

Table C.1: The parameters entering the definition of $\psi'_{\rm MEC}$ for ^{12}C.

The usual definition of $\psi'_{\rm QE}$ can be recovered from the above equations by setting $m_* = m_N$ (hence $\rho' = 1$) and replacing $\xi_F^{eff}(q)$ by ξ_F.

Appendix D

Monopole and dipole axial form factor

With the assumptions of conserved vector current and partially conserved axial current, the only undetermined form factor in the analysis of CCQE neutrino scattering is the axial nucleon form factor, $G_A(Q^2)$. In this appendix, we explore the sensitivity of the neutrino and antineutrino cross sections to the description of $G_A(Q^2)$. As introduced in Chapters 1 and 2, neutrino experiments do not have, up to date, the precision required to test explictly the Q^2 dependence of the weak form factors. Although without a strict theoretical basis, a dipole functional form, similar to the Galster one for the vector form factors [18], is assumed in most theoretical models. The assumption of the dipole ansatz is a crucial element in many of the recent neutrino experiments [20, 21, 46, 47, 191]. A reasonable description of $G_A(Q^2)$ by dipole approximation with $M_A \simeq 1$ GeV/c^2 was found in the analysis of electroproduction data on free proton [17] and from $d\sigma/dQ^2$ neutrino-deuterium data cite Bodek:axial2008.

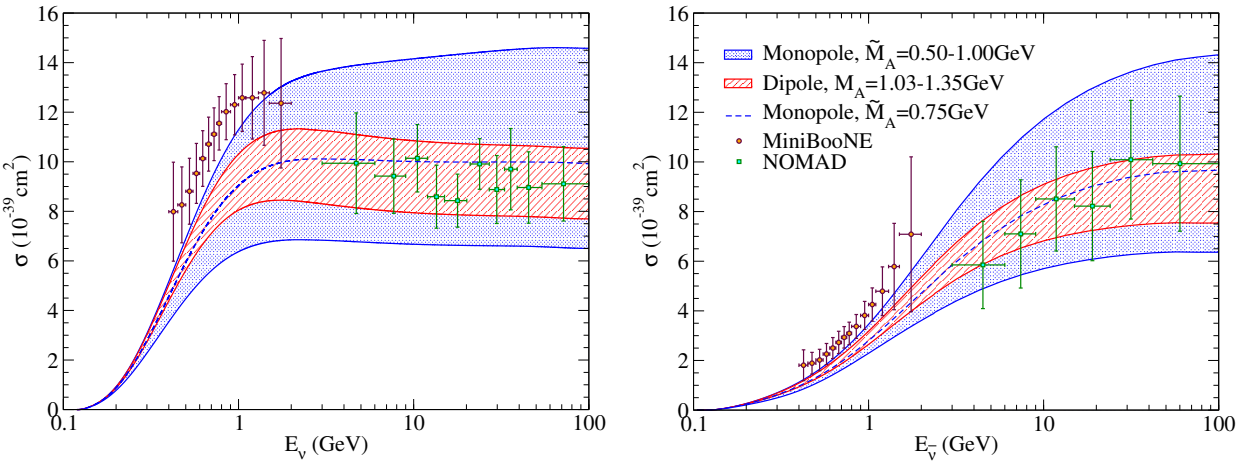

Figure D.1: CCQE ν_μ–^{12}C (left panel) and $\overline{\nu}_\mu$–^{12}C (right panel) cross section per nucleon evaluated in the SuSA model for monopole (blue outer band) and dipole (red inner band) parametrizations of the nucleon axial-vector form factor. A larger axial mass yields a higher cross section. The results for $\widetilde{M}_A = 0.75$ GeV/c^2 are also shown as reference.

When employing a dipole parametrization for the above processes the "standard" value of the axial-vector dipole mass is M_A =1.032 GeV/c^2, whereas in analyzing the MiniBooNE data a larger value of M_A =1.35 GeV/c^2 was proposed [20] without considering the effects of multi-nucleon excitations. The range spanned by these two M_A-values is shown in Fig. D.1 for neutrino and antineutrino scattering on ^{12}C within the semiphenomelogical SuSA approach. Similar effects can be also found in the SuSAv2 model. Clearly the modified axial-vector mass (M_A = 1.35 GeV/c^2)

produces an increase of the cross section improving the agreement at MiniBoone kinematics without considering 2p-2h effects. However, the addition of the 2p-2h contributions, which has been proved as essential to interpret properly the MiniBooNe data, would result in an overstimation of the MiniBooNE data for $M_A = 1.35$ GeV/c^2. Furthermore, the increase due to the enlarged axial mass is excessive to explain the NOMAD data. This reinforces the idea that the world-averaged axial mass ($M_A = 1.032$ GeV/c^2) is the appropriate value for the dipole ansatz.

Although phenomenologically successful, the dipole parametrization has not been justified from a field-theoretical point of view [72] and it is well-known that, for instance, in vector-meson dominance (VMD) models [192], the fact that at moderate momentum transfers the EM form factors are roughly dipole-like is a conspiracy involving the (monopole) ρ and ω poles leading to an effective dipole behaviour (see also the discussions in [70]). Therefore, in addition to the standard dipole form, we also consider here a monopole form $G_A^{(M)}(Q^2) = g_A/(1 + |Q^2|/\widetilde{M}_A^2)$ motivated by VMD-based analyses such as those in [148, 149]. Using the monopole axial-vector masses $\widetilde{M}_A$ =0.5 GeV/c^2 and $\widetilde{M}_A$ =1 GeV/c^2 (the range considered in [71]) and employing the SuSA model, we obtain the band also shown in Fig. D.1. Note that increasing the axial-vector mass produces an increment of the cross sections with both parametrizations and a monopole axial-vector form factor with $\widetilde{M}_A \simeq 1$ GeV/c^2 gives similar results at MiniBooNE kinematics as using $M_A = 1.35$ GeV/c^2, but overstimating significantly the higher-energy NOMAD data. In fact, the band width linked to the two $\widetilde{M}_A$-values used with the monopole axial-vector form factor is much larger than the one corresponding to the dipole parametrization. This is in accordance with previous results shown within the framework of parity-violating electron scattering [71].

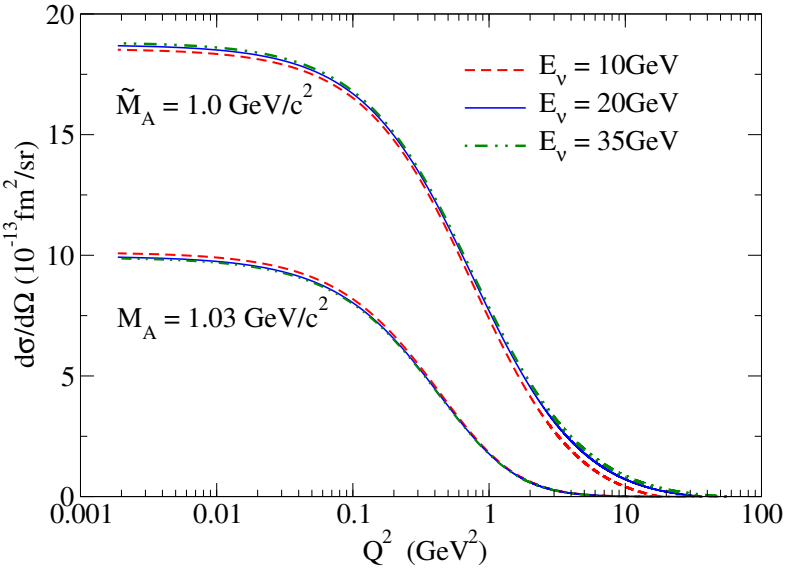

Figure D.2: Elastic neutrino-nucleon $d\sigma/d\Omega$ cross section versus $|Q^2|$. Upper lines: Monopole form factor ($\widetilde{M}_A = 1$ GeV/c^2). Lower lines: Dipole form factor ($M_A = 1.03$ GeV/c^2). The cross section rises slightly with E_ν for the monopole form factor at higher energies whereas the opposite occurs for the dipole ansatz. This effect is noticed, after integrating, in the total cross section.

We should notice that a dipole axial-vector form factor with $M_A = 1.35$ GeV/c^2 (in the SuSA model) produces a cross section that is slightly lower in the MiniBooNE energy region than that obtained using $\widetilde{M}_A = 1$ GeV/c^2, but gives a "reasonable (or a better)" explanation of the NOMAD data. On the other hand, $\widetilde{M}_A = 1$ GeV/c^2 is probably not a good choice because the neutrino cross section keeps rising even at high energies. Indeed if one were to accept the monopole parametriza-

tion and fit the NOMAD data one would find that $\widetilde{M}_A = 0.70 \pm 0.06\,(0.72 \pm 0.14)$ GeV/c^2 for neutrinos (antineutrinos). For completeness, we also show in Fig. D.1 the results for $\widetilde{M}_A = 0.75$ GeV/c^2. It is noteworthy to mention that old experiments with deuterium bubble chambers also performed fits of the data using a monopole axial form factor, obtaining $\widetilde{M}_A = 0.57 \pm 0.05$ GeV/c^2 [25] and $\widetilde{M}_A = 0.54 \pm 0.05$ GeV/c^2 [193].

As generally observed, the monopole form factor descreases slower than the dipole one as $|Q^2|$ rises, which is linked to the different $(1 + |Q^2|/M_A^2)^n$ dependence. This is also observed for elastic neutrino-nucleon reactions (see Fig. D.2 for details) where for $\widetilde{M}_A = 1$ GeV/c^2 the differential cross section keeps rising with E_ν even at high $|Q^2|$. In contrast, the analysis of the dipole form ($M_A = 1.032$ GeV/c^2) shows a slight reduction of the results as E_ν increases.

In summary, while these and previous studies suggest that a dipole axial-vector form factor with the standard value of the dipole mass is preferred, given the modern interest in a potentially different behaviour, especially at high momentum transfers, new studies of neutrino desintegration of deuterium as well as VMD-based theoretical analysis would be very valuable in clarifying this issue before drawing further conclusions.

Appendix E

Quenching of the axial coupling constant

One of the uncertainties in the modeling of weak interactions is the axial-vector coupling constant of the nucleon which has been widely studied theoretically as well as experimentally for many years. This parameter can be defined as the value of the axial form factor of the nucleon in the elastic limit $Q^2 \to 0$, *i.e.*, $g_A = G_A(0)$. As previously introduced in Chapters 2 and 7, the accurately measured beta decay lifetime of the neutron in vacuum, $n \to p + e^- + \overline{\nu}_e$, has allowed to determine the ratio of the axial and vector couplings of the neutron as $|g_A/g_V| = 1.2671 \pm 0.0025$ [73], assuming $g_V \cong 1$.

On the contrary, the analysis of beta-decay in nuclei have suggested that a lower value of $|g_A/g_V| \simeq 1$ would fit better the observed systematics [194]. This quenched value also seems to be consistent with pion-nucleus optical potentials [195, 196] and the analysis of Gamow-Teller resonances in nuclei [197]. Nevertheless, studies of muon capture on nuclei, including detailed nuclear structure effects [198], have concluded that a quenched g_A is not necessary to account for the data. Similar results have also been obtained from lattice QCD [199].

Accordingly, in theoretical calculations related to very low-energy calculations of the axial part of the weak interaction, such as Gamow Teller transitions, a quenching of the axial form-factor is often introduced in order to reproduce the experimental data. This quenching can incorporate many-body effects that are not explicitly introduced in the calculation. This is analogous to what is sometimes done with charges and magnetic moments in electromagnetic studies (*e.g.*, effective charges and moments, core polarization effects, etc.). However, at the energies and momenta of interest for neutrino oscillation experiments, and for kinematical conditions that highly favour scattering under quasielastic conditions, there is little evidence of the need for such a quenching. A similar situation is seen for electron scattering, for which no effective charges are needed to reproduce electron-nucleus scattering under quasielastic conditions and moderately large values of momentum and energy transfer.

Although the neutrino case may be different, due to the axial form factor, quenching of g_A does not appear to be supported by any experiment performed at quasielastic kinematics. Impulse approximation calculations, for which the weak interaction of bound nucleons is taken identical to the one of free ones (no quenching), agree with neutrino-nucleus experimens at intermediate energies. In this regard, we shown in Figs. E.1—E.3 the effect of a quenched g_A value of 0.94, similar to the one suggested by some of the previous studies at very-low energies, in comparison with recent CCQE measurements from the MiniBooNE [20,21], MINERνA [171,172] and NOMAD [24] Collaborations.

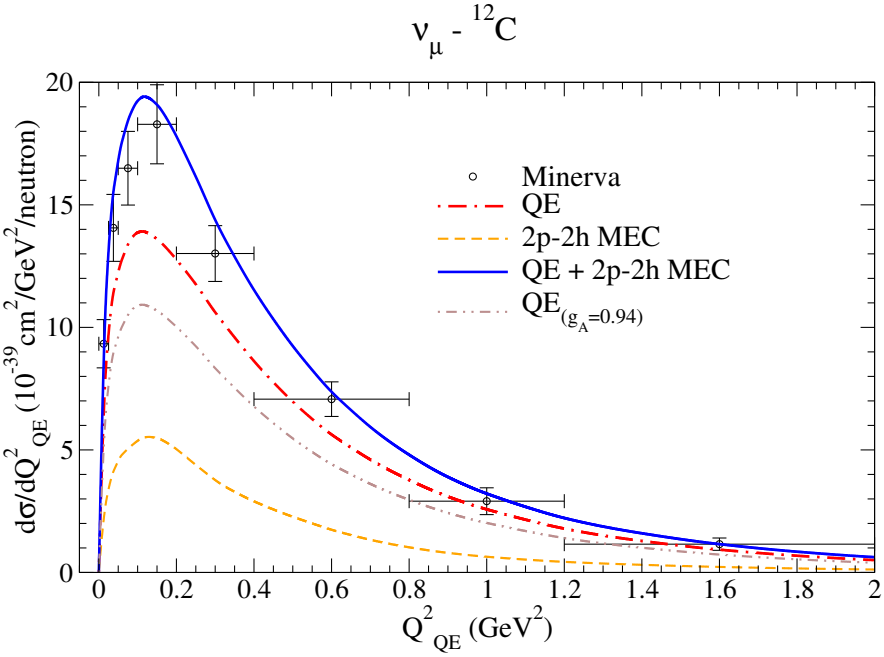

Figure E.1: Flux-folded ν_μ–^{12}C CCQE (upper panel) and $\overline{\nu}_\mu$–CH (lower panel) scattering cross section per target nucleon as a function of Q^2_{QE} and evaluated in the SuSAv2 and SuSAv2-MEC models. The QE results are also shown for the quenched g_A value. MINERνA data are from [172].

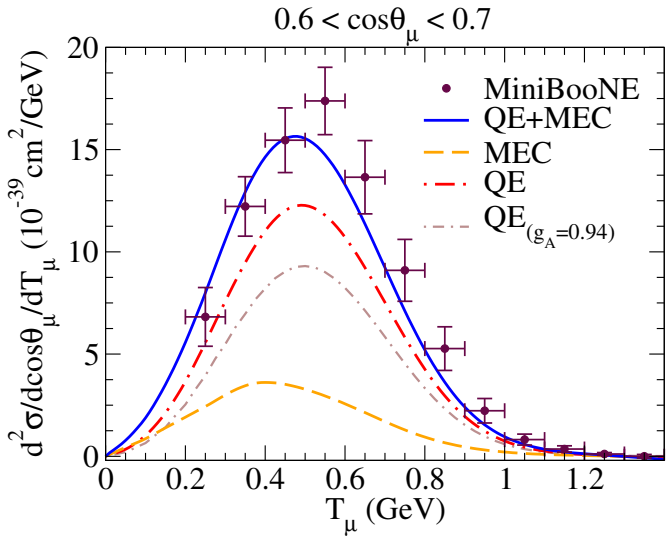

Figure E.2: MiniBoone flux-folded double differential cross section per target nucleon for the ν_μ CCQE process on ^{12}C displayed versus the μ^- kinetic energy T_μ for $\cos\theta_\mu \approx 0.65$ obtained within the SuSAv2-MEC approach. The QE results are also shown for the quenched g_A value. MiniBooNE data are from [20].

Clearly, this choice ($g_A = 0.94$) would put the theory below data as we observe a reduction of $\sim 30\%$ in the QE response (dot-dashed brown line), thus underpredicting the MINERνA (Fig. E.1) and MiniBooNE (Figs. E.2 and E.3) data even if considering 2p-2h MEC contributions. This reduction on g_A would also imply an underestimation of the higher-energy NOMAD data (Fig. E.3). Notice that for this experiment the data are supposed not to include 2p-2h effects. Moreover, the effect of the quenched axial coupling is smaller for the antinetrino cross section ($\sim 20-25\%$) due to the transverse $V-A$ cancellation (see bottom panel of Fig. E.3).

We conclude that, although more experimental analysis would be valuable in order to broaden our knowledge about the axial form factor and their corresponding parameters, these results can be of relevance in this connection as they completely rule out the validity of using a quenched g_A in this energy domain.

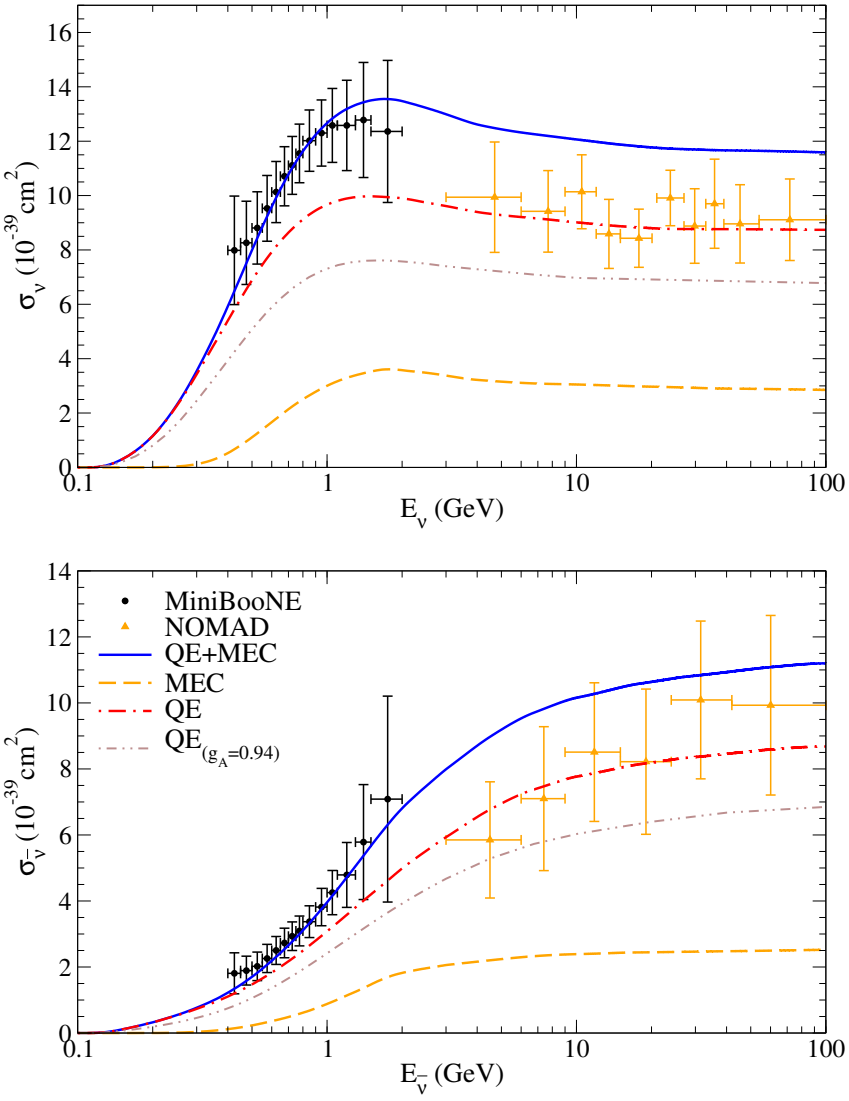

Figure E.3: MiniBooNE CCQE ν_μ-^{12}C ($\overline{\nu}_\mu$-^{12}C) total cross section per nucleon as a function of the neutrino energy. The QE results are also shown for the quenched g_A value. The top panel corresponds to neutrino cross sections and the bottom one to antineutrino reactions. Data are from [20, 21, 24].

Appendix F

Energy reconstruction effects in the study of neutrino oscillations

The interpretation of neutrino oscillation experiments requires an accurate knowledge of the neutrino energy which influences the oscillation length. As previously mentioned in Chapters 1 and 7, neutrino beams are not monochromatic, involving a broad energy distribution around a maximum. Hence, the true energy for a detected event is unknown. One approach to determine these neutrino energies is to employ a energy reconstruction method defined in terms on the kinematics of the CCQE-like events detected, as done in the MiniBooNE, T2K or MINERνA experiments based on Cherenkov detectors. This method was introduced in Chapter 7 (see Eqs. 7.1—7.3) where the measured final-lepton kinematics (E_l and θ_l) are used to obtain a reconstructed neutrino energy E_ν^{QE} and 4-momentum transfer Q_{QE} assuming an initial-state nucleon at rest for QE neutrino-nucleus reactions. However, the determination of these reconstructed magnitudes depends largely on model assumptions and can be affected by different nuclear effects, such as Pauli blocking, low-energy excitations, pion-absorption or multinucleon contributions. These effects have been widely studied within the RPA approach and considering 2p-2h effects by Martini *et al.* [180, 200] and Nieves *et al.* [201]. In particular, the 2p-2h excitations introduce important effects in the energy reconstruction distributions where a large variety of neutrino energies can be related to one reconstructed value.

In what follows, we analyze the corresponding distribution of charged current events, $D_{rec}(\overline{E_\nu})$, in terms of the reconstructed energy ($E_\nu^{QE} \equiv \overline{E_\nu}$). This distribution can be described in terms of the double differential neutrino cross section as

$$\begin{aligned} D_{rec}(\overline{E_\nu}) &= \int dE_\nu \Phi(E_\nu) \int_{E_l^{min}}^{E_l^{max}} dE_l \frac{ME_l - m_l^2/2}{\overline{E_\nu}^2 k_l} \left[\frac{d^2\sigma}{d\omega\, d\cos\theta}\right]_{\omega=E_\nu-E_l}^{\cos\theta=\cos\theta(E_l,\overline{E_\nu})} \\ &= \int dE_\nu \Phi(E_\nu) d(E_\nu, \overline{E_\nu}). \end{aligned} \tag{F.1}$$

where the integral limits E_l^{min} and E_l^{max} represent the minimum and maximum values of the final-lepton energy given in terms of $\overline{E_\nu}$. The second integral in the previous expression refers to the spreading function $d(E_\nu, \overline{E_\nu})$ which allow to study the $\overline{E_\nu}$ dependence for different E_ν values. This can be observed in Fig. F.1, where we represent the QE, 2p-2h MEC and pion production contributions at kinematics of relevance for the MiniBooNE and T2K experiments.

As can be noticed, the spreading function is asymmetrical around E_ν and the 2p-2h effects are of special relevance at low $\overline{E_\nu}$ where a long energy tail emerges. For completeness, we have also

included the contributions related to the Δ-resonance and the subsequent pion production that appear at large true kinematics and clearly extend to the lowest values of the reconstructed energies. In general, we observe that the corrections introduced from the reconstructed kinematics in the experimental measurements imply that charged current events tend to escape from the region of high flux, being shifted to the low-energy region.

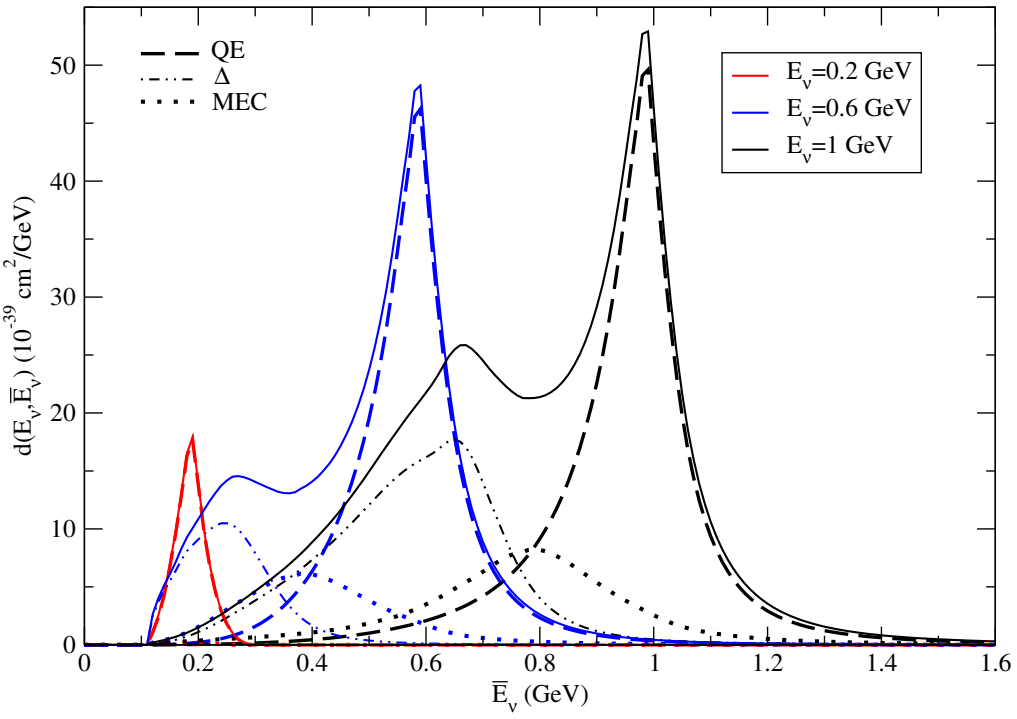

Figure F.1: The spreading function $d(E_\nu, \overline{E_\nu})$ per neutron for the ν_μ-^{12}C scattering process. The quasielastic, 2p-2h MEC and Δ-resonance contributions are shown separately. The net contribution (solid lines) is also displayed.

The results shown in this appendix are of interest for the $\nu_\mu \to \nu_e$ oscillation probability analyses of MiniBooNE [202–204] and T2K [205, 206] as well as for the MiniBooNE low-energy excess [202, 207], where the latter can be explained by nuclear effects beyond IA and the QE regime, in particular, by multi-nucleon excitations. More specific analysis on this issue can also be found on [200, 201, 208].

Bibliography

[1] ATLAS COLLABORATION, *Phys. Lett. B* **716**, 1.

[2] PARTICLE DATA GROUP COLLABORATION, *Phys. Rev. D* **86**, 166 (2012).

[3] M. ERICSON and M. MARTINI, *Phys. Rev. C* **91**, 035501 (2015).

[4] F. REINES and C. L. COWAN, *Phys. Rev.* **92**, 8301 (1953).

[5] R. DAVIS and D. S. HARMER, *Bulleting of the American Physiological Society* **4**, 217 (1959).

[6] [LSND COLLABORATION], C. ATHANASSOPOULOS, et al., *Phys. Rev. Lett.* **75**, 2650 (1995).

[7] [SUPER-KAMIOKANDE COLLABORATION], Y. FUKUDA, et al., *Phys. Rev. Lett.* **81**, 1562 (1998).

[8] [SNO COLLABORATION], Q. R. AHMAD, et al., *Phys. Rev. Lett.* **87**, 071301 (2001).

[9] [K2K COLLABORATION], M. H. AHN, et al., *Phys. Rev. Lett.* **90**, 041801 (2003).

[10] B. PONTECORVO, *Journal of Exp. and Theo. Physics* **26**, 984 (1968).

[11] Z. MAKI, M. NAGAKAWA, and S. SAKATA, *Progress of Theo. Physics* **28**, 870 (1962).

[12] S. WEINBERG, *Phys. Rev. Lett.* **19**, 1264 (1967).

[13] A. SALAM, *Elementary Particle Physics (ed. N. Scartholm, Stockholm)* .

[14] S. L. GLASHOW, *Phys. Rev. D* **2**, 1285 (1970).

[15] J. A. FORMAGGIO and G. P. ZELLER, *Rev. Mod. Phys.* **84**, 1307 (2012).

[16] J. D. WALECKA, *Theoretical Nuclear And Subnuclear Physics*, Editorial World Scientific Pub. Co. Inc., 2004.

[17] V. BERNARD, L. ELOUADRHIRI, and U.-G. MEISSNER, *J. Phys. G* **28** (2002).

[18] S. GALSTER et al., *Nucl. Phys. B* **32**, 221 (1971).

[19] G. D. MEGIAS, J. E. AMARO, M. B. BARBARO, J. A. CABALLERO, and T. W. DONNELLY, *Phys. Lett. B* **725**, 170 (2013).

[20] [MINIBOONE COLLABORATION], A. A. AGUILAR-AREVALO, et al., *Phys. Rev. D* **81**, 092005 (2010).

[21] [MINIBOONE COLLABORATION], A. A. AGUILAR-AREVALO, et al., *Phys. Rev. D* **88**, 032001 (2013).

[22] G. M. RADECKY et al., *Phys. Rev. D* **25**, 1161 (1982).

[23] T. KITAGAKI et al., *Phys. Rev. D* **42**, 1331 (1990).

[24] [NOMAD COLLABORATION], V. LYUBUSHKIN, et al., *Eur. Phys. J. C* **63**, 355 (2009).

[25] N. J. BAKER et al., *Phys. Rev. D* **23**, 2499 (1981).

[26] S. J. BARISH et al., *Phys. Rev. D* **16**, 3103 (1977).

[27] W. A. MANN et al., *Phys. Rev. Lett.* **31**, 844 (1973).

[28] M. POHL et al., *Lett. Nuovo Cimento* **26**, 332 (1979).

[29] S. BONETTI et al., *Nuovo Cimento* **38**, 260 (2006).

[30] M. MARTINI, M. ERICSON, G. CHANFRAY, and J. MARTEAU, *Phys. Rev. C* **80**, 065501 (2009).

[31] J. NIEVES, I. RUIZ SIMO, and M. J. VICENTE VACAS, *Phys. Lett. B* **707**, 72 (2012).

[32] A. MEUCCI, M. B. BARBARO, J. A. CABALLERO, C. GIUSTI, and J. M. UDIAS, *Phys. Rev. Lett.* **107**, 172501 (2011).

[33] O. BENHAR, A. LOVATO, and N. ROCCO, *Phys. Rev.* **C92**, 024602 (2015).

[34] O. LALAKULICH, U. MOSEL, and K. GALLMEISTER, *Phys. Rev. C* **86**, 045606 (2012).

[35] T. W. DONNELLY and I. SICK, *Phys. Rev. Lett.* **82**, 3212 (1999).

[36] T. W. DONNELLY and I. SICK, *Phys. Rev. C* **60**, 065502 (1999).

[37] C. MAIERON, T. W. DONNELLY, and I. SICK, *Phys. Rev. C* **65**, 025502 (2002).

[38] G. D. MEGIAS, J. E. AMARO, M. B. BARBARO, J. A. CABALLERO, and T. W. DONNELLY, *Phys. Rev. D* **94**, 013012 (2016).

[39] G. D. MEGIAS, J. E. AMARO, M. B. BARBARO, J. A. CABALLERO, T. W. DONNELLY, and I. RUIZ SIMO, *Phys. Rev. D* **94**, 093004 (2016).

[40] H. HARARI, *Lecture at the "Neutrino 88" conference, Tufts University, 1988* .

[41] Y. NAKAJIMA et al., *Phys. Rev. D* **83**, 012005 (2011).

[42] [MINOS COLLABORATION], P. ADAMSON, et al., *Phys. Rev. D* **83**, 012005 (2008).

[43] [NOVA COLLABORATION], P. ADAMSON, et al., *Phys. Rev. Lett.* **116**, 151806 (2016).

[44] [T2K COLLABORATION], K. ABE, et al., *Phys. Rev. D* **87**, 092003 (2013).

[45] [T2K COLLABORATION], K. ABE, et al., *Phys. Rev. Lett.* **113**, 241803 (2014).

[46] [MINERνA COLLABORATION], G. A. FIORENTINI, et al., *Phys. Rev. Lett.* **111**, 022502 (2013).

[47] [MINERνA COLLABORATION], L. FIELDS, et al., *Phys. Rev. Lett.* **111**, 022501 (2013).

[48] C. ANDERSON et al., *Phys. Rev. Lett.* **108**, 161802 (2012).

[49] R. ACCIARRI et al., *Phys. Rev. D* **89**, 112003 (2014).

[50] [HARP COLLABORATION], M. APOLLONIO, et al., *Phys. Rev. C* **82**, 045208 (2010).

[51] T. KATORI and M. MARTINI, *arXiv:1611.07770 [hep-ph]* (2016).

[52] R. ACCIARRI et al., *JINST* **12** (2017).

[53] [MINERνA COLLABORATION], J. WOLCOTT, et al., *Phys. Rev. Lett.* **116**, 081802 (2016).

[54] [MINERνA COLLABORATION], J. MOUSSEAU, et al., *Phys. Rev. D* **93**, 071101 (2016).

[55] [T2K COLLABORATION], K. ABE, et al., *arXiv:1704.06409 [hep-ex]* (2017).

[56] [T2K COLLABORATION], K. ABE, et al., *Phys. Rev. D* **93**, 112012 (2016).

[57] K. ABE et al., *arXiv:1412.4673 [physics.ins-det]* (2014).

[58] [νSTORM COLLABORATION], P. KYBERD, et al., *arXiv:1206.0294 [hep-ex]* (2012).

[59] [νSTORM COLLABORATION], D. ADEY, et al., *arXiv:1308.6822 [physics.acc-ph]* (2013).

[60] R. ACCIARRI et al., *arXiv:1601.05471 [physics.ins-det]* (2016).

[61] R. GONZALEZ-JIMENEZ, *Violación de paridad en dispersión elástica y cuasielástica de electrones por nucleones y núcleos*, PHD Thesis, 2014.

[62] T. W. DONNELLY, *General notes on Scaling* (2012).

[63] G. D. MEGIAS, *Interacción neutrino-núcleo mediada por corrientes cargadas*, MSc Thesis, 2012.

[64] J. E. AMARO, M. B. BARBARO, J. A. CABALLERO, T. W. DONNELLY, A. MOLINARI, and I. SICK, *Phys. Rev. C* **71**, 015501 (2005).

[65] N. CABIBBO, *Phys. Rev. Lett.* **10**, 531 (1963).

[66] M. N. ROSENBLUTH, *Phys. Rev.* **79**, 615 (1950).

[67] T. R. GENTILE and C. B. CRAWFORD, *Phys. Rev. C* **83**, 055203 (2011).

[68] J. KELLY, *Phys. Rev. C* **70**, 068202 (2004).

[69] M. GARI and W. KRUPELMANN, *Z. Phys. A* **322**, 689 (1985).

[70] C. CRAWFORD, T. W. DONNELLY, E. LOMON, et al., *Phys. Rev. C* **82**, 045211 (2010).

[71] R. GONZÁLEZ-JIMÉNEZ, J. A. CABALLERO, and T. W. DONNELLY, *Phys. Rep.* **524**, 1 (2013).

[72] P. MASJUAN, E. RUIZ-ARRIOLA, and W. BRONIOWSKI, *Phys. Rev. D* **87**, 014005 (2013).

[73] [PARTICLE DATA GROUP COLLABORATION], D. E. GROOM, et al., *Eur. Phys. J. C* **15**, 1 (2000).

[74] A. W. THOMAS and W. WEISE, *The Structure of the Nucleon*, Wiley-VCH Verlag Berlin GmbH, 2001.

[75] W. ALBERICO, A. MOLINARI, T. DONNELLY, L. KRONENBERG, and J. V. ORDEN, *Phys. Rev. C* **38**, 1801 (1988).

[76] E. J. MONIZ et al., *Phys. Rev. Lett.* **26**, 445 (1971).

[77] G. B. WEST, *Phys. Rep.* **18**, 263 (1975).

[78] D. B. DAY, J. S. MCCARTHY, T. W. DONNELLY, and I. SICK, *Annu. Rev. Nucl. Part. Sci.* **40**, 357 (1990).

[79] J. A. CABALLERO, M. B. BARBARO, A. N. ANTONOV, M. V. IVANOV, and T. W. DONNELLY, *Phys. Rev. C* **81**, 055502 (2010).

[80] A. N. ANTONOV, M. V. IVANOV, J. A. CABALLERO, M. B. BARBARO, J. M. UDIAS, E. M. DE GUERRA, and T. W. DONNELLY, *Phys. Rev. C* **83**, 045504 (2011).

[81] J. E. AMARO, M. B. BARBARO, J. A. CABALLERO, and T. W. DONNELLY, *Phys. Rev. C* **73**, 035503 (2006).

[82] J. JOURDAN, *Nucl. Phys. A* **603**, 117 (1996).

[83] M. V. IVANOV, A. N. ANTONOV, J. A. CABALLERO, G. D. MEGIAS, M. B. BARBARO, J. M. UDIAS, and E. M. DE GUERRA, *Phys. Rev. C* **89**, 014607 (2014).

[84] C. MAIERON, J. E. AMARO, M. B. BARBARO, J. A. CABALLERO, T. W. DONNELLY, and C. F. WILLIAMSON, *Phys. Rev. C* **80**, 035504 (2009).

[85] J. E. AMARO, M. B. BARBARO, J. A. CABALLERO, T. W. DONNELLY, and C. MAIERON, *Phys. Rev. C* **71**, 065501 (2005).

[86] J. A. CABALLERO, *Phys. Rev. C* **74**, 015502 (2006).

[87] J. A. CABALLERO, J. E. AMARO, M. B. BARBARO, T. W. DONNELLY, C. MAIERON, and J. M. UDÍAS, *Phys. Rev. Lett.* **95**, 252502 (2005).

[88] J. A. CABALLERO, J. E. AMARO, M. B. BARBARO, T. W. DONNELLY, and J. M. UDÍAS, *Phys. Lett. B* **653**, 366 (2007).

[89] P. RING, *Prog. Part. Nucl. Phys.* **37**, 193 (1996).

[90] Y. HORIKAWA, F. LENZ, and N. C. MUKHOPADHYAY, *Phys. Rev. C* **22**, 1680 (1980).

[91] J. E. AMARO, M. B. BARBARO, J. A. CABALLERO, T. W. DONNELLY, and J. M. UDÍAS, *Phys. Rev. C* **75**, 034613 (2007).

[92] C. MAIERON et al., *Phys. Rev. C* **68**, 048501 (2003).

[93] A. MEUCCI, F. CAPUZZI, C. GIUSTI, and F. D. PACATI, *Phys. Rev. C* **67**, 054601 (2003).

[94] A. MEUCCI, J. A. CABALLERO, C. GIUSTI, F. D. PACATI, and J. M. UDIAS, *Phys. Rev. C* **80**, 024605 (2009).

[95] J. A. CABALLERO, M. C. MARTINEZ, J. L. . HERRAIZ, and J. M. UDÍAS, *Phys. Lett. B* **688**, 250 (2010).

[96] R. ROSENFELDER, *Ann. Phys.* **128**, 188 (1980).

[97] G. D. MEGIAS, M. V. IVANOV, R. GONZÁLEZ-JIMÉNEZ, M. B. BARBARO, J. A. CABALLERO, T. W. DONNELLY, and J. M. UDÍAS, *Phys. Rev. D* **89**, 093002 (2014).

[98] L. LANDAU and E. M. LIFSHITZ, *Statistical Physics, Part I*, Pergamon Press, 1980.

[99] [MINIBOONE COLLABORATION], A. A. AGUILAR-AREVALO, et al., *Phys. Rev. Lett.* **100**, 032301 (2008).

[100] O. BENHAR, D. DAY, and I. SICK, *Rev. Mod. Phys.* **80**, 189 (2008).

[101] O. BENHAR, D. DAY, and I. SICK, *arXiv:nucl-ex/0603032* (2006).

[102] J. E. AMARO, M. B. BARBARO, J. A. CABALLERO, T. W. DONNELLY, and C. F. WILLIAMSON, *Phys. Lett. B* **696**, 151 (2011).

[103] O. LALAKULICH, K. GALLMEISTER, and U. MOSEL, *Phys. Rev. C* **86**, 014614 (2012).

[104] J. E. AMARO, M. B. BARBARO, J. A. CABALLERO, and T. W. DONNELLY, *Phys. Rev. Lett.* **108**, 152501 (2012).

[105] I. RUIZ SIMO, J. E. AMARO, M. B. BARBARO, J. A. CABALLERO, A. DE PACE, and T. W. DONNELLY, *J. Phys. G* **44**, 065105 (2017).

[106] J. E. AMARO, M. B. BARBARO, J. A. CABALLERO, T. W. DONNELLY, and A. MOLINARI, *Phys. Rep.* **368**, 317 (2002).

[107] J. E. AMARO, M. B. BARBARO, J. A. CABALLERO, T. W. DONNELLY, and A. MOLINARI, *Nucl. Phys. A* **723**, 181 (2003).

[108] W. ALBERICO, T. DONNELLY, and A. MOLINARI, *Nucl. Phys. A* **623**, 471 (1998).

[109] J. E. AMARO, M. B. BARBARO, J. A. CABALLERO, T. W. DONNELLY, C. MAIERON, and J. M. UDIAS, *Phys. Rev. C* **81**, 014606 (2010).

[110] A. DE PACE, M. NARDI, W. M. ALBERICO, T. W. DONNELLY, and A. MOLINARI, *Nucl. Phys. A* **726**, 303 (2003).

[111] A. DE PACE, M. NARDI, W. M. ALBERICO, T. W. DONNELLY, and A. MOLINARI, *Nucl. Phys. A* **741**, 249 (2004).

[112] I. R. SIMO, C. ALBERTUS, J. E. AMARO, M. B. BARBARO, J. A. CABALLERO, and T. W. DONNELLY, *Phys. Rev. D* **90**, 053010 (2014).

[113] I. RUIZ SIMO, C. ALBERTUS, J. E. AMARO, M. B. BARBARO, J. A. CABALLERO, and T. W. DONNELLY, *Phys. Rev. D* **90**, 033012 (2014).

[114] J. E. AMARO, A. M. LALLENA, and G. CO, *Nucl. Phys.* **A578**, 365 (1994).

[115] G. D. MEGIAS, T. W. DONNELLY, O. MORENO, C. F. WILLIAMSON, J. A. CABALLERO, R. GONZÁLEZ-JIMÉNEZ, A. DE PACE, M. B. BARBARO, W. M. ALBERICO, M. NARDI, and J. E. AMARO, *Phys. Rev. D* **91**, 073004 (2015).

[116] J. E. AMARO, G. CO', V. M. FASANELLI, and A. M. LALLENA, *Phys. Lett. B* **277**, 249 (1992).

[117] J. W. V. ORDEN and T. W. DONNELLY, *Annals Phys.* **131**, 451 (1981).

[118] W. ALBERICO, M. ERICSON, and A. MOLINARI, *Annals Phys.* **154**, 356 (1984).

[119] M. J. DEKKER, P. J. BRUSSAARD, and J. A. TJON, *Phys. Rev.* **C49**, 2650 (1994).

[120] I. RUIZ SIMO, J. E. AMARO, M. B. BARBARO, J. A. CABALLERO, G. D. MEGIAS, A. DE PACE, and T. W. DONNELLY, *arXiv:1606.06480 [nucl-th]* (2016).

[121] A. GIL, J. NIEVES, and E. OSET, *Nucl. Phys.* **A627**, 543 (1997).

[122] [T2K COLLABORATION], T. YUAN, et al., *arXiv:1611.03536 [hep-ex]* (2016).

[123] J. BJORKEN, *Phys. Rev.* **179**, 1547 (1969).

[124] C. G. CALLAN and D. J. GROSS, *Phys. Rev. Lett.* **22**, 156 (1959).

[125] A. GONZALEZ-ARROYO, C. LOPEZ, and F. J. YNDURAIN, *Phys. Lett. B* **98**, 215 (1981).

[126] S. MANTRY, J. RAMSEY-MUSOLF, and G. F. SACCO, *Phys. Rev. C* **82**, 065205 (2010).

[127] C. PASTORINA, *Phys. Rev. D* **65**, 097502 (2002).

[128] D. BOER et al., *Eur. Phys. J. A* **48**, 187 (2012).

[129] V. MAMYAN, *arXiv:1202.1457 [nucl-ex]* (2012).

[130] D. BOER et al., *arXiv:1108.1713 [nucl-th]* (2011).

[131] E. PEREZ and E. RIZVI, *Rep. Prog. Phys.* **76**, 046201 (2013).

[132] [PARTICLE DATA GROUP COLLABORATION], K. NAKAMURA, et al., *J. Phys. G* **37**, 075021 (2010).

[133] A. BODEK and J. L. RITCHIE, *Phys. Rev. D.* **23**, 1070 (1981).

[134] A. BODEK and J. L. RITCHIE, *Phys. Rev. D.* **24**, 1400 (1981).

[135] H. HAIDER, M. SAJJAD-ATHAR, S. K. SINGH, and I. RUIZ-SIMO, *Nucl. Phys. A* **940**, 138 (2015).

[136] T. HOBBS and W. MELNITCHOUK, *Phys. Rev. D* **77**, 114023 (2008).

[137] J. H. KIM et al., *Phys. Rev. Lett.* **81**, 3595 (1998).

[138] J. H. KIM et al., *Phys. Rev. Lett.* **79**, 1213 (1997).

[139] M. GHERMANN, R. G. ROSS, and M. R. WHALLEY, *J. Phys. G* **25**, 12 (1999).

[140] A. BODEK, *Phys. Rev. D* **20**, 1471 (1979).

[141] A. STEIN et al., *Phys. Rev. D.* **12**, 1884 (1975).

[142] M. B. BARBARO, J. A. CABALLERO, T. W. DONNELLY, and C. MAIERON, *Phys. Rev. C* **69**, 035502 (2004).

[143] P. E. BOSTED and M. E. CHRISTY, *Phys. Rev. C* **81**, 055213 (2010).

[144] P. E. BOSTED and M. E. CHRISTY, *Phys. Rev. C* **77**, 065206 (2008).

[145] Y. LIANG et al., *arXiv:nucl-ex/0410027* (2004).

[146] M. GLUECK, E. REYA, and A. VOGT, *Eur. Phys. J. C* **5**, 461 (1998).

[147] A. BODEK and U. YANG, *arXiv:hep-ph/1011.6592* (2013).

[148] E. L. LOMON, *Phys. Rev. C* **64**, 035204 (2001).

[149] E. L. LOMON, *Phys. Rev. C* **66**, 045501 (2002).

[150] C. CRAWFORD et al., *Phys. Rev. C* **82**, 045211 (2010).

[151] V. PANDEY, N. JACHOWICZ, T. V. CUYCK, J. RYCKEBUSCH, and M. MARTINI, *Phys. Rev. C* **92**, 024606 (2015).

[152] R. M. SEALOCK et al., *Phys. Rev. Lett.* **62**, 1350 (1989).

[153] R. GONZÁLEZ-JIMÉNEZ, G. D. MEGIAS, M. B. BARBARO, J. A. CABALLERO, and T. W. DONNELLY, *Phys. Rev. C* **90**, 035501 (2014).

[154] J. E. AMARO, G. CO', and A. M. LALLENA, *arXiv:nucl-th/9902072* (1999).

[155] R. GONZÁLEZ-JIMÉNEZ, M. V. IVANOV, M. B. BARBARO, J. A. CABALLERO, and J. M. UDIAS, *Phys. Lett. B* **718**, 1471 (2013).

[156] J. E. AMARO, M. B. BARBARO, J. A. CABALLERO, A.DE PACE, T. W. DONNELLY, G. D. MEGIAS, and I. RUIZ-SIMO, *arXiv:1704.01539 [nucl-th]* (2017).

[157] M. ANGHINOLFI et al., *Nucl. Phys.* **A602**, 405 (1996).

[158] J. S. O'CONNELL et al., *Phys. Rev.* **C35**, 1063 (1987).

[159] C. WILLIAMSON et al., *Phys. Rev.* **C56**, 3152 (1997).

[160] Z. E. MEZIANI et al., *Phys. Rev. Lett.* **52**, 2130 (1984).

[161] D. B. DAY et al., *Phys. Rev.* **C48**, 1849 (1993).

[162] J. NIEVES, I. RUIZ SIMO, and M. J. VICENTE VACAS, *Phys. Lett. B* **721**, 90 (2013).

[163] M. V. IVANOV, R. GONZÁLEZ-JIMÉNEZ, J. A. CABALLERO, M. B. BARBARO, T. W. DONNELLY, and J. M. UDÍAS, *Phys. Lett. B* **727**, 265 (2013).

[164] M. MARTINI, M. ERICSON, G. CHANFRAY, and J. MARTEAU, *Phys. Rev. C* **81**, 045502 (2010).

[165] [MINERνA COLLABORATION], L. REN, et al., *Phys. Rev. D* **95**, 072009 (2017).

[166] T. W. DONNELLY, J. W. VAN ORDEN, T. DE FOREST JR., and W. C. HERMANS, *Phys. Lett.* **B76**, 393 (1978).

[167] J. E. AMARO, C. MAIERON, M. B. BARBARO, J. A. CABALLERO, and T. W. DONNELLY, *Phys. Rev. C* **82**, 044601 (2010).

[168] R. GRAN, J. NIEVES, F. SÁNCHEZ, and M. J. VICENTE VACAS, *Phys. Rev. D* **88**, 113007 (2013).

[169] A. MEUCCI and C. GIUSTI, *Phys. Rev. D* **89**, 117301 (2014).

[170] U. MOSEL, O. LALAKULICH, and K. GALLMEISTER, *Phys. Rev. D* **89** (2014).

[171] [MINERνA COLLABORATION], L. ALIAGA, et al., *Phys. Rev. D* **94**, 092005 (2016).

[172] K. MCFARLAND, *Private communication* .

[173] V. PANDEY, N. JACHOWICZ, M. MARTINI, R. GONZALEZ-JIMENEZ, T. V. CUYCK, J. RYCKEBUSCH, and N. VAN DESSEL, *Phys. Rev. C* **94**, 054609 (2016).

[174] N. VAN DESSEL, N. JACHOWICZ, R. GONZALEZ-JIMENEZ, V. PANDEY, and T. V. CUYCK, *arXiv:1704.07817 [nucl-th]* (2017).

[175] J. E. AMARO, M. B. BARBARO, J. A. CABALLERO, and T. W. DONNELLY, *Phys. Rev. Lett.* **98**, 242501 (2007).

[176] W. ALBERICO et al., *Nucl. Phys. A* **623**, 471 (1997).

[177] J. BLIETSCHAU, GARGAMELLE COLLABORATION, et al., *Nucl. Phys. B* **133**, 205 (1978).

[178] [NOvA COLLABORATION] and X. BU, *arXiv:1601.01213 [hep-ex]* (2016).

[179] R. ACCIARRI et al., *Phys. Rev. D* **95**, 072005 (2017).

[180] V. PANDEY, N. JACHOWICZ, T. V. CUYCK, J. RYCKEBUSCH, and M. MARTINI, *Phys. Rev. C* **94**, 015501 (2016).

[181] [T2K COLLABORATION], K. ABE, et al., *Phys. Rev. D* **91** (2015).

[182] A. M. ANKOWSKI, M. B. BARBARO, O. BENHAR, J. A. CABALLERO, C. GIUSTI, R. GONZALEZ-JIMENEZ, G. D. MEGIAS, and A. MEUCCI, *Phys. Rev. C* **92**, 025501 (2015).

[183] [T2K COLLABORATION], K. ABE, et al., *Phys. Rev. D* **90**, 052010 (2014).

[184] M. V. IVANOV, G. D. MEGIAS, R. GONZÁLEZ-JIMÉNEZ, O. MORENO, M. B. BARBARO, J. A. CABALLERO, and T. W. DONNELLY, *J. Phys. G* **43**, 045101 (2016).

[185] P. BARREAU et al., *Nucl. Phys. A* **402**, 515 (1983).

[186] M. MARTINI and M. ERICSON, *Phys. Rev. C* **90**, 025501 (2014).

[187] K. GALLMEISTER, U. MOSEL, and J. WEIL, *Phys. Rev. C* **94**, 035502 (2016).

[188] A. MEUCCI and C. GIUSTI, *Phys. Rev. D* **91**, 093004 (2015).

[189] I. RUIZ SIMO, J. E. AMARO, M. B. BARBARO, A. DE PACE, J. A. CABALLERO, G. D. MEGIAS, and T. W. DONNELLY, *Phys. Lett.* **B762**, 124 (2016).

[190] E. J. GUMBEL, *Annales de l'Institut Henri Poincare (1935)* **5**.

[191] T2K COLLABORATION, K. ABE, et al., *Phys. Rev. D* **93**, 112003 (2015).

[192] A. V. BUTKEVICH and D. PEREVALOV, *Phys. Rev. D* **89**, 053014 (2014).

[193] K. MILLER et al., *Phys. Rev. D* **26**, 537 (1982).

[194] B. BUCK and S. M. PEREZ, *Phys. Rev. Lett.* **50**, 1975 (1983).

[195] M. ERICSON, A. FIGUREAU, and C. THÉVENET, *Phys. Lett. B* **45**, 19 (1973).

[196] A. BOHR and B. MOTTTELSON, *Phys. Lett. B* **100**, 10 (1981).

[197] C. GOODMAN, *Prog. Part. Nucl. Phys.* **11**, 475 (1984).

[198] E. KOLBE, K. LANGANKE, and P. VOGEL, *Phys. Rev. C* **62**, 055502 (2000).

[199] A. ALI KHAN et al., *Phys. Rev. D* **74**, 094508 (2006).

[200] M. MARTINI, M. ERICSON, and G. CHANFRAY, *Phys. Rev. D* **85**, 093012 (2012).

[201] J. NIEVES, F. SÁNCHEZ, I. RUIZ SIMO, and M. J. VICENTE VACAS, *Phys. Rev. D* **85**, 113008 (2012).

[202] [MINIBOONE COLLABORATION], A. A. AGUILAR-AREVALO, et al., *Phys. Rev. Lett.* **98**, 231801 (2007).

[203] [MINIBOONE COLLABORATION], A. A. AGUILAR-AREVALO, et al., *Phys. Rev. Lett.* **102**, 101802 (2009).

[204] [MINIBOONE COLLABORATION], A. A. AGUILAR-AREVALO, et al., *Phys. Rev. Lett.* **110**, 161801 (2013).

[205] [T2K COLLABORATION], K. ABE, et al., *Phys. Rev. Lett.* **107**, 041801 (2011).

[206] [T2K COLLABORATION], K. ABE, et al., *Phys. Rev. D* **85**, 031103 (2012).

[207] [MINIBOONE COLLABORATION], A. A. AGUILAR-AREVALO, et al., *Phys. Rev. Lett.* **103**, 111801 (2009).

[208] M. MARTINI, M. ERICSON, and G. CHANFRAY, *Phys. Rev. D* **87**, 013009 (2013).

List of publications

ISI PUBLICATIONS

1. **"Neutrino-Oxygen CC0π scattering in the SuSAv2-MEC model"**
   G. D. Megias, J. E. Amaro, M. B. Barbaro, J. A. Caballero, T. W. Donnelly and I. Ruiz Simo.
   To be submitted (2017).

2. **"Density dependence of 2p-2h meson-exchange currents"**
   J. E. Amaro, M. B. Barbaro, J. A. Caballero, A. De Pace, T. W. Donnelly, G. D. Megias and I. Ruiz Simo.
   Physical Review C (2017). In Press.

3. **"The frozen nucleon approximation in two-particle two-hole response functions"**
   I. Ruiz Simo, J. E. Amaro, M. B. Barbaro, J. A. Caballero, G. D. Megias and T. W. Donnelly.
   Physics Letters B (2017). In Press.
   DOI: 10.1016/j.physletb.2017.04.063

4. **"Charged-current neutrino-nucleus reactions within the SuSAv2-MEC approach"**
   G. D. Megias, J. E. Amaro, M. B. Barbaro, J. A. Caballero, T. W. Donnelly and I. Ruiz Simo.
   Physical Review D **94**, 093004 (2016)
   DOI: 10.1103/PhysRevD.94.093004
   Times cited (ISI): 2

5. **"Inclusive electron scattering within the SuSAv2-MEC approach"**
   G. D. Megias, J. E. Amaro, M. B. Barbaro, J. A. Caballero and T. W. Donnelly.
   Physical Review D **94**, 013012 (2016)
   DOI: 10.1103/PhysRevD.94.013012
   Times cited (ISI): 4

6. **"Relativistic Modeling of Inclusive Neutrino-Nucleus Interactions in the SuperScaling Approach"**
   G. D. Megias, J. E. Amaro, M. B. Barbaro, J. A. Caballero and T. W. Donnelly.
   Springer Proceedings in Physics **182**, 179 (2016)
   DOI: 10.1007/978-3-319-21191-6_9

7. **"Emission of neutron-proton and proton-proton pairs in neutrino scattering"**
   I. Ruiz Simo, J. E. Amaro, M. B. Barbaro, A. De Pace, J. A. Caballero, G. D. Megias and T. W. Donnelly.
   Physics Letters B **762**, 124-130 (2016)
   DOI: 10.1016/j.physletb.2016.09.021
   Times cited (ISI): 1

8. **"Charged-current inclusive neutrino cross sections in the SuperScaling model including quasielastic, pion production and meson-exchange contributions"**
G. D. Megias, M.V. Ivanov, R. González-Jiménez, O. Moreno, M. B. Barbaro, J. A. Caballero, T. W. Donnelly and J. M. Udías.
Journal of Physics G **43**, 045101 (2016)
DOI: 10.1088/0954-3899/43/4/045101
Times cited (ISI): 8

9. **"Emission of neutron-proton and proton-proton pairs in electron scattering induced by meson-exchange currents"**
I. Ruiz Simo, J. E. Amaro, M. B. Barbaro, A. De Pace, J. A. Caballero, G. D. Megias and T. W. Donnelly.
Physical Review C **94**, 054610 (2016)
DOI: 10.1103/PhysRevC.94.054610
Times cited (ISI): 1

10. **"Charged-current inclusive neutrino cross sections in the SuperScaling Model"**
M. V. Ivanov, G. D. Megias, R. Gonzalez-Jimenez, O. Moreno, M. B. Barbaro, J. A. Caballero, A. N. Antonov, E. M. de Guerra and J. M. Udias.
AIP Conference Proceedings **1722**, 030005 (2016)
DOI: 10.1063/1.4944128

11. **"Charged-current inclusive neutrino cross sections in the SuperScaling Model"**
M. V. Ivanov, G. D. Megias, R. Gonzalez-Jimenez, O. Moreno, M. B. Barbaro, J. A. Caballero, A. N. Antonov, E. M. de Guerra and J. M. Udias.
Journal of Physics Conference Series **724**, 012020 (2016)
DOI: 10.1088/1742-6596/724/1/012020

12. **"Meson-exchange currents and quasielastic predictions for charged-current neutrino-12C scattering in the superscaling approach"**
G. D. Megias, T. W. Donnelly, O. Moreno, C. F. Williamson, J. A. Caballero, R. Gonzalez-Jimenez, A. De Pace, M. B. Barbaro, W. M. Alberico, M. Nardi and J. E. Amaro.
Physical Review D **91**, 073004 (2015)
DOI: 10.1103/PhysRevD.91.073004
Times cited (ISI): 19

13. **"Estimate of the theoretical uncertainty of the cross sections for nucleon knockout in neutral-current neutrino-oxygen interactions"**
A. M. Ankowski, M. B. Barbaro, O. Benhar, J. A. Caballero, C. Giusti, R. Gonzalez-Jimenez, G. D. Megias and A. Meucci.
Physical Review C **92**, 025501 (2015)
DOI: 10.1103/PhysRevC.92.025501
Times cited (ISI): 1

14. **"Star Formation Across the W3 Complex"**
C. G. Román-Zuñiga, J. E. Ybarra, G. D. Megias, M. Tapia, E. A. Lada and J. F. Alves.
The Astronomical Journal **150**, 80 (2015)
DOI: 10.1088/0004-6256/150/3/80
Times cited (ISI): 7

15. **"Extensions of Superscaling from Relativistic Mean Field Theory: the SuSAv2 Model"**
R. González-Jiménez, G.D. Megias, M.B. Barbaro, J.A. Caballero and T.W. Donnelly.

Physical Review C **90**, 035501 (2014)
DOI: 10.1103/PhysRevC.90.035501
Times cited (ISI): 13

16. **"Nuclear effects in neutrino and antineutrino CCQE scattering at MINERνA kinematics"**
G. D. Megias, M.V. Ivanov, R. González-Jiménez, M. B. Barbaro, J. A. Caballero, T. W. Donnelly and J. M. Udías.
Physical Review D **89**, 093002 (2014). [Erratum-ibid. D 91, no. 3, 039903 (2015)]
DOI: 10.1103/PhysRevD.89.093002
Times cited (ISI): 14

17. **"Charged-current quasielastic neutrino cross section on ^{12}C using realistic spectral function and its relation to the scaling function"**
M. V. Ivanov, A. N. Antonov, J. A. Caballero, G. D. Megias, M. B. Barbaro, E. Moya de Guerra and J. M. Udías.
Physical Review C **89**, 014607 (2014)
DOI: 10.1103/PhysRevC.89.014607
Times cited (ISI): 8

18. **"Neutrino and antineutrino CCQE scattering in the SuperScaling Appro-ximation from MiniBooNE to NOMAD energies"**
G. D. Megias, J. E. Amaro, M. B. Barbaro, J. A. Caballero and T. W. Donnelly.
Physics Letters B **725**, 170-174 (2013)
DOI: 10.1016/j.physletb.2013.07.004
Times cited (ISI): 17

19. **"Elastic Neutrino Scattering: Analysis of Charged-Current Neutrino-Nucleon Cross Section extended to Relativistic Fermi Gas Model"**
G. D. Megias and J. A. Caballero.
AIP Conference Proceedings **1541**, 177-178 (2013)
DOI: 10.1063/1.4810835

JOURNAL CITATION REPORT

Articles Published	18
Sum of the Times Cited	95
Sum of Times Cited without self-citations	57
Citing Articles	54
Citing Articles without self-citations	40
Average Citations per Item	5.59
h-index	7

NON-ISI PUBLICATIONS

1. **"Relativistic description of meson-exchange currents and SuperScaling predictions in charged-current neutrino reactions"**
   G. D. Megias, J. E. Amaro, M. B. Barbaro, J. A. Caballero and T. W. Donnelly.
   Proceedings of the XVII International Workshop on Neutrino Factories and Future Neutrino Facilities (NuFact15), Rio de Janeiro, 2015, edited by H. da Motta and J. Morfin, eConf C1508102, 193 (2016)
   DOI: Provisional link

2. **"The role of meson exchange currents in charged current (anti)neutrino -nucleus scattering"**
   M. B. Barbaro, J. E. Amaro, J. A. Caballero, A. De Pace, T. W. Donnelly, G. D. Megias and I. Ruiz Simo.
   Nuclear Theory, Vol. 35 (2016)
   ISSN: 1313-2822

3. **"Charged-current inclusive neutrino cross sections: Superscaling extension to the pion production and realistic spectral function for quasielastic region"**
   M.V. Ivanov, A.N. Antonov, M.B. Barbaro, J.A. Caballero, G.D. Megias, R. Gonzalez-Jimenez, E. Moya de Guerra, J.M. Udias.
   Nuclear Theory, Vol. 34 (2015)
   Nucl.Theor. 34 (2015) 55-61. Conference: C15-06-21.4 ISSN: 1313-2822

4. **"Charge-current and neutral-current quasielastic neutrino (antineutrino) scattering on ^{12}C with realistic spectral and scaling functions"**
   A.N. Antonov, M.V. Ivanov, M.B. Barbaro, J.A. Caballero, G.D. Megias, R. Gonzalez-Jimenez, C. Giusti, A. Meucci, E. Moya de Guerra, J.M. Udias.
   Nuclear Theory, Vol. 34 (2015)
   Nucl.Theor. 34 (2015) 45-54. Conference: C15-06-21.4 ISSN: 1313-2822

5. **"Testing nuclear models via neutrino scattering"**
   M. B. Barbaro, C. Albertus, J. E. Amaro, A. N. Antonov, J. A. Caballero, T. W. Donnelly, R. Gonzalez-Jimenez, M. V. Ivanov, G. D. Megias, E. Moya de Guerra, I. Ruiz Simo and J. M. Udias.
   Nuclear Theory, Vol. 33 (2014)
   ISSN: 1313-2822

6. **"Relativistic descriptions of quasielastic charged-current neutrino-nucleus scattering"**
   G. D. Megias, J. E. Amaro, M. B. Barbaro, J. A. Caballero, T. W. Donnelly and R. Gonzalez-Jimenez.
   Nuclear Theory, Vol. 32 (2013)
   ISSN: 1313-2822

7. **"Relativistic analysis of neutrino/antineutrino CCQE interactions"**
   G. D. Megias, J. E. Amaro, M. B. Barbaro, J. A. Caballero, T. W. Donnelly and R. Gonzalez-Jimenez.
   Abstracts Digital Book of the "XXXIV Reunión Bienal de la Real Sociedad Española de Física", 2013)
   Online publication

8. **Book: "Física de Materiales (Physics of Materials). Contenidos de la asignatura del año 2010-2011"**
A. Domínguez-Rodríguez, A. M. Lara-Bocanegra, G. D. Megias et al.
Ed. Secretariado de Publicaciones de la Universidad de Sevilla, 2011
ISBN: 978-84-694-6047-4

9. **Book: "Física de Materiales: Apuntes y ejercicios (Physics of Materials: Notes and exercises)"**
A. M. Lara-Bocanegra, G. D. Megias, C. Romero-Muñiz et al.
Ed. Bubok Publishing, 2011
ISBN: 978-84-15489-82-5; ISBN e-book: 978-84-15489-83-2

10. **"A Possible Distributed Population Near the Cluster Forming Region W3(OH)"**
C. G. Román-Zúñiga, G. D. Megias, J. F. Alves and E. A. Lada.
Stellar Clusters & Associations: A RIA Workshop on Gaia. Proceedings. Granada, Spain, May 23-27, 2011. Edited by: Alfaro Navarro, E. J.; Gallego Calvente, A. T.; Zapatero Osorio, M. R., pp.148-150, 2011
2011sca..conf..148R

11. **"The mistery of the Floating Stars around W3(OH)"**
C. G. Román-Zúñiga, G. D. Megias, J. F. Alves and E. A. Lada.
Stellar Clusters & Associations: A RIA Workshop on Gaia. Proceedings. Granada, Spain, May 23-27, 2011. Edited by: Alfaro Navarro, E. J.; Gallego Calvente, A. T.; Zapatero Osorio, M. R., pp.387-388, 2011
2011sca..conf..387R

Cosmic Gall

Neutrinos, they are very small.
They have no charge and have no mass
And do not interact at all.
The earth is just a silly ball
To them, through which they simply pass,
Like dustmaids down a drafty hall
Or photons through a sheet of glass.
They snub the most exquisite gas,
Ignore the most substantial wall,
Cold-shoulder steel and sounding brass,
Insult the stallion in his stall.
And, scorning barriers of class,
Infiltrate you and me! Like tall
And painless guillotines, they fall
Down through our heads into the grass.
At night, they enter at Nepal
And pierce the lover and his lass
From underneath the bed - you call
It wonderful; I call it crass.

John Updike
Telephone Poles and Other Poems
1963